On the role of microtubules in cell polarity

A reconstituted minimal system

Vendel, K.J.A.

DOI
10.4233/uuid:34f174d5-f8ad-4bf2-86f7-47660a84fe64

Publication date
2020

Document Version
Final published version

Citation (APA)
Vendel, K. J. A. (2020). *On the role of microtubules in cell polarity: A reconstituted minimal system*. [Dissertation (TU Delft), Delft University of Technology]. https://doi.org/10.4233/uuid:34f174d5-f8ad-4bf2-86f7-47660a84fe64

On the role of microtubules in cell polarity

A reconstituted minimal system

ON THE ROLE OF MICROTUBULES IN CELL POLARITY

A RECONSTITUTED MINIMAL SYSTEM

Proefschrift

ter verkrijging van de graad van doctor
aan de Technische Universiteit Delft,
op gezag van de Rector Magnificus Prof. dr. ir. T. H. J. J. van der Hagen,
voorzitter van het College voor Promoties,
in het openbaar te verdedigen op 21 september 2020 om 12:30 uur

door

Kim Jikke Anna VENDEL

Master in physics,
Universiteit Leiden, Nederland

geboren te Amsterdam, Nederland.

Dit proefschrift is goedgekeurd door de promotor:

prof. dr. M. Dogterom

Samenstelling promotiecommissie:

Rector Magnificus,	voorzitter
Prof. dr. M. Dogterom,	Technische Universiteit Delft, promotor
Onafhankelijke leden:	
Prof. dr. G.H. Koenderink,	Technische Universiteit Delft
Prof. dr. T. Mitchison,	Harvard Medical School
Prof. dr. S. Grill,	MPI-CBG and TU Dresden
Prof. dr. B. Mulder,	AMOLF and Universiteit Utrecht
Dr. E. Spruijt,	Radboud Universiteit
Prof. dr. ir. S. Tans,	Technische Universiteit Delft, reservelid
Overige leden:	
Dr. ir. L. Laan,	Technische Universiteit Delft

Keywords: cell polarity, emulsion droplets, microtubules, reconstitution

Printed by: Gildeprint

Cover: Mirte Vendel

Casimir PhD series 2020-20
ISBN 978-90-8593-447-9

An electronic version of this dissertation is available at
http://repository.tudelft.nl/.

Voor mijn ouders

Magalhaes voer de wereld rond,
langs de Bosporus en de Hellespont,
maar hij zag veel minder dan wij.
Hij zag veel minder dan wij.

Ivo de Wijs - Vroege Vogels Vliegen

CONTENTS

SUMMARY

EVERY living organism consists of cells. Even for the simplest single-cell organism, this cell is extremely complex. Thousands of components (such as DNA, cytoskeletal filaments, proteins, lipids, nutrients and energy) are organized both spatially and temporally to ensure proper functioning of vital cellular processes. One of those processes is pattern formation, or cell polarity. Cell polarity is defined as the morphological and functional differentiation of cellular compartments in a directional manner. This directionality is crucial for processes like cell division, cell migration and cell growth, which require an asymmetric action of the cell. When polarity is inhibited by silencing of cell polarity proteins, cells become deformed and have trouble to function, if viable at all. It is well-known that cell polarity is the result of reaction-diffusion and cytoskeleton-based mechanisms, but the exact mechanisms remain unknown. In this thesis, we focus on the latter, and more specifically on one type of cytoskeletal filaments: microtubules (MTs). Our goal is to study the role of MTs in cell polarity establishment.

Because cells form the basis of life, a question that drives many researchers is "how does a cell work?". Even though this question is short and simple, the answer is not. A wealth of *in vivo*, *in vitro* and theoretical studies have been performed and we are just starting to understand the essential cellular mechanisms like cell polarity. One relatively new research approach are *in vitro* minimal systems. A minimal system is a bottom-up approach where a certain cellular function is reconstituted with the minimal number of components. It provides a way to check hypotheses in an experimental setting which is less complex than a live cell yet more similar to a cell than conventional *in vitro* reconstitutions.

Our aim was to employ the minimal system approach to investigate the minimal requirements for MT-based cell polarity. **We defined polarity in a minimal system as an asymmetric accumulation of proteins at the periphery of a 3D confinement induced by MTs.** We focused on the general mechanisms of cell polarity establishment, rather than to mimic the specific polarity system from a certain organism. To that end, we first investigated what is known about MT-based cell polarity from previous *in vivo, in vitro* and theoretical studies. From this, we concluded that the main ingredients of our minimal system had to be:

1. radially organized MTs in a spherical, cell-sized confinement with a cortex: water-in-oil emulsion droplets,

2. concentration of polarity proteins on the cortex by MTs,

3. positive feedback between cortical polarity proteins and the MT stability.

The next step towards reconstitution of such a system was to optimize existing methods for MT networks inside emulsion droplets. After optimization of the MT visibility and the interaction of polarity proteins with the droplet cortex, we reconstituted MT asters inside water-in-oil emulsion droplets. The MT tips could interact with the droplet cortex through MT-associated proteins (MAPs). We studied the effect of this MT capture on MT stability and MT organization in the droplets, and investigated whether this was enough for an asymmetric accumulation of proteins on the cortex.
Our experiments showed that merely the interaction between MT tips and droplet cortex through MAPs sufficed to locally accumulate the proteins and to stabilize the MT aster position. However, this accumulation was not sustainable and disappeared as soon as a MT detached from the cortex. Several potential improvements were formulated with the help of theoretical models and knowledge from *in vivo* studies. Amongst those ideas are positive feedback between cortical proteins and MT dynamics, molecular motors for directed transport of polarity proteins and variation of the droplet geometry.
In parallel to these attempts to achieve spontaneous symmetry breaking, we explored optogenetics as a tool to mimic external cues that usually initiate cell polarity establishment *in vivo*, such as the chemical gradient originating from a nearby food source. We tested and characterized two light-sensitive protein systems inside emulsion droplets and the preliminary results were promising.

In summary, we reconstituted a basis of a minimal system for MT-based cell polarity and managed to locally accumulate cortical proteins at the tips of MTs that reach the cortex. By this we did not yet achieve a polarized distribution of proteins in our system, but we did make a step towards the realization of that goal.

SAMENVATTING

IEDER levend organisme bestaat uit cellen. Zelfs voor het meest simpele eencellige organisme is die cel immens complex. Duizenden componenten (zoals DNA, cytoskelet, eiwitten, lipiden, voedingsstoffen en energie) moeten zowel in ruimte als in tijd worden georganiseerd om te zorgen dat alle processen in een cel goed kunnen verlopen. Een van die processen is patroonvorming, ook wel polariteit genoemd. Polariteit van cellen is gedefinieerd als "morfologische en functionele differentiatie van cellulaire componenten met een ruimtelijke scheiding". In andere woorden: componenten in de cel worden asymmetrisch georganiseerd. Deze asymmetrie is noodzakelijk voor processen in de cel waarbij de richting relevant is, zoals groei, deling en voortbeweging. Experimenten waarbij polariteit onmogelijk was gemaakt door polariteitseiwitten uit te schakelen resulteerden in vervormde cellen die abnormaal functioneerden, als ze al levensvatbaar waren. We weten inmiddels dat polariteit in een cel het resultaat is van zowel reactie-diffusie mechanismes als van mechanismes gebaseerd op het cytoskelet. Het cytoskelet (bestaande uit microtubuli, actine en intermediaire filamenten) zijn eiwitpolymeren binnenin de cel. Ze geven de cel bijvoorbeeld stevigheid en vorm of vormen snelwegen waarlangs eiwitten getransporteerd kunnen worden. In deze thesis focussen we ons op microtubuli en hun rol in cel polariteit.

Omdat cellen de basis vormen van het leven worden vele onderzoekers gedreven door de vraag "hoe werkt een cel?". Hoewel dit een korte en simpele vraag is, is het antwoord dat geenszins. Een enorme hoeveelheid *in vivo*, *in vitro* en theoretische studies zijn al uitgevoerd en toch beginnen we nog maar net de meest essentiële cellulaire processen te begrijpen. Een relatief nieuwe onderzoeksmethode zijn zogenaamde minimale systemen. Dit is een bottom-up aanpak waarbij een bepaalde functie van de cel wordt nagebouwd met het minimaal aantal benodigde componenten. Deze aanpak biedt de mogelijkheid om hypotheses te testen in een kunstmatige en gecontroleerde omgeving zonder de complexiteit van een levende cel. Tegelijkertijd is het minimale systeem wel complexer en dus realistischer dan conventionele *in vitro* experimenten, zoals eiwitten op een glasplaatje.

Ons doel was om de minimale vereisten te bestuderen om polariteit in een cel te bereiken door middel van microtubuli. Dit deden we met het eerder genoemde minimale systeem. In dit geval definiëerden we polariteit van het minimale systeem als volgt: **een asymmetrische verdeling van eiwitten in de periferie van een driedimensionale omgeving met de afmetingen van een cel, waarbij die verdeling tot stand is gebracht door microtubuli**.

In ons onderzoek keken we naar de algemene mechanismes van polariteit in cellen, niet naar één specifiek celtype of eiwit. Om te beginnen hebben we ons verdiept in wat eerdere onderzoeken hebben opgeleverd omtrent de rol van microtubuli in polariteit.

Daaruit concludeerden we de volgende onmisbare ingrediënten voor ons minimale systeem:

1. radiaal georganiseerde microtubuli in een afgesloten bolvormige omgeving met de afmetingen van een cel (ongeveer 20 µm in diameter): een microscopisch klein water-in-olie emulsie druppeltje,
2. concentratie van polariteitseiwitten door microtubuli op de wand van de druppeltjes,
3. positieve feedback tussen deze eiwitten en de stabiliteit van microtubuli die in contact zijn met de wand van de druppel.

De volgende stap was om al bestaande methodes te optimaliseren waarmee microtubuli in water-in-olie druppels worden gevangen. We verbeterden onder andere de zichtbaarheid van microtubuli en het binden van polariteitseiwitten aan de wand van de druppels. Na deze optimalizatie konden we radiaal georganiseerde microtubuli in microscopisch kleine water-in-olie druppeltjes bestuderen. Op de wand van deze druppels zaten specifieke eiwitten. De uiteindes van de microtubuli gingen via deze eiwitten een verbinding aan met de wand van de druppeltjes. Dit noemen we gevangen microtubuli, een fenomeen dat veel voorkomt in cellen. We vroegen ons af wat het effect van gevangen zijn was op de stabiliteit en organisatie van microtubuli in de druppels. Ook was de vraag of het uiteindelijk kon leiden tot een asymmetrische verdeling van eiwitten op de wand van de druppel.
Onze experimenten in druppels hebben laten zien dat enkel de interactie tussen microtubuli en de cortex van de druppels genoeg was om de positie van de microtubuul aster te stabiliseren en om lokaal eiwitten te concentreren. Echter was dit laatste maar van korte duur. De concentratie verdween zodra de microtubule losliet van de cortex. We stellen verschillende verbeteringen voor, gebaseerd op *in vivo* experimenten en theoretische modellen. Onder deze ideeën zijn het invoeren van positieve feedback tussen microtubuli en eiwitten op de cortex, moleculaire motoren om eiwitten langs de microtubuli naar de cortex te transporteren en het aanpassen van de vorm van de druppels.

Tegelijkertijd werkten we aan het realiseren van een uitwendige stimulus voor de polarisatie. Cellen reageren namelijk vaak op uitwendige factoren, zoals een gradient van voedingsstoffen, door te polariseren om in de juiste richting te bewegen. Ons experimentele equivalent van zo'n stimulus is gevonden in de optogenetica. We hebben twee licht-gevoelige eiwitten gekarakteriseerd om te onderzoeken of ze geschikt zijn om te gebruiken als externe stimulus voor polarisatie in de druppels. De eerste resultaten hiervan waren veelbelovend.

Samengevat, we hebben een basis gecreëerd voor een minimaal systeem voor cel polariteit gebaseerd op microtubuli, waarbij we lokaal eiwitten konden concentreren op de wand van een druppel met behulp van een microtubuul. Een gepolariseerde verdeling van eiwitten op de cortex van druppels is hiermee nog niet bereikt, maar we hebben een aantal belangrijke stappen gezet richting de verwezenlijking van dat doel.

1

INTRODUCTION

Kim Vendel, Sophie Tschirpke, Liedewij Laan and Marileen Dogterom

'Ik,' zei de slak op een keer tegen de mier,
'ga net zolang oefenen tot ik harder kan lopen dan jij.'
'Nou...' zei de mier en hij keek de slak van terzijde aan,
'dan zou ik maar meteen beginnen.'

Toon Tellegen

Cell polarity – the morphological and functional differentiation of cellular compartments in a directional manner – is required for processes such as orientation of cell division, directed cellular growth and motility. How the interplay of components within the complexity of a cell leads to cell polarity is still heavily debated. In this thesis, we focus on one specific aspect of cell polarity: the non-uniform accumulation of proteins on the cell membrane. In cells, this is achieved through reaction–diffusion and/or cytoskeleton-based mechanisms. We will focus on the latter, where cellular components (i.e. proteins) are actively transported by microtubules and/or actin filaments to specific locations in the cell. In this chapter, we introduce microtubules and discuss what is known about their role in cell polarity establishment from both in vitro and in vivo studies. Next, we examine how minimal systems – in vitro reconstitutions of a particular cellular function with a minimal number of components – are designed, how they contribute to our understanding of cell polarity (i.e. protein accumulation), and how they complement in vivo investigations. Finally, we outline an approach to reconstitute a minimal system for microtubule-based cell polarity.

Parts of this chapter have been published in Journal of Cell Science **132**, 4 (2019) [Vendel et al., 2019].

1

1.1. THE CYTOSKELETON

THE cytoskeleton is a network of protein filaments in the cytoplasm of cells. These filaments are responsible for among others the cells shape and rigidity, for transport of proteins through cells and they play a role in processes like cell migration. Three different types of cytoskeletal filaments exist in eukaryotic cells: actin filaments, intermediate filaments and microtubules (MTs). The three consist of different proteins and as a result they have different structural properties and functions in the cell (Fig. 1.1).

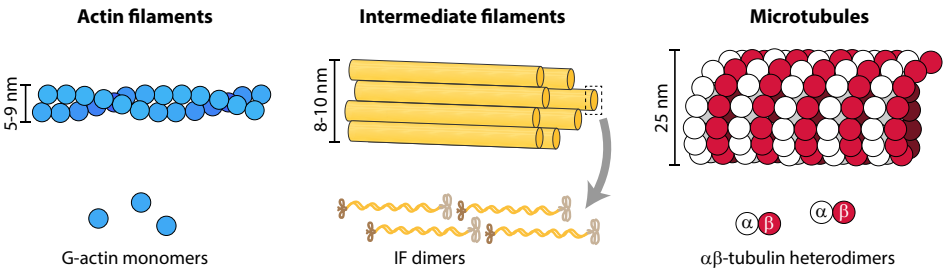

Figure 1.1: Schematic pictures of the three types of cytoskeletal filaments and the subunits they polymerize from.

Actin filaments (AFs) are protein polymers consisting of globular actin (G-actin) subunits. The AFs are formed by two strands of polymers that are wrapped around each other into a helix with a diameter of 5-9 nm (Fig. 1.1). All G-actin subunits are stacked on top of each other, therefore AFs have a polarized structure with a so-called barbed and a pointed end. Because of the geometrical structure, it is easier for G-actin subunits to be incorporated at the barbed end so the AF grows faster on this end. G-actin monomers are ATP-bound when they are incorporated in the AF. Over time, ATP is hydrolyzed to ADP, which makes the AF less stable. Because the barbed end grows faster, it contains relatively more ATP-bound subunits than the pointed end. Therefore, depolymerization of the AF happens more often at the pointed end. When an AF grows at the barbed end and simultaneously shrinks at the pointed end, treadmilling of the AF can occur.
A single AF is relatively floppy with a persistence length of 18 micrometer, therefore AFs usually organize into bundles, 2D networks or 3D gels. In this arrangement, AFs are responsible for many functions concerning cell morphology, for example cell motility, cell division, organelle movement and the establishment of cell shape. For those purposes, AFs are generally most abundant at the cell periphery, close to and often interacting with the cellular membrane. Many actin binding proteins interact with AFs, one of the most important ones is the molecular motor myosin. AFs together with myosin forms a contractile network, involved in e.g. cytoplasmic flows and cell migration.

Intermediate filaments (IFs) owe their name to their diameter which is with 8-10 nm in between that of the other two cytoskeletal filaments. IFs are generally a few microns long and even though there is some evidence for dynamic properties, most IFs are fully

polymerized and very stable. The role of IFs is mostly a structural one, by providing mechanical strength to cells and tissues. To this end, IFs interact with both MTs and actin filaments. IFs are composed of different yet homologous proteins, depending on the cell type, in contrast to the other cytoskeletal filaments that are always build up from either actin or tubulin dimers. The many different observed IFs are categorized into six types, examples are keratins and vimentins. Another difference with the other filaments is that IFs do not have a nucleotide triphosphate binding site, in contrast to ATP-bound actin and GTP-bound tubulin.

Finally, MTs are the stiffest and thickest of the three cytoskeletal filaments, with a persistence length in the order of magnitude of 1 mm and a diameter of 25 nm [Venier et al., 1994, Kurz and Williams Jr, 1995, Mickey and Howard, 1995, Felgner et al., 1996, Dogterom and Yurke, 1997, Felgner et al., 1997, Fygenson et al., 1997, Cassimeris et al., 2001, Janson and Dogterom, 2004a,b, Pampaloni et al., 2006, Van Den Heuvel et al., 2007]. In mammalian interphase cells, MTs are generally organized in a radial manner, from the cell interior towards the cell periphery. The radial MTs play an important role in transport of cellular components (e.g. proteins and even organelles) through the cell. This transport is performed by molecular motors like dynein and kinesin that walk along a MT and take their cargo along. During cell division however, a totally different MT organization is needed to form the mitotic spindle and pull the chromosomes apart. And during cell migration, the majority of MT ends is connected to the leading edge of the migrating cell. So the organization of MTs in a cell depends strongly on the state of the cell and the corresponding functionality of the MTs.
In this section, we will discuss the properties of MTs and the proteins that interact with MTs to fulfill their function in cells.

MICROTUBULE NUCLEATION AND DYNAMICS

The MT cytoskeletal arrangement in a cell needs to be quickly adjusted in case of changing functionality (for example during cell division for formation of the mitotic spindle). To rearrange quickly, MTs must be highly dynamic. The constant alternation between polymerization and depolymerization of MTs is called dynamic instability [Mitchison and Kirschner, 1984a] and it is characterized by four parameters: polymerization rate, depolymerization rate, catastrophe rate and rescue rate. This dynamic behavior of MTs is possible because they are protein polymers with $\alpha\beta$-tubulin heterodimers as building blocks. The GTP-bound heterodimers assemble into a hollow cylinder with 25 nm diameter, consisting of about 13 protofilaments [Tilney et al., 1973]. The number of protofilaments can vary depending on cell type *in vivo* or experimental conditions *in vitro* [Tilney et al., 1973, Burton et al., 1975, Pierson et al., 1978, Wade et al., 1990, Andreu et al., 1992, Raviv et al., 2007, Cueva et al., 2012]. Since the $\alpha\beta$-tubulin heterodimers are stacked in a head-to-tail fashion in all protofilaments (Fig. 1.2), MTs have a polarized structure with β-tubulin exposed at the plus end and α-tubulin at the minus end. As a consequence of this polarity, MTs grow faster on their plus end than their minus end *in vitro*, and also the plus end catastrophe rate is higher [Desai et al., 1997]. *In vivo* however, MTs usually only grow on their plus ends. The difference between *in vivo* and *in vitro* is explained by regulation through MT associated

proteins (MAPs). In addition, *in vivo* MTs are usually anchored at a MT nucleation site with their minus ends.

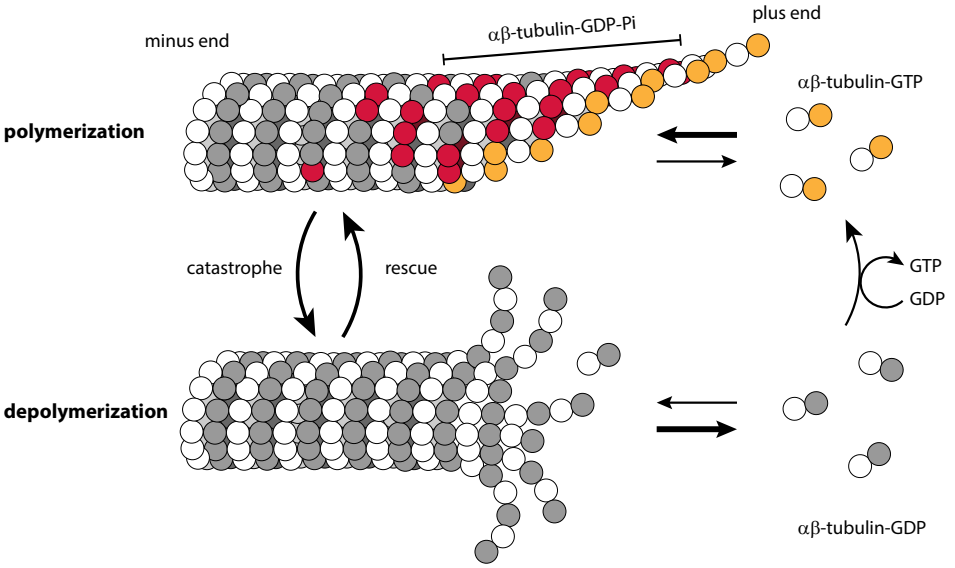

Figure 1.2: Dynamic instability of MTs. During polymerization, GTP-bound $\alpha\beta$-tubulin heterodimers are incorporated at the MT plus end. Over time, GTP is hydrolyzed into GDP, and as a consequence the MT lattice consists of GDP-bound tubulin and the MT tip of GTP-bound tubulin. The GDP-P$_i$ region of the MTs is also the place where end-binding proteins (p. 7) can bind. MTs can switch from polymerization to depolymerization (catastrophe) and the other way around (rescue). Adapted from [Kumar and Wittmann, 2012].

After addition of new GTP-bound heterodimers to the MT, the GTP which is bound to β-tubulin hydrolyzes. As a result, MTs have a GDP-bound lattice and a GTP-bound tip region (Fig. 1.2). Since the GTP cap is structurally different from the GDP-bound MT lattice, it has major influence on MT dynamics and the binding affinity of specific proteins. It is shown that GTP-bound tubulin has a slightly more straight conformation than the more bent GDP-tubulin [Caplow et al., 1994, Müller-Reichert et al., 1998, Gigant et al., 2000]. As a consequence, the GTP cap of a MT is more stable than the MT lattice. The size of the GTP cap continuously fluctuates [Howard and Hyman, 2009], and when it disappears the MT undergoes a catastrophe. Some of the energy from GTP hydrolysis is stored in the MT lattice, because the bent GDP-dimer conformation is not possible inside the geometry of the lattice. The stored energy is released during depolymerization, leading to rapid depolymerization, curved MT ends and force production by disassembling MTs [Grishchuk et al., 2005].

In contrast to the elongation of existing MTs, the nucleation of new MTs is less understood. As for all polymerization processes, there is a nucleation barrier that has to be overcome [Fygenson et al., 1995, Wieczorek et al., 2015, Roostalu and Surrey, 2017]. Because of this barrier, spontaneous MT nucleation *in vitro* occurs at tubulin concentrations above 20 µM, while the tubulin concentration minimally needed for MT

elongation is only 1 µM [Voter and Erickson, 1984]. The typical tubulin concentration in cells is below 20 µM, so there are several mechanisms *in vivo* to stimulate MT nucleation. One is templated nucleation, with examples like the gamma tubulin ring complex (γTuRC, Fig. 1.3) [Moritz et al., 1995, 2000, Kollman et al., 2011, Teixidó-Travesa et al., 2012, Lin et al., 2015], axonemes [Walker et al., 1988] and pre-existing MTs which are severed by enzymes [Srayko et al., 2005, McNally et al., 2006, Lindeboom et al., 2013]. Such templates lower the nucleation barrier, e.g. by bringing together tubulin dimers to more easily get a critical nucleus, or by providing a stable cap on the MT minus-end that prevents depolymerization [Keating and Borisy, 2000]. In addition to templated nucleation, another important mechanism to stimulate MT nucleation in cells are MT-stabilizing MAPs, which enhance longitudinal or lateral contacts between heterodimers [Wieczorek et al., 2015, Roostalu and Surrey, 2017]. Those stabilized contacts enable a more rapid formation of a critical nucleus and hence a lower barrier for MT nucleation. Examples of such MAPs are XMAP215 family proteins, CAMSAP and CLASP [Wieczorek et al., 2015]. In the next section, we take a closer look at the main MT nucleator in animal cells: the centrosome, which employs a combination of templated nucleation and MAPs.

CENTROSOMES AS MICROTUBULE NUCLEATION SITES

Centrosomes are one of the most common MT organizing centers (MTOCs) inside cells. They consist of two orthogonally oriented centrioles, surrounded by a dense amorphous mass [Woodruff et al., 2014] containing hundreds of proteins [Conduit et al., 2015], called the pericentriolar material (PCM). Centrioles are cylindrical structures and in a top view of the cylinder show a spoke-like structure consisting of SAS6 proteins [Rale et al., 2017]. Each of the nine spokes is connected to a blade of MT triplets at the end [Rale et al., 2017]. Ever since the first observations of MT nucleation by centrosomes [McIntosh, 1983, Mitchison and Kirschner, 1984b], the question has been how centrosomes nucleate MTs.

In vitro experiments with purified centrosomes and tubulin showed that dynamic MTs can nucleate from a centrosome at concentrations where spontaneous nucleation of single MTs is impossible [Mitchison and Kirschner, 1984b]. But how does the centrosome lower the nucleation barrier? γ-tubulin was found to be a PCM component that is involved in MT nucleation [Joshi et al., 1992]. γ-tubulin is a member of the tubulin protein family which is not incorporated in the MT lattice but binds to the MT minus end [Wiese and Zheng, 2006]. Later, immuno electron microscopy (EM) tomography studies revealed that γ-tubulin organizes in ring structures called the γ-tubulin ring complex (γTuRC) [Moritz et al., 1995, 2000], as shown in Fig. 1.3A. The diameter of such a γTuRC is 25-30 nm, it has a 13-fold symmetry (giving rise to the 13 protofilaments usually found for MTs in cells and from purified centrosomes, and was located at the minus ends of MTs nucleating in the PCM [Moritz et al., 2000].
There was however not yet convincing evidence that the γTuRC indeed serves as the template for MT nucleation in cells. It was even found that γTuRCs are inefficient at nucleating MTs *in vitro* [Woodruff et al., 2014, Wiese and Zheng, 2006] and that knockdown of γ-tubulin in cells does not abolish MT assembly completely [Strome et al.,

2001, Hannak et al., 2002, Lüders et al., 2006, Rogers et al., 2008], suggesting that other mechanisms for MT nucleation in the PCM exist.

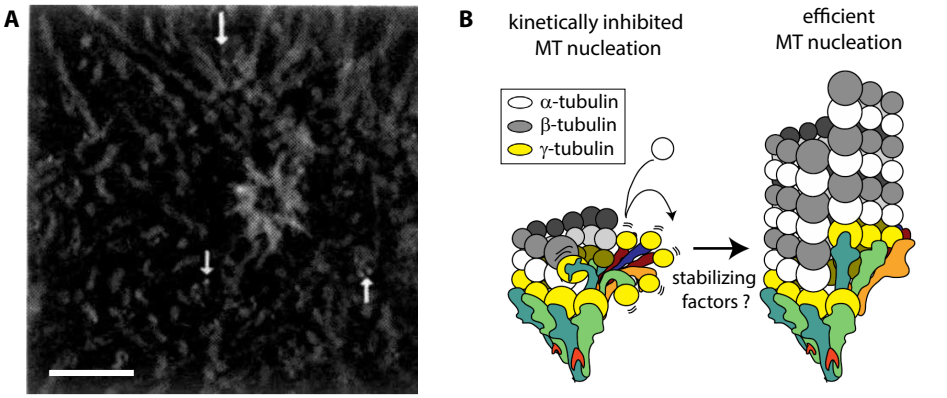

Figure 1.3: The γTuRC. **(A)** Computer generated reconstruction of a γTuRC imaged with immuno-electron microscopic tomography by Moritz et al. [Moritz et al., 1995]. Scalebar is 200 nm. **(B)** Schematic representation from Consolati et al. [Consolati et al., 2019] of the two configurations of γTuRC: open (left) or closed (right). The closed configuration is hypothesized to be more efficient at MT nucleation.

Recently, more has been learned about the MT nucleating abilities of γTuRCs. *In vitro* reconstitutions with purified γTuRCs elucidated that γTuRC-templated MT nucleation is stochastic and more efficient than spontaneous nucleation [Consolati et al., 2019, Thawani et al., 2019]. The critical nucleus on γTuRC consists of 3-4 $\alpha\beta$-tubulin dimers [Thawani et al., 2019]. Still, γTuRC-templated nucleation was not as efficient as MT elongation [Consolati et al., 2019]. An explanation for this inefficient nucleation comes from cryo-electron microscopy (cryo-EM) [Consolati et al., 2019, Wieczorek et al., 2020]. Both labs created high-resolution structure images of human γTuRC. Those images show proof of an open and a closed configuration of the γTuRC, as schematically pictured in Fig. 1.3B. Hypothesized is that only the closed configuration can nucleate a MT. Regulatory processes, for example through MAPs, could control the level of MT nucleation in a cell by closing the γTuRC configuration. This would explain the relatively low MT nucleating efficiency of purified γTuRCs *in vitro*.

An alternative hypothesis for MT nucleation in absence of γ-tubulin is that proteins from the XMAP215 and TPX2 families are involved [Woodruff et al., 2017]. These localize to the PCM and are known to regulate MT dynamics. A recent *in vitro* experiment with purified *C. elegans* proteins showed that under macromolecular crowding, SPD5 - a key PCM protein - phase separates into spherical condensates [Woodruff et al., 2015]. Next, ZYG-9 (from the chTOG family) and TPXL-1 (a TPX2 family protein) are recruited, resulting in a 4 times higher concentration of tubulin within the condensates compared to the surrounding solution [Woodruff et al., 2017]. This increased tubulin concentration is enough for MT aster nucleation. A review on centrosomal proteins that undergo phase transitions can be found in [Rale et al., 2017].
One question is how MTs are anchored at the condensates to withstand the strong pulling forces that are exerted on the MTs, for example during mitosis. A possible ex-

planation is found in the solidification of the SPD5 condensates in time [Woodruff et al., 2017]. Initially, condensates show liquid-like behaviour, where (fluorescent) SPD5 can diffuse around, components are exchanged with the bulk solution and condensates can coalesce [Woodruff et al., 2017]. After about 10 minutes this behaviour disappears. Since other PCM proteins can still move around in the solidified SPD5 condensates, Woodruff et al. hypothesize that pores exist [Woodruff et al., 2017]. So the condensates would provide a porous platform for other PCM proteins, that can nucleate MTs by concentration of tubulin, and is strong enough to withstand pulling forces on MTs.

Summarizing, it is not yet entirely clear how centrosomes nucleate and organize MTs. It is most likely a combination of γTuRCs and MT-stabilizing MAPs. Further investigation is still needed on how big the role of phase-separation in centrosome functioning is. In our *in vitro* experiments, we either used purified centrosomes to nucleate radial MT arrays or artificial MTOCs consisting of microbeads coated with centrosomal proteins that we will introduce in Sec. 2.2.2.

MICROTUBULE ASSOCIATED PROTEINS

Initially, MT associated-proteins (MAPs) were discovered because they copurified with MTs, and only later it became clear what the functionalities of MAPs are. MTs are involved in many cellular processes, and MAPs are responsible for the temporal and spatial regulation of MTs to arrange the correct MT conformation for a certain process at the right time [Alfaro-Aco and Petry, 2015]. To this end, MAPs locally regulate MT nucleation, dynamics, stability and interactions with other cellular components [Kinoshita et al., 2001, Faivre-Moskalenko and Dogterom, 2002, Jiang and Akhmanova, 2011, Akhmanova and Steinmetz, 2015]. Examples of MAPs are molecular motors (e.g. dynein and kinesin) that transport cargo along the MT but also have an effect on MT dynamics, MT polymerases from the XMAP215 family, end-binding proteins that associate with the MT plus end (see next section) and the tau protein that can connect MTs and actin filaments [Bieling et al., 2007, Honnappa et al., 2009, Zanic et al., 2013, Duellberg et al., 2014, Alfaro-Aco and Petry, 2015, Elie et al., 2015]. For the experiments in this thesis, we used end-binding proteins, plus-end trackers and a protein called MAP7 (Sec.2.2.3 and Chapter 3). More about the role of MAPs in cell polarity is discussed in Sec. 1.2.

END-BINDING PROTEINS

End-binding (EB) proteins are the only type of MAPs that autonomously track growing MT tips by transient interaction with the tip region [Bieling et al., 2007] (Fig. 1.4A). EB proteins are conserved in all eukaryotes, like the fission yeast Mal3p, the budding yeast Bim1p and the three EB1/EB2/EB3 homologs found in mammalian cells. The association time of EB to a MT tip is in the subsecond regime (dwell times around 0.28 s were reported for Mal3p *in vitro* by Bieling et al. [Bieling et al., 2007]). Despite those short dwell times, EB proteins have a strong influence on MTs. EB itself affects MT dynamics, and EB can bind MT plus-end tracking proteins (+TIPs), which can bind

1

MT tips only through EB and influence the MTs as well. *In vitro* experiments with purified tubulin demonstrated increased growth velocitiy, catastrophe rate and rescue rate by EB [Nakamura et al., 2001, Tirnauer et al., 2002, Ligon et al., 2003, Bieling et al., 2007, Manna et al., 2008, Vitre et al., 2008, Komarova et al., 2009]. *In vivo* however, the influence of EB on MT dynamics varied a lot between the different experimental systems. This was most likely the effect of the +TIPs that are present in a cell, but not in an *in vitro* experiment with purified tubulin. We will discuss the effect of +TIPs further in the next section.

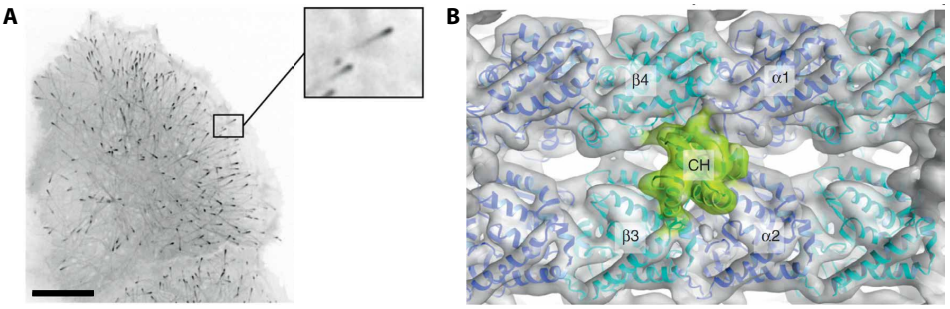

Figure 1.4: End-binding proteins binding to MTs. **(A)** EB1-GFP comets track growing MT tips in a tissue-culture cell from [Kumar and Wittmann, 2012]. The scalebar is 10 µm. **(B)** Cryo-electron microscopy reconstruction of tubulin (greyscale) with the atomic tubulin structure (purple and blue) and the location where the CH-domain of EB can bind to the MT (green), from [Maurer et al., 2012].

EB binds the MT through its N-terminal calponin homology (CH) domain [Hayashi and Ikura, 2003]. Cryo-electron microscopy revealed that EB binds MTs in between protofilaments, except at the seam [Maurer et al., 2012] (Fig. 1.4B). Each EB contacts four tubulin dimers, close to the β-tubulin GTP binding site. In that position it can sense the nucleotide state, which is suggested to influence EB binding. Why exactly EB binds to the growing MT tip is not yet resolved, but the most accepted theory involves the GTP cap [Duellberg et al., 2016]. Fluorescence imaging of *in vitro* MTs has shown a lag of several tens of nanometers between the actual tip of a MT and the so-called EB comet (the accumulation of EB proteins at the MT tip) [Maurer et al., 2014]. This is explained by a two-step mechanism for GTP hydrolysis (from GTP via GDP-P$_i$ to GDP [Maurer et al., 2014]) where the MT has a slightly different conformation in the three stages. The hypothesis is that EB has the highest affinity for the GDP-P$_i$ conformation, so not for the actual GTP cap (Fig. 1.2). This was mainly studied with slowly hydrolyzable GTP analogs like GMPCPP and GTPγS [Zanic et al., 2009, Maurer et al., 2011]. For physiological salt concentrations, there was no increased affinity for GMPCPP, but a strongly increased one for GTPγS [Maurer et al., 2011]. GMPCPP-bound tubulin is believed to resemble the GTP-tubulin tip of a MT, while GTPγS resembles the GDP-P$_i$ cap [Maurer et al., 2011]. This hypothesis of nucleotide-sensitive binding of EB is supported by the finding that the three mammalian EB homologs have preferred binding sites with different nucleotide properties [Roth et al., 2019a].

On the other hand, there is an alternative hypothesis from Reid et al. that EB is not binding the GDP-P$_i$ state, but rather the tapered MT tip structures [Reid et al., 2019].

EB would have a preference for open, structurally disrupted MTs compared to closed and intact MTs. After binding to edge sites of the MT, the addition of new GTP-bound tubulin dimers stabilizes the EB1 binding by completing the four tubulin dimer configuration [Reid et al., 2019] (Fig. 1.4). GTP hydrolysis disturbs the stable binding site of four tubulin dimers, leading to dissociation of EB. Because the final number of EB binding sites on the MT lattice is higher than at the tapered tip, the EB comet peak intensity would still be expected a few tens of nanometers behind the very tip of the MT.

MICROTUBULE PLUS-END TRACKING PROTEINS (+TIPS)

Many more plus-end tracking proteins (+TIPs) exist than aforementioned EB proteins. +TIPs are MAPs that only bind to growing MT ends, and thus they can have very different regulatory functions from MAPs that bind the complete MT lattice. For that reason, +TIPs are especially involved in regulation of MT dynamics at the tip and in connecting MTs to other cellular components like membranes, actin filaments, regulatory proteins and the kinetochore. A few examples of +TIPs are the MT-actin crosslinking factor (MACF, see Fig. 1.5 for an example), cytoplasmic linker protein (CLIP-170), MT dypolymerizing MCAK, and the MT stabilizing Cytoplasmic Linker Associated Proteins (CLASP). Most +TIPs cannot autonomously tiptrack growing MT ends, but rely on EB. The majority of those +TIPs binds EB through a short motif of four amino acids: Serine-x-Isoleucine-Proline (SxIP), where x can be any amino acid [Honnappa et al., 2009]. Isoleucine and proline are the most important residues of the SxIP motif, which engage in hydrophobic interactions with EB [Kumar and Wittmann, 2012]. Usually, +TIPs contain multiple tandemly repeated SxIP motifs to increase the affinity for EB [Honnappa et al., 2009].

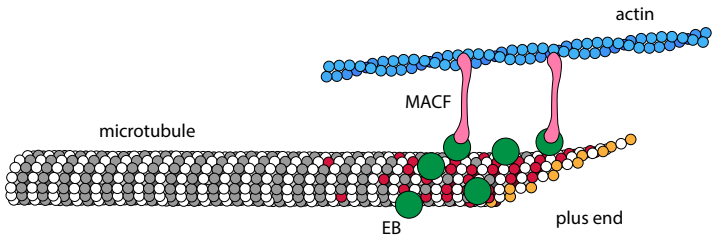

Figure 1.5: Schematic picture of a +TIP, the MT-actin crosslinking factor (MACF, pink), which binds the plus end of MTs through EB (green) and crosslinks it with actin filaments (blue). In this figure, EB binds to the GDP-P_i tubulin dimers (red) close to the MT tip.

For the experiments in this thesis, we often employed the EB-binding capability of +TIPs to engineer proteins for our *in vitro* experiments. Truncations of +TIPs were designed, which contained the SxIP motifs and any other desired part of the proteins. An example is the 18 amino acid truncated MACF2 peptide, which contains SxIP motifs to bind EB and to which a histidine-tag was added so we could recruit the truncated protein *in vitro* to anything with a nickel-NTA anchor. The *in vivo* function of the protein to bind actin filaments was not relevant and hence that part of the pro-

tein sequence was left out. More about such designed proteins will be discussed in the chapters where they are used in the experiments.

1.2. MICROTUBULE-BASED CELL POLARITY

ACCORDING to the second law of thermodynamics, any system of particles naturally tends to maximize its entropy, increasing the disorder of the system. How is it then possible that cells are intracellularly structured and organized? Spatial organization in cells – the non-uniform distribution of cellular components – is the result of dynamic interactions between molecules under dissipation of energy [Karsenti, 2008]. Cell polarity is a special form of spatial organization that refers to the morphological and functional differentiation of cellular compartments in a directional manner [Théry et al., 2006], which is important for processes where spatial separation is necessary (e.g. growth, division, differentiation and motility). This is illustrated by epithelial cells that must be highly polarized to function as a barrier between two totally different environments: their apical side facing the external environment and their basal side the extracellular matrix. This strongly polarized morphological and functional distinction is accomplished by temporal and spatial localization of polarity proteins and other molecules [Wen and Zhang, 2017].

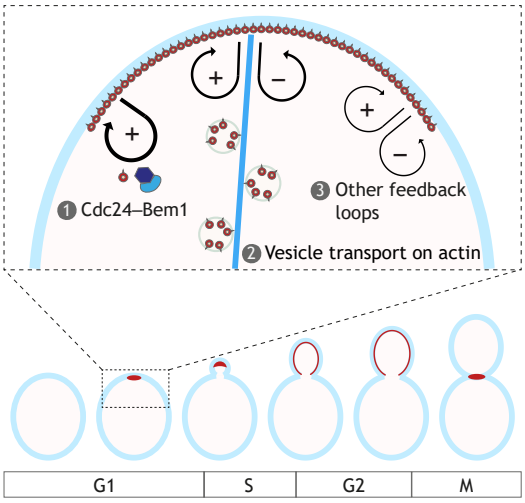

Figure 1.6: Schematic of a budding yeast cell with three different feedback mechanisms: reaction-diffusion-based feedback through Cdc24 and Bem1, cytoskeleton-based through actin and a third more unknown one. From [Vendel et al., 2019]

During cell polarity, not only polarity proteins are spatially reorganized, yet also other cellular components like phospholipids, cytoskeletal filaments, Golgi structures, vesicles and regulatory factors. In this thesis, we will focus on only one specific aspect of cell polarity: the non-uniform accumulation of specific proteins at the cell membrane. An example is the accumulation of the cell division control protein Cdc42 at the loca-

tion of the bud-site in budding yeast cells, acting as a division precursor [Mazel, 2017], see Fig. 1.6.

Cells employ reaction–diffusion and cytoskeleton-based mechanisms to distribute and accumulate proteins (i.e. establish polarity). In reaction–diffusion systems, components are transformed into each other by chemical reactions and are moving in space by diffusion. Under specific conditions, these systems can establish polarity. The most famous example is the Min system employed by bacteria to determine the location of the division plane. In cytoskeleton-based processes, cellular components (e.g. proteins) are actively transported by MTs and actin filaments to specific locations in the cell. For many systems however, a combination of reaction-diffusion and cytoskeleton based mechanisms leads to cell polarity. For the accumulation of Cdc42 at the future bud location in budding yeast mentioned before, at least three partially independent feedback loops have been identified (see Fig. 1.6) [Bose et al., 2001, Wedlich-Soldner et al., 2003, 2004, Slaughter et al., 2009, Howell et al., 2012, Rubinstein et al., 2012, Freisinger et al., 2013, Klünder et al., 2013, Wu and Lew, 2013, Martin, 2015]: a feedback loop based on a reaction–diffusion system, the so-called GDI-based mechanism, another one based on the actin cytoskeleton [Wedlich-Soldner et al., 2003] and a third (weak) feedback loop, which is at least partly independent from both the GDI and actin [Bendezú et al., 2015]. For budding yeast the relation between the three feedback mechanisms and the relative importance are still unknown. The same is true for other cells.

Cells are complex systems, hence combinations of *in vivo*, *in vitro* and *in silico* approaches are required to elucidate the principles of polarity establishment (Box 1). In this chapter, we will discuss the role and importance of *in vitro* approaches in general, and minimal system approaches in particular. Minimal systems are a subgroup of the *in vitro* methodology in which a particular cellular function is reconstituted with a minimal number of required components. The examination of a reaction-diffusion system, the Min protein system in Escherichia coli, can be found in Vendel et al. [Vendel et al., 2019]. In that review, we show what led to the first reconstitutions in 2008 [Loose et al., 2008] and discuss what the follow-up investigations taught us. In this thesis however, we will limit ourselves to how cytoskeleton-based processes establish polarity.

Polarized cells are characterized by an asymmetric internal organization of components, and the cytoskeleton is often also asymmetrically oriented [Li and Gundersen, 2008]. A main role of the cytoskeleton in polarity establishment and maintenance is the active, directed transport of cargo (e.g. proteins, vesicles or even organelles) through the cell; for example, by motor proteins walking along cytoskeletal filaments or cytoplasmic flows that are generated by cytoskeletal network contractions [Theurkauf, 1994, Serbus et al., 2005, Yi et al., 2013, Suzuki et al., 2017]. Both MTs and actin filaments are involved in cell polarity, but this thesis focuses on MTs – highly dynamic intrinsically polarized filaments whose properties can be influenced by a wealth of MT-associated proteins (MAPs). Besides MAPs themselves, post-translational modifications of tubulin influence MT dynamics by regulating MAP binding or affecting the behavior of molecular motors [Westermann and Weber, 2003, Janke and Bulinski,

2011, de Forges et al., 2012].

Although MT organization has been reconstituted in minimal systems, a minimal system for MT-based polarity has not yet been established. We will examine what we have learned from *in vivo* and *in vitro* approaches, and discuss which steps towards a minimal system still need to be taken.

Box 1. Interplay of *in vivo*, *in vitro* and *in silico* approaches
In vivo experiments deal with complex living systems, reveal the components behind cellular functionalities and characterize their interplay within an organism. Traditionally, this is how biological experiments are conducted. In addition, *in vitro* experiments play an increasingly important role. *In vitro* experiments use purified components to dissect exact molecular mechanisms and obtain more quantitative information. Both *in vivo* and *in vitro* results contribute to the design of *in silico* models. Based on the knowledge from *in vivo* and *in vitro* experiments and guided by model predictions, minimal systems can be established. Minimal systems are specific types of *in vitro* systems that contain enough complexity to reconstitute a specific cellular function (e.g. the formation of a protein gradient), while still using a minimal number of components. Ideally, this allows the conclusive comparison of theoretical predictions and experimental results. The figure below is a schematic representation of the development of *in vivo*, *in vitro* and *in silico* approaches **(A)** and the functionality levels the different methodologies deal with **(B)**.

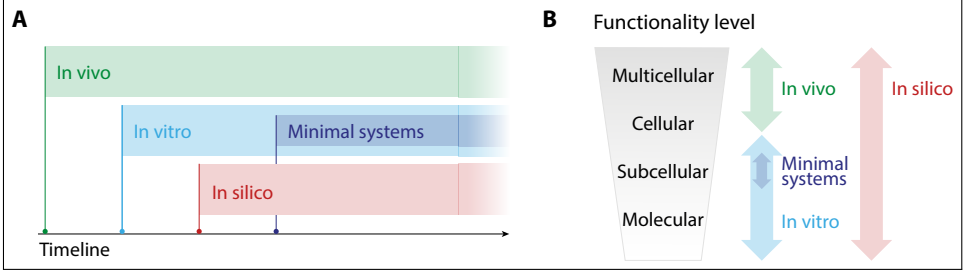

WHAT DO WE KNOW FROM *in vivo* WORK ABOUT THE ROLE OF MTS IN CELL POLARITY?

In vivo experiments led to the discovery of many proteins that are involved in cell polarity, and revealed the roles of MTs in the polarization of different cell types [Drubin and Nelson, 1996, Siegrist and Doe, 2007, Li and Gundersen, 2008, Chang and Martin, 2009, Huisman and Brunner, 2011, St Johnston, 2018]. In fission yeast, for example, tip elongation aberrant protein 1 (Tea1p) is a protein that is involved in MT-dependent polarized cell growth [Behrens and Nurse, 2002, Sawin and Snaith, 2004]. Tea1p is transported to the cell poles through MTs by association with, among others, a molecular motor (Tea2p) and a MT-tip-binding protein (Mal3p) [Mata and Nurse, 1997, Brunner and Nurse, 2000] (Fig. 1.7A). At the cell membrane, Tea1p interacts with anchoring proteins like Mod5p to bind to the membrane and establish an accumulation of Tea1p at the cell poles [Snaith and Sawin, 2003]. Mod5p itself operates in a

positive-feedback loop with Tea1p, which is in a complex with Tea4p, as Mod5p gets localized to the cell poles only in the presence of Tea1p, a process that promotes further anchoring of MT-delivered Tea1 [Snaith and Sawin, 2003]. Remarkably, most of the involved proteins are MAPs, which are known to influence MT length and dynamics by controlling nucleation, orientation, forces and dynamics (Sec. 1.1). This fact suggests additional feedback loops; for example, stable MTs can deliver proteins during longer time periods resulting in an increased accumulation of Tea1p at the cell poles [Siegrist and Doe, 2007].
Two features of the mechanism for MT-based polarity establishment emerge from the fission yeast example (Fig. 1.7A):

1. MTs transport and deliver cargo (e.g. polarity proteins) to the cell membrane, therefore the MT architecture strongly influences polarity by determining where polarity proteins are delivered;

2. polarity proteins can influence MT stability and architecture directly or indirectly through MAPs, often in a (positive) feedback loop between MTs and those proteins.

Studies in other cell systems, such as fibroblast migration, neuronal growth cone formation and apical–basal polarity in epithelial cells [Siegrist and Doe, 2007] (Fig. 1.7B,C) show that aforementioned two features play a role beyond fission yeast, only with different molecular components [Fukata et al., 2002, Watanabe et al., 2004, Siegrist and Doe, 2007]. The essential difference is that fission yeast cells have elongated shapes. For geometrical reasons, MTs primarily grow towards the cell poles [Daga et al., 2006] to deliver proteins (Fig. 1.7A); this automatically results in a to some extent asymmetric protein accumulation [Recouvreux et al., 2016]. However, in less-elongated cells with more symmetric MT conformations, the feedback between polarity proteins and MTs (feature 2) is required to achieve asymmetric MT organization and protein accumulation. Different types of feedback mechanisms exist. As observed for fission yeast, a possible feedback mechanism is the stabilization of MTs by delivered proteins [Li and Gundersen, 2008, Yoo et al., 2012, Jiang et al., 2015], resulting in increased delivery of proteins by molecular motors. Other examples of feedback loops are enhanced binding of polarity proteins to the cortex (like the Tea1p–Mod5p positive feedback loop in fission yeast) [Snaith and Sawin, 2003, Bicho et al., 2010] and local actin assembly as a result of MT-based delivery of polarity proteins [Glynn et al., 2001, Martin, 2015, Minc et al., 2009]. Thus, in the latter, both cytoskeletal filaments work together to break symmetry.

Since MT architecture dictates where polarity proteins are delivered, many *in vivo* studies have investigated how proteins that are involved in cell polarity change MT architecture. In eukaryotic cells, MTs often nucleate from a centrosome, and proteins that are functionally associated with cell polarity, such as the partitioning defective (Par) proteins or Moesin are found to influence centrosome position in a cell [Feldman and Priess, 2012, Inaba et al., 2015, Jiang et al., 2015, Abeysundara et al., 2018]. This can change the balance from a symmetric to an asymmetric MT network and is crucial for proper polarization of cells [Burute et al., 2017]. In contrast, in epithelial

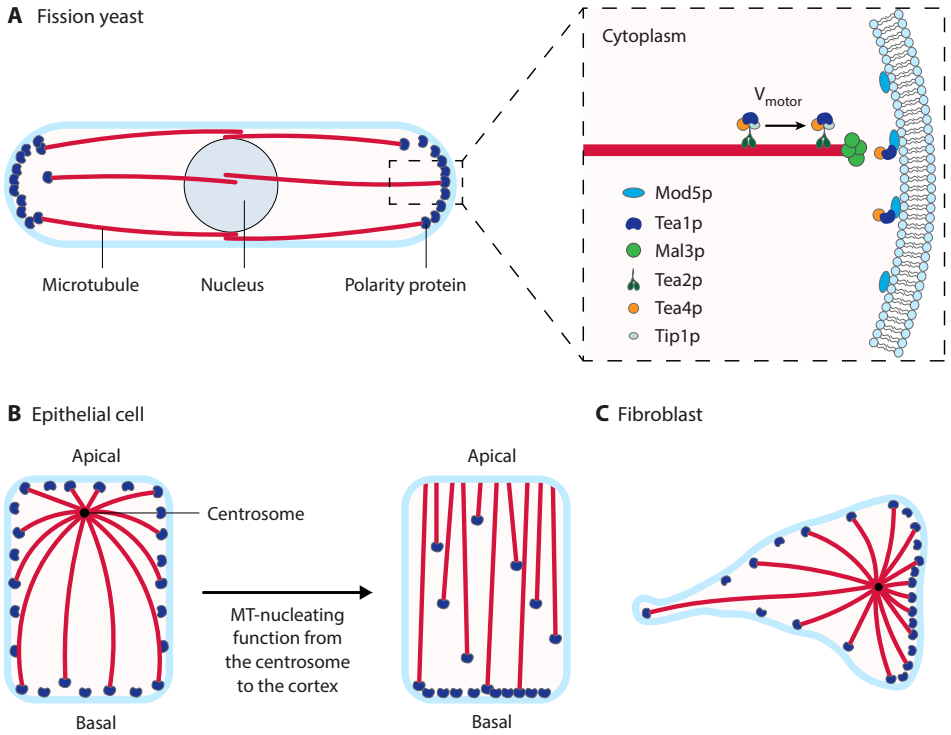

Figure 1.7: Schematic representation of MT architectures in three different cell types and the minimal system. (A–C) Examples from three different cells types that illustrate how MT architecture can influence cell polarity by defining where proteins are delivered by MTs, either through molecular motors or through association with growing MT plus ends. **(A)** In fission yeast cells, MTs nucleate from the nucleus and orient longitudinally, thereby mainly delivering proteins to the cell poles. The magnified view shows the proteins involved, where polarity protein Tea1p is transported to the cell membrane by, among others, the molecular motor Tea2p and end-binding protein Mal3p. At the cell membrane, Mod5p helps to anchor Tea1p, working in a positive feedback loop with Tea1p and Tea4p. **(B)** Epithelial cell where the MT architecture and, therefore, delivery location of polarity proteins depends on the origin of MT nucleation, since it can shift from being centrosome-based to being located at the cell cortex. **(C)** In a migrating fibroblast, MTs nucleate from the centrosome, which is located on one side of the cell, resulting in an asymmetric MT architecture and protein delivery.

cells, endothelial cells and mouse airway cilia, regulatory proteins ensure that MTs grow mainly from the apical membrane, rather than from a centrosome [Feldman and Priess, 2012, Vladar et al., 2012, Guillabert-Gourgues et al., 2016, Toya et al., 2016]. The result is that MTs grow in parallel bundles instead of a radial conformation, which leads to different transport directions (Fig. 1.7B,C). Although it has been well established that MTs ans MAPs play a role in the establishment of polarity, additional proteins are still being discovered and many questions remain. For example, we do not know what the minimum requirements for MT-based symmetry breaking are, what exactly the roles of the different regulatory proteins are, and how MTs and proteins interact to break symmetry. The complexity of the cells makes it difficult to answer these

questions with *in vivo* studies. Reducing complexity by performing *in vitro* reconstitutions has provided additional understanding on a molecular level.

HOW HAS *in vitro* WORK CONTRIBUTED TO OUR KNOWLEDGE?

Polarity is the result of an intricate interplay between MTs, proteins and membranes. Thus, the first step to understand the impact of each contribution is to investigate the separate components of the two aforementioned features for MT-based polarity establishment. MAPs regulate MT nucleation, dynamics, orientation and transport of proteins along MTs (Sec. 1.1) [Kinoshita et al., 2001, Faivre-Moskalenko and Dogterom, 2002, Jiang and Akhmanova, 2011, Akhmanova and Steinmetz, 2015]. Therefore, specific combinations of MAPs can guide the self-organization of MTs into functional architectures [Alfaro-Aco and Petry, 2015]. A few examples of MAPs are the MT polymerase XMAP215, the dynein and kinesin molecular motors, the MT depolymerase mitotic centromere-associated kinesin (MCAK), and the end-binding proteins (EB proteins), which recruits other MAPs to the growing MT tip [Bieling et al., 2007, Honnappa et al., 2009, Zanic et al., 2013, Duellberg et al., 2014, Alfaro-Aco and Petry, 2015]. Their influence on MT dynamics has typically been studied *in vitro* by reconstitution of dynamic MTs [Mitchison and Kirschner, 1984a, Alfaro-Aco and Petry, 2015] together with purified proteins, for example, on a glass slide or in an optical trap. For several motor proteins, the walking mechanism and quantitative information, such as step size, absolute force and binding–unbinding kinetics have been elucidated [Vale et al., 1985, Svoboda et al., 1993, Hirokawa, 1998, Vale and Milligan, 2000, Reck-Peterson et al., 2006, Block, 2007, Gennerich et al., 2007, Gennerich and Vale, 2009], which is relevant both for MT architecture and for directed transport of cargo along MTs. Summarizing, *in vitro* experiments on single MTs provide qualitative and quantitative information on basic molecular mechanisms that contribute to polarity establishment. However, one molecular mechanism on its own, such as protein transport by a molecular motor, does not establish cell polarity *in vitro*. To accomplish that, *in vitro* experiments are needed that combine multiple of the features known to contribute to polarity, to study how MTs, proteins and membranes work together in a confinement to break symmetry of the protein distribution, namely a minimal system (see Box 1).

WHAT DID WE LEARN FROM THE FIRST MINIMAL SYSTEMS FOR MT ORGANIZATION?

More than two decades ago, the foundation was laid for the type of MT-based minimal system that we are currently working on in our lab. The *in vitro* MT reconstitutions described in the previous section were done in flow channels of approximately 2 mm wide, 2 cm long and 0.1 mm thick. Compared to the scale of MTs this is almost infinite. At some point, people started to study the influence of confinement on MT networks, as cells are a confined space as well. These first confinements were 2D glass chambers of a few micrometers deep and a few tens of micrometers in diameter [Holy et al., 1997, Nédélec et al., 1997]. Later also 3D confinements were used, by encapsulating MTs in emulsion droplets or liposomes. Two types of MT organization in confinement were studied: the positioning of MT asters and the self-organization of MTs and motors.

For the positioning of MT asters (like in the mitotic spindle), initially experiments in 2D glass chambers showed that pushing forces from polymerizing MTs can suffice to center a MT aster [Holy et al., 1997, Faivre-Moskalenko and Dogterom, 2002]. However, when MTs grow too long and buckle, decentering occurs. Laan et al. continued this line of research by adding cortical dynein motors and study their role in MT aster positioning [Laan et al., 2012a,b, Roth et al., 2014, 2019b]. Dynein attached to the walls of glass chambers was found to capture MTs, inhibit growth and trigger catastrophes [Laan et al., 2012a]. Because of this, cortical dynein exerts pulling forces on the MTs and combined with the aforementioned pushing forces this robustly centers the MT asters not only in 2D chambers [Laan et al., 2012a] but also in 3D confinements (water-in-oil emulsion droplets or liposomes) [Laan et al., 2012b, Roth et al., 2014, 2019b] (see Fig. 1.8). The centering of asters by MT pushing and dynein pulling forces was confirmed by theoretical modeling of MT aster mechanics. These reconstitution experiments provided new insights in MT aster positioning mechanisms that might play a role in cells. Insight that would not have been possible with only flow channel reconstitutions and *in vivo* studies of MT asters.

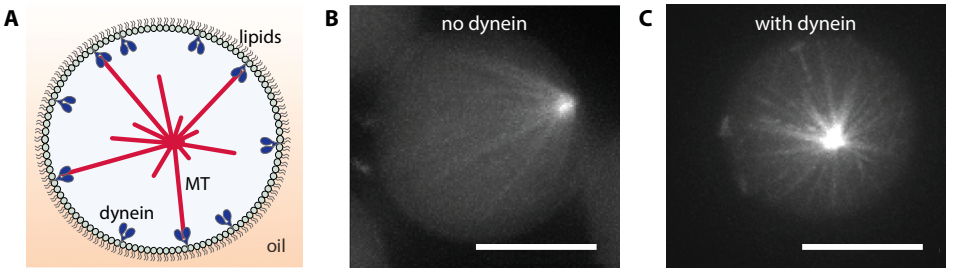

Figure 1.8: Schematic picture **(A)** and emulsion droplet experiments **(B,C)** from Roth et al. [Roth et al., 2019b] on MT aster positioning in a 3D confinement with and without cortical dynein. The combination of pushing forces by growing MTs and pulling forces from cortical dynein was found to result in MT aster centering. Scalebars are 10 µm.

In parallel, the influence of confinement on the self-organization of MTs and molecular motors was studied. Nédélec et al. observed that different MT network conformations could form (e.g. vortices, asters or bundles), either by varying the relative MT-motor concentrations or by imposing a 2D confinement [Nédélec et al., 1997]. Varying the size of 3D emulsion droplets with encapsulated tubulin demonstrated that the size of the confinement determines the final MT organization, together with the presence and concentration of kinesin14 motors [Baumann and Surrey, 2014]. This result was confirmed by Juniper et al. [Juniper et al., 2018], who showed in thousands of droplets with the same diameter that constriction of a spherical network of dynamic MTs and crosslinking motors can lead to reproducible production of a single, centered MT aster per droplet (see Fig. 1.9). In their findings, the exact pathway and final MT organization naturally depends on motor concentration but also on the chemical properties of the droplet interface.

These minimal systems for MT organization demonstrate a couple of things. Firstly, they illustrate how minimal systems helped to get a better understanding of the mech-

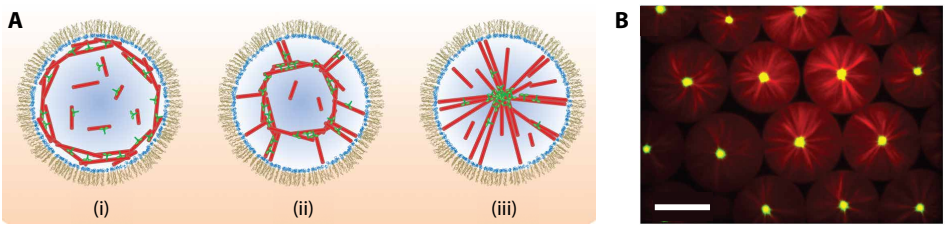

Figure 1.9: (A) Schematic of MT aster formation by crosslinking kinesin14 motors (green) and dynamic MTs (red) in 3D emulsion droplets from Juniper et al. [Juniper et al., 2018]. **(B)** Confocal image of emulsion droplets with MT asters as in (iii), formed by MTs (red) and crosslinking motors (yellow) [Juniper et al., 2018]. Scalebar is 100 µm.

anisms in MT aster positioning and MT network formation. In addition, they show that a cell-sized confinement can have a huge influence on the outcome of *in vitro* reconstitutions compared to conventional flow channel experiments. Moreover, they reveal the sensitivity of this type of systems for confinement size, relative protein concentrations and chemical composition of the water-oil interface of emulsion droplets. We will need to carefully fine-tune these three parameters every time that we change something in our minimal system. In fact, this parameter-sensitivity is perhaps the biggest challenge of reconstituting a minimal system.

1.3. TOWARDS A MINIMAL SYSTEM FOR MICROTUBULE-BASED CELL POLARITY

UP to now, MT-based minimal system reconstitutions have focused on MT aster positioning and MT network organization in 2D and 3D confinements. We use this as a basis and expand it step by step towards a minimal system for MT-based cell polarity. It is therefore important to formulate a clear definition of a "minimal system for cell polarity", see Box 2:

Box 2. Definition of a minimal system for cell polarity
An asymmetric accumulation of proteins at the periphery of a 3D confinement induced by MTs, reconstituted with the minimal number of components possible.

Two different scenarios of protein accumulation are being studied in our lab (Fig. 1.10). The first is polarized growth in fission yeast, which was explained in Sec. 1.2. The aim of that project is to reconstitute cell polarity with purified fission yeast proteins in a minimal system. On the other hand, Recouvreux et al. established an accumulation of a chimera protein at the cell poles of fission yeast cells [Recouvreux et al., 2016]. This chimera protein could only bind to MT plus-ends and to the cell membrane, and apparently that is enough to result in a polarized distribution of chimera proteins. An intriguing result, but the question is if it also suffices in a system without predefined asymmetry. Yeast cells have elongated shapes so for geometrical reasons the MTs grow predominantly in the on-axis direction. Hence proteins that bind the MT plus-end will

mostly be deposited at the cell poles [Recouvreux et al., 2016]. What changes if we consider a spherical system? Can the mere fact of a protein binding both MT plus end and membrane still result in asymmetric accumulation of proteins? Or do we need more? These questions lead to the second scenario and main topic of this thesis: **what are the minimal requirements for MT-based cell polarity in a confinement without predetermined geometrical asymmetry?** We devoted ourselves to answering this question by *in vitro* experiments and some theoretical modeling.

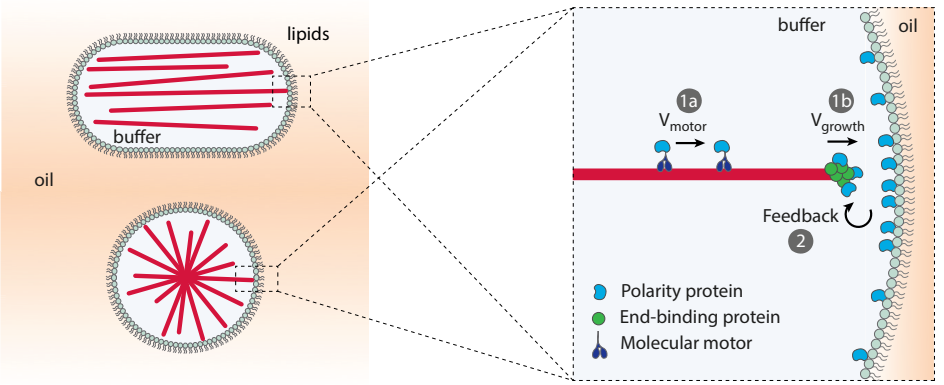

Figure 1.10: Schematic example of two scenarios for protein accumulation in a minimal system. Elongated or spherical emulsion droplets of aqueous buffer in oil could be used (left), where both features of MT-based polarity establishment (protein transport by MTs and feedback of polarity proteins on MT architecture) are included (right). Transport can be achieved either through molecular motors (1a) or through transient interaction with tip-tracking proteins (1b). MT architecture strongly depends on the size and shape of droplet confinement, as illustrated by the spherical and elongated (yeast-sized) droplet; therefore, exact conditions and requirements for the establishment of a polarized cortical protein distribution will depend on this as well.

1.3.1. THE ARTIFICIALITY OF MINIMAL SYSTEMS

The approach of *in vitro* reconstitutions may sound very artificial: mimicking the cell by water-in-oil emulsion droplets, using truncated versions of proteins, everything to create a system that obeys our rules. And in fact it is very artificial. Our goal is to reconstitute a cellular function with the minimal number of components. But the actual objective behind this goal is to gain more understanding of the cellular process. Minimal systems provide a tool to test the general mechanisms behind cellular process in an *in vitro* system which resembles the cellular environment, but without the immense complexity of cells. In that way, they complement already existing *in vivo*, *in vitro* and *in silico* studies. To test the general mechanisms, we are not always interested to incorporate all involved proteins, because it makes the system too complex. Instead, we try to understand the mechanism and formulate hypotheses. Next, we design the simplest possible system to test those hypotheses. For example, *in vivo* experiments showed that at least eight fission yeast proteins are involved to create a Pom1 gradient, which is needed for proper spatiotemporal regulation of the cell division plane. A

complex of Mal3p-Tea2p-Tip1p moves to the MT tip and delivers Tea1p and Tea4p to cortical Mod5p at the cell poles. Next, the Tea1p-Tea4p complex recruits Dis2p, which dephosphorylates Pom1p. Dephosphorylated Pom1p has a higher binding affinity to the cell membrane. The result is a Pom1p gradient: high concentration at the cell poles, low in the center. This is a complex interplay of eight proteins, but the underlying mechanism seems directed transport of some protein to the cell poles by MTs, which leads to local accumulation and hence cell polarity. To test those mechanisms, one or two chimera proteins suffice.

1.3.2. OUTLINE OF THIS THESIS

As a starting point for the experiments, we needed to optimize the existing protocols for MT asters inside water-in-oil emulsion droplets as 3D confinements [Roth et al., 2014, Vleugel et al., 2016, Roth et al., 2019b] (Chapter 2). Among the components we changed are lipid composition (to enable protein interactions with the droplet cortex) and fluorescent MAP7 as a tool for improved MT visualization (Chapter 3). With the new protocols, we created emulsion droplets containing MT asters with EB protein comets (Chapter 4), which allowed us to compare MT dynamics in confinement and in flow channels. The next step was to induce a connection between MT plus end and droplet cortex through a cortical +TIP that can interact with EB protein comets on MT plus ends (Chapter 4). Such tethering of a MT tip could locally accumulate cortical proteins at the position of the MT tip. In addition, the tethering of MTs influenced MT aster positioning in the confinement. Because our final goal was to asymmetrically accumulate proteins at the cortex through MTs, the question was if the local protein accumulation at the cortex at the position of a MT tip as in Chapter 4 could accomplish this in a spherical confinement.

As described in Sec. 1.2, there are two features of the mechanism for MT-based polarity:

1. MTs transport and deliver cargo (e.g. polarity proteins) to the cell membrane;
2. Polarity proteins can influence MT stability and architecture directly or indirectly through MAPs, often in a (positive) feedback loop between MTs and those proteins.

The first feature was represented in our system by the MT-cortex interactions through cortical +TIPs, but the second feature was not yet integrated. A first attempt at incorporating this second feature was to replace the cortical +TIP in the system by one that stabilizes MTs. Furthermore, in cells, polarization generally follows some asymmetric external cue (e.g. a chemical gradient). If stabilization of MTs at the site of cortex interaction does not suffice to locally accumulate proteins spontaneously, an asymmetric cue might be needed. An elegant way of reconstituting such a cue *in vitro* is by optogenetics. We employed proteins that (in)activate reversibly when exposed to blue light. The application of this reversible and local process in our minimal system is discussed in Chapter 5.

Furthermore, in Chapter 6, we put our efforts to build a minimal system for MT-based

cell polarity in context with the help of theoretical modeling. As discussed before in Box 1, theoretical modeling is of great importance when building a minimal system. It provides predictions about the mechanisms that are minimally needed for protein accumulation, which can guide the construction of our minimal system. At the same time, a minimal system provides a platform to test the different predictions on minimally required mechanisms for pattern formation in a spherically symmetric confinement.

Finally, in Chapter 7, we discuss how far we got in answering the question what is minimally needed for MT-based cell polarity and suggest future experiments to further answer that question.

AUTHOR CONTRIBUTIONS

K.V. wrote the chapter, S.T., L.L. and M.D. were co-authors on the review paper [Vendel et al., 2019] that formed a basis for Sec. 1.2 on the function and development of minimal system reconstitutions.

2

METHODS AND OPTIMIZATION STEPS

'Wat is onmeetbaar?' vroeg de eekhoorn.
'Ja...' zei de mus, 'dat is bijvoorbeeld hoe warm de tijd is
of wie er het meest van de lucht houdt of het jarigst is...'
'O,' zei de eekhoorn.

Toon Tellegen

Minimal system reconstitutions of cellular processes provide new insights complementary to those from in vivo and traditional in vitro studies. To set up a minimal system for microtubule-based cell polarity, we need in vitro techniques to resemble the cellular environment. For example, water-in-oil emulsion droplets as cell-sized confinements, and functionalized beads as artificial microtubule organizing centers. In this chapter, we introduce the different components of our minimal system and the methods to prepare them. In addition, we discuss necessary optimization steps to achieve functional behavior of all components combined into one system which is extremely sensitive to experimental parameters.

Parts of this chapter have been published in Cytoskeleton Dynamics, Methods and Protocols (2020) [Vendel et al., 2020]

THE intended minimal system to study microtubule-based cell polarity introduced in the previous chapter consists of multiple components. In this chapter, we describe the general methods and optimization steps of existing protocols as employed in this thesis to create that minimal system.

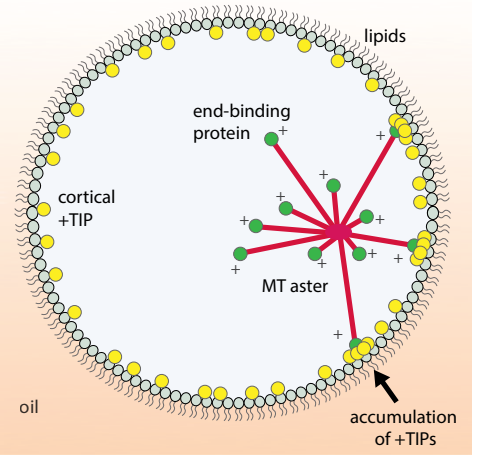

Figure 2.1: Example of a reconstitution experiment with MTs (red) nucleating radially from an MTOC inside water-in-oil emulsion droplets. Furthermore, end-binding proteins (green) bind to growing MT tips, and connect those to the cortical +TIPs (yellow).

As a basis, we needed a suitable microtubule (MT) architecture. For our purpose we mimicked MT organization in cells, where MTs grew radially from a microtubule organizing center (MTOC) (Fig. 2.1). During the course of this project, we have utilized two types of MTOCs. Initially we worked with purified centrosomes (Sec. 2.2.1) and later with artificial MTOCs (Sec. 2.2.2). The next component of the minimal system were tiptracking proteins or +TIPs, proteins associated with the growing plus-end of MTs (Sec. 2.2.4). One example is the end-binding protein EB3, which autonomously binds to the tip of a growing MT. As discussed in Chapter 1, we wanted to locally accumulate cortical +TIPs at the position of the MT tip through interaction with EB3. The different +TIPs we explored are discussed in the corresponding chapters.

Tubulin, MTOCs and additional proteins were encapsulated in cell-sized water-in-oil emulsion droplets to mimic the cellular environment (Sec. 2.1). Some extra challenges needed to be dealt with for experiments inside emulsion droplets compared to *in vitro* assays in a flow channel (Sec. 2.5). Firstly, to visualize the MT asters with protein comets we used confocal fluorescence microscopy. Different methods exist to fluorescently label MTs *in vitro*, some of which are more useful than others in emulsion droplets (Sec. 2.2.3). Secondly, functionalized phospholipids provided the possibility to bind proteins to the emulsion droplet cortex to mimic the behavior in cells. These lipids are chemically linked to for example a Ni-NTA or biotin group, such that respectively histidine-tagged or biotinylated proteins are recruited to these lipids. In Sec. 2.3 we discuss under which conditions these lipids function sufficiently well.

Parts of this chapter are based on a chapter for *Methods in Molecular Biology* [Vendel et al., 2020]. The original chapter contains detailed notes on the experimental procedures, problems that one can encounter and how to prevent them. The interested reader can find those in [Vendel et al., 2020].

2.1. WATER-IN-OIL EMULSION DROPLETS

EMULSIONS are widely known for applications in food science, pharmaceutics, cosmetics and more recently also in biochemical reconstitutions. For the latter, it is an appealing method to encapsulate a set of components in a closed confinement. This is also what we did, using water-in-oil emulsion droplets as a rigid container for MT networks. Emulsion droplets are generally formed by shear stress on a water phase inside an oil phase. Surfactants - molecules with a hydrophilic and a hydrophobic part (e.g. phospholipids) - stabilize the spherical oil-water interface to prevent demixing.

LIPID MIX PREPARATION

The lipid mix consisted of mineral oil, phospholipids and a surfactant, where the latter two formed a monolayer at the interface between water and oil to stabilized the emulsion droplets. Important for our *in vitro* reconstitutions was the biocompatibility of phospholipids, surfactants and oil phase. The procedure for making the lipid mix was as described before by Roth et al. [Roth et al., 2014] and Vleugel et al. [Vleugel et al., 2016].

1. Rinse glass syringes 3 times with chloroform before use;
2. Pipette the chloroform-dissolved, 1,2-dioleoyl-sn-glycero-3-phospho-L-serine (DOPS) into a glass vial using a glass syringe;
3. Dry the lipids into a thin film on the wall of the glass vial by evaporating the chloroform in a gentle nitrogen gas flow;
4. Evaporate all remaining chloroform in a vacuum dessicator for about one hour;
5. Dissolve the lipids in mineral oil and 2.7% (v/v) Span80 to a total lipid concentration of 0.64 mg/ml by sonication for 30 minutes in a bath sonicator (40 kHz);
6. Store the lipid mix at 4°C until use.

REACTION MIX PREPARATION

A reaction mix contains all components required to nucleate MT asters with protein comets in an *in vitro* environment. The exact composition differed per experiment and is therefore described in each chapter. In general, it contained components as listed in table 2.1. After mixing all components, the reaction mix was always centrifuged in an AirFuge at 150.000 g for 5 minutes.

EMULSION DROPLETS

We used two different strategies to create water-in-oil emulsion droplets with the previously prepared reaction mix and lipid mix. The first was to create droplets on a microfluidic chip, see Fig. 2.2A and Section 2.1. The second strategy was to emulsify 0.5 µl of reaction mix into 40 µl of lipid mix by pipetting up and down 40 times with a 10 µl pipette, as schematically depicted in Fig. 2.2B. Both methods have advantages and

component	final concentration	
50x oxygen scavenger mix*	1	x
D-glucose	50	mM
BSA	2	mg/ml
κ-casein	1	mg/ml
KCl	50	mM
GTP	3	mM
tubulin	30-40	µM
MAP7	10-100	nM
EB3-GFP	20-300	nM
+TIP	20-300	nM
centrosomes/beads	5-10	% of total volume

Table 2.1: Composition of the reaction mix for encapsulation of MT asters with EB3-GFP comets. All components were dissolved and diluted in MRB80 buffer (80 mM Pipes, 4 mM $MgCL_2$, 1 mM EGTA, pH 6.8). *200 mM DTT, 10 mg/ml catalase, 20 mg/ml glucose oxidase.

disadvantages that we will shortly discuss. Microfluidics produces uniformly sized droplets and in addition it is supposed to be a more gentle way of droplet production, which is advantageous for certain fragile proteins (like tubulin) or protein complexes (like centrosomes). However, proteins tend to stick to the polydimethylsiloxane (PDMS) walls of the microfluidic channels, leading to a decrease of protein concentration and functionality in the droplets and possibly also to a loss of centrosomes. Droplet production by pipetting produces a wider variety of droplet sizes - which can be both an advantage and a disadvantage depending on the goal of the experiment - but does not have the problem of proteins sticking to channels. Also, the droplet production is much faster, which is especially convenient for experiments that compare different experimental conditions. Finally, a much smaller volume of the reaction mix is needed to produce droplets by pipetting (0.5 µl instead of 10-15 µl for microfluidics). This allows multiple droplet batches of the same reaction mix while optimizing a single parameter, like temperature. We have been able to achieve MT asters with protein comets inside droplets with both strategies for droplet production. Yet most experiments in this thesis were performed in droplets prepared by pipetting unless stated otherwise. The main reasons for this choice were sticking of proteins, centrosomes and beads to the PDMS of microfluidic chips and the faster procedure when pipetting.

MICROFLUIDIC CHIPS

The procedure for microfluidic chip preparation was exactly as described in previous methods papers [Roth et al., 2014, Taberner et al., 2015, Vleugel et al., 2016], but for completeness we repeat the steps here. First, an SU-8 mold was prepared in the cleanroom (step 1 to 5). With this reusable mold, microfluidic PDMS chips were prepared (step 6 to 13).

1. Design a photomask with three inlets as in [Roth et al., 2014];

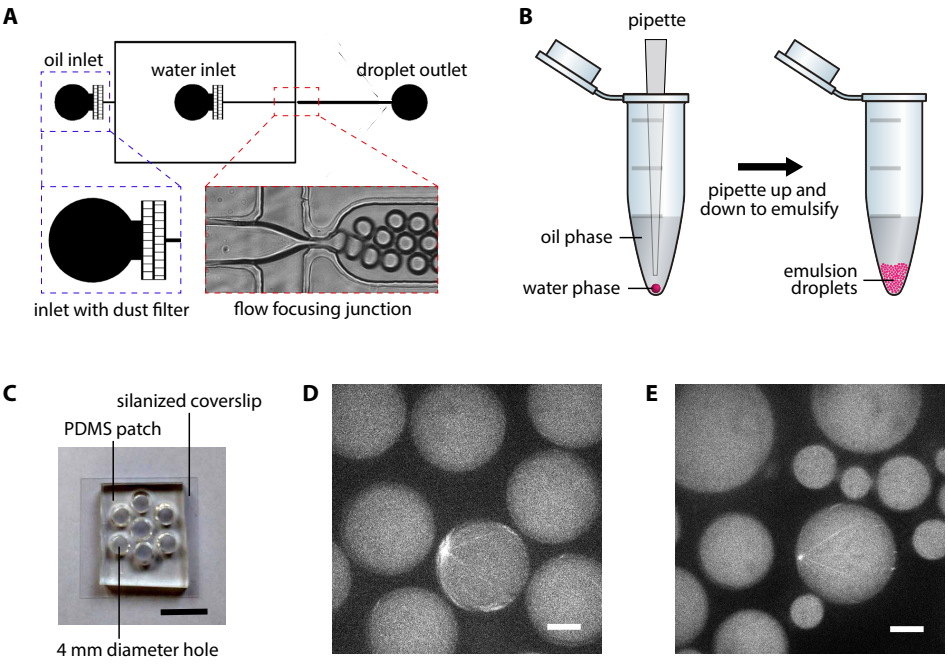

Figure 2.2: Water-in-oil emulsion droplets were produced in two ways, as schematically visualized in (A) and (B). **(A)** Microfluidic chip for emulsion droplet production with one inlet for the oil phase and one for the water phase, which come together at a flow focusing junction where droplets are pinched off. Dust filters at the inlets prevent (PDMS) particles from entering the channels and blocking the junction. **(B)** Another method for emulsion droplet formation involves pipetting the oil phase and water phase up and down to generate the shear stress that leads to droplet formation. **(C)** For long-term imaging, droplets are transferred into a PDMS well consisting of a PDMS patch with holes on a silanized coverslip. **(D)** and **(E)** are typical fields of view observed when imaging emulsion droplets containing centrosomes and fluorescent rhodamine-tubulin (Table 2.1) with a confocal spinning disc fluorescence microscope, for droplets produced with microfluidics (D) or by pipetting (E). Scale bars: 10 mm for C, and 10 µm for D and E.

2. Order a low-cost flexible photomask with the desired design at Selba S.A. with a negative polarity, i.e. a dark photomask with transparent structures;

3. The mold is then produced in the cleanroom according to standard photolithography protocols. Follow the SU-8 manufacturer's instructions for exact times, spinning velocities, temperatures, etc. Spincoat the SU-8 photoresist onto a 4 inch silicon wafer and perform a soft bake at 95°C;

4. Expose to UV light through the photomask and bake again at 95°C;

5. Develop with the manufacturer's developer for the SU-8 type you used (again follow the manufacturer's instructions on time). Rinse the wafer first with acetone to remove the developer and subsequently with isopropanol to remove the acetone. Dry in nitrogen flow and perform a final hard bake at 150°C to make the structures more robust.

6. To prepare PDMS chips from these SU-8 molds, mix PDMS pre-polymer with the PDMS curing agent in a volume ratio of 9 to 1, prepare 40 ml PDMS per SU-8 mold;
7. Centrifuge for 3 minutes in a 50 ml falcon tube at 300 rcf to remove large air bubbles;
8. Create a cup of aluminum foil around each 4 inch silicon wafer so the wafer is the bottom of the cup and the sides of aluminum foil are at least 2 cm high;
9. Pour the PDMS into the cup to get a 5 mm thick layer of PDMS on top of the wafer, place in a vacuum dessicator for approximately 1 hour to remove remaining air bubbles and afterwards cure for 30 minutes at 100°C;
10. In the meantime, spincoat the leftover PDMS onto glass slides (5 sec at 200 rpm followed by 30 sec at 4,000 rpm) and cure for at least 1 hour at 100°C;
11. Carefully remove the PDMS from the mold, cut out the areas of the chips (one wafer usually contains structures for four microfluidic chips) and punch 0.75 mm inlet and outlet holes;
12. Apply an oxygen plasma to the PDMS surfaces of glass slide and PDMS chip with a corona discharger for a few seconds. Immediately place the PDMS chip onto the glass slide and bake at 100°C for at least 1 hour to bond the surfaces together;
13. Store in a dust-free place until use (for a few months to a year).

MICROFLUIDIC SETUP

The flow for the droplet formation was controlled by an MFCS^{TM} pressure controller connected to a Fluiwell accessory. The microfluidic chip, and specifically droplet production at the junction (Fig. 2.2A), were monitored with an inverted bright-field microscope with a 10x magnification air objective.

1. Put water phase and oil phase mixtures into two MicrewLock tubes suitable for the Fluiwell assessory and connect the polyether ether ketone (PEEK) tubing to the microfluidic chip inlets;
2. Adjust the pressure such that first all channels of the microfluidic chip are filled with oil phase;
3. Introduce the water phase and tune the pressures to obtain a stable production of droplets with the desired diameter at the junction;
4. Wait until a few microliters of droplets have emerged at the outlet (Fig. 2.2A), harvest 1.5 µl using a pipette with cut-off tip, mix with 8.5 µl lipid mix and transfer to the PDMS well (Section 2.1);
5. Clean the tubing with isopropanol after use. It is also possible to rinse the microfluidic chip with isopropanol and store it until the next use. In that case, al-

ways check at the microscope if the channels of the chip are not clogged before using it the next time.

COVERSLIP SILANIZATION WITH RAIN-X

Emulsion droplets must be placed onto a coverslip for imaging with the confocal spinning disc fluorescence microscope. In principle coverslips are hydrophilic, often resulting in a collapse of the aqueous interior of the droplets onto the coverslip. Coverslips were made hydrophobic to prevent this, for example by spincoating a thin layer of PDMS or by silanization. The advantage of silanization compared to a layer of PDMS is that the image quality is much better because the light is not refracted and diffused by the non-transparent PDMS. One can silanize glass in various ways, and we used Rain-X [Baumann and Surrey, 2014] as it contains less harmful chemicals than other silanization solutions and can be purchased at the local car shop.

1. Place 24 x 24 mm^2 coverslips in a holder, bath sonicate the coverslips in ethanol for 20 minutes and dry in nitrogen air flow;
2. Immerse the coverslips in Rain-X for 5 minutes; and leave to dry in air;
3. Store between paper tissues until use.

PDMS WELL PREPARATION

To immobilize the droplets during imaging over longer time periods, a PDMS well was placed onto the Rain-X silanized coverslips (Fig. 2.2C) to hold the emulsion droplet mix [Vleugel et al., 2016]. In general, one can use the PDMS that is left over after cutting out the required areas for microfluidic chips (Section 2.1). If emulsion droplets are produced with the pipetting method instead of microfluidics, first follow steps 6 to 9 from the microfluidic chips protocol in Section 2.1 with a 4 inch silicon wafer (preferably without structures, because otherwise those might create a connection between neighboring wells).

1. Cut the 5 mm thick PDMS slab into 2 x 2 cm^2 squares;
2. Punch as many 5 mm diameter holes as possible in each square and store them in a dust free box;
3. Before use: press a PDMS square onto a Rain-X-coated coverslip with the smooth side (the side that was in contact with the silicon wafer) facing the coverslip;
4. After use: discard the Rain-X coverslip and carefully rinse the PDMS well with isopropanol to clean it for the next use. You can keep cleaning and re-using PDMS wells for years until they break or get lost.

2.2. DYNAMIC MT ASTERS WITH PROTEIN COMETS

THE basis of our minimal system was a dynamic MT aster with proteins tiptracking the growing MT tips inside a water-in-oil emulsion droplet. To get the desired MT

conformation (radially oriented with their plus ends pointing outwards), we used a microtubule organizing center (MTOC).

2.2.1. CENTROSOMES

Centrosomes are a common MTOC in cells for radially organized MTs (Sec. 1.1). Growing MTs from centrosomes is an established method in our lab to obtain MT asters [Laan et al., 2012b, Roth et al., 2014, Vleugel et al., 2016, Roth et al., 2019b], hence we started with this approach as well.

CENTROSOME PURIFICATION

Centrosomes were isolated from human lymphoblastic KE37 cells by Florian Huber and Sophie Roth following the protocol from Moudjou et al. [Moudjou and Bornens, 1998]. In addition, we received a batch of centrosomes from the Pierre Gönczy lab (Swiss Institute for Experimental Cancer Research (ISREC), School of Life Sciences, Swiss Federal Institute of Technology (EPFL) Lausanne, Switzerland).
A high concentration of functional centrosomes is neccessary to get encapsulation in a high enough fraction of the water-in-oil emulsion droplets. It was challenging however to obtain high centrosome concentrations by purification. This complicated experiments, so we were looking for alternative MTOCs (Sec. 2.2.2).

USE OF CENTROSOMES IN RECONSTITUTION EXPERIMENTS

After purification, centrosomes were contained in a high sucrose buffer (50 - 60%) and stored at -150°C. To encapsulate them inside emulsion droplets we did the following:

1. Thaw the centrosomes quickly (in your hands) and incubate at 37 °C for 10-15 minutes. This has been found empirically to stimulate MT nucleation *in vitro* [Vleugel et al., 2016];
2. In the meantime, prepare a reaction mix containing all other components (table 2.1) and centrifuge in an AirFuge at 150.000 g for 5 minutes;
3. Add the centrosomes and mix very well but gently by pipetting up and down at least 20 times to dissolve the high sucrose with centrosomes;
4. Use this mix to prepare droplets as described in Sec. 2.1.

2.2.2. ARTIFICIAL MTOCS: AURORA KINASE A BEADS

Artificial MTOCs in this context were paramagnetic beads coated with centrosomal proteins that are potent MT nucleators [Tsai and Zheng, 2005]. The beads used in our experiments were prepared by James Pelletier and Tim Mitchison as described by Tsai and Zheng [Tsai and Zheng, 2005]. Paramagnetic dynabeads of 1 µm diameter were coated with protein A and subsequently with Aurora kinase A (AurkA) antibodies.

Those beads were mixed with frog cell extract such that Aurora kinase A proteins from the extract could bind the antibodies. Finally, the beads (in cell extract) were stored in 30 µl aliquots at -150°C until use.

COMPOSITION OF ARTIFICIAL MTOCS

To unravel why these AurkA beads are so powerful for nucleating MTs and what is minimally needed to create artificial MTOCs, Tim Mitchison performed mass spectrometry experiments on the beads (unpublished data). Amongst the proteins that were found on the beads were Aurora kinase A, CENPE (centrosome associated protein E), CKAP5 (homolog of XMAP215), CEP85 (centrosomal protein 85), TACC3 (role in the MT-dependent coupling of the nucleus and the centrosome), CLASP1 (CLIP associated protein, involved in MT stabilization) and γ-tubulin (creates a template for MT nucleation, Sec. 1.1). All of these proteins are known to be either centrosomal proteins or to localize to the centrosome by binding to centrosomal proteins.

The exact composition of the artificial MTOCs and the mechanisms behind their MT nucleating ability are still unknown. However, as they are potent MTOCs in cell extract and also work very well with purified tubulin, we used them for our *in vitro* reconstitutions. The main advantage was that we could control the bead concentration in the reaction mix and hence increase the fraction of droplets with a MT aster compared to the situation with purified centrosomes. The major disadvantage was that the beads sank to the bottom of the emulsion droplets as a result of gravity, because the density of the metal beads was higher than of the watery interior of the droplets. A solution would be to use polystyrene beads instead of paramagnetic ones. Another disadvantage was that we were not sure what is exactly on the beads and how they nucleate MTs. But since this was true for centrosomes as well, it did not influence our choice for either of the two MTOCs.

USE OF ARTIFICIAL MTOCS IN RECONSTITUTION EXPERIMENTS

AurkA beads can be used as MTOCs in cell extracts [Nguyen et al., 2014, Ishihara et al., 2014, 2016] (Fig. 2.3A), yet for our *in vitro* reconstitutions the cell extract must be washed away:

1. Thaw the frog cell extract with beads on ice;
2. Dilute 25 µl extract in 500 µl washing buffer (25 mM KCl, 10 mM HEPES (pH 7.5), 1 mM $MgCl_2$, 0.1 mM ATP);
3. Collect the dynabeads with a magnet, dispose the washing buffer and redissolve the beads in 500 µl of fresh washing buffer;
4. Collect the beads with a magnet and resuspend in 5-10 µl of washing buffer (fine-tune this volume to get a bead concentration that when added to the experiment results in a high percentage of droplets containing one bead but a low percentage of droplets with many beads);
5. The beads can be stored on ice for a couple of hours.

6. In the meantime, prepare a reaction mix containing all other components (table 2.1) and centrifuge in an AirFuge at 150.000 g for 5 minutes;
7. Add 1 µl of beads and mix very well but gently;
8. Use this mix to prepare droplets as described in Sec. 2.1.

To verify the *in vitro* MT nucleation capability of the beads, we performed a simple assay with beads and purified tubulin in a channel (Fig. 2.3B) and in emulsion droplets (Fig. 2.3C). These data were obtained in the presence of 100 nM XMAP215, as previous *in vitro* reconstitutions by Johanna Roostalu and Tim Mitchison (in Woods Hole, unpublished) suggested that without additional XMAP215 the nucleation from the AurkA beads was poor. XMAP215 is known to be a MT nucleation factor and increase growth velocity and catastrophy rate [Zanic et al., 2013] (Fig. 2.3E,F). Further testing however proved that the beads are adequate MT nucleators as well without additional XMAP215 (Fig. 2.3D). The number of MTs nucleating from the beads as well as their length were visibly smaller for washed beads compared to those in cell extract. This difference was most likely the result of washing the beads, during which part of the proteins bound to the beads dissociated. Also the presence of higher tubulin concentration and a high number of MAPs in the cell extract (that regulate MT nucleation and growth) were likely to play a role. Nevertheless, the MT asters nucleating from beads after washing in Fig. 2.3B-D were sufficient for our *in vitro* reconstitutions.

2.2.3. VISUALIZING MTS

The conventional way to visualize MTs in reconstitution experiments is by fluorescently labelled tubulin. Tubulin dimers covalently linked to fluorescent proteins are mixed with unlabelled tubulin dimers in a ratio of 1:29. The dimers get incorporated in the MTs, making it possible to image those with fluorescence microscopy. For total internal reflection fluorescence (TIRF) microscopy, where only a slab of 100 nm is illuminated, this results in images with good signal to noise ratio. In emulsion droplets however, where an approximately ten times thicker slab is illuminated with spinning disc confocal microscopy, the background signal increases due to the fluorescent tubulin dimers in solution and therefore the signal to noise ratio decreases. This makes it difficult to resolve MTs in droplets, as becomes clear from Fig. 2.3C,D. Possible solutions are molecules with an increased fluorescence intensity upon binding to the MT lattice (e.g. SiR dyes) or fluorescently-labeled proteins that only bind to MTs and not to tubulin (e.g. MAP7 family members), as they reduce the background intensity in droplets. We will discuss both possibilities below.

SIR-TUBULIN

Lukinavičius et al. introduced far-red fluorogenic probes of silicon-rhodamine (SiR) conjugated to the MT-binding drug docetaxel [Lukinavičius et al., 2014]: SiR-tubulin. SiR derivatives possess a non-fluorescent spirolactone (off state) and a fluorescent zwitterion (on state), and interaction with polar protein surfaces (like MTs) turns them

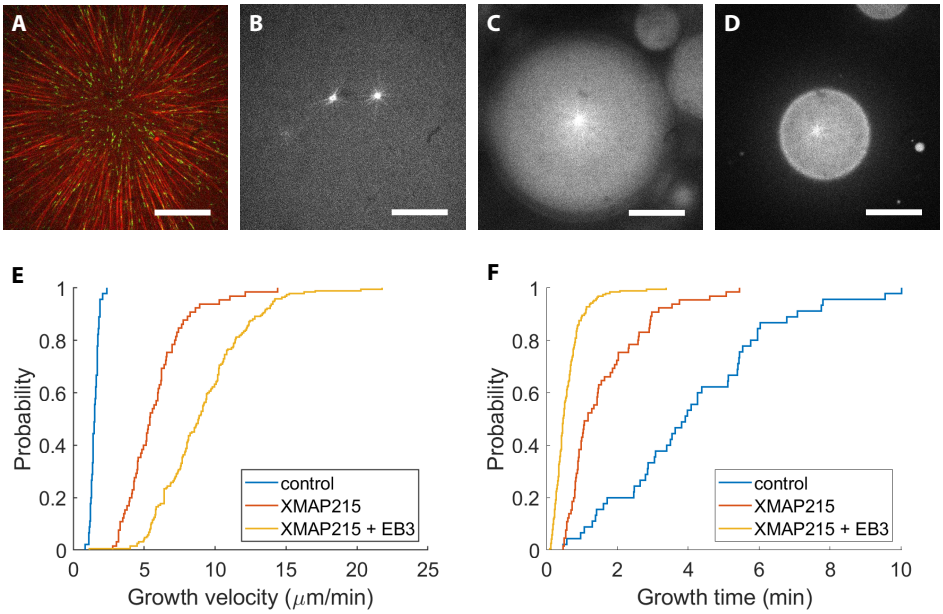

Figure 2.3: **(A)** AurkA bead in cell extract on a glass slide with 1 µM rhodamine tubulin (red) to visualize MTs nucleating from the bead and 20 nM end-binding protein EB3-GFP (green). The bead itself is not visible in this TIRF image as it is above the glass surface, pushed up by the nucleating MTs. **(B)** Two washed rhodamine-labeled AurkA beads on a glass slide in the presence of 15 µM tubulin and 100 nM XMAP215. **(C,D)** Water-in-oil emulsion droplet containing washed AurkA beads, 40 µM tubulin (3.75% Rhodamine-labeled) with 100 nM XMAP215 (C) or without it (D). **(E,F)** The synergistic effect of 100 nM XMAP215 and 100 nM EB3 on the MT dynamics. Probability distribution functions show that the MT growth velocity increases with XMAP215 and EB3 (E), while the growth time decreases (F). Our results are in agreement with those reported by Zanic et al. [Zanic et al., 2013]. All scalebars are 20 µm

from the off state to the on state. This switch results in a tenfold increase in intensity when bound to a MT compared to when in solution. SiR-tubulin was shown suitable for efficient staining of MTs in both live-cell imaging and *in vitro* reconstitutions [Lukinavičius et al., 2014]. Normally, docetaxol has a stabilizing effect on MTs even at 1 nM concentrations. SiR-tubulin however does not have this stabilizing effect up to concentrations of 100-200 nM, indicating that the addition of SiR to the docetaxol molecules changes their function [Lukinavičius et al., 2014].

To use SiR-tubulin instead of rhodamine tubulin, dissolve SiR-tubulin in dimethyl sulfoxide (DMSO) to a concentration of 500 µM and store at -20°C. The use of SiR-tubulin in flow channel experiments has proven to work quite well: add SiR-tubulin in DMSO to the reaction mix to a concentration of 100-200 nM. For labeling MTs in emulsion droplets the procedure was more tricky as SiR-tubulin was found to be highly hydrophobic (partition coefficient of 4.4 (logD) for octanol/water [Lukinavičius et al., 2014]). As a result, SiR-tubulin partitioned more into the oil phase than into the water phase. The total volume of the oil phase was much larger than the total volume of the water phase for water-in-oil emulsion droplets, therefore one needs to add about 1

μM of SiR-tubulin to the oil phase before making droplets. A small fraction of the 1 μM partitioned into the water phase (reaction mix) and labeled the MTs without stabilizing them (Fig. 2.4A).

A major disadvantage of SiR-tubulin was that we have limited control over its effective concentration in droplets. We observed variations of SiR intensity and MT stabilization between droplets within one sample. Another disadvantage emerged once functionalized lipids (Sec. 2.3) were used for the formation of emulsion droplets.

SiR-tubulin in combination with Ni-NTA functionalized lipids

As can be seen in Fig. 2.4B, SiR-tubulin did not behave as expected in a lipid mix which contains DGS-NTA lipids. We show images of emulsion droplets containing 40 μM tubulin, 1.5 μM Rhodamin-tubulin, 100 nM EB3-GFP, 100 nM XMAP215 and AurkA beads. Further, 1 μM SiR-tubulin was dissolved into a lipid mix with either DOPS lipids (2.4A) or DOPC and DGS-NTA lipids (2.4B). While for the first the Rh-tubulin and SiR-tubulin signals overlapped, this was not the case in the latter. With DGS-NTA lipids we observed very stable MT networks in most droplets (Fig. 2.4B, left), but no visible SiR-tubulin signal for those same droplets (Fig. 2.4B, right). Instead, some bright fluorescent droplets could be seen that did not appear in the Rhodamine image.

Clearly something was influencing the SiR-tubulin, but more experiments would be needed to check if DGS-NTA lipids were the problem or DOPC instead of DOPS or the higher lipid concentration that we needed to use in case of DGS-NTA lipids (explained in Sec. 2.3). Because of the problems with SiR-tubulin, we explored an alternative method to visualize MTs inside emulsion droplets: the protein MAP7.

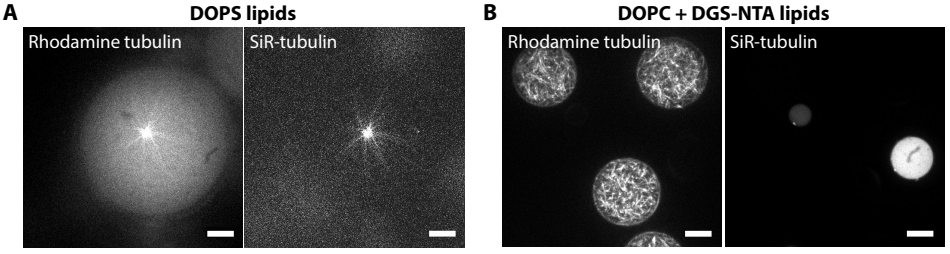

Figure 2.4: (A) One FOV imaged with 561 nm (Rhodamine tubulin, left) and 642 nm (SiR-tubulin, right) for an emulsion droplet with a cortex containing 0.64 mg/ml DOPS lipids and 2.7% Span80. **(B)** Same as in (A) but the lipid mix contains 16.3 mg/ml DOPC lipids, 1 mg/ml DGS-NTA lipids and 1% Span80.

MAP7

MAP7 is a MT-associated protein which has a high affinity for MTs, stabilizes MTs and also greatly increases the affinity of kinesin-1 molecular motors to MTs. We will introduce the MAP7 protein in more detail in Chapter 3. For now we mention that the high affinity for MTs (a MT binding affinity of 3.03 ± 1.2 μM was reported [Monroy et al.,

2018]) and the possibility to add a fluorescent label made MAP7 an interesting candidate for MT labeling. Figures as in [Hooikaas et al., 2019] show that MTs can easily be visualized by looking at the fluorescent MAP7 signal. Since MAP7 has a strong affinity for MTs yet not for tubulin dimers, we expected a lower background signal than when using fluorescently labeled tubulin dimers to visualize MTs.

We tested MAP7-Alexa647 *in vitro* in flow channels (Fig. 2.5A,B), and it was evident that MAP7 had some effects on MT dynamics, like a slower MT depolymerization rate. This and other effects will be discussed in Chapter 3. Most important for our experiments was that the MTs were dynamic, clearly visible in droplets and that end-binding proteins bound the plus-end. These three requirements were met.

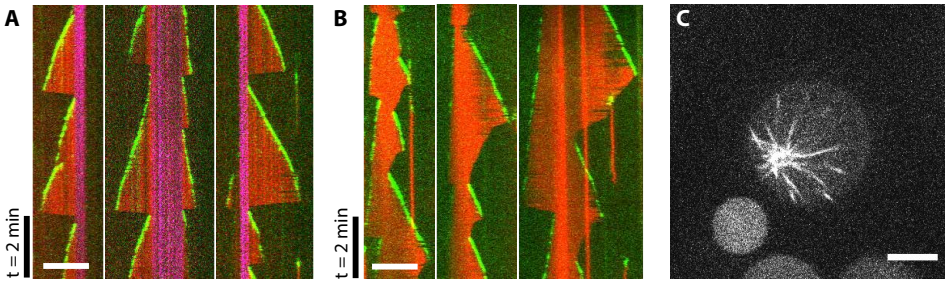

Figure 2.5: The influence of MAP7 on MT dynamics. **(A)** Kymographs of MTs growing from gmpcpp stabilized seeds (magenta) in the presence of 1.5 μM Rhodamine-tubulin (red) and 100 nM EB3-GFP (green). **(B)** Kymographs of MTs growing from GMPCPP stabilized seeds in the presence of 100 nM MAP7 (red) and 100 nM EB3-GFP (green) where the MT growth looks normal but the depolymerization is much slower than normally. **(C)** Water-in-oil emulsion droplet with MTs (30 μM tubulin, 100 nM MAP7) nucleating from an AurkA bead. Scalebars are 10 μm.

To use MAP7 as a fluorescent marker for MTs, we simply replaced the fluorescently labeled tubulin by 100 nM MAP7. Figure 2.5C shows an emulsion droplet with a MT aster which was visualized through MAP7. Comparing this image with Fig. 2.4A demonstrated that the MTs were better distinguishable with MAP7 compared to Rhodamine-tubulin and SiR-tubulin. It was even possible to see individual MTs inside the emulsion droplet. This has meant a great improvement for experiments where we needed to determine co-localization of MTs with cortical proteins (Chapter 4).

2.2.4. PROTEINS

Most of the proteins we used were gifts from other labs as specified in the list below. All proteins that were purified in-house were the work of Eli van der Sluis, Esengül Yildirim, Ashmiani van den Berg and Anne Doerr.

1. **Tubulin**: lyophilized porcine brain tubulin (unlabeled, or labeled with TRITC Rhodamine, HiLyte®488, or HiLyte®647) was obtained from Cytoskeleton (Denver, USA) and resuspended at 25-100 μM in MRB80, snap-frozen and stored at -80°C until use.

2. **MAP7**: full length MAP7-Alexa647 proteins, purified from HEK cells, were a kind

gift from Peter Jan Hooikaas and Anna Akhmanova (Department of Biology, Utrecht University, the Netherlands).

3. **EB3**: 6xHis-tagged recombinant human EB3, GFP-EB3 and mCherry-EB3 with the 6xHis-tag cleaved off [Komarova et al., 2009], purified from bacteria, were kind gifts from Michel Steinmetz (Laboratory of Molecular Research, Paul Scherrer Institute, Switzerland) and Anna Akhmanova (Department of Biology, Utrecht University, the Netherlands).

4. **MACF-derived peptides**: 10xHis-tagged recombinant MACF2 derivatives with 18 or 43 amino acids, purified from bacteria, were a kind gift from Anna Akhmanova (Department of Biology, Utrecht University, the Netherlands). Both MACF18 and MACF43 peptides contain a dimerization domain and an eGFP label. A 10xHis-tagged mScarlet-MACF18 was purified inhouse from bacteria. See Chapter 4 for more details.

5. **Photo-dissociable EB1**: EB1-LOV2 and EB1-Zdk1 were designed by van Haren et al. [van Haren et al., 2018] and purified inhouse from bacteria, see Chapter 5 for more details.

6. **iLID and SspB**: the improved light-induced dimer (iLID) and binding partner SspB from Guntas et al. [Guntas et al., 2015] were purified inhouse from bacteria, see Chapter 5 for more details.

7. **Centrosomes**: isolated from human lymphoblastic KE37 cells by Sophie Roth and Florian Huber following the protocol from [Moudjou and Bornens, 1998], or a kind gift from the Pierre Gönczy lab (Swiss Institute for Experimental Cancer Research (ISREC), School of Life Sciences, Swiss Federal Institute of Technology (EPFL) Lausanne, Switzerland).

8. **XMAP215**: recombinant XMAP215 from Xenopus laevis purified from SF+ cells [Brouhard et al., 2008] was a kind gift from Tony Hyman (Max Planck Institute of Molecular Cell Biology and Genetics, Dresden, Germany) to Tim Mitchison (Department of Systems Biology, Harvard Medical School, Boston, Massachusetts, United States of America), who shared it with us to use in combination with AurkA beads.

2.3. FUNCTIONALIZED LIPIDS

ESSENTIAL for our minimal system was the recruitment of specific proteins to the cortex of water-in-oil emulsion droplets. One option to achieve this was by incorporation of functionalized lipids in the oil-lipid mix that can specifically recruit our proteins of interest. Phospholipids with a functionalized headgroup are commercially available from *Avanti Polar Lipids, Inc.*, and we explored two types:

- DGS-NTA(Ni): *1,2-dioleoyl-sn-glycero-3-[(N-(5-amino-1-carboxypentyl) iminodiacetic acid) succinyl] (nickel salt)*

- biotinyl cap PE: *1,2-dioleoyl-sn-glycero-3-phosphoethanolamine-N-(cap biotinyl) (sodium salt)*

The first recruits histidine-tagged proteins, while the second can be used in combination with streptavidin to bind biotinylated proteins. We encountered a few problems that forced us to take a slightly different approach than with the normal lipid mix. It turned out that the surfactants we used (Tween20 and Span80) can inhibit specific protein recruitment to the cortex and in certain conditions destabilize the emulsion.

SPAN80 INHIBITS RECRUITMENT TO DGS-NTA(NI) LIPIDS

Histidine tags (his-tags) are widely used in protein purification due to their affinity for nickel-bound nitrilotriacetic acid (Ni-NTA). As a result, many of the proteins we use for *in vitro* reconstitution experiments still possess a histidine-tag which we can employ to bind those proteins to the droplet cortex. This bond is orders of magnitude weaker than for example a biotin-streptavidin bond, but still strong enough for our purpose.

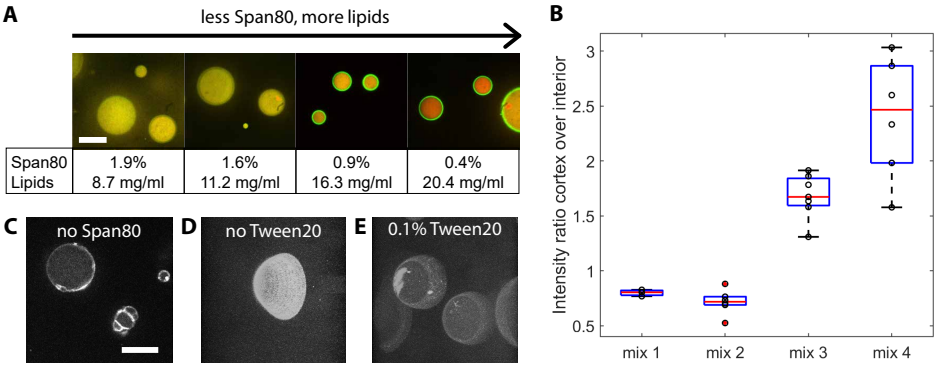

Figure 2.6: The effect of surfactants Span80 and Tween20 on emulsion droplets with DGS-NTA lipids: **(A)** A higher ratio of Span80 to lipids in the lipid mix results in lower recruitment of histidine-tagged protein (EB3-GFP, green) to the DGS-NTA lipids. A control protein (fluorescent streptavidin-568, red) shows that not all proteins are binding to the cortex for lower Span80. **(B)** Quantification of the intensity of histidine-tagged EB3-GFP on the cortex compared to the intensity in the interior of the droplet for the four lipid mixes shown in (A). **(C)** In absence of Span80 in the lipid mix droplets tend to merge and clump together, but histidine-tagged EB3 (greyscale) was recruited very efficiently to the cortex. **(D,E)** 3D reconstruction of EB3 (greyscale) recruitment in droplets without (D) and with (E) 0.1% Tween20 in the reaction mix. The presence of Tween20 seems to cause crashing of droplets onto the surface, creating a dome-shape rather than a sphere. Note that we only imaged the bottom half of the droplet as in the top half the imaging suffers from aberrations due to refraction by the spherical oil-water interface. Scalebars are 20 µm.

First control experiments showed no recruitment at all of histidine-tagged proteins to the cortex of emulsion droplets containing DGS-NTA lipids. This turned out to be the result of some interference between the surfactant Span80 and the DGS-NTA lipids (Fig. 2.6A,B). Complete removal of Span80 from the lipid mix resulted in very efficient recruitment of histidine-tagged GFP. But now the droplets were prone to merging (Fig.

2.6C) and crashing onto the silanized surface of the coverslip, making it practically impossible to perform experiments with those droplets. By varying the concentrations of lipids and Span80, while keeping the combined concentration around 25 mg/ml (Fig. 2.6A), we found an optimum where Ni-NTA lipids are not inhibited to recruit histidine-tagged protein while the droplets are stable enough to perform experiments. These conditions are listed in table 2.2 and we used this lipid mix for all experiments with DGS-NTA lipids in this thesis. The preparation of the lipid mix was as before, yet the composition was different: we were using different phospholipids at higher concentration combined with a lower Span80 concentration (table 2.2).

Further control experiments also showed that recruitment of histidine-tagged proteins to the DGS-NTA lipids was more efficient in the presence of DOPC lipids compared to DOPS lipids, so we decided to use the DOPC lipids.

Component	**Stock concentration**		**Final concentration**			
DOPC	25	mg/ml	16.3	mg/ml	20.7	µM
DGS-NTA(Ni)	10	mg/ml	1.0	mg/ml	1.0	µM
Span80	100	%	1.0	%	23.1	µM

Table 2.2: Composition of the lipid mix with DGS-NTA lipids and 1% Span80 (v/v).

The other surfactant, Tween20, was not dissolved in the lipid mix but in the reaction mix [Roth et al., 2014, Vleugel et al., 2016]. Its function is to prevent aspecific binding of proteins to the cortex. A problem we observed during experiments with DGS-NTA lipids was crashing of droplets onto the silanized glass coverslip, creating a dome instead of a sphere (Fig. 2.6E). This turned out to be a side effect of Tween20, as leaving it out stopped the crashing of droplets (Fig. 2.6D). We will discuss properties of surfactants and lipids and how they might interact with each other in Sec. 2.3.1. The downside of not using Tween20 inside water-in-oil emulsion droplets was that certain proteins (especially molecular motors) stuck aspecifically to the cortex. In our experiments, we accepted this disadvantage and left Tween20 out of the reaction mix.

TWEEN20 REDUCES RECRUITMENT OF STREPTAVIDIN TO BIOTINYL CAP PE LIPIDS

The high-affinity bond between biotin and streptavidin is used in many biotechnological applications. In our case, the biotin-group was attached to a lipid headgroup, allowing streptavidin inside water-in-oil emulsion droplets to bind those lipids. Subsequently, the biotinylated protein of interest, e.g. dynein [Laan et al., 2012b, Roth et al., 2014, 2019b] or a +TIP, could be recruited to the droplet cortex.
We encountered problems when first trying to establish recruitment of fluorescently labeled streptavidin to the cortex of droplets made with a lipid mix as in table 2.3. The recruitment seemed to be partially inhibited by Tween20. Leaving this surfactant out made proteins (like molecular motors) bind aspecifically the droplet cortex, but it also enabled streptavidin to bind to the cortex with higher affinity (Fig. 2.7).

Interestingly, the interaction of streptavidin with biotinylated lipids was not inhibited by the presence of Span80 in the lipid mix (as it did for the DGS-NTA lipids). There-

fore we could use a relatively high percentage of 2.7% Span80 which kept the droplets stable.

Component	Stock concentration		Final concentration			
DOPS	10	mg/ml	0.56	mg/ml	0.69	µM
biotinyl cap PE	10	mg/ml	0.080	mg/ml	0.080	µM
Span80	100	%	2.7	%	62.4	µM

Table 2.3: Composition of the lipid mix with biotinyl cap PE lipids and 2.7% Span80 (v/v).

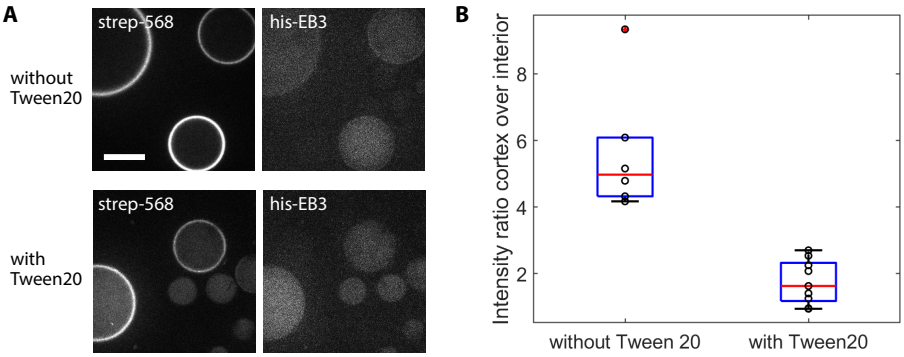

Figure 2.7: Effect of the surfactant Tween20 on emulsion droplets with biotinyl cap PE lipids: **(A)** comparison of the recruitment of a fluorescent streptavidin and a control protein (his-tagged EB3-GFP in this case) to the biotinyl cap PE lipids in the cortex with and without 0.1% Tween20 in the reaction mix. Scalebar is 10 µm. **(B)** Quantification of the intensity ratio of strep-568 on the cortex and in the droplet interior shows a negative effect of Tween20 on recruitment of streptavidin to biotinyl cap PE lipids.

2.3.1. NONIONIC SURFACTANTS AND FUNCTIONALIZED LIPIDS

We summarized the results of Span80 and Tween20 in combination with different functionalized phospholipids in table 2.4.

	DGS-NTA	biotinyl cap PE
Tween20	unstable droplets	decreased recruitment of histidine-tagged proteins
Span80	decreased recruitment of streptavidin-labeled proteins	no influence

Table 2.4: Influence of surfactants Tween20 and Span80 on emulsion droplets with a lipid mix containing either DGS-NTA lipids or biotinyl cap PE lipids.

Both Tween20 and Span80 are nonionic surfactants. Surfactants accumulate at the water-oil interface and orient themselves with the polar/hydrophilic part in the water and the apolar/hydrophobic part in the oil. Hereby they reduce the surface tension of the emulsion droplets. A back of the envelope calculation on 0.1% (v/v) Tween20 in

a droplet of 10 µm radius gives a total of $2 \cdot 10^{12}$ molecules. This is orders of magnitude more than the number of protein molecules typically encapsulated in a droplet - assuming 100 nM which results in about $2 \cdot 10^5$ molecules. In addition, the critical micelle concentration (CMC) of Tween20 in water is 0.0074% [Mahmood and Al-Koofee, 2013]. This value is much lower than the concentration of 0.1% in our experiments, so many Tween20 micelles were present in the water phase.

When looking into the material safety data sheets of Tween20 it states that polysorbates (alternative name for Tween20 is polysorbate 20) are incompatible with among others heavy metal salts. The DGS-NTA lipids contain nickel salts and nickel is a heavy metal. So this could explain the destabilization of emulsion droplets by the combination of Tween20 and DGS-NTA lipids. Furthermore, the data sheet of Span80 states that Span80 is incompatible and reactive with oxidizing agents. Nickel salt in solution is an oxidizer, though not a strong one ($E^0 = -0.257$ V), so this might explain why Span80 partially inhibits the recruitment of proteins to DGS-NTA lipids.

We have two hypotheses on how Tween20 inhibited streptavidin-labeled protein recruitment to biotinyl cap PE lipids at the droplet cortex. On the one hand, by shielding the biotinyl cap PE lipids at the droplet cortex so they became unavailable for binding. Tween20 is used to block aspecific sticking of proteins to the water-oil interface, so it might also (partially) block specific interaction. On the other hand, Tween20 could prevent streptavidin-labeled proteins to bind the cortex when some proteins get incorporated in the Tween20 micelles.
The results with Tween20 were surprising since previous work in our lab showed recruitment of biotinylated-dynein through streptavidin to biotinyl cap PE lipids in the cortex in the presence of Tween20 [Laan et al., 2012b, Roth et al., 2014, 2019b]. Molecular motors like dynein tend to bind aspecifically to the oil-water interface. Shielding of the interface by Tween20 prevents aspecific binding. At the same time, Tween20 lowers the specific binding of streptavidin to biotinyl cap PE lipids as we found, but it does not inhibit binding completely. Therefore, adding Tween20 to the reaction mix is a good choice for proteins with high aspecific binding affinity for the oil-water interface. For proteins that do not bind aspecifically to the oil-water interface, we preferred to leave out Tween20.

Summarizing, additional experiments are needed to find out why Span80 and Tween20 have the reported disturbing effects on specific recruitment of proteins to functionalized phospholipids. For the experiments in this thesis, we found conditions that work good enough by lowering the Span80 concentration in case of DGS-NTA lipids and not using Tween20 anymore.

2.4. IMAGING EMULSION DROPLETS

We imaged the interior of water-in-oil emulsion droplets with an inverted Spinning Disc confocal fluorescence microscope with a Nikon CFI Plan Apo Lambda 100x oil immersion lens (NA 1.45, working distance 0.13 mm). A custom-made temperature control system with a heating ring around the objective lens established a

sample temperature of 27-30°C, which was required for MTs to polymerize inside emulsion droplets at the tubulin concentrations we used (20-40 μM). To image emulsion droplets, transfer 10 μl of emulsion droplets, either prepared by microfluidics (Fig. 2.2A) or by pipetting (Fig. 2.2B), into the PDMS well (Fig. 2.2C). Typical fields of view of an experiment with droplets prepared by microfluidics or by pipetting are shown in Fig. 2.2D and E, respectively. Depending on the yield of the centrosome purification or the concentration of beads after washing, between 0.01% and 10% of droplets contains a MT aster.

Previous studies on MTs encapsulated in emulsion droplets have followed for example MT aster positioning over time, with or without additional MT-associated proteins [Laan et al., 2012a, Roth et al., 2014, Vleugel et al., 2016], or MT organization in the presence of crosslinking motors [Baumann and Surrey, 2014, Juniper et al., 2018]. In those situations, one snapshot every minute suffices to track the aster position or MT organization. However, now the objective was to study MT dynamics by tracking end-binding protein comets at the growing MT tips, we needed to acquire timelapses with much smaller timesteps, in the order of one per second. To establish this while keeping the signal-to-noise ratio high enough to visualize MTs and protein comets, we increased laser power and used exposure times of 150-500 ms. Other tricks to speed up image acquisition were dual color imaging (no need to switch filters and laser color) and using only the center part of the camera (faster readout). But as dual-imaging comes at the expense of the intensity of the two wavelengths signals, this could only be used in case of sufficiently high intensities. Which brings us to another challenge in imaging dynamic co-organization of MTs and cortical proteins in emulsion droplets: the choice of fluorescent dyes.

Compared to imaging MT asters only, the system had become more complex with more components to consider for imaging. To visualize proteins inside 3D emulsion droplets, the brightness of the fluorescent probe was more important than for quasi-2D experiments in a flow channel, where TIRF microscopy resulted in good contrast. For confocal Spinning Disc imaging of emulsion droplets, the background intensity was much higher as a result of the larger depth of focus than for TIRF microscopy. Moreover, light was refracted by the spherical water-oil interface, which induced aberrations that further decreased the image quality. Hence it was necessary to think carefully about which fluorescent probe to put on which protein. As GFP was the brightest probe we had available, we usually labeled the protein of interest with GFP. Depending on the goal of the experiment this could be EB3 or a cortical +TIP. For the MTs, we generally used MAP7-A647 (Sec. 2.2.3), but otherwise rhodamine-tubulin worked in our hands the best out of the commercially available fluorescent tubulins. Any additional component to the minimal system meant reconsidering the fluorescent labels of the present proteins to optimize visualization of the process we wanted to study.

2.5. FLOW CHANNELS

EVEN though the main reconstitution experiments described in this thesis were performed in droplets, flow channel experiments were performed as well. Because the MTs were attached to a glass surface they were less motile than inside emulsion droplets. In addition, we could image with TIRF microscopy which yields images with much better SNR than spinning disc confocal images. These two factors made flow channels a far better way to characterize the interaction of MTs and proteins than emulsion droplets. Therefore, all proteins used in the emulsion droplets were first tested and characterized in flow channels.

2.5.1. PREPARATION

1. Clean glass slides and coverslips (24 mm x 24 mm, 1.5 thickness) by sonication in ethanol: sonicate 20 minutes in 70% ethanol, rinse with H_2O, sonicate 20 minutes in H_2O and store in fresh H_2O until use. Note that one can do more thorough cleaning by piranha treatment of the glass, which was not necessary for most of the experiments in this thesis. Dry the glass before use with nitrogen air flow;
2. Cut channels (2 mm width) from a piece of parafilm (Fig. 2.8) and assemble the flow channel with glass slide, parafilm and coverslip as in Fig. 2.8. Finally, melt the parafilm on a 120°C hot plate;
3. Flush the channels (count 20 µl per channel) with 0.2 mg/ml PLL-PEG-biotin, incubate for 10 minutes, rinse with MRB80 buffer;
4. Repeat this step first with 0.2 mg/ml neutravidin and then with 0.5 mg/ml k-casein;
5. Dilute GMPCPP stabilized microtubule seeds in MRB80 (room temperature), flush into the channels, incubate 10 minutes with the coverslip facing down and the glass slide facing up such that gravity makes the seeds bind mostly to the coverslip. Next, rinse with MRB80 buffer (room temperature).

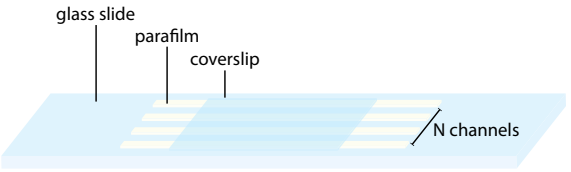

Figure 2.8: Schematic of a flow channel with $N = 3$ channels.

2.6. KYMOGRAPH ANALYSIS

THE conventional way to study MT dynamics is by kymographs, which show a representation of the MT growth over time. To prepare a kymograph, we project the movie in time (Fig. 2.9A,B) and draw lines of 5 pixels width along the MTs in a certain field of view using ImageJ. Next, the ImageJ plugin *KymoResliceWide* creates kymographs (Fig. 2.9C). The slope of a growing/shrinking MT in such a kymograph provides the MT growth/shrinkage velocity, but also the duration of growth events can be extracted. Slopes of all growth events are determined by manually drawing lines in ImageJ. All line properties are saved and loaded into Matlab for further analysis and plotting.

In the cumulative distribution functions (cdf) of the MT growth velocities in this thesis one can sometimes note a sharp kink in the plot. This kink is an artifact resulting from the image analysis in ImageJ. When making a kymograph of a MT which is oriented under an angle (like the MT indicated with the white dashed line in Fig. 2.9B), projections are involved. For at the moment unknown reasons, the probability to measure a slope of 45° is higher than for any other slope, leading to the kink we observe in most cdf plots. This kink can be relatively discrete in the tail of the distribution or very outstanding in the middle of the distribution, depending on the average growth velocity of the MTs in a certain experiment and the timestep of the image acquisition.

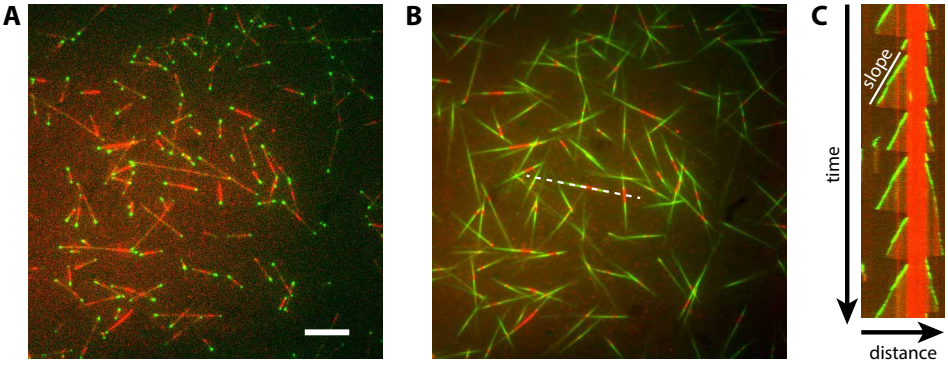

Figure 2.9: The procedure to make kymographs. **(A)** Frame from a movie with MTs (red) and EB3 protein comets (green) tracking the growing MT ends. Scalebar is 10 µm. **(B)** Time-projection of the movie in (A). The white dashed line indicates how a line is drawn along which to create a kymograph. **(C)** Kymograph of the MT indicated by the white dashed line in (B).

3

THE INFLUENCE OF MAP7 ON MT DYNAMICS AND STRUCTURE

'En ik heb nog iets waarvan ik de naam niet weet,' zei de eekhoorn.
'Dus geen beukennoot?' vroeg de mier.
'Nee, want daar weet ik de naam van.'

Toon Tellegen

Different cellular processes require different MT organizations. For proper functioning of those processes, spatial and temporal reorganization of the MT conformation is crucial, which is regulated by microtubule-associated proteins. One of them is the protein MAP7, which binds to microtubules, and hereby stabilizes them and enhances the recruitment of kinesin-1 molecular motors. Because of the strong affinity for microtubules, we explored the application of fluorescent MAP7 for indirect visualization of microtubules in vitro. In this chapter, we characterize the influence of MAP7 on microtubules in vitro. We found a strong stabilizing effect of MAP7 on microtubules, but also a very good visibility of MAP7-covered microtubules, which makes MAP7 a suitable tool for in vitro microtubule visualization. During the MAP7 characterization, we ran into unexpected features in the microtubule shrinkage trajectory. A sharp transition from fast to slower microtubule depolymerization seemed to coincide with saturation of the MT lattice with MAP7. We propose and discuss some hypotheses for this observation.

3.1. INTRODUCTION

In cells, microtubules (MTs) are involved in various cellular processes, including formation of the mitotic spindle, cell migration and intracellular transport of cargo like vesicles. The dynamic nature of MTs is crucial to quickly reorganize them, for example during spindle formation for cell division. In other situations, like in neuronal cells, stable MTs are abundant to serve as tracks for molecular motors for transport of cargo between the cell body and the ends of the axon. Microtubule-associated proteins (MAPs, introduced in Sec. 1.1) are involved in the regulation of MT dynamics, stability and interaction with other cellular components.

MAP7, also called E-MAP-115 [Masson and Kreis, 1993] or ensconsin [Bulinski and Bossler, 1994], is one of those regulatory MAPs. Initially, people found a stabilizing effect of MAP7 on MTs [Masson and Kreis, 1993, Bulinski and Bossler, 1994], but it was not clear if this was the main function of the protein in vivo [Faire et al., 1999]. Later, the most important function turned out to be recruitment of kinesin-1 to MTs [Sung et al., 2008, Metzger et al., 2012, Barlan et al., 2013, Gallaud et al., 2014, Yadav et al., 2014, Monroy et al., 2018, Chaudhary et al., 2019, Hooikaas et al., 2019]. The N-terminal domain of MAP7 proteins interacts with MTs while the C-terminal domain binds to kinesin-1 [Sun et al., 2011, Metzger et al., 2012, Monroy et al., 2018]. In addition, the linker of MAP7 contains regions with MT affinity [Yadav et al., 2014]. So MAP7 is tightly bound to MTs and can transiently interact with kinesin-1 [Hooikaas et al., 2019]. The combination of these two properties increases the kinesin-1 binding to MTs [Chaudhary et al., 2019]. *In vitro* reconstitutions showed a 150-fold increase of kinesin-1 binding [Monroy et al., 2018]. Because of this influence on kinesin-1 recruitment, MAP7 plays a role in MT organization in mitosis and neuronal branching and in the regulation of organelle transport [Gallaud et al., 2014, Chaudhary et al., 2019]. However, the exact mechanism of kinesin recruitment by MAP7 is still unknown. One hypothesis is that MAP7 changes the spatial structure of the MT lattice, which increases the binding efficiency and processivity of kinesin on MTs.

In this chapter, we performed *in vitro* characterization of the effect of a full-length MAP7-Alexa647 (called MAP7 from now on) on MT dynamics, because we wanted to use MAP7 for indirect MT visualization inside water-in-oil emulsion droplets (Sec. 2.2.3). We found a major stabilizing effect of MAP7 on MTs, because it decreased the MT depolymerization rate and catastrophe rate. In addition, we observed non-linearities in the MT shrinkage trajectories: a sharp transition from fast depolymerization for MT sections with low MAP7 density to slower depolymerization of MT sections with maximum MAP7 density. We formulated two hypotheses for this effect. One involving MT-surface interactions that could be enhanced by MAP7 decoration of MTs. The other one proposes a structural change of the MT lattice by binding of a certain amount of MAP7, possibly related to the effect on kinesin-1 recruitment. We discuss both hypotheses and propose future experiments to get a better idea of the mechanism behind the MT depolymerization rate changes.

3.2. RESULTS

THE influence of MAP7 on MTs was characterized in flow channels (Sec. 2.5). MTs nucleated from GMPCPP-stabilized seeds attached to the glass surface in the presence of free tubulin, GTP and either Rhodamine-tubulin or MAP7. The difference between the two is shown in Fig. 3.1. Rhodamine-MTs were straight, stiff and highly dynamic, while MAP7-MTs were a bit curved (Fig. 3.1A). Moreover, in the movies we could see that MAP7-MTs wiggled around more and were more stable (fewer catastrophes) than Rhodamine-MTs. It is known that MAPs can change the flexibility of MTs [Hawkins et al., 2010, Portran et al., 2013]. Furthermore, over time we observed a net increase of the total polymerized MT length for MAP7 (Fig. 3.1B,C), while this length was stable for Rhodamine-MTs. We knew from previous experiments (data not shown) that the time to reach equilibrium is a few minutes for Rhodamine-MTs at 30°C. The time to reach this equilibrium in the presence of MAP7 was clearly much longer (> 10 minutes, Fig. 3.1C).

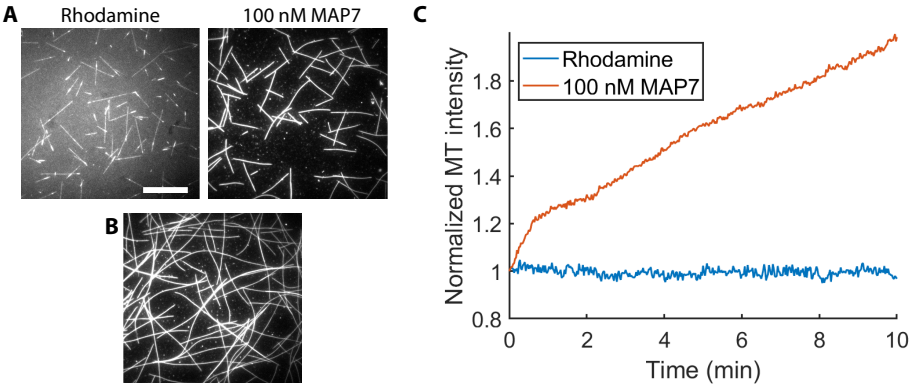

Figure 3.1: (A) Snapshots of dynamic MTs in a flow channel nucleating from GMPCPP-stabilized MT seeds, the MTs were labeled with either fluorescent rhodamine-tubulin (left) or 100 nM MAP7 (right). Scalebar is 20 µm. **(B)** MTs with 100 nM MAP7 after about 1 hour. The MTs are clearly much longer then in (A). **(C)** Comparison of the total MT increase (quantified by their total intensity in one field of view of the microscope) over time for either Rhodamine or MAP7-labeled MTs.

Next, we quantified the MT dynamics with MAP7 compared to Rhodamine-tubulin (Fig. 3.2). For easier determination of growth events and MT growth velocities, we added end-binding protein EB3-GFP to the experiment, which tiptracked the growing MT tips. EB3 also affects MT dynamics, by increasing the growth velocity and catastrophe rate [Nakamura et al., 2001, Tirnauer et al., 2002, Ligon et al., 2003, Bieling et al., 2007, Manna et al., 2008, Vitre et al., 2008, Komarova et al., 2009]. The difference in dynamics between MTs with Rhodamine-tubulin versus MAP7 could be seen in the kymographs in Fig. 3.2A,B, but they were more clear in the cumulative distribution functions in Fig. 3.2C-F. One might note a sharp kink in the cdf plot of the MT growth velocity around 1.6 µm/min. This issue resulted from data analysis in ImageJ and is discussed in Sec. 2.6. The growth velocity of MTs was slightly lower in the presence of MAP7 (Fig. 3.2C), and the growth time was increased (Fig. 3.2D), but mostly for higher

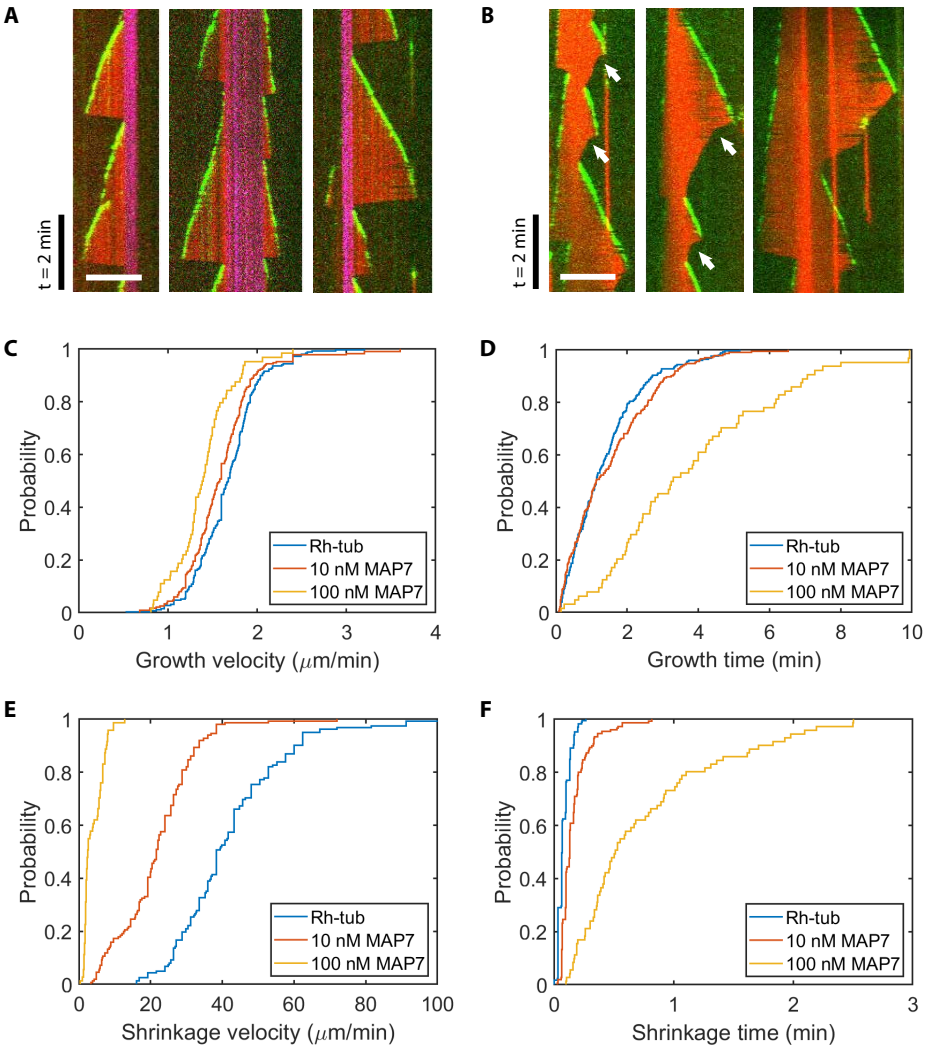

Figure 3.2: (A) Kymographs of MTs growing from GMPCPP stabilized seeds (magenta) in the presence of 1.5 µM Rhodamine-tubulin (red) and 100 nM EB3-GFP (green). Scalebar is 10 µm. **(B)** Kymographs of MTs in the presence of 100 nM MAP7-A647 (red) and 100 nM EB3-GFP (green) where the MT growth is similar as in (A) but the depolymerization is much slower than without MAP7. White arrows indicate the location of kinks, sharp transitions in the depolymerization rate. **(C-F)** Cumulative distribution function of the MT growth rate (C), MT growth time (D), depolymerization rate (E) and depolymerization time (F) for MTs in the presence of Rhodamine-tubulin compared to different concentrations of MAP7-A647. We observed a small effect of 10 nM MAP7 on MT dynamics and a much larger effect for 100 nM MAP7.

MAP7 concentration. For reasons explained in the discussion (Sec. 3.3), shorter MTs were over-represented, which could have distorted the growth time data. But despite any potential distortion, the enhancing effect of MAP7 on MT growth time is significant. Since practically no rescues were observed we concluded that the catastrophy

rate was lower for MTs decorated with MAP7. In addition, when a MT underwent a catastrophe, the shrinkage velocity was much slower for higher MAP7 concentration (Fig. 3.2E) and hence the shrinkage time increased (Fig. 3.2F). A slower MT depolymerization rate makes sense when the MT lattice is covered with proteins like MAP7. The data suggested that MAP7 stabilized MTs in two ways: both the catastrophe rate and the depolymerization rate were reduced.

Striking in Fig. 3.2B,E was that two depolymerization rates occurred: initially a MT depolymerized fast and later it slowed down. The transition from one depolymerization rate to the other was usually a sharp "kink", as visible in the kymographs. For dynamic Rhodamine-MTs, an acquisition framerate of 0.5-1 s^{-1} was not high enough to follow the fast depolymerization (Fig. 3.2A). But since MAP7 substantially reduced the depolymerization rate, we did acquire enough data points of the depolymerization to note any variations.

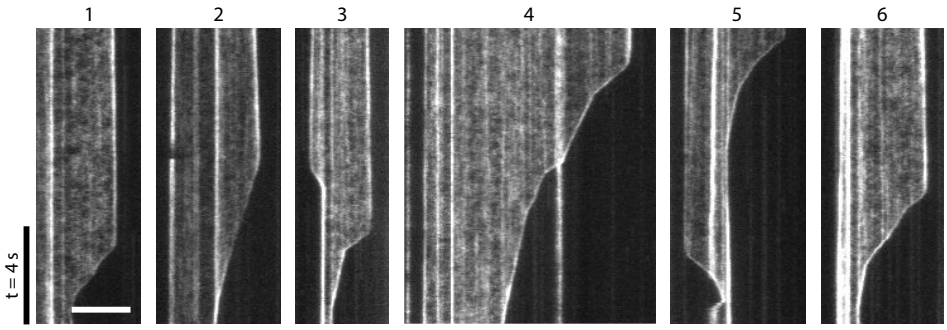

Figure 3.3: Kymographs of MTs in the absence of MAP7 but with 50 nM of the MT-binding MACF43-GFP peptide (greyscale). The acquisition framerate of 12.5 s^{-1} was high enough to capture the rapid MT depolymerization. We observe linear depolymerization (1,2), with a kink (3), with multiple transitions (4) or more gradual change of depolymerization rate (5,6). Scalebar is 5 µm.

To study the kinks in more detail, we repeated the MAP7 experiment without EB3. First, we looked at the occurrence of transitions in the depolymerization rate. Even though we also observed multiple transitions (21.5% for 10 nM MAP7, see Fig. 3.5A) or no kink at all (7%) in some occasions, the majority of kymographs showed precisely one kink (71.5%). One possibility was that we were looking at stochastic variations of the depolymerization rate. So we compared the shrinkage trajectories with those acquired at 12.5 s^{-1} framerate for MTs in the presence of the 43 amino acid long truncate of MACF2 (MACF43-GFP) used in Chapter 4. In those trajectories (Fig. 3.3), we also observed transitions in the depolymerization rate. However, one sharp kink was more rare than for MAP7-covered MTs (18%), while linear depolymerization and multiple transitions were more abundant with 33% and 36% respectively. Also more gradual change of the depolymerization rates were observed (12%), in contrast to the sharp transitions.

The occurrence of single sharp kinks in the MT depolymerization trajectories were more abundant in the presence of MAP7 than without it. Therefore, we were wondering if there could be another reason for the kinks than just stochastic variations. To

answer this question, performed a detailed analysis of the shrinkage trajectories (Fig. 3.5). We have kymographs for 10, 50 and 100 nM MAP7, but most of the analysis could only be done for 10 nM MAP7. The MTs with higher MAP7 concentrations were too long, soft and therefore motile to reliably follow the shrinking MT tip.

First, we looked at the accumulation of MAP7 on the MT lattice over time (Fig. 3.5C). We analyzed the MAP7 intensity along the pink dotted line in Fig. 3.5B1, and fitted an exponential to these data:

$$I(t) = A + Be^{-k_{on}t} \tag{3.1}$$

Note that we fitted k_{on} to the data. It is known from fluorescence recovery after photobleaching (FRAP) experiments that MAP7 binds very strongly to the MT lattice, recovering with a half-time of 411 s [Tymanskyj et al., 2018]. Therefore we assumed that the off-rate was very low and did not significantly influence the increase of MAP7 on the MT lattice. The accumulation of MAP7 on the MT lattice was twice as fast for 50 nM MAP7 (k_{on} = 0.016± 0.001 s^{-1}) as for 10 nM MAP7 (k_{on} = 0.0073± 0.0003 s^{-1}). The absolute saturation intensity of MAP7 on the MT lattice seemed on average higher for higher MAP7 concentration (Fig. 3.4). But the variations between individual curves was very large as a result of the inhomogeneity of the TIRF microscope illumination field. Therefore we could not draw a solid conclusion from these data whether the maximum MAP7 level indicates that the MT lattice is saturated with MAP7 or whether it is only an equilibrium level depending on concentration, on-rate and off-rate. In the remainder of the chapter, we will call it the equilibrated MAP7 level.

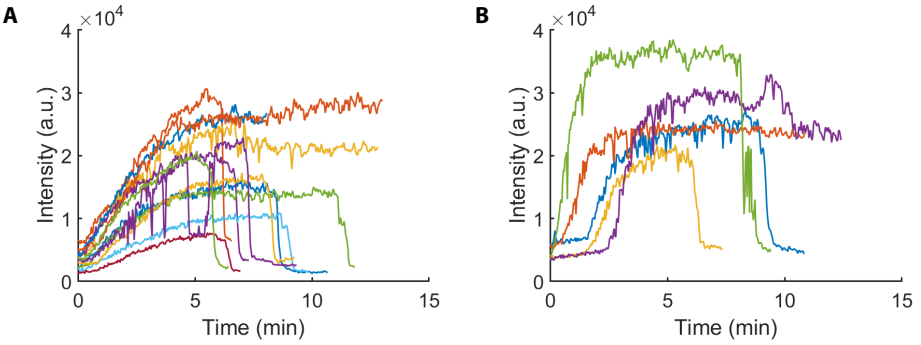

Figure 3.4: Absolute intensities of MAP7 on the MT lattice, measured along lines as in Fig. 3.5B2 for 10 nM MAP7 **(A)** and 50 nM MAP7 **(B)**.

While studying the MAP7 intensities, we noticed in some of the kymographs for 10 nM MAP7 that the initial fast depolymerizing part of the MT (the newest part of the MT) showed inhomogeneous MAP7 intensity. We quantified the intensity along the shrinkage trajectory before and after the kink (Fig. 3.5B2,D). Obviously the MAP7 intensity fluctuated a lot, but a clear trend appeared after averaging. Before the kink, the MAP7 intensity on the lattice was increasing along the trajectory from catastrophe to the kink (purple line). After the kink, the average MAP7 intensity was constant along the shrinkage trajectory (green line). We did not only analyze those intensities for kymographs

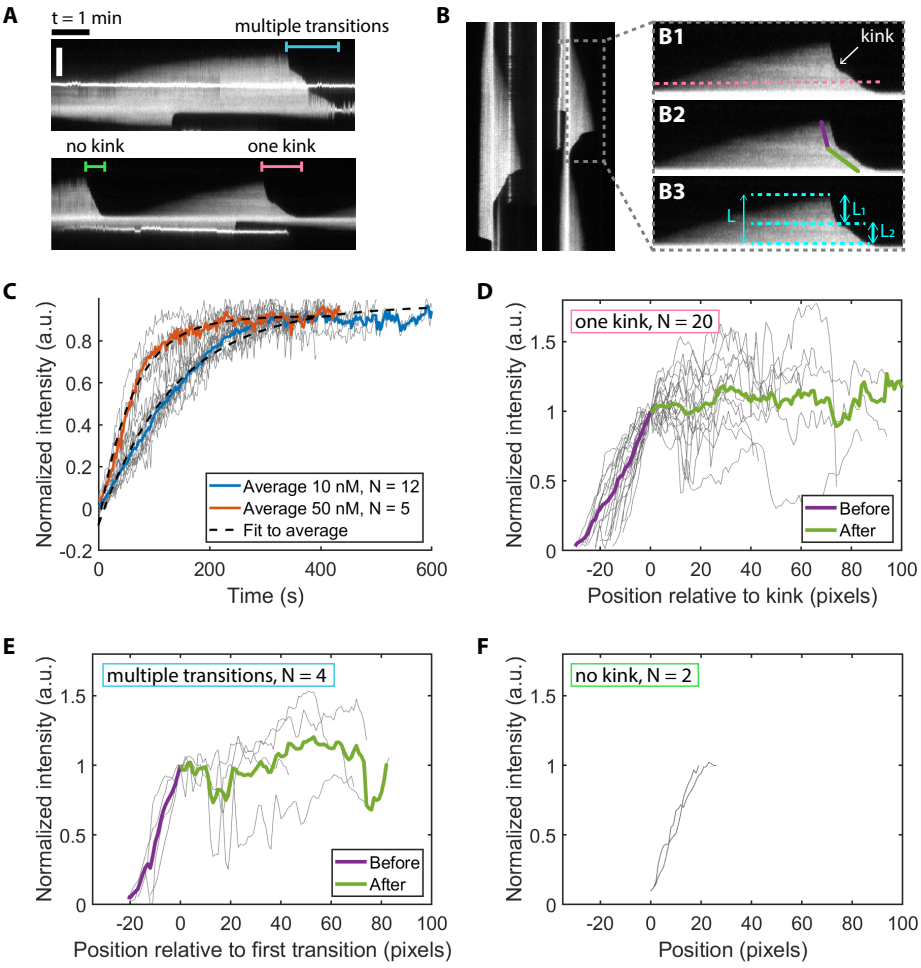

Figure 3.5: (A) Kymographs for 10 nM MAP7 showing examples of the different types of shrinkage trajectories: multiple transitions (21.5%, N = 6), no kink (7%, N = 2) and one sharp kink (71.5%, N = 20). Vertical scalebar is 5 µm. **(B)** Two examples of kymographs for 10 nM MAP7 in absence of EB3. Some important parameters in the analysis are indicated in the enlarged part of the kymograph. **B1**: Line along which the MAP7 intensity on the MT lattice over time is measured (see (C)). **B2**: Regions of interest before and after the kink in the shrinkage trajectory, corresponding to the curves in (D-F). **B3**: The total MT length L at the moment of catastrophe and the length of the slowly depolymerizing regime L_2, corresponding to the analysis in Fig. 3.6. **(C)** Intensity plots for the accumulation of MAP7 on the MT lattice, along a line like indicated in B1. **(D-F)** MAP7 intensity at the depolymerizing MT plus end for 10 nM MAP7 in the case of one kink (D), multiple transitions (E) or no transition at all (F) in the shrinkage trajectory. We distinguish the regimes before (purple) and after (green) the first transition, as indicated in B2. Because only two trajectories without a kink were analyzed, we did not calculate the average but just show the two intensities from the moment of catastrophe back to the seed in (F).

with only one kink, but also for those with no kink or with multiple transitions. In absence of a kink we only had two kymographs, in both of them the MAP7 intensity was

increasing along the trajectory starting at catastrophe (Fig. 3.5F). In case of multiple transitions, we had a few more kymographs to analyze. We observed an increasing MAP7 intensity before the first transition in depolymerization rate. Interestingly, the MAP7 intensity was constant on average after this first transition, despite the presence of the other transitions. Therefore we plotted the intensity before the first transition in purple and after it in green (Fig. 3.5E).

These data suggested that something happened at the moment that the MT lattice was saturated with MAP7, because that moment coincided with a sudden decrease of the depolymerization rate. It makes sense that coverage of the MT lattice with proteins influences its depolymerization rate, but since the increase of MAP7 on the lattice is gradual we would expect a more gradual change of the depolymerization rate. Instead, we observed sharp transitions (Fig. 3.5A,B), which made us wonder if there was another explanation than just MAP7 coverage.

To find out more about the kink from our kymographs, we compared the lengths of the MT sections before and after the kink with the total MT length at the moment of catastrophe (Fig. 3.5B3 and Fig. 3.6). Because in the cases with multiple transition the MAP7 intensity was increasing only to the moment of the first transition, we counted this transition as the "kink" in the following analysis. We distinguished the cases with one kink from the ones with multiple transitions by color in Fig. 3.6. The length of the fastly depolymerizing MT section before the kink (L_1) was approximately constant with an average length of $L_1 = 3.7 \pm 1.6$ µm. This length was similar for shrinkage trajectories with one kink and multiple transitions. In contrast, the slower depolymerizing MT section after the kink (L_2) showed a linear dependence on the total MT length. Fitting of the equation

$$L_2 = \alpha \cdot L - L_0. \tag{3.2}$$

with Matlab yielded $\alpha = 0.90 \pm 0.18$ and $L_0 = 2.8 \pm 1.6$ µm (errors come from the 95% confidence bounds of the fit). The data from shrinkage trajectories with one kink or multiple transitions were approximately on one line.

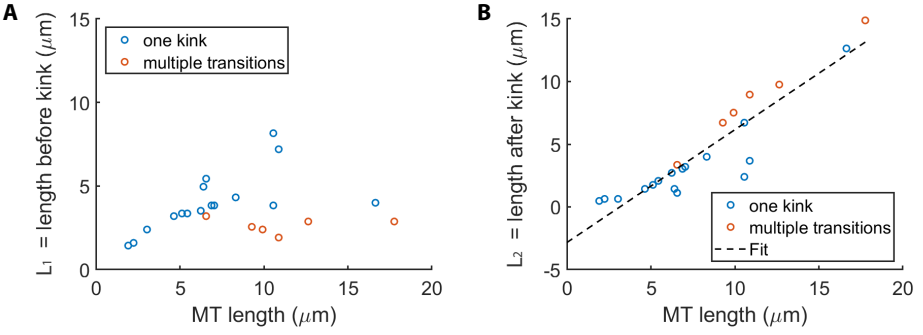

Figure 3.6: (A,B) Correlation plots of the length of the fast/slow depolymerization regimes (before/after the kink respectively) and the total MT length L at the moment of catastrophe for 10 nM MAP7, also see Fig. 3.5B3.

Summarizing, we made a number of observations:

1. Sharp transitions were observed in the depolymerization rate of MTs in the presence of 10 nM MAP7. We also observed such transitions for higher MAP7 intensities, but quantification was problematic due to the long and motile MTs.
2. MT depolymerizations with only one kink in the shrinkage trajectory were more abundant for short MTs (<7.5 μm), while multiple transitions were more frequently observed for long MTs (>7.5 μm).
3. The MAP7 intensity on the MT lattice increased exponentially over time, with a half-time of 120 s for 10 nM MAP7.
4. The intensity of MAP7 on the MT section which depolymerized rapidly (before the first kink) was increasing along the shrinkage trajectory from catastrophe to kink. In contrast, the intensity of MAP7 on the MT section which depolymerized slowly (after the first kink), was on average constant along the shrinkage trajectory.
5. The length of the MT section which depolymerized rapidly (before the first kink) was more or less independent of the total MT length at the moment of catastrophe, and was found to be $L_1 = 3.7 \pm 1.6$ μm.
6. The length of the MT section which depolymerized slowly (after the first kink) depended linearly on the total MT length at the moment of catastrophe. A fit of this linear relation yielded a slope of $\alpha = 0.90 \pm 0.18$ and an offset of 2.8 ± 1.6 μm. This slope was around 1 and the offset very close to the average $L_1 = 3.7 \pm 1.6$ μm, which would mean that the relation $L_2 = L - L_1$ holds.

Taken together, these findings suggested that the first sharp kink in the shrinkage trajectories always occurred at the transition from a MT section only partially covered with MAP7 (fast depolymerization) to a MT section where the MAP7 coverage has equilibrated (slower depolymerization). Because it takes a certain time before the MAP7 density on the MTs reaches its maximum, the fast depolymerizing MT section before the kink L_1 has a constant length. The remaining part of the MT depolymerizes slower because of the MAP7 molecules.

A few questions remained unanswered: 1. what is the relation between MAP7 coverage and the change in MT depolymerization rate? 2. why did we observe sharp transitions between depolymerization rates instead of gradual ones? 3. why did we often observe multiple transitions in depolymerization rate for longer MTs? 4. why was only the first of those transitions related to saturation of the MT with MAP7?

3.2.1. POSSIBLE HYPOTHESES

In this section, we will speculate about possible explanations for the observed transitions in depolymerization rate in the presence of 10 nM MAP7. To that end, we first summarize the mechanism behind MT depolymerization. The process of MT depolymerization is driven by the release of mechanical stress stored in the MT lattice. GTP-

bound tubulin dimers are straight and extended when they are incorporated in the MT. During GTP hydrolysis, the dimers undergo a conformational change towards a more twisted and compacted form. As a consequence, the MT lattice is spring-loaded and only held together by the GTP-cap. When this cap disappears, the MT falls apart into outward curling protofilaments. (review by [Barsegov et al., 2017]) Because of the released energy, depolymerization is very rapid and depolymerizing MTs are even capable of exerting pulling forces. Stochastic variations in the MT depolymerization rate can occur, for example due to MT lattice defects. It makes sense that coverage of the MT lattice with a MAP like MAP7 lowers its depolymerization rate, because it might stabilize the lateral tubulin-tubulin bonds and decrease mechanical tension. This is in agreement with our observation that higher MAP7 concentrations lead to reduced depolymerization rates and reduced catastrophe frequencies (Fig. 3.2).

However, MAP7 coverage of the MTs and stochastic variations do not explain why a sharp transition from fast to slow depolymerization would occur at the moment that the MAP7 intensity on the MT lattice is maximum.

One hypothesis is that MAP7 on the MT lattice enhanced the MT-surface interactions, which influenced the depolymerization rate. Previous experiments in our lab for example have shown a reduction of the MT depolymerization rate and catastrophe rate caused by electrostatic interactions between MTs and a silicon carbide coated coverslip [Kok, 2019]. The transitions might be the consequence of MTs sticking to the coverslip as a result of the MAP7 molecules on the MT lattice. The chance of sticking would then be lower for sections of the MT with lower MAP7 density, which could explain that we observe the first transition at the point where the MAP7 intensity on the MT lattice was maximum. Because MAP7 reduces the MT depolymerization rate, this rate is higher for the MT section before the kink (L_1) with the lower MAP7 density. Also, longer MTs would have a higher chance on multiple spots where they stick to the coverslip, leading to multiple transitions.

Another hypothesis is that a certain level of MAP7 bound to the MT lattice induced some structural change of the MT lattice leading to a different depolymerization rate. A different MT lattice structure would lead to a different depolymerization rate, because depolymerization is driven by mechanical stress stored in the MT lattice. Furthermore, it was shown that kinesin-1 introduced some structural changes to the MT lattice upon binding, which in turn increased the binding affinity of kinesin-1 molecules for the MT lattice [Shima et al., 2018]. So it is not impossible that another MAP like MAP7 could also change the MT structure. The fact that saturation of the MT lattice with MAP7 coincides with a sudden change of the MT depolymerization rate could be explained by this hypothesis.
Pushing it even further, we could pose the question if a structural change of the MT lattice induced by MAP7 could be related to the recruitment of kinesin-1. MAP7 increases the kinesin-1 recruitment to MTs 150-fold [Monroy et al., 2018], and kinesin-1 recruitment is increased by a self-imposed structural change of the MT [Shima et al., 2018].

3.3. DISCUSSION

IN this chapter, we have looked at the influence of MAP7 on MT dynamics, because we aim to use MAP7 for indirect visualization of MTs inside water-in-oil emulsion droplets. We observed that MAP7-covered MTs were more stable but also more flexible than control MTs without MAP7. We measured lower catastrophe rates and slower MT shrinkage velocities, explaining the increased stability of the MTs. The effect on MT dynamics was significant for 100 nM MAP7, but so was the improvement of MT visibility compared to Rhodamine-MTs. Therefore we decided that MAP7 would be suitable to visualize MTs in emulsion droplets (Chapter 4). The increased stability of MTs will affect their organization inside emulsion droplets. But we are confident that we can modify the MT conformation to a regime which is suitable for our experiments on MT-cortex interactions by fine-tuning the tubulin, MAP7 and EB3 concentrations.

One of the main problems during characterization of the effect of MAP7 on MTs was that MTs became softer. Fluorescently labeled MTs are straight due to their high persistence length, but MAP7-covered MTs were bent and therefore did not always grow parallel to the glass surface of the flow channel. Image acquisition was done with TIRF microscopy, which only works up to 100 nm into the sample. We often observed MTs wiggling out of this 100 nm imaging plane (Fig. 3.7), leading to a temporary loss of signal (visible as horizontal dark stripes in the kymographs of Fig. 3.2B). The longer the MTs, the stronger this effect, inhibiting reliable quantification of their slope, intensity or the moment of catastrophe. As a result, shorter MTs were over-represented in our analysis, which may have led to an underestimation of the growth times. Nevertheless, the results showing decreased growth and shrinkage velocities and increased growth and shrinkage times were convincing enough to conclude that MAP7 stabilized MTs by decreasing both catastrophe rate and shrinkage velocity.

During characterization of MAP7, we also ran into the unexpected observation of sudden transitions in the MT depolymerization rate, which we called kinks. Usually, the MT initially depolymerized fast, until a sharp transition to a slower depolymerization rate. Variations in depolymerization rate are not exceptional for MTs, only the depolymerization rate is very fast and therefore usually not captured with common imaging framerates around 1 s^{-1}. Since MAP7 slows down depolymerization, the variations became visible. We compared the MAP7 kymographs with kymographs of MTs in the absence of MAP7, but with MACF43, a 43 amino acid truncation of MACF2 which binds end-binding proteins and has a minor affinity for the MT lattice as well (Chapter 4). This is not ideal, but it was the only dataset without MAP7 we had at high enough framerate to study the rapid MT depolymerization. A better control experiment would be with bare MTs fluorescently labeled with Rhodamine-tubulin, but due to time constraints we did not do that yet. However, the influence of MACF43 on MTs was negligible (Chapter 4) and therefore we assumed the observed depolymerization rate variations to be unrelated to MACF43. In the depolymerization trajectories without MAP7 we observed cases with linear depolymerization, one sharp kink, multiple sharp transitions and gradual transitions. The trajectories with one sharp kink were far more abundant in the presence of MAP7, suggesting that MAP7 might influence the varia-

tions in MT depolymerization rate.

We performed a quantitative analysis on the kymographs with MAP7 to find the origin of the depolymerization trajectories with one sharp kink. To this end, we studied the lengths of the fastly/slowly depolymerizing MT sections compared to the total MT length and the MAP7 intensities on those sections. First of all, we measured a relatively slow on-rate of MAP7 on MTs of $k_{on} = 0.0073 \pm 0.0003\ s^{-1}$. This was not surprising, because also the recovery of MAP7 signal on MTs after photobleaching was very slow with a half time of 411 s [Tymanskyj et al., 2018].

As a result of the slow binding of MAP7 to the MT lattice, the newer MT parts (close to the tip) usually have lower MAP7 levels than the older MT parts (close to the seed). We measured the MAP7 intensity along the depolymerization trajectories and observed a relation between the MAP7 intensity and MT depolymerization rate. In general, the newest part of the MT with the lower MAP7 intensity was depolymerizing rapidly with constant rate. After the kink, the first sharp transition in depolymerization rate, the MAP7 intensity was constant and the depolymerization rate slower than before. So it seemed that the first sharp kink in the MT depolymerization trajectory coincided with the transition from a MT section partially covered with MAP7 to a section with maximum MAP7 levels. We observed this relation for shrinkage trajectories with one sharp kink, as well as for trajectories with multiple transitions. For the latter, the first transition coincided with the MAP7 saturation, although we only had limited data for the multiple transition cases. This observation suggested only a relation between the first transition and the MAP7 decoration. Which leaves the question what the origin is of the subsequent transitions.

We formulated two possible explanations for the relation between MAP7 density on the MT lattice and the transitions in MT depolymerization rate. One explained the transitions by increased MT-surface interactions in the presence of MAP7. The other suggested a structural change of the MT lattice induced by a certain MAP7 density on the lattice. Our data did not allow us to reach a firm conclusion on this. Further experiments are needed to determine whether any of the two is correct or that a different explanation exists. To that end, the proposed future experiments are on the one hand repetition experiments to obtain better and more data, and on the other hand additional experiments that will yield new information.

First of all we need a better control experiment for the depolymerization trajectories of MTs without MAP7. We would repeat the experiment with bare MTs (without MAP7) at high framerate.

Another future experiment would be to vary the MAP7 concentration and study how this changes the MT depolymerization rates. So far we did not have sufficient data for MAP7 concentrations above 10 nM, because in those conditions MTs were too long, bent and motile to analyze (Fig. 3.7). Therefore we could only perform the quantitative analysis of the MT depolymerization trajectories for 10 nM MAP7. Going to lower MAP7 concentrations than 10 nM could provide additional information.
Decreasing the MAP7 concentration increases the time needed to reach a maximum MAP7 density on the MT lattice. First of all we need to quantify whether this level is the

same or different for varying MAP7 concentration. This will disclose whether the MT lattice becomes saturated with MAP7 or merely reaches an equilibrium. In addition, if MAP7 coverage of the MT lattice is the origin of the kinks, we expect to have a longer length of the MT section before the kink (L_1) and a shorter length after the kink (L_2), because it takes more time to cover the MT lattice with MAP7 for lower concentration. Quantitative data on varying MAP7 concentrations could tell us whether coverage of the MT lattice with MAP7 is the reason for the kinks.

A different type of experiment would be with GDP-MTs, that could serve as a method to check the relation between MAP7 saturation of the MT lattice and MT depolymerization changes. We would first grow GTP-MTs in the presence of MAP7 and then flush out the GTP-containing buffer and replace it by a high-glycerol buffer to prevent catastrophes. After hydrolysis of GTP to GDP, flush-out of the high-glycerol buffer induces catastrophes of the GDP-MTs. In this way, we would force all MTs to undergo catastrophes, which would result in more depolymerization trajectories and thus better quantification, even for higher MAP7 concentrations than 10 nM. But even more important is that we could control the MAP7 density profile on the GDP-MTs. If the high-glycerol buffer contains MAP7, each MT will have a homogeneous MAP7 density from tip to seed. When MAP7 is absent in that buffer, the MTs will have the MAP7 density profile we observed in this chapter: low MAP7 at the newest section of the MT (the tip) and increasing towards the older section (closer to the seed) up to a certain maximum MAP7 density. Such an experiment would provide more information on the relation between MAP7 density profile and the occurrence of transitions in MT depolymerization rate.

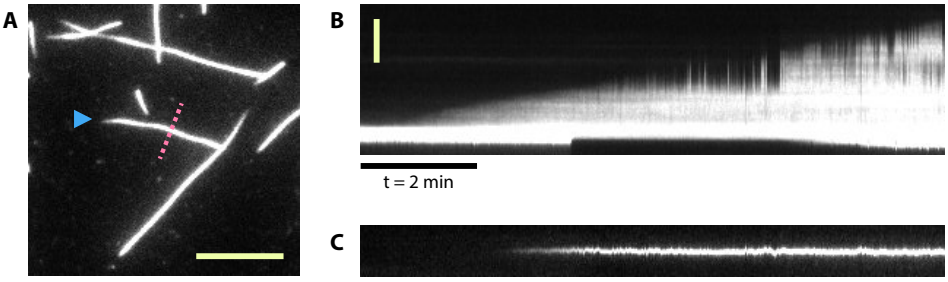

Figure 3.7: (A) Field of view with MTs in the presence of 10 nM MAP7. For one of these (indicated with the blue arrow), we created kymographs parallel to the MT as usual for generating kymographs **(B)** and perpendicular to the MT along the pink dotted line **(C)**. Yellow scalebar in (A) is 10 µm and in (B) 5 µm. The kymographs show the wiggling of the MT in three dimensions over time

Furthermore, repetition of the experiments on a supported lipid bilayer (SLB) may help to verify whether surface interactions are the reason for MT depolymerization changes. A fluid lipid bilayer provides a very different surface than the glass coverslip coated with PLL-PEG-biotin, neutravidin and κ-casein in our experiments. Supposedly the surface interactions of MTs would be less in case of an SLB compared to a functionalized glass coverslip.

In the hypothesis of MAP7 inducing a structural change, we asked the question if this

could be related to the increased recruitment of kinesin-1 to MTs in the presence of MAP7. A way to test this is by adding kinesin-1 to the experiment and study its binding affinity to MT sections with lower MAP7 levels and MT sections saturated with MAP7.

Finally, of course many more experimental methods exist to study the influence of MAP7 on MTs and check for potential structural changes, like X-ray diffraction or cryo-electron microscopy.

3.4. MATERIALS AND METHODS

3.4.1. REACTION MIX

Experiments were performed in flow channels (Sec. 2.5) passivated with consecutively PLL-PEG-biotin, neutravidin, k-casein and GMPCPP-stabilized MT seeds (with 18% biotinylated and 12% rhodamine-labeled tubulin dimers). The reaction mix contained 15 μM tubulin, either 0.5 μM rhodamine tubulin or 10-100 nM FL-MAP7-A647, 0-20 nM GFP-EB3, 0.5 mg/ml k-casein, 0.1% methylcellulose, 50 mM KCl, 1 mM GTP, 50 mM D-glucose, 4 mM DTT, 0.2 mg/ml catalase, 0.4 mg/ml glucose oxidase. All components were dissolved and diluted in MRB80 buffer (80 mM Pipes, 4 mM $MgCL_2$, 1 mM EGTA, pH 6.8). The proteins tubulin, EB3, MAP7 and MACF43 were obtained from the sources listed in Sec. 2.2.4.

3.4.2. IMAGE ACQUISITION AND DATA ANALYSIS

We imaged MTs in the flow channel with total internal reflection fluorescence (TIRF) microscopy using a Nikon CFI Plan Apo Lambda 100x oil immersion lens (NA 1.45, working distance 0.13 mm).

The background was subtracted with ImageJ data processing tools. To make kymographs, we drew lines of 5 pixels width and used the ImageJ plugin *KymoResliceWide*. Next, MT dynamics and shrinkage trajectory analysis were performed with ImageJ and Matlab.

4

EB3-MEDIATED INTERACTION BETWEEN MTS AND THE DROPLET CORTEX

Er ging een gerucht door het bos dat de kikker de maan had opgegeten. In de eerste plaats was er al zeven nachten lang geen maan te zien geweest en in de tweede plaats was de kikker dikker dan ooit.

Toon Tellegen

The capture of microtubules at the cell cortex is known to play a role in cell polarity. Often, microtubule end-binding proteins interact with cortical plus-end-tracking proteins (+TIPs) to establish polarity. At the position of such microtubule-cortex interactions, certain proteins can locally accumulate on the cortex. Here, we studied the effect of microtubule-cortex interactions in an in vitro minimal system consisting of water-in-oil emulsion droplets with microtubule asters, end-binding proteins and different cortical +TIPs. When microtubules were captured, the cortical +TIPs accumulated at the capture site, but only for the duration of the interaction. When not only the tip of a microtubule was captured, but the lattice as well, we observed increased rescue rates, stabilized microtubules and spontaneous nucleation of cortical microtubules. Finally, we found that microtubule capture influences both the motility and position of a microtubule aster, and thereby the microtubule organization inside the emulsion droplet.

4.1. INTRODUCTION

CELLS are complex systems that are able to organize their components into a living entity that can grow, convert energy and reproduce. In order to understand how a cell as a whole works, we need to gain more understanding of cellular processes individually, like cell division, growth and motility. For example: how does a migrating fibroblast regulate in which direction to move? Or how does a neuron grow its axon in the right direction? Such directional processes are regulated by cell polarity. During the establishment of cell polarity, cellular components (e.g. cytoskeleton, proteins, receptors) reorganize asymmetrically in the cell. This can happen either spontaneously or in response to an external cue, like a chemical gradient. As a result, the cell will show directional behavior. In this thesis, we study the role of microtubules (MTs) in the establishment of cell polarity, and we defined cell polarity as an inhomogeneous distribution of proteins at the cell periphery. *In vivo* studies provided information on the role of MTs (Chapter 1). It is known that MTs concentrate proteins to the cell cortex, and therefore the MT organization strongly influences cell polarity by determining where specific proteins are concentrated. This concentration can take place either by molecular motor transport along MTs or by association of proteins with the MT tip.

In this chapter, we studied the cortical concentration of proteins using a minimal system: an *in vitro* bottom-up reconstitution of a specific cellular function using a minimal number of components [Vendel et al., 2019] (Sec. 1.2). Our minimal system consisted of MT asters encapsulated inside water-in-oil emulsion droplets. One way to establish concentration of proteins at the cortex is by MT capture [Recouvreux et al., 2016]. MTs can be captured by the droplet cortex through end-binding (EB) proteins and cortical MT plus end-tracking proteins (+TIPs, introduced in Sec. 1.1) which interact with EB. This design for the interaction between MTs and droplet cortex was based on cellular mechanisms as reviewed by Lansbergen and Akhmanova [Lansbergen and Akhmanova, 2006]. Their summary of +TIP-mediated MT-cortex interactions in different organisms (budding yeast, fission yeast and animal cells) is shown in Fig. 4.1. Interaction with the cell cortex usually happens either through direct interaction of MAPs with the cell membrane or through interaction with cortical actin [Fukata et al., 2002, Watanabe et al., 2004, Wen et al., 2004, Knaus et al., 2005, Martin et al., 2005]. Some striking similarities can be observed when looking at the interactions in different organisms in Fig. 4.1. The end-binding proteins (EB in mammalian cells, Bim1p in budding yeast and Mal3p in fission yeast) play a role in most examples to concentrate proteins at MT plus-ends. They interact with other +TIPs that are directly or indirectly connected to either the cell membrane or to cortical actin. Usually, interactions and feedback loops between +TIPs and MTs result in stabilization of the MTs, local accumulation of proteins at the cortex and eventually in cell polarity.

For our minimal system, we mimicked *in vivo* mechanisms with an artificial cortical +TIP: a small dimeric fragment of MACF2 (MT-actin crosslinking factor 2) of 18 or 43 amino acids long (called MACF18 and MACF43 respectively). These dimeric MACF peptides contained an SxIP motif with affinity for EB3 and therefore for the MT plus-

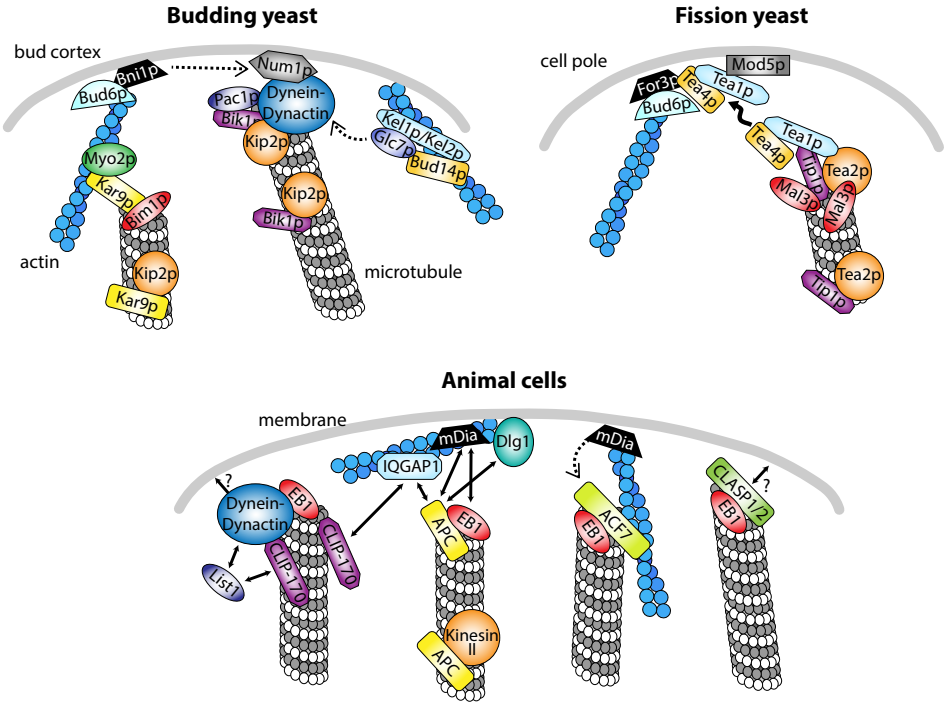

Figure 4.1: Examples of mechanisms for MT capture at the cell cortex in three different organisms, adapted from Lansbergen and Akhmanova [Lansbergen and Akhmanova, 2006]. Proteins homologs are indicted with similar shape and color (e.g. end-binding proteins Bim1p, EB1 and Mal3p). Often, end-binding proteins help to concentrate other proteins at the MT tips, like Kar9p, CLASP, APC or Tip1-Tea2. These proteins can interact with the cell cortex, cortical actin or cortical proteins which leads to MT capture.

end. MACF43 also had a MT lattice affinity independent of EB3. Further, both peptides contained an eGFP fluorescent label and a 10x histidine tag to bind to the droplet cortex through Ni-NTA functionalized phospholipids. Those MACF peptides enabled an interaction between MT and droplet cortex. The interaction of an analogous chimera protein with both MT tip and cell membrane in fission yeast cells sufficed to establish a polarized protein distribution [Recouvreux et al., 2016] (as discussed in the introduction in Sec. 1.3). However, this experiment was performed in live fission yeast cells and those cells have a predefined asymmetry because of their elongated shape. It is unclear whether the interaction between MT tip and cell membrane has the same result *in vitro* and in a spherical geometry.

In this chapter, we first studied MT asters in confinement with only EB3 and no MACF peptides, which allowed us to quantify the effect of confinement on MT dynamics. Next, we added the cortical MACF peptides and monitored local protein accumulations and MT organization as two characteristics of cell polarity, and investigated how they are affected by MT capture at the droplet cortex. Two possible scenarios were observed: only the MT tip was captured by MACF or also (part of) the MT lattice was

captured. For the first, we observed that captured MTs could locally accumulate cortical MACF peptides, but only for the duration of MT-cortex tethering. In the second scenario, MT rescues were more frequent, leading to more stable MTs and an increase of the total tethering duration. Finally, MT capture stabilized MT aster positioning and motility inside the emulsion droplet for both scenarios, even without stabilization of the MTs. This reorganization of the MT organization might be important for cell polarity as well.

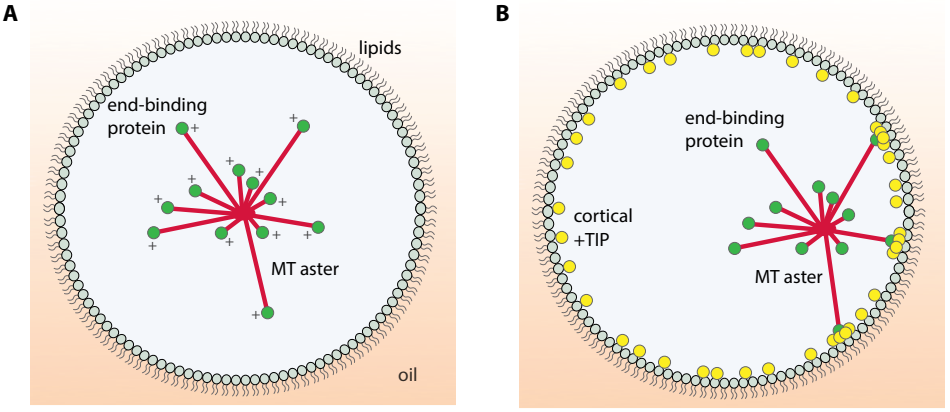

Figure 4.2: Schematic of the experiments in this chapter. **(A)** EB3 proteins tiptracking dynamic MTs inside water-in-oil emulsion droplets with MT asters. **(B)** Addition of Ni-NTA functionalized lipids and histidine-tagged MACF peptides that can bind to EB3 results in EB3-mediated tethering of MTs to the droplet cortex.

4.2. INFLUENCE OF CONFINEMENT ON MT DYNAMICS

We built the minimal system step by step, starting from MT asters in confinement reproducing previously published systems [Roth et al., 2014, Laan et al., 2012a]. The next step was adding end-binding proteins EB3, which tracked the MT plus ends (see Fig. 4.2A). The accumulation of tiptracking EB3 proteins at the MT tip is called a protein comet. Such EB3 comets serve as clear signals at the MT tips allowing easy visualization of MT dynamics in cells and in *in vitro* assays. Similarly, we performed experiments with MT asters and EB3-GFP inside emulsion droplets to study the influence of confinement on MT dynamics. See Sec. 4.5.2 for the details of the experimental conditions.

As one can see in Fig. 4.3A, comets of EB3 were clearly visible (white arrows). In addition, EB3 had an affinity for proteins on the the Aurora kinase A coated beads (AurkA beads, introduced in Sec. 2.2.2) serving as a MT organizing center (MTOC), explaining the accumulation of protein at the center of the MT aster (indicated by the cyan arrow). Kymographs of EB3 comets in droplets are shown in Fig. 4.3B, where we observed two things. Firstly, clear protein traces were visible, from which we could extract MT growth velocities. Secondly, the MTOC moved around as well, disturbing the observed protein traces. Therefore, we only analyzed those traces where the MTOC position was

approximately stable in the direction of movement of the protein comet.

To study the influence of confinement on MT dynamics, we compared weighted MT growth velocity distributions in droplets (confined) and channels (unconfined) in Fig. 4.3C. One reaction mix was prepared and split over the droplet and flow channel experiments to ensure equal protein concentrations. The only difference in addition to geometrical confinement was that MTs nucleated from AurkA beads in droplets and from GMPCPP-stabilized MT seeds in a flow channel.
The first impression from Fig. 4.3C was that MTs grew slower in droplets (red) than in channels (blue). However, MTs from the radial MT asters in droplets grow in 3D, but we only imaged in one plane (see Fig. 4.4A). Therefore we acquired a 2D projection of the actual growth traces, so the measured growth velocities were an underestimation of the actual ones. To see if this explained the difference in growth velocity from Fig. 4.3C, we created a 3D Gaussian distribution of growth velocities using weighted mean and standard deviation as extracted from the flow channel experiments (dashed line). Projecting these 3D velocities onto a 2D plane resulted in a different velocity distribution (dash-dotted line). A detailed explanation of the projection procedure can be found in Sec. 4.5.3.
The projection explained most of the differences observed between channels and droplets: the mean velocity was lower for the projection and the shape of the distribution matched better with the droplet data.

Next, to study the influence of confinement on MT growth velocity, we correlated the mean growth velocity of MTs in droplets with the droplet diameter (Fig. 4.3D). This correlation plot did not show a relation between confinement size and MT growth velocity.

A similar analysis was performed comparing the MT lengths in droplets and channels, resulting in exponential distributions of MT lengths (Fig. 4.3E,F). MT length in droplets was defined by the distance from MTOC to EB3 comet, and in channels by the distance from seed to plus-end EB3 comet. MTs in droplets seemed on average smaller than in channels (Fig. 4.3E), 4.5 ± 4.5 µm and 7.7 ± 7.7 µm respectively (found by fitting an exponential distribution to the data in Matlab, errors are the 95% confidence bounds of the fit). But this difference could also be explained by the 2D projection of 3D MTs we discussed before. We imaged a projection of the 3D MTs, so short MTs were overrepresented because even for larger z-components their plus end with EB3 comet still lied within the depth of field (DOF), while longer MTs grew out of it (see Fig. 4.4B). So we simulated MT lengths in 3D and projected only those that fell within the DOF onto a 2D plane, see Fig. 4.3E and Sec. 4.5.3. The 2D projection explained the observed difference between channels and droplets very well. Finally, the MT length was independent of droplet diameter (Fig. 4.3F).

In short, the MT growth velocity and MT length were not influenced by confinement under the conditions of our experiments. Why this is surprising and how we explain it can be found in the discussion (Sec. 4.4).

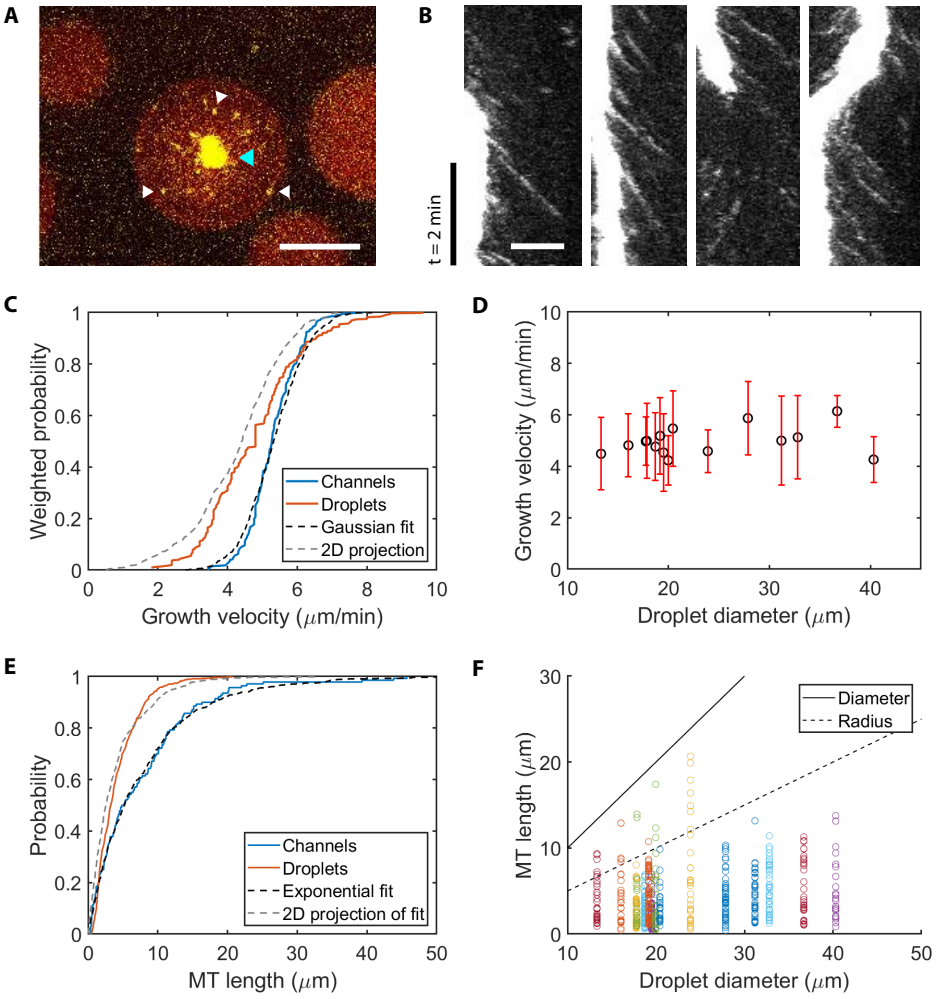

Figure 4.3: **(A)** water-in-oil emulsion droplet containing a MTOC (cyan arrow), 40 µM tubulin (red) and 200 nM EB3 (yellow). Some EB3 protein comets are indicated with white arrows. Scalebar is 10 µm. **(B)** Kymographs of protein comets on MTs growing from a MTOC as in (A) The EB3-GFP signal is shown in these images, which also binds to the MTOC. Scalebar is 5 µm. **(C)** Cumulative distribution functions of the weighted growth velocity distributions found in droplets and in channels (solid lines) for exactly the same reaction mix composition. For comparison, we fitted a Gaussian distribution to the data (black dashed line) and projected this onto a 2D plane (grey dashed line). One might note a sharp kink in the cdf plot around 5 µm/min. This issue resulted from data analysis in ImageJ and is discussed in Sec. 2.6. **(D)** Correlation plot of the MT growth velocity inside emulsion droplets versus the droplet diameters. Errorbars were calculated from the standard deviation of the MT growth velocities measured for each droplet diameter. **(E)** Cumulative distribution functions of the MT lengths found in droplets and in channels (solid lines) and exponential fit to the data in channels (black dashed line). The values of the exponential fit are projected onto 2D assuming a depth of field of 5.5 µm (grey dashed line). **(F)** Correlation plot of the MT length inside emulsion droplets versus the droplet diameters. The solid and dashed lines indicate when the MT length is equal to the droplet diameter or radius respectively.

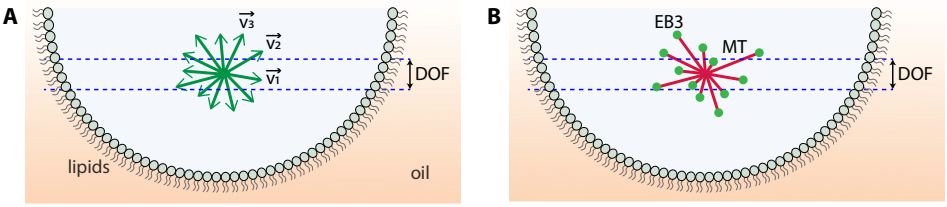

Figure 4.4: Schematic picture of an emulsion droplet where we imaged a certain plane with a thickness defined by the depth of field (DOF). The MT aster was in the center of this plane. **(A)** Green arrows represent possible growth vectors of MTs growing from a MTOC. Vectors $\vec{v}_1$, $\vec{v}_2$ and $\vec{v}_3$ have different z-components to examplify how projection will influence their appearance. **(B)** MT (red) lengths in a droplet are measured from MTOC to EB3 comet (green). For larger z-components, long MTs have their plus end outside the DOF, while short MTs are still within. Therefore short MTs are over-represented in the measurement.

4.3. MT CAPTURE AT THE DROPLET CORTEX

MT ASTERS with EB3 comets inside water-in-oil emulsion droplets formed the basis of our minimal system. The next step was MT capture at the droplet cortex. To that end, we introduced Ni-NTA-functionalized phospholipids and histidine-tagged MACF peptides that capture the MT tip through EB3 (see Fig. 4.2B). But first, we characterized the new components in flow channels.

4.3.1. CHARACTERIZATION OF MACF PEPTIDES

Knowing more about the binding kinetics of the MACF peptides in our minimal system will help us to understand the effect of both peptides on MT capture and MT organization inside emulsion droplets. Two MT plus end trackers (+TIPs) were explored, both derived from a MACF2 protein. One consisted of 18 amino acids and the other of 43 amino acids, that we call MACF18 and MACF43 respectively. For more details, see Sec. 4.5.1. Both peptides were dimers and contained the SxIP motif which can interact with EB [Bieling et al., 2007], so they tiptracked growing MT tips (Fig. 4.5A). The main difference between the two peptides is that MACF43 has a stronger affinity for the MT lattice than MACF18. Apparently the 25 amino acids difference between MACF43 and MACF18 provided MT lattice affinity (Fig. 4.5A).

To understand the influence of the peptides on MTs, we studied the MT dynamics and the binding kinetics of both peptides to MTs. We performed flow channel experiments (Sec. 2.5) using TIRF microscopy. For characterization of MT dynamics, an acquisition framerate of 0.5 s^{-1} suffices (Fig. 4.5A). To study binding kinetics of MACF peptides to MTs, a higher framerate of 12.5 s^{-1} was used (Fig. 4.5B).

Figure 4.5D,E show the influence of MACF18 and MACF43 on MT dynamics. Both induced slightly higher growth velocities: $v_{MT} = 2.9 \pm 0.4$ µm/min for MACF18 (mean ± standard deviation, $N = 97$) and $v_{MT} = 3.3 \pm 0.4$ µm/min for MACF43 ($N = 94$), compared to $v_{MT} = 2.6 \pm 0.5$ µm/min in the presence of only EB3 ($N = 113$). The catastrophe rate was similar within the error for the three conditions (Fig. 4.5E), and the

differences were not significant according to a two-sample Kolmogorov-Smirnov test. No effect on MT shrinkage velocity or rescue rate was observed.

Next, we looked at the binding kinetics of MACF peptides to MTs by fluorescence recovery after photobleaching (FRAP) measurements (see Fig. 4.5B,C). We studied MTs with 1) only EB3, 2) EB3 and MACF18, and 3) EB3 and MACF43. We bleached all fluorescent proteins in a certain region of interest and analyzed the intensity recovery profiles of EB3 ($N = 15$), MACF18 ($N = 15$), MACF43 on the MT tip ($N = 16$) and MACF43 on the MT lattice ($N = 16$) (Fig. 4.5F-H). For the intensity of EB3, MACF18 and MACF43 at the tip we observed an initial recovery of the signal after photobleaching, later followed by a decay. This can be explained because initially the bleached proteins were replaced by new proteins. Over time however, the particular part of the MT that we were looking at was changing from GTP-bound tip to GDP-bound lattice by GTP hydrolysis. This change means that the affinity of tip-binding proteins decreases, which explains the decay in the recovery plots that we observed (Fig. 4.5F,G). The rate of initial recovery provides information on the off-rate (k_{off}) of the proteins at a MT, and the subsequent rate of decay tells us more about the transition rate ($k_{hydrolyze}$). To get those rates, the average recovery curves were fitted with Eq. 4.4 on p. 83 (see Fig. 4.5I). The rates for the different proteins are summarized in table 4.1. The fitted value for $k_{hydrolyze}$ was similar for all proteins, which was expected since the process of GTP hydrolysis depends on EB3, which was the same in all conditions. In contrast, k_{off} varied for the different molecules: MACF18 had a 4-5 times lower affinity for the MT tip than MACF43. The affinities of MACF43 for the MT tip and lattice were similar. One might note that our value for EB3 k_{off} is approximately 2-3 times smaller than found in literature [Bieling et al., 2007, Gouveia et al., 2010, Buey et al., 2011, Preciado Lopez, 2015], which we will elaborate on in the discussion.

Fit parameter	EB3	MACF18	MACF43 (tip)	MACF43 (lattice)
k_{off} (1/s)	0.80 ± 0.07	1.3 ± 0.4	0.25 ± 0.03	0.33 ± 0.03
$k_{hydrolyze}$ (1/s)	0.19 ± 0.01	0.17 ± 0.01	0.17 ± 0.01	–

Table 4.1: Fitting parameters with 95% confidence bounds obtained by fitting Eq. 4.4 (p. 83) to the FRAP recovery curves in Fig. 4.5F-H. EB3 and MACF18 were measured at the MT tips, MACF43 was measured both at the MT tip and at the lattice.

Figure 4.5 ***(following page)*:** Characterization of the behavior of MACF18 and MACF43 peptides. **(A)** Kymographs showing the interaction of MACF18 with the MT tip and MACF43 with both MT tip and lattice. White scalebar is 5 µm. **(B)** Kymographs of FRAP experiments where the MACF was bleached after after 10 frames (blue arrow). White scalebar is 5 µm. **(C)** To analyze the binding kinetics of the peptides we drew vertical lines of 3 pixel width at the position of the protein comet just before bleaching, indicated by the magenta region in the zoom-in of the MACF43 kymograph from (B). The intensities along this line were used to plot (F-H). White scalebar is 2.5 µm. **(D,E)** MT dynamics of MTs in the presence of EB3 only or EB3 and MACF18 or MACF43 obtained from analyzing kymographs as in (A). **(F,G,H)** FRAP curves (grey) and averages (blue) of MACF18 at the MT tip (F), MACF43 at the MT tip (G) or MACF43 at the MT lattice (H) obtained as shown in (C). **(I)** The average recovery curves from (F-H) and fits (black dashed lines) of Eq. 4.4 to the data.

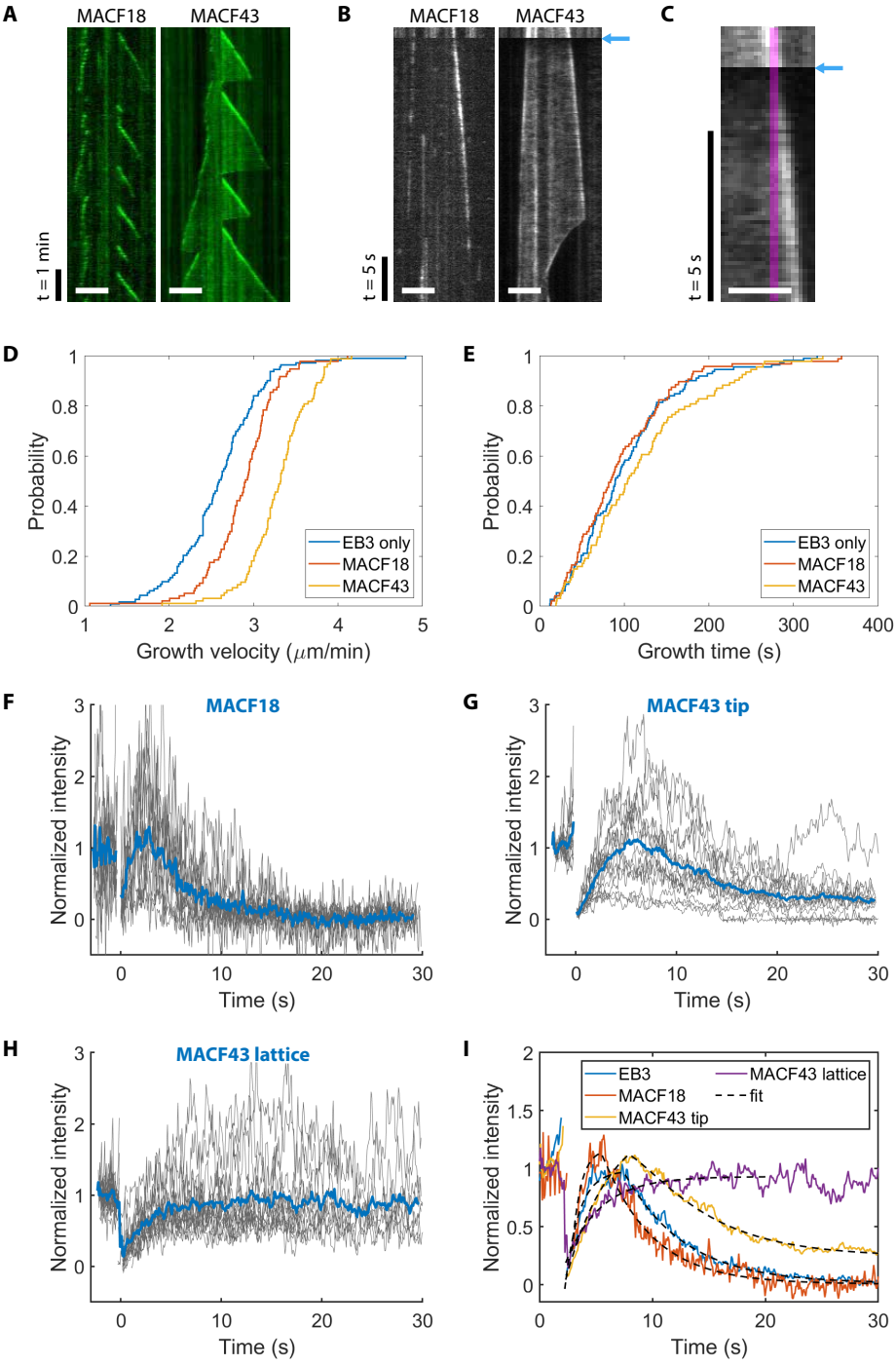
A
MACF18
MACF43
t = 1 min
B
MACF18
MACF43
t = 5 s
C
t = 5 s
D
Probability
Growth velocity (μm/min)
EB3 only
MACF18
MACF43
E
Probability
Growth time (s)
EB3 only
MACF18
MACF43
F
MACF18
Normalized intensity
Time (s)
G
MACF43 tip
Normalized intensity
Time (s)
H
MACF43 lattice
Normalized intensity
Time (s)
I
EB3
MACF18
MACF43 tip
MACF43 lattice
fit
Normalized intensity
Time (s)

4.3.2. MT TIP TETHERED TO THE CORTEX THROUGH MACF18

We introduced functionalized phospholipids to study the effect of MT-cortex interactions on local accumulation of cortical proteins and MT organization in the emulsion droplets - both characteristics of cell polarity. His-tagged GFP-MACF18 could bind to DGS-NTA phospholipids in the droplet cortex. In Fig. 4.6A one can see that practically all MACF18 (yellow) is bound to the droplet cortex, or to the MTOC. The end-binding protein mCh-EB3 did not have a histidine-tag so it was in solution and tiptracked the MTs as we observed for GFP-EB3 in Sec. 4.2. When a MT (visualized through MAP7-A647, see Sec. 2.2.3) reached the droplet cortex, EB3 molecules at the tip interacted with cortical MACF18 molecules, leading to a local accumulation of MACF18. We call these accumulations hotspots and some examples can be seen in the cross section of a droplet in Fig. 4.6A. The number of MACF18 molecules in a hotspot was roughly estimated by comparing the intensities at the cortex and in the hotspot using Eq. 4.8 (p. 85). Such calculations resulted on average in 500 molecules per hotspot. This number is of the same order of magnitude as the 270 EB1 molecules found *in vivo* at a MT tip in epithelial cells [Seetapun et al., 2012]. Assuming 500 MACF molecules, 13 protofilaments, 8 nm length of a tubulin dimer and 1 EB3-binding site per tubulin dimer, a MT tip region of 300 nm would be fully covered with EB3 and MACF18.

To monitor the effects of MACF18-induced tethering of MT tips to the droplet cortex, we followed the hotspots over time. To that end we projected the 3D stack of each timepoint onto one 2D plane, see Fig. 4.6B. Two types of behavior were visible in those projections: either only the MT tip was tethered or the MT lattice was also partially tethered. In the further analysis we treated the two behaviors separately.

The first parameter of interest was how long a MT was tethered to the cortex through MACF18. Figure 4.6C shows the tethering duration for tip tethering ($T_{tip} = 65 \pm 47s$ (mean ± standard deviation), $N = 285$) versus partial lattice tethering ($T_{lattice} = 261 \pm 223s$, $N = 128$). The tethering duration was clearly much longer if the MT lattice was partially tethered. Moreover, the tethering duration in the latter case was merely an underestimation, as about half of these lattice tethering events lasted longer than the acquisition time (see Fig. 4.6D) so the real tethering duration was even longer.

What caused the difference between tip tethering and lattice tethering? Snapshots from a movie in Fig. 4.7A showed an event where the MT lattice was partially tethered to the cortex. While tethered, the MT underwent multiple catastrophe and rescue events. Dynamic instability of tethered MTs explained the difference in tethering duration from Fig. 4.6C. The time a tethered MT spends growing before catastrophe (Fig. 4.7B) was the same for tip tethering (blue) and lattice tethering (yellow). This suggested that the catastrophe rate was not affected by lattice tethering. The fact that a MT tethered with its lattice could undergo multiple catastrophe and rescue events ($r_{res} = 0.05 \pm 0.02$ s^{-1}) before fully detaching from the droplet cortex, resulted in the long tethering times we observed (compare red and purple in Fig. 4.7B). In the situation of MT tip tethering only, catastrophes immediately led to detachment of the MT and hence to disappearance of the hotspot.

As we know from Fig. 3.2, MTs decorated with MAP7 typically grow for 1 to 3 minutes

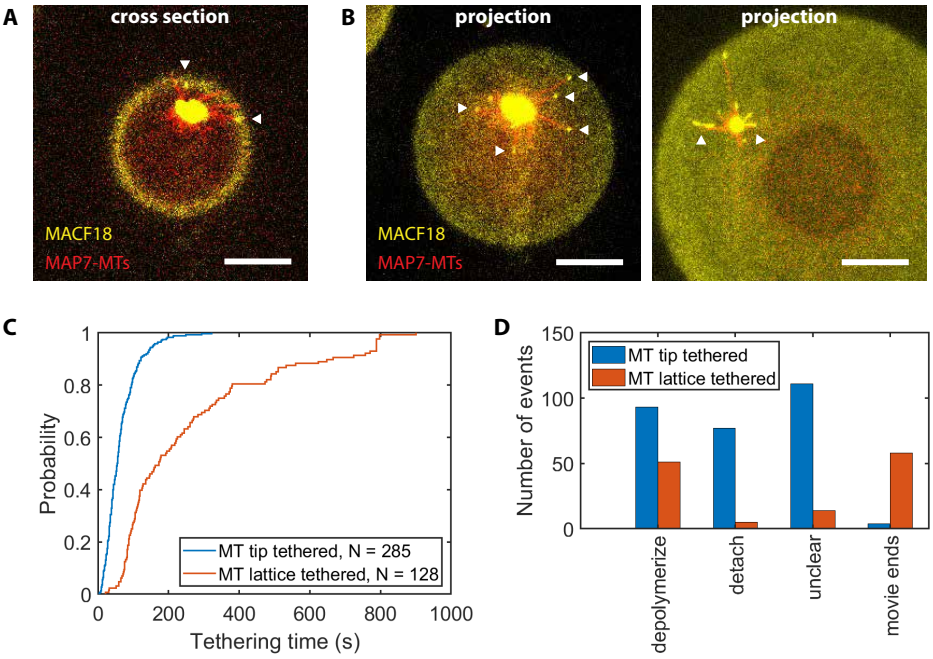

Figure 4.6: Tethering of MTs to the droplet cortex through MACF18. Scalebars are 10 µm. **(A)** Cross section of an emulsion droplet with histidine-tagged MACF18 (yellow) bound to the droplet cortex and MAP7-A647 labeled MTs (red) growing radially from an AurkA bead. At the sites where MTs encounter the droplet cortex, a hotspot of MACF18 is observed (white arrows). **(B)** Two z-projections of emulsion droplets showing the two types of tethering we observed: only MT tip tethering (left) and partial tethering of the MT lattice (right). **(C)** Comparison of the total tethering times for the two situations depicted in (B). **(D)** Classification of how the tethering events from (C) end: by depolymerization of the tethered MT, by detachment of the tethered MT, unclear from the images or no end but the acquisition ended.

before undergoing a catastrophe. If we take into account that the time a MT is tethered is by definition shorter than or equal to the time it is growing, this value is quite similar to a tethering duration of $T_{tip} = 65 \pm 47s$ for MT-tip tethering only, and to $T_{lat} = 83 \pm 20s$ for MTs partially tethered through their lattice. So the data suggest that tethering of a MT, either only through the MT tip or also through part of the MT lattice, does not influence its catastrophe rate. The rescue rate however is influenced by tethering, as rescues were not observed for tip-tethering, but frequently for lattice-tethering ($r_{res} = 0.05 \pm 0.02$ s^{-1}). Moreover, additional rescues were only observed in droplets, and not in flow channels, suggesting that the increased rescue rate was indeed the result of lattice tethering to the droplet cortex.

An interesting effect of MT tips being tethered to the droplet cortex is shown in Fig. 4.8A,B. This shows a MT aster being kept at a certain location for more than 74 seconds by tethering of only one MT. When the MT detached, the aster started moving around through the droplet (Fig. 4.8B). Examples like this suggest that MT tethering can influence MT aster movement and positioning inside a droplet. Hence we quantified the velocity as the diffusive movement of the MTOC per timestep and correlated this ve-

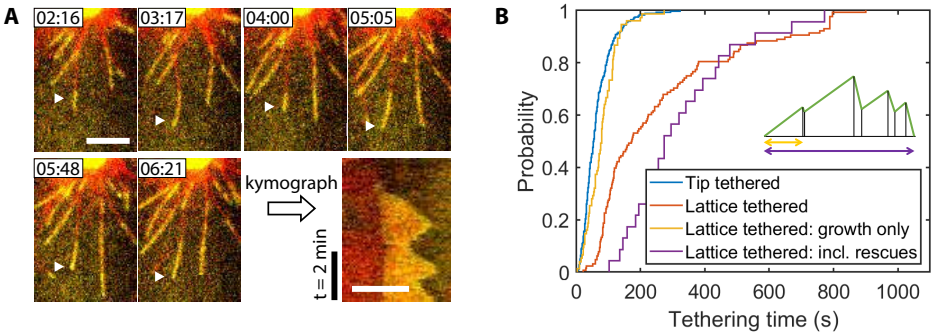

Figure 4.7: Partial lattice tethering of MTs to the droplet cortex through MACF18. Scalebars are 5 µm. **(A)** Snapshots from a projection with a MT (red) which is partially tethered with its lattice through MACF18 (yellow) to the cortex, while showing dynamic instability (white arrows). A kymograph (right bottom) makes the dynamic instability more clear. **(B)** Comparison of the tethering times when only the MT tip is tethered (blue) with the cases where part of the MT lattice is tethered as well. Here we distinguish the total tethering times as shown in Fig. 4.6C (red), only the time when the tethered MT is growing (yellow) and the total times where the MT is tethered and showing dynamic instability (purple). The inset shows a schematic kymograph to clarify the yellow and purple categories in the plot.

4

locity with the number of tethering MACF18 hotspots at that moment (Fig. 4.8C). The higher velocities occurred more often for low number of hotspots. The same trend is visible in Fig. 4.8D, where the cumulative distribution function (cdf) of Fig. 4.8C was plotted, which shifts to lower velocities for higher hotspot numbers. We repeated this data analysis for MT asters in droplets without DGS-NTA lipids (only DOPS lipids and surfactant are present), so no hotspots could be formed. This cdf (black line) overlaps with the low hotspot number data (Fig. 4.8D).

In addition to the motility of MT asters being tethered to the cortex, we inspected the positioning of the MT asters inside the droplets. In Fig. 4.9A we show a droplet in 3D with an MTOC (red dot) at the cortex in the bottom half of a droplet. After making a projection of this droplet as we do during image analysis, the MTOC appeared as in Fig. 4.9B. Because of its z-position it ended up in the middle of the projection, even though in reality the MTOC was at the droplet cortex (as becomes clear from Fig. 4.9C). It was important to take this effect into account during the interpretation of the data. Inspecting the z-positions of MTOCs in droplets with and without DGS-NTA lipids - with and without MT-cortex interactions - resulted in Fig. 4.9D. If MTs could tether to the droplet cortex, the MTOC was located only a few microns above the bottom of the droplet. In the case of only DOPS lipids, the MTOC was located just below the center of the droplet, which varied from a few microns up to 25 µm (Fig. 4.9D) depending on the droplet radius.
Next, we studied the relative MTOC position in a droplet (defined as r/R in Fig. 4.9B) as a function of hotspot number (Fig. 4.9E). Three things became clear from this figure. Firstly, there was a clear effect of MT-cortex tethering. In the case of DOPS lipids (where MT-cortex tethering could not happen), the MT aster positioned closer to the droplet center than for DGS-NTA lipids (where MT-cortex tethering was possible). Sec-

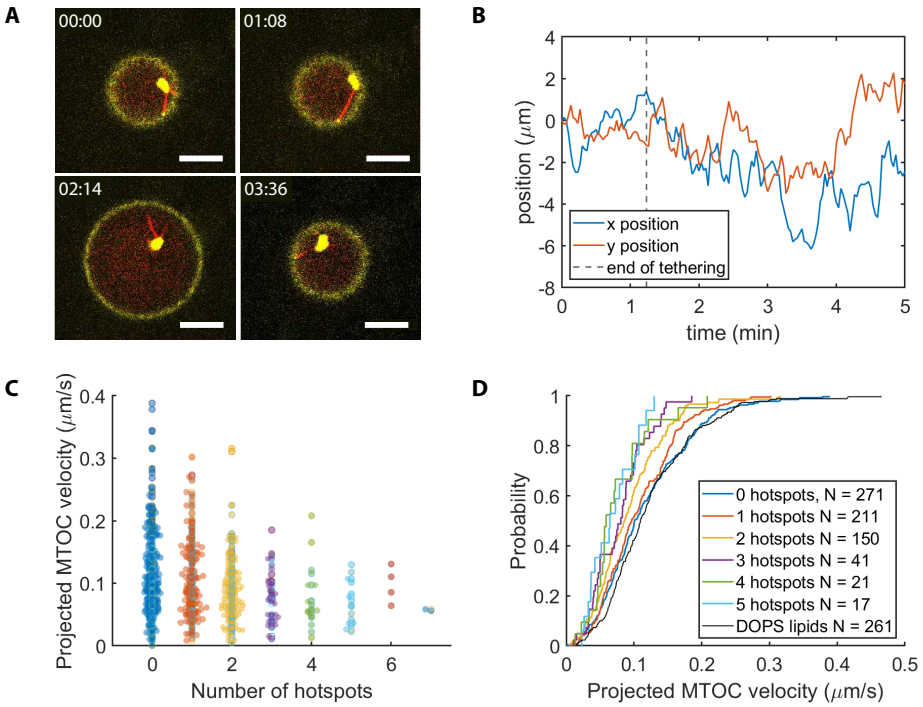

Figure 4.8: Influence of MACF18-induced MT tethering on the MT aster movements. **(A)** Snapshots from a movie where the MT aster was kept in place by a tethered MT and as soon as the MT detached the MT aster moved around through the whole droplet. These images are cross sections so the radius of the droplet cross section can vary between images. Scalebars are 10 µm. **(B)** xy-position of the MTOC position over time for the data shown in (A). The tethering ended after 74 s, after which the bead position fluctuates more. **(C)** Quantification of the MTOC (AurkA bead) velocity per timeframe correlated with the number of hotspots in that timeframe. **(D)** Cumulative distribution functions (cdf) of the data in (C), showing a trend towards lower bead velocities in case of more hotspots. The cdf for droplets with DOPS lipids only (so no MACF18 at the droplet cortex) overlaps with the cdfs for low hotspot number.

ondly, there were only small variations in MTOC positioning from 0 to 5 hotspots. This can be explained because the number of hotspots constantly varied and the MTOC did not instantly move away from the cortex when there were 0 hotspots for a while. Apparently, even one or few hotspots were enough to keep the MTOC close to the droplet cortex. Thirdly, the maximum observed relative MTOC position (r/R) was approximately 0.5. A quick calculation on the projection from 3D to 2D explained this. For example, at a z-position of 4 µm above the bottom of a droplet with a radius of 15 µm, the radius of the droplet cross section is only 10 µm (situation as in Fig. 4.9A). So in a projection as Fig. 4.9B, the observed r/R will only be 0.67 even though the MTOC is right at the cortex as can be seen in Fig. 4.9C.

The data in this section suggested that tip-tethering of the MT tip to the droplet cortex did not influence the MT stability. Nevertheless, we observed stabilization of the MTOC position as a result of MT-cortex interactions: the MTOC moved slower and was

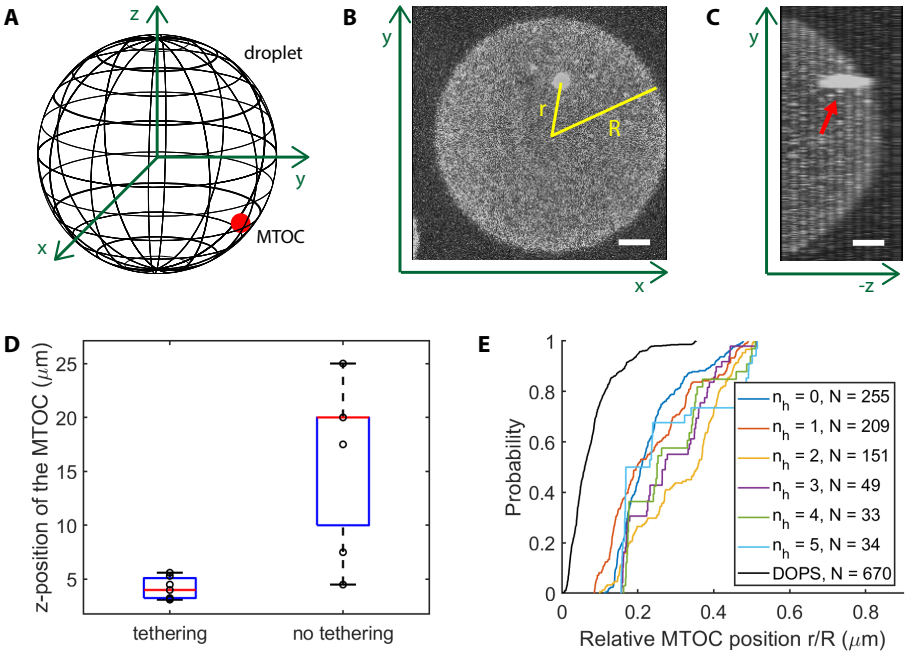

Figure 4.9: Influence of MACF18-induced MT tethering on the MT aster positioning. **(A)** Schematic of a droplet with MTOC (red) close to the bottom and close to the cortex of a water-in-oil emulsion droplet. **(B)** Cross section in the xy-plane of a droplet for the situation as in (A), with the relative MT aster position r/R indicated. Scalebar is 5 µm. **(C)** Cross section in the yz-plane of the same situation, where we can see that the MT aster (MTOC indicated with red arrow) is positioned very close to the droplet cortex. Scalebar is 5 µm. **(D)** Quantification of the z-position (measured from the bottom of the droplet to the MTOC) of MT asters in emulsion droplets with DGS-NTA lipids (MT tethering possible) or DOPS only (no MT tethering possible). The z-position in case of MT tethering is rather constant, while without tethering the MT aster is located just below the center of the droplet so the z-position depends on the droplet radius. **(E)** Relative MT aster position r/R as defined in (B) for DGS-NTA lipids with varying hotspot number n_h and for DOPS lipids (black line) where no tethering is possible.

located closer to the droplet cortex in case of MT tip tethering. When not only the MT tip but also the MT lattice was (partially) tethered, the tethering duration increased from 65 ± 47 s to more than 261 s by an increase of rescues. So in this case, MTs did get stabilized by the MT-cortex interactions. If rescues are more frequent when the MT lattice is weakly bound to a surface like the droplet cortex, we expect an even stronger effect on rescue rate for MACF43 with its higher MT lattice affinity.

4.3.3. MT LATTICE TETHERED TO THE CORTEX THROUGH MACF43

In this section, we replaced the cortical MACF18 by cortical MACF43 and looked at the effect on MT dynamics and MTOC positioning. In addition to stronger MT tip interactions than MACF18, MACF43 also showed a strong affinity for the MT lattice (Sec. 4.3.1). Figure 4.10A shows an experiment with histidine-tagged MACF43 bound

to DGS-NTA phospholipids at the cortex of emulsion droplets.

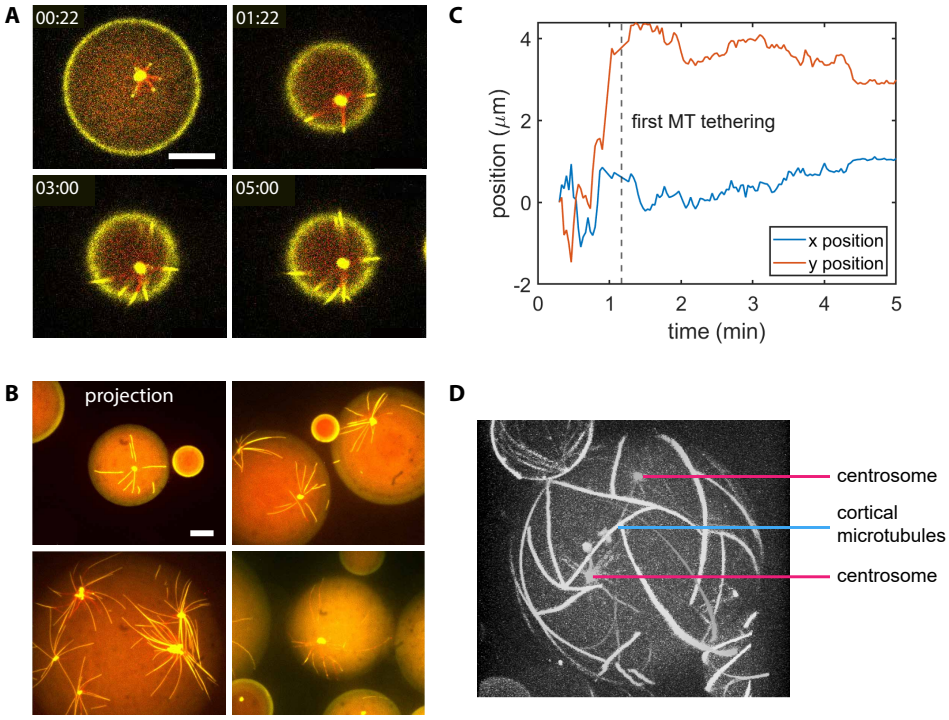

Figure 4.10: Tethering of MTs to the droplet cortex through MACF43. **(A)** Snapshots from a movie with cross sections of a droplet with histidine-tagged MACF43 (yellow) bound to the cortex and MTs covered with FL-MAP7-A647 (red) growing radially from an AurkA bead. Scalebar is 10 µm. **(B)** Z-projections of emulsion droplets as in (A). Scalebar is 10 µm. **(C)** xy-position of the MT aster in the movie of (A), the z-position is not taken into account but is varying as well. The first moment of MT tethering is around 1:10 min and indicated with the dashed line. **(D)** 3D reconstruction of a droplet with bundles of spontaneously nucleated MTs at the cortex covered with MACF43 (white). Inside this droplet, two MT asters nucleated from centrosomes are visible.

Most MACF43 was bound to the droplet cortex, yet also some MACF43 comets were tiptracking growing MTs, unlike the MACF18 experiments in the previous section where no comets were observed. The presence of comets could either be explained by the higher affinity of MACF43 to the MT tip, or by a lower affinity of histidine-tagged MACF43 for the Ni-NTA lipids in the cortex than histidine-tagged MACF18. The MT aster was moving around through the droplet until one or more MTs touched the droplet cortex (around 1:10 min). These MTs got tethered through the cortical MACF43 and over time more and more MTs got tethered, as we show in Fig. 4.10A. We observed that tethering times were as long as the image acquisition lasted. In this example the acquisition lasted 5 minutes and was performed right after droplet formation and transfer of those droplets to the coverslip. All acquisitions later in time resulted in images as in Fig. 4.10B, where long MTs were organized along the droplet cortex and fully covered with MACF43. So once captured, no MT was able to detach from the cortex. In addi-

tion, the MTOC position became much more stable as soon as MTs were tethered (see Fig.4.10C).

With the findings from Sec. 4.3.2 on MACF18 we can explain this behaviour. Many rescue events were observed when the MT lattice was (partially) tethered to the droplet cortex (Fig. 4.7). Since MACF43 had a higher MT lattice affinity than MACF18, the lattice tethering to the cortex was stronger and hence we hypothesized that also the effect on rescues was larger. From data on MACF43 like Fig. 4.10B and the fact that MTs bound to the cortex through MACF43 did not detach, it seemed that the rescue rate was so high that MTs did not depolymerize visibly. Instead, they were stable over time.

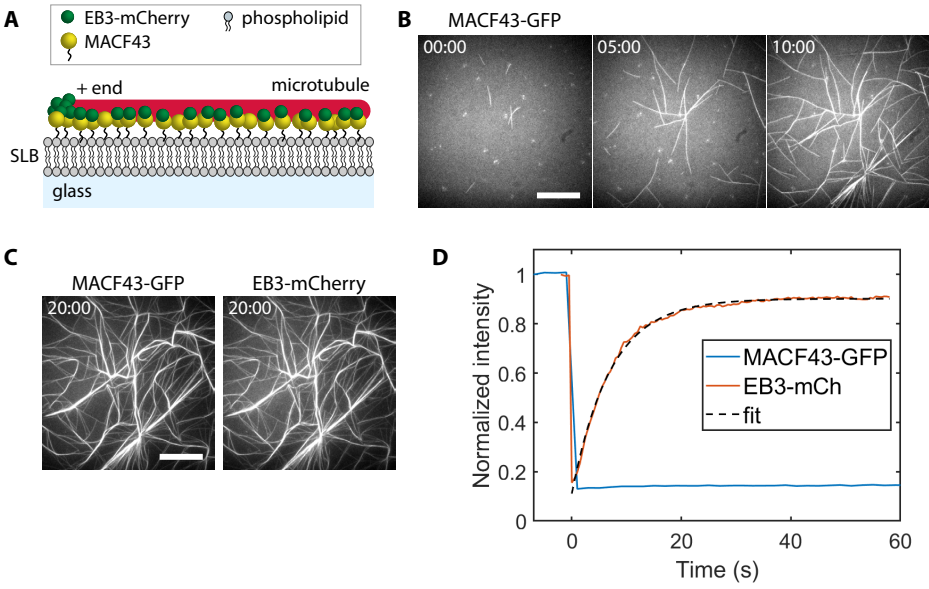

Figure 4.11: Supported lipid bilayer (SLB) containing DGS-NTA lipids, with histidine-tagged MACF43-eGFP (greyscale), mCherry-EB3 and tubulin (both not shown here). **(A)** Schematic representation of the MTs being tethered by MACF43 to the DGS-NTA lipids in the SLB and the mCh-EB3 molecules interacting with MACF43. **(B)** Spontaneous nucleation of MTs on the SLB that form very stable bundles over time and are fully covered with SLB-bound MACF43. **(C)** Comparison of the MACF43-GFP and EB3-mCherry signals after 20 minutes in the acquisition from (B). **(D)** FRAP measurement of the MACF43-eGFP and mCh-Eb3 on the SLB in a MT bundle. Scalebars are 20 µm.

A side effect of this stability can be seen in Fig. 4.10D. Under certain conditions (e.g. high tubulin and protein concentrations, high temperature), cortical MTs could be observed that were not connected to a MTOC. To check if cortical MACF43 is capable of stimulating spontaneous MT nucleation, we performed experiments on a supported lipid bilayer (SLB) with DGS-NTA lipids (Fig. 4.11A). The reaction mix was comparable to the one for emulsion droplets (30 µM tubulin, 120 nM EB3, 120 nM histidine-tagged MACF43), but without any MTOC. Indeed this resulted in spontaneous MT nucleation (Fig. 4.11B). Those MTs were fully covered with EB3 and SLB-bound MACF43, and over time we observed MT bundles and strongly bent MTs(Fig. 4.11C). Depolymeriz-

ing MTs were not observed, suggesting that indeed the cortical MACF43 bound to the MT lattice was preventing catastrophes.
FRAP analysis of the MT bundles covered with SLB-bound MACF43 showed recovery of the EB3 signal in less than a minute, while the MACF43 signal did not recover visibly (Fig. 4.11D). We could fit the EB3 recovery with Eq. 4.3 (p. 83), which yielded a value for the off-rate of EB3 of $k_{off} = 0.142 \pm 0.003\ s^{-1}$. We expected that MACF43 was bound to both MT lattice and SLB, based on characterizations as in Fig. 4.5A where we observed a clear affinity of MACF43 for the MT lattice. EB3 binds in principle to the MT tip, but for higher EB3 concentrations it also binds to the MT lattice. In addition, it can bind the MT lattice through MACF43. From Fig. 4.5 we knew that both EB3 and MACF43 bind only transiently to MTs and each other. So the only explanation for the absence of recovery for MACF43 was its interaction with the SLB. Supposedly, the strong bond of the histidine-tagged MACF43 to DGS-NTA lipids combined with the relatively slow diffusion of SLB-bound MACF43 molecules inhibited MACF43 molecules to diffuse away when unbinding from the MT lattice before rebinding to it.

For comparison, we repeated the experiment with histidine-tagged EB3 but without MACF43. In that situation, no spontaneous MT nucleation was observed (Fig. 4.12A). When GMPCPP-stabilized MT seeds were present, MT nucleation was possible, but these MTs were dynamic and neither bundled nor bent (Fig. 4.12B,C). Apparently, the interaction between lipid bilayer and MT tip was not enough to result in MT stabilization like we observed with MACF43; an interaction with the MT lattice was required.

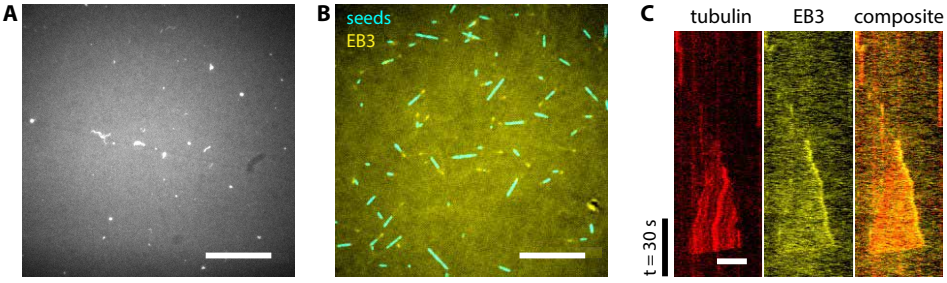

Figure 4.12: **(A)** No spontaneous MT nucleation was observed on an SLB containing DGS-NTA lipids, with 30 µM tubulin and 120 nM histidine-tagged EB3-GFP (greyscale) in solution. Scalebar is 20 µm. **(B)** In a similar experiment as (A), MTs did nucleate when GMPCPP-tabilized MT seeds (cyan) were present. Protein comets of 20 nM histidine-tagged EB3 (yellow) were tiptracking growing ends of dynamic MTs. Scalebar is 20 µm. **(C)** Kymograph of a MT on SLB from (B) with rhodamine-tubulin (red) and an EB3-GFP protein comet at the plus end. MTs wiggled around over time because the MT seeds were not attached to the SLB. Scalebar is 5 µm.

Summarizing, we observed a strong stabilizing effect of cortical MACF43 on tethered MTs. Since cortical EB3 did not have this effect, it was caused by the interaction of MACF43 with both MT lattice and cortex. Because of this stabilization, the MT length as well as the MT aster position were very stable. In addition, spontaneous MT nucleation was enhanced by cortical MACF43, both on emulsion droplet cortices and on SLBs.

4.4. DISCUSSION

IN this chapter, we studied MT asters in confinement. First, comets of end-binding proteins were used to compare MT dynamics inside water-in-oil emulsion droplets and in flow channels. We did not find any influence of confinement on the MT dynamics in the current conditions. Next, we introduced MACF18 and MACF43 as cortical +TIPs to capture MTs at the droplet cortex. MT capture locally accumulated MACF18 at the MT tip or part of the MT lattice. However, after depolymerization of the MT, this hotspot of MACF18 immediately disappeared. As a result of the MT tip capture, MT asters were positioned closer to the droplet cortex and to the bottom of the droplet, and the aster position was more stable over time. When not only the MT tip but also the lattice is tethered by cortical MACF18 or MACF43, we see an increase of MT rescues and therefore of the tethering duration. For MACF43, the effect of MT lattice capture at the cortex was so strong that MT depolymerization and detachment were inhibited. Also the aster position was extremely stable and located right at the droplet cortex.

From the experiments with EB3 protein comets in droplets, we concluded that the MT growth velocity and MT length in droplets and channels were similar under similar conditions. Since MT length is the result of both growth velocity and catastrophe rate, we assumed that the catastrophe rate was similar as well. Neither the presence of a confinement, nor the size of the confinement seemed to influence MT dynamics. We want to mention though that the outcome may be different for a regime of longer MTs compared to the droplet size (illustrated in Fig. 4.13). In our experiments, the MTs were on average smaller than the droplet radius, so they did not have a lot of contact with the confinement. For longer MTs, more contact may lead to altered MT lengths or MT growth velocities.
Nevertheless, the lack of influence of the confinement on MT dynamics was surprising, as in our experience we need a higher tubulin concentration in droplets than in channels to observe any MTs at all. Considering our results this was more likely a nucleation problem than an elongation problem of MTs in emulsion droplets. This reasoning is supported by (unpublished) experiments in our lab where additional crowding was required inside emulsion droplets to nucleate MTs from GMPCPP-stabilized seeds, while they nucleated without crowding agents in flow channels. The nature of the difference is however not yet understood.

To establish a connection between MT tips and the droplet cortex we used two +TIP peptides derived from MACF2: MACF18 and MACf43. *In vitro* characterization showed that MACF43 has MT lattice affinity while MACF18 does not, and that the MT tip-binding affinity of MACF43 is 4-5 times higher than for MACF18. Our values for the hydrolysis of the MT lattice from GTP to GDP-bound and the off-rate k_{off} for EB3 are a factor 2 smaller than previously reported values [Bieling et al., 2007, Gouveia et al., 2010, Buey et al., 2011, Preciado Lopez, 2015]. It could not be the influence of MACF because we measured the influence of EB3 and EB3 plus MACF separately. One difference was the salt concentration, which was 50 mM KCl in our experiments and 65-85 mM in the others. It is well known that salt influences EB3 affinity for the MT lattice

[Zanic et al., 2009, Buey et al., 2011], so it might also influence MT tip affinity.

Both MACF18 and MACF43 established a connection between MT and droplet cortex. The difference was as expected from the MT affinities: cortical MACF18 captured mostly MT tips, while cortical MACF43 strongly bound the whole MT lattice to the cortex.
It is however unclear why MACF18 in some droplets led to tip tethering only and in other droplets to lattice tethering as well while in channels it did not have affinity for the MT lattice. Within one batch of emulsion droplets, both situations occurred. Therefore, our hypothesis is that a deterioration of MACF18 quality leads to an affinity for the MT lattice. During water-in-oil emulsion droplet production by pipetting (Sec. 2.1), shear stress is breaking up the water phase into smaller volumes to create micron-sized droplets. This is a vigorous process with large variability from droplet to droplet. As a result, properties of the mixing region of water and oil at the water-oil interface will also vary between droplets. In this hydrophobic mixing region, proteins are more likely to denature. We hypothesize that in some droplets the MACF18 peptides are affected by this mixing region, and become more likely to bind the MT lattice. This hypothesis is supported by the fact that when the MACF18 peptide aliquots were stored for longer period, which deteriorates protein quality as well, we observed more lattice tethering. Another explanation could be the MT lattice affinity of EB3, which depends on factors like salt concentration and EB3 concentration. Variations of such factors between droplets could lead to variations in lattice affinity of EB3 and hence also of MACF18.

We chose to analyze MT-cortex interactions in projections of the 3D movies. We projected each z-stack onto one plane so we were left with (x,y,t) movies that are much easier to analyze than (x,y,z,t) movies. This has the advantage that we can follow one feature over time. The major disadvantage is that information of the z-positions is lost. The z-position is irrelevant for quantifying tethering duration and number of hotspots. However, for measuring the movement and position of MT asters inside droplets it is not. The consequence is that the MTOC velocities in Fig. 4.8 only give a lower limit, because the z-component of the velocity is not taken into account. But we expect that an MTOC moves in z in a similar way as in xy, and therefore we can draw conclusions about MT aster motility from the projections.
For the MT aster positioning however, the z-position has a strong influence on the relative MT aster position in the projection (illustrated in Fig. 4.9). Therefore we also determined the z-position separately from the 3D data. The MT aster z-position was difficult to measure precisely because it is smeared out in the image due to depth of field and optical abberrations (see Fig. 4.9C). We did notice that within the error the z-position appeared approximately stable over the time of the measurements. So we determined the approximate z-position of each MT aster, which is plotted in Fig. 4.9D and clearly different for tethered and free MT asters. Also the xy-position from projected data shows clear differences between tethered and free MT aster positions. We can not say quantitatively how close the MTOCs are to the cortex, but qualitatively we clearly observe that they are much closer to the cortex when tethering is possible.

Over time, we observed that MT asters sank to the lower half of emulsion droplets. Gravity is to blame for this, because the metal magnetic dynabeads which form the basis of our artificial MTOC are 1 µm diameter and have higher density than water. When MTs are long enough but not longer than the droplet radius, they exert pushing forces on the droplet cortex. These pushing forces counteract gravity on the bead and usually suffice to position the MTOC just below the midplane of the droplet, as expected based on previous positioning experiments [Holy et al., 1997, Laan et al., 2012a].
But when MT-cortex tethering is possible, MT asters position only a few microns above the bottom of a droplet, even though the average MT length does not seem influenced by tethering. Moreover, the MTOC positions close to the droplet cortex not only in z but also in xy (Fig. 4.9E). This suggests a limitation on MT aster motility as a result of MT-cortex interactions. But how does tethering limit aster motility? A pulling force is unlikely because the MACF18-induced MT-cortex connection disappears as soon as the MT depolymerizes. We estimated from hotspot intensities that approximately 500 cortical MACF18 molecules are bound to a MT tip. These 500 connections between MT tip and droplet cortex are apparently enough to withhold the MT aster from diffusing around.
This story might be different in other MT length regimes. We can distinguish three regimes [Holy et al., 1997, Laan et al., 2012a, Roth et al., 2019b]: (i) short, (ii) intermediate and (iii) long MTs compared to the droplet radius, as depictured in Fig. 4.13. In regime (i), a MT aster is usually diffusing around and can be found anywhere in the droplet, but not likely close to the cortex. In regime (ii), the MTs are long enough to exert pushing forces on all sides of the droplet cortex, which can lead to centering of the MT aster. It can however also happen that some MTs buckle and the system converges quickly towards a steady state situation with the MT aster pushed to the side. In regime (iii) the MTs are so long that the latter situation is practically always the case.
Our system is in regime (i) or (ii) as a result of the tubulin concentration, EB3 concentration and droplet sizes in our experiments. These regimes explain that we observed the MT aster usually more towards the center of the droplet when tethering was not possible. With tethering, when one or more MTs were captured at the droplet cortex, the MT aster was limited in its motility and held closer to the cortex than to the droplet center. In a higher MT length regime, the MT aster positions are probably less influenced by tethering, because the asters are already pushed to the side of a droplet.

For tethering through MACF43 we observed a much stronger effect on MTOC positioning inside droplets. This makes sense because the binding affinity of MACF43 to the MT tip was found to be 4 times higher than for MACF18, and in addition MACF43 had an affinity to the MT lattice which MACF18 did not have. If only tip tethering through MACF18 is enough to keep the MT aster in a certain position for some time, a stronger connection to a much larger area of the MT through MACF43 is likely to keep the MT aster in place for a long time. And when a certain part of the MT lattice is bound to cortical MACF43, the neighboring lattice sites are more likely to bind cortical MACF43 as well because they are brought close to the cortex. By such zippering, soon the whole MT is strongly bound to cortical MACF43 and the MTOC is located close to the droplet cortex.

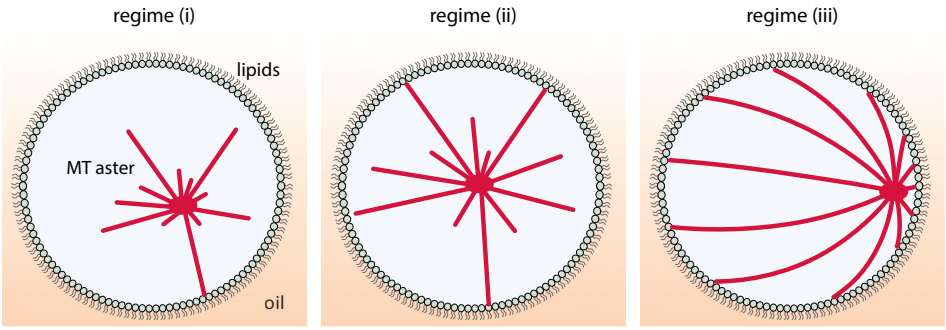

Figure 4.13: Schematic of the three regimes of MT lengths inside water-in-oil emulsion droplets: (i) short, (ii) intermediate and (iii) long MTs compared to the droplet radius.

Another effect we observed was that the tethering duration increased from 65 ± 47 s for tip tethering to many minutes for lattice tethering. Dynamic instability of tethered MTs (Fig. 4.7A) was observed for partial lattice tethering through MACF18. Quantification of this dynamic instability revealed that the MT catastrophe rate was unaffected by tethering while the rescue rate increased when the MT lattice was covered with cortex-bound proteins. In case of stronger lattice binding through cortical MACF43 we obtained very stable MTs that did not depolymerize visibly, suggesting a very high rescue rate. However, in channels we did not observe a significant increase in rescues by either MACF18 or MACF43. Apparently this effect is a result of the presence of the cortex binding, as it is observed for both droplet cortices and SLBs. An alternative explanation is that the shrinkage speed is reduced by the MT-MACF-cortex interaction. When MTs spend more time depolymerizing, the chance of a rescue increases if we assume rescues to be stochastic. It is well known that MAPs can affect the depolymerization rate of MTs, like we observed for MAP7 in Chapter 3 (Fig. 3.2). During characterization of MACF18 and MACF43 in flow channels we did not observe any effect on depolymerization rate (Fig. 4.5A). Nevertheless it is possible that the interaction of the MT lattice with the cortex through MACF changes the depolymerization rate. Further testing is needed to verify whether this is the case.

Finally, we return to the question whether MT-cortex interactions suffice to locally accumulate proteins *in vitro* at the cortex of an emulsion droplet. We observed local accumulations of MACF18 and MACF43 at the sites of MT-cortex interactions. However, the accumulations disappeared as soon as the interaction ended. So what is the difference between the chimera protein in fission yeast cells that accumulated at the cell poles purely by an interaction with both MT tips and cell membrane [Recouvreux et al., 2016]? Taberner et al. might give an answer to this question [Taberner and Dogterom, 2019]. They found that only motor-mediated protein clusters (consisting of fission yeast Tip1p, Tea1p and Mal3p) at MT ends were delivered to Ni-NTA functionalized microchamber walls, while non-clustered end-binding proteins disappeared from the wall as soon as the MT depolymerized. Note that those experiments were performed in microchambers with fixed Ni-NTA anchors on the wall and not in emulsion droplets with diffusing DGS-NTA phospholipids. Nevertheless, a cluster of

histidine-tagged proteins binds multiple Ni-NTA constructs at the same time. This enhances the total affinity of the cluster for either wall or cortex. In addition, a larger protein cluster diffuses slower than a single protein, and even slower when bound to multiple functionalized lipids. After the MT depolymerizes or detaches, the cluster will remain around the same position longer than a single protein. So we expect that protein clustering will make it possible to deposit proteins at the cortex by MTs that remain there when the MT disappears.

4.5. MATERIALS AND METHODS

MOST of the methods are as described in Chapter 2. In this section we only list the conditions, additional methods and data analysis that are specific for the experiments in this chapter.

4.5.1. PROTEIN PURIFICATION

All proteins used for this chapter were obtained from the sources listed in Sec. 2.2.4.

MACF18 AND MACF43

The MACF18 and MACF43 peptides were 10x histidine-tagged recombinant MACF2 derivatives with 18 or 43 amino acids (Fig. 4.14), purified from bacteria. A GCN4 dimerization domain is located in between the MACF sequence and an eGFP.

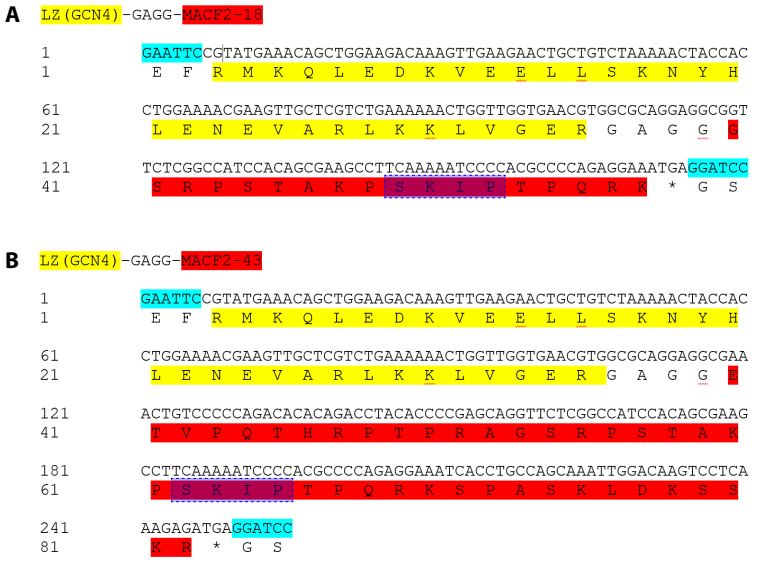

Figure 4.14: Sequence of the MACF2 protein, indicating the GCN4 dimerization domain (yellow), the sequences used for the MACF18 (A) or MACF43 (B) peptides (red) and the SxIP domain (blue dotted).

4.5.2. EMULSION DROPLET PREPARATION AND IMAGING

Two different lipid mixes were used, one of which contains Ni-NTA lipids so histidine-tagged proteins are recruited to the emulsion droplet cortex. Mix 1 contains

- 0.56 mg/ml *1,2-dioleoyl-sn-glycero-3-phospho-L-serine (sodium salt)* (DOPS)
- 2.7% (v/v) Span80

in mineral oil. Mix 2 contains

- 16.25 mg/ml *1,2-dioleoyl-sn-glycero-3-phosphocholine* (DOPC)
- 1 mg/ml *1,2-dioleoyl-sn-glycero-3- [(N-(5-amino-1-carboxypentyl) iminodiacetic acid) succinyl] (nickel salt)* (DGS-NTA(Ni))
- 1% (v/v) Span80

in mineral oil. Lipid mixes were prepared as described in Sec. 2.1.

The composition of the reaction mix which was used for the experiments in this chapter (unless indicated otherwise) is listed in Table 4.2.

component	final concentration	
50x oxygen scavenger mix*	1	x
D-glucose	50	mM
BSA	2	mg/ml
κ-casein	1	mg/ml
KCl	50	mM
GTP	3	mM
tubulin	30	μM
FL-MAP7-A647	100	nM
mCherry-EB3	300	nM
MACF18-GFP or MACF43-GFP	300	nM
beads	6.7	% of total volume

Table 4.2: Composition of the reaction mix for encapsulation of MT asters with EB3-GFP comets and a MACF-derived peptide which can bind the droplet cortex through its histidine-tag. All components are dissolved and diluted in MRB80. *200 mM DTT, 10 mg/ml catalase, 20 mg/ml glucose oxidase.

Water-in-oil emulsion droplets were created by pipetting and transferred into a PDMS well on top of a Rain-X coated coverslip, as described in Chapter 2. We imaged MTs and proteins inside the droplets with a Nikon Eclipse Ti2 Spinning Disc confocal microscope with an Nikon CFI Plan Apo Lambda 100X oil immersion lens (NA 1.45). For 3D acquisition of the emulsion droplets, a z-stack ($\Delta z = 0.75$ μm) of the bottom half of the droplet was acquired at each time step of the image acquisition. Only the bottom half was imaged as it suffered less from optical aberrations than the top half. When acquiring a z-stack at each timestep, the maximum framerate was determined by the exposure time, the number of wavelengths, the speed of the piezo and the number of z-planes. As changing filter to image in a different wavelength is relatively slow, we used

dual imaging mode where a beam splitter allows to image two wavelengths simultaneously on the cost of some intensity loss. Using dual imaging, the time between two z-stacks of 11 planes with 0.75 µm spacing was around 4 seconds.

SUPPORTED LIPID BILAYERS (SLB)

All lipids we used were dissolved in chloroform. We mixed the following lipids:

- 75 µg *1,2-dioleoyl-sn-glycero-3-phospho-L-serine (sodium salt)* (DOPS)
- 669 µg *1,2-dioleoyl-sn-glycero-3-phosphocholine* (DOPC)
- 25 µg *1,2-dioleoyl-sn-glycero-3-[(N-(5-amino-1-carboxypentyl) iminodiacetic acid) succinyl] (nickel salt)* (DGS-NTA(Ni))

Next, we evaporated the chloroform in gentle nitrogen flow followed by 2 hours in vacuum. Rehydration of the lipids was done in 2 ml H-Buffer150 (150 mM NaCl, 10 mM HEPES, pH 7.4) for 30 minutes. Finally, we prepared small unilamellar vesicles (SUVs) with a vesicle extruder using a 100 nm pore size filter.

Acid piranha cleaned coverslips (3:1 sulphuric acid:hydrogen peroxide) were used to prepare a flow channel. We rinsed the channel(s) with H-Buffer150 before flushing in the 2x diluted SUVs. After a few minutes incubation we rinsed with H-Buffer150. Afterwards, we flushed in a reaction mix like the one in Table 4.3. The fluidity of the SLB was checked by bleaching an area and measuring the recovery of the intensity profile over time.

component	**final concentration**	
50x oxygen scavenger mix*	1	x
D-glucose	50	mM
κ-casein	0.5	mg/ml
KCl	50	mM
GTP	1	mM
tubulin (1% labeled with Alexa-647)	31	µM
mCherry-EB3	120	nM
MACF43-GFP	120	nM

Table 4.3: Composition of the reaction mix for dynamic MTs on a supported lipid bilayer with Ni-NTA functionalized lipids that bind histidine-tagged MACF43. All components were dissolved and diluted in MRB80. *200 mM DTT, 10 mg/ml catalase, 20 mg/ml glucose oxidase.

4.5.3. DATA ANALYSIS

KYMOGRAPHS

Kymographs were made with the KymoResliceWide plugin in ImageJ using a line with 5 pixel width along a growing MT as a region of interest. Next, we manually determined the slope of the growing MTs from the kymographs in ImageJ and calculated

relevant parameters like growth velocity and catastrophe rate from those slopes in Matlab.

2D PROJECTIONS OF 3D MTS IN EMULSION DROPLETS

Inside emulsion droplets, image quality is always worse than in TIRF images, compare Fig. 4.3B and Fig. 4.5A. Also, often one is imaging a 3D process (radial growth of MTs from a MTOC) only in one plane because 3D imaging is too slow to capture a fast process like MT growth. A major consequence of 2D imaging in one plane is that we only obtain the x- and y-components of a 3D process. Thus measured values - for example for MT growth velocity and length - provide a different distribution than the actual 3D values would give. If a MT is oriented parallel to the imaging plane (no z-component), its measured velocity and length equal the actual 3D value. In contrast, a MT under an angle (z-component more than 0) is located only partially within the imaging plane, leading to an underestimation of its length and growth velocity (Fig. 4.4).

We estimated the depth of field (DOF) of our microscope as a measure for the thickness of the imaging plane. This estimation yielded a DOF of 5.5 µm, the details can be found below at the end of this section.
For MT growth velocities, a MT with large z-component of the growth vector will rapidly grow out of the DOF, which limits the time the EB3 comet at the MT tip is visible and hence the observed duration of the growth event. We used this time to calculate the weights of the measured velocities and plot the weighted velocity distribution. The procedure to calculate the projected MT growth velocities is as follows:

1. Determine mean and standard deviation of the velocity distribution in channels, and create a Gaussian distribution with those parameters. Those are the absolute values of our 3D velocity distribution.

2. Also create random normalized 3D directional vectors $(\vec{x}, \vec{y}, \vec{z})$ for the directions of the 3D velocities.

3. Determine mean and standard deviation of the growth times in channels, and create a Gaussian distribution with those parameters.

4. Project the 3D velocities (composed from the absolute values and the 3D directional vectors) using the following equation:

$$|v_{2D}| = \sqrt{v_x^2 + v_y^2} \tag{4.1}$$

5. Calculate the time it would take each MT with its 3D velocity to grow out of the DOF. This time is the weight of the corresponding projected 2D velocity. Since growing out of the DOF is only limiting for MT growth events with large z-component, we compare the calculated time with a random growth time from step (3). The smallest of the two is the weight we will use.

6. Calculate the weighted cumulative distribution function (see Fig. 4.3C).

A similar calculation was done for the MT lengths observed in droplets (Fig. 4.3E). MT length was measured as the distance between MTOC and EB3 comet. When the z-component of the MT length was too large, the comet was not anynore within the imaging plane, so small MT lengths are over-represented in the distribution. We corrected for this by only counting MTs whose z-component (L_z) was less than half the DOF (assuming that the MTOC lies in the center of the imaging plane), see Fig. 4.3E.

Calculation of the depth of field

Every microscope has a certain DOF: the thickness of the slab perpendicular to the optical axis which can be observed with maximal spatial resolution [Borovytsky and Fesenko, 2010]. The DOF is the same as axial resolution, or z-resolution. Usually the following equation is used to calculate it

$$DOF \approx \frac{\lambda n}{NA^2} + \frac{n}{MNA} e \tag{4.2}$$

with λ the wavelength of the laser light, n the refractive index (1.5 for immersion oil), NA the numerical aperture of the lens, M the magnification and e the smallest distance that can be resolved by a detector in the image plane of the objective lens. We estimate e with $e \approx 1.22\lambda/2NA \approx 0.2$ µm. Further, our microscope objective NA is 1.45, $M = 100$ and when imaging GFP-labeled fluorescent proteins the wavelength is 488 nm, so the theoretical DOF is approximately 0.35 µm.

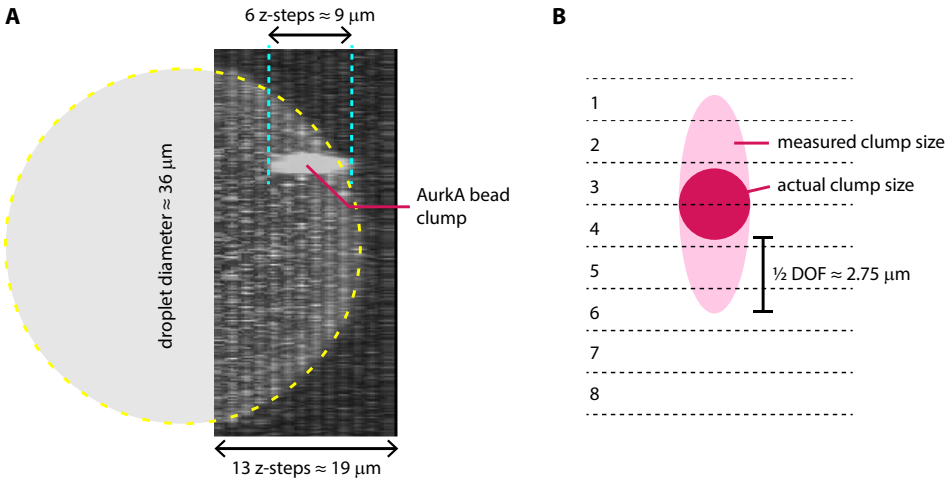

Figure 4.15: Experimental determination of the depth of field (DOF) of our microscope. **(A)** A spherical AurkA bead clump with 2.5 µm diameter in xy was visible in a z-stack. We draw the remainder of the droplet, knowing that the z-stack was taken from the bottom of the droplet to just below the center. This provides a calibration for distances in the z-direction. One slice in our z-stack corresponds to approximately 1.5 µm. **(B)** Comparison of the number of z-planes in which we observed the bead clump (6 slices) to the number of planes in which we expected to observe the bead clump based on its size (2 slices). This means that if an image was acquired in slice 6, we still see some signal origination from the bead clump in slice 4, which gives us a measure for the DOF.

In reality, we expect the DOF to be larger than 0.35 µm as a result of optical aberrations.

Especially the curved water-oil interface induces aberrations, because of the different refractive indices. We used an AurkA bead clump of 2.5 µm diameter in xy to get an experimental estimation of the DOF. Assuming the bead clump is approximately symmetric in 3D, we would need only 1.7 imaging steps of $dz = 1.5$ µm to image the whole bead in a z-stack (see Fig. 4.15A). Instead, the bead was visible in 6 of the imaging steps, so we estimated a DOF of about 5.5 µm (see Fig. 4.15B). Even though the error on this experimental determination of the DOF is around 1 µm, this value is an order of magnitude larger than the theoretical DOF of 0.35 µm.

FRAP ANALYSIS OF BINDING KINETICS

Binding and unbinding of proteins to MTs is often determined with fluorescence recovery after photobleaching (FRAP). When we bleach MACF molecules at the MT lattice, the signal recovers through dissociation of these molecules and new ones binding. Assuming fast equilibration of the soluble pool of EB3 or MACF, recovery can be described by a reaction-limited recovery curve [Sprague et al., 2004, Preciado Lopez, 2015]:

$$I(t) = (A - B * \exp(-t * k_{off})). \tag{4.3}$$

When a molecule like EB3, MACF18 or MACF43 is not bound to the MT lattice but to the tip the equations becomes less simple. We have to multiply Eq. 4.3 by a decaying exponential because the EB3 affinity for a MT site reduces when that MT site changes from tip-like to lattice-like due to GTP hydrolysis [Maurer et al., 2014]. A heavyside function brings in the time delay t_0 for a MT site to make this transition. Because the affinity of EB3 (and MACF18 and MACF43) for a MT lattice site is non-zero, we add a slowly rising exponential curve [Preciado Lopez, 2015]:

$$\begin{aligned} I(t) = (A - B * \exp(-t * k_{off})) * \\ \exp\left[-H(t-t_0) * (t-t_0) * k_{hydrolyze}\right] + \\ D * (1 - \exp\left[-H(t-t_0) * (t-t_0) * k_{decayhydrolyze}\right]) \end{aligned} \tag{4.4}$$

We analyze recovery by drawing a vertical, 3 pixels wide line in the kymographs at the position of the MT tip just before bleaching. Measuring intensity along this line and fitting Eq. 4.4 to it gives us k_{off} and $k_{hydrolyze}$.

QUANTIFICATION OF THE NUMBER OF MOLECULES IN A HOTSPOT

We would like to know how many cortical MACF proteins are recruited by a MT tip touching the droplet cortex. But since fluorescent proteins are smaller than the diffraction limit of the objective lens, the signal is smeared out over multiple pixels. Hence we needed to integrate the intensity ($I(x)$) to find the number of molecules within a certain region of interest (ROI). For a MACF18 hotspot on the droplet cortex, we

Fit parameter	EB3	MACF18	MACF43 (tip)	MACF43 (lattice)
A	0.99 ± 0.02	1.2 ± 0.1	1.5 ± 0.1	0.93 ± 0.01
B	1.02 ± 0.04	0.88 ± 0.09	1.4 ± 0.1	0.74 ± 0.03
D	0.011 ± 0.002	0.01 ± 0.02	0.24 ± 0.01	–
$k_{hydrolyze}$ (1/s)	0.19 ± 0.01	0.23 ± 0.01	0.17 ± 0.01	–
k_{off} (1/s)	0.80 ± 0.07	1.3 ± 0.21	0.25 ± 0.03	0.33 ± 0.03
t_0 (s)	5.2 ± 0.1	2.6 ± 0.3	5.6 ± 0.2	–

Table 4.4: All values for the fitting parameters obtained by fitting Eq. 4.4 to the averaged FRAP recovery curves in Fig. 4.5I. For MACF43, the signal was measured and fitted both on the MT tip and on the MT lattice. The other proteins were only present on the MT tip.

assumed that the intensity consists of two parts: a background of cortical MACF18 molecules which were evenly distributed on the cortex (I_c) and additional MACF18 molecules recruited by MT tips ($I_{hotspot}$). The latter was what we were interested in, so we subtracted the background and integrated over the region of interest (from x_1 to x_2):

$$I_{hotspot} = \int_{x_1}^{x_2} (I(x) - \langle I_c \rangle)\, dx. \tag{4.5}$$

This hotspot intensity was also equal to the number of recruited MACF18 molecules in the hotpot times the average intensity of one fluorescently labeled MACF18:

$$I_{hotspot} = N_h^{MACF} \cdot I_{MACF}. \tag{4.6}$$

To be able to use this equation we needed an estimation of the intensity of two fluorescent eGFP molecules (as MACF18 is tagged with eGFP and it is a dimer), I_{MACF}. This could be obtained from the background of cortical MACF18 that was everywhere on the cortex. So we integrated the cortex intensity outside the ROI of the hotspot and used an equation similar to Eq. 4.5 and 4.6:

$$I_{cortex} = \int_{x_3}^{x_4} I(x) dx = N_c^{MACF} \cdot I_{MACF} \tag{4.7}$$

where N_c^{MACF} is the number of MACF18 molecules in the cortex area where the intensity is integrated. It is calculated from the MACF18 density on the cortex (n_c), the length of the ROI ($L_{ROI} = x_4 - x_3$) and the depth of field (DOF) of the microscope. An estimation for n_c is obtained by dividing the total number of molecules in the droplet N by the surface of the droplet cortex A and multiplying this by a factor α for the fraction of MACF18 molecules in a droplet that is bound to the droplet cortex. Part of the MACF18 molecules is bound to the AurkA bead and sometimes also a fraction is in solution instead of bound to the cortex. The total number of MACF18 in the droplet (N) was calculated from the concentration of MACF (300 nM) and the droplet volume.

$$N_c^{MACF} = n_c \cdot L_{ROI} \cdot DOF = \frac{\alpha \cdot N}{A} \cdot L_{ROI} \cdot DOF \tag{4.8}$$

Plugging thus found values of N_c^{MACF} into Eq. 4.7 gave us a value for I_{MACF} which we could use in Eq. 4.6 to find the number of MACF18 molecules accumulated in a hotspot by a MT tip.

PROJECTIONS AND TETHERING TIME ANALYSIS

Projections of (x,y,z,t) image stacks were performed in ImageJ with the *Z Project* function, see Fig. 4.6B. From these images, tethering events were analyzed manually. The following parameters were noted down for each tethering event: timepoint that hotspot appears, timepoint that hotspot disappears, whether or not the MT lattice is decorated and if possible how the tethering event ends (MT depolymerized, MT detached from the cortex but does not (visibly) depolymerize or movie ended).

5

OPTOGENETIC TOOLS INSIDE EMULSION DROPLETS

Kim VENDEL, Nemo ANDREA, Maurits KOK, Erik BERDING, Anne DOERR, Eli VAN DER SLUIS and Marileen DOGTEROM

De egel wilde heel graag eens in de lucht hangen. Net als de zon.
Maar niet zo hoog. Dat vond hij niet nodig.

Toon Tellegen

Cell polarity is often the response of a cell to some external cue, like the chemical gradient from a food source or the physical presence of a neighboring cell. In this chapter, we studied the feasibility of using light as an in vitro external cue for polarized microtubule-cortex interactions in our minimal system. Optogenetics is a technique where proteins are genetically modified to become light-sensitive. In budding yeast cells, optogenetics was used to locally recruit the polarity protein Cdc24, which resulted in bud emergence at that site [Witte et al., 2017]. Here, we explored two light-sensitive proteins to control microtubule-cortex interactions inside water-in-oil emulsion droplets. On the one hand we tested a photo-activatible iLID-SspB binding pair. We showed local and reversible recruitment of SspB upon local activation of iLID at the cortex of emulsion droplets. On the other hand we tested a photo-dissociable π-EB1 protein. We characterized the light-response of π-EB1 and its interaction with microtubules in flow channels. Furthermore, we proved the activity of π-EB1 inside emulsion droplets. Finally, we discussed the current difficulties for using π-EB1 as an external cue in our minimal system and strategies to overcome those difficulties.

5.1. INTRODUCTION

In nature, many different external cues exist that locally trigger a cell to break its symmetry and make one part of the cell different from the rest. An example is a nutrient gradient causing a cell to migrate in the direction of higher nutrient concentration. This directed migration is the result of cell polarity, the morphological and functional reorganization of cellular components (e.g. proteins, cytoskeleton and organelles) in a directional and usually asymmetric manner [Théry et al., 2006]. Even though spontaneous polarization is observed as well (see Chapter 6), usually an external cue, like the aforementioned nutrient gradient, precedes cell polarity establishment. In the previous chapters, we worked on a minimal system where we could locally accumulate cortical proteins and reorganize the MT cytoskeleton by MT-cortex interactions. These are two characteristics of cell polarity, as we explained in Chapter 1. However, this was not yet cell polarity *in vitro*, because the local accumulation of cortical proteins at the site of MT-cortex contact was short-lived and did not continue to exist when the MT detached. In Chapter 6 and Chapter 7 we will discuss strategies to achieve polarity of emulsion droplets, but in this chapter we explore the addition of an external cue to trigger MT-cortex interactions.

Optogenetics - a technique where light is used to control living cells (for examples, see [Levskaya et al., 2009, Wu et al., 2009, Yazawa et al., 2009, Wang et al., 2010, Yoo et al., 2010, Strickland et al., 2012, Witte et al., 2017]) - provides a possibility to mimic external cues *in vitro*. For this technique, cellular components (like proteins or ion channels) are genetically modified to become light-sensitive (for a review, see Pudasaini [Pudasaini et al., 2015]). An example are experiments in budding yeast with optogenetic tools to recruit polarity proteins to specific sites at the cell cortex [Witte et al., 2017]. By local light-activation of these polarity proteins, researchers could trigger bud emergence at that site.
Inspired by this technique, we looked into the possibility of using light to locally switch the MT-cortex interactions on and off *in vitro*. Two systems were investigated to create photo-switchable behaviour of proteins: iLID to SspB interactions [Guntas et al., 2015] and LOV2 to Zdk1 interactions [Wang et al., 2016, van Haren et al., 2018]. We showed that it is possible to locally recruit SspB fused to mCherry (SspB-mCh) to the droplet cortex by activation of biotinylated iLID (bio-iLID), which is bound to biotinylated phospholipids at the cortex. However, the recruitment of iLID to lipids at the droplets cortex was thus far not efficient enough, so we additionally explored the use of a photodissociable EB1 (π-EB1) [van Haren et al., 2018]. This π-EB1 employed a LOV2 - Zdk1 interaction to dissociate upon blue light illumination. We characterized this protein *in vitro* in flow channels, and made the first steps to encapsulate π-EB1 inside emulsion droplets. Preliminary results demonstrated that even though π-EB1 is active inside droplets, more fine-tuning of π-EB1 with cortical +TIPs is required.

5.2. BACKGROUND

PLANTS grow towards the light. This means that they must possess light-sensitive components that detect light and trigger pathways that make the plant respond to light. Phototropins are light-activated kinases [Huala et al., 1997, Sakamoto and Briggs, 2002] in plant cells that contain two flavin-binding light-oxygen-voltage-sensing domains (LOV domains), which respond to blue light [Huala et al., 1997, Harper et al., 2003]: LOV1 and LOV2. From these two domains, LOV2 plays the dominant role in light-sensitivity [Christie et al., 2002]. NMR studies on the LOV2 domain of *Avena sativa* (oat) phototropin revealed that an amphipatic α-helix - called Jα - is responsible for the light-sensitivity [Harper et al., 2003]. Upon blue light illumination, a noncovalent protein-flavin mononucleotide (FMN) complex within LOV2 is converted into a covalent adduct, which is accompanied by a conformational change of LOV2 [Salomon et al., 2001, Swartz et al., 2001, Harper et al., 2003, Yao et al., 2008]. A side effect is that the bond between LOV2 and the Jα helix weakens, so the Jα can unfold and undock from LOV2.

This unfolding of the Jα helix is the basis of several optogenetic tools. In those tools, the LOV2-Jα sequence is fused to a protein in such a way that the binding sites for effectors are blocked by the Jα-helix in the dark state. Upon illumination, the Jα helix unfolds and undocks from LOV2. Due to this conformational change, the binding site for effectors becomes accessible (Fig. 5.1). In this way, optogenetic tools like CRY2/CIB1, iLID/SspB and LOVpep/ePDZ pairs were developed. All employ the undocking of Jα and the corresponding conformational change to change a certain binding affinity from dark to light state. In this thesis, we have worked with the iLID/SspB pair and the LOV2/Zdk1 pair, which we elaborate on in the following sections.

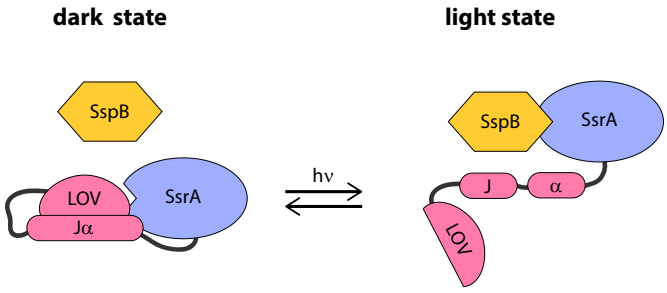

Figure 5.1: Schematic picture of the improved light-inducible dimer (iLID). A LOV2-Jα sequence was fused to the N-terminus of SsrA, such that only upon illumination with blue light the binding site for its effector SspB becomes available due to unfolding of the Jα helix.

iLID AND SSPB BINDING PAIR

To create an improved light-inducible dimer (iLID), Guntas et al. first determined the important properties of an effective photodimer [Guntas et al., 2015]. These are a large change in binding affinity upon blue light illumination, absence of cross-reactions with other molecules and applicability in a wide range of organisms. To meet these

criteria, they fused the *E. coli* SsrA peptide to the C-terminal domain of *Avena sativa* LOV2. SsrA is unavailable for its binding partner SspB in the dark state (Fig. 5.1). In the light state however, the Jα-helix unfolds and SsrA becomes accessible to bind SspB. As the structures of LOV2, SsrA and SspB are known, it was possible to improve the design by computational tools and phage-display screening [Guntas et al., 2015]. Mutations in the LOV2 eventually led to an improved version - iLID - that increases its affinity for SspB 50-fold upon blue light illumination compared to the original SsrA-SspB affinity. Three different SspB constructs were made, called SspB nano, SspB micro and SspB milli, based on their affinities to iLID. We used SspB nano, which is the wild-type SspB and whose iLID affinity changes from 4.7 µM in the dark to 130 nM under blue light [Guntas et al., 2015].

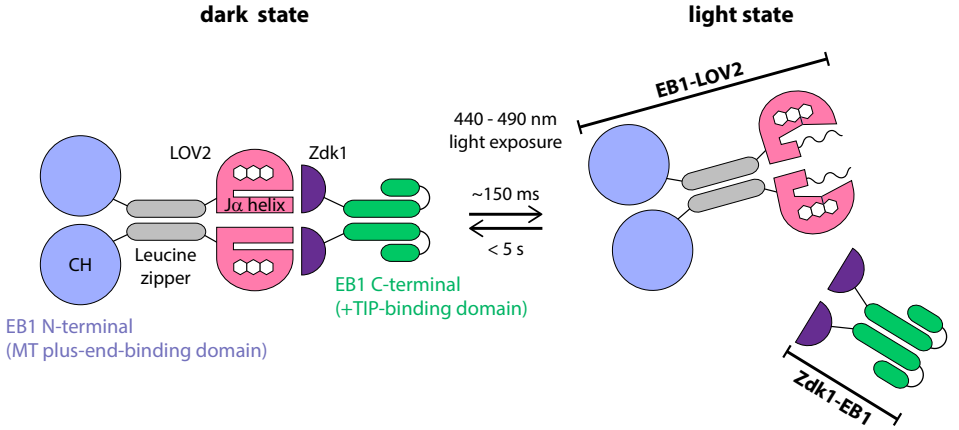

Figure 5.2: Schematic illustration of the light-response of π-EB1, adapted from [van Haren et al., 2018]. The LOV2 is fused to the MT-binding N-terminal domain of EB1, and Zdk1 to the +TIP-binding C-terminal domain of EB1. The result is a light-sensitive EB1 protein that dissociates upon blue light exposure.

LOV2 AND ZDK1 BINDING PAIR (PHOTO-DISSOCIABLE EB1)

In contrast to most optogenetic tools, the photo-dissociable EB1 (π-EB1) from van Haren et al. binds in the dark and dissociates in light instead of the other way around [van Haren et al., 2018]. This is possible with a small protein called Zdark (Zdk1) which binds selectively to the dark state of LOV2 [Wang et al., 2016]. When the LOV2 complex is illuminated and the Jα helix unfolds, Zdk1 cannot bind the LOV2 anymore. To incorporate this light-sensitive module into the EB1 protein, LOV2 is fused to the N-terminal CH domain of EB1, which binds the MT plus-end (Fig. 5.2). Zdk1 is fused to the C-terminal EBH domain of EB1, which can bind +TIPs. In blue light, the two halves of π-EB1 dissociate with a halftime of $t_{1/2} \approx 200$ ms [van Haren et al., 2018]. The N-terminal part of π-EB1 stays bound to the MT, while the C-terminal part dissociates together with any eventual +TIPs. The dissociation is reversible. In absence of blue light, EB1-Zdk1 reassociates to EB1-LOV2 with a half time of $t_{1/2} < 5$ s [van Haren et al., 2018].

OPTOCONTROL IN EMULSION DROPLETS

The goal of using optogenetic tools inside emulsion droplets is to create a local on-off switch for the interaction between cortical proteins and MT dynamics. One way to achieve this is with a photoactivatible probe (like iLID) bound to the droplet cortex and its binding partner (SspB) in solution fused to a protein of interest (+TIP) which influences MT dynamics (Fig. 5.3A). In this situation, only when (locally) illuminating the cortex with blue light, the +TIP is recruited to the cortex. A major disadvantage is that the +TIP can also influence the MT dynamics in solution, introducing a global background effect. The question is if the local effect caused by light-induced recruitment of the +TIP to the cortex is strong enough to make a difference compared to this background. Experiments are needed to provide an answer to this question.
A second way to create a local switch is with the photo-dissociable EB1 (π-EB1) [van Haren et al., 2018]. Our protein for influencing MT dynamics is a cortical +TIP, which needs an end-binding protein (EB) to track the growing MT tip. By locally illuminating the emulsion droplet with blue light we can locally inhibit the interaction of the cortical +TIP with MT tips through π-EB1 (Fig. 5.3B). The advantage of the π-EB1 approach over iLID-SspB is that the +TIP is at the cortex, so it only interacts with MTs that are in contact with the cortex through π-EB1. Mainly because of this advantage, we expect the π-EB1 system to work better for our purpose than the iLID-SspB system.

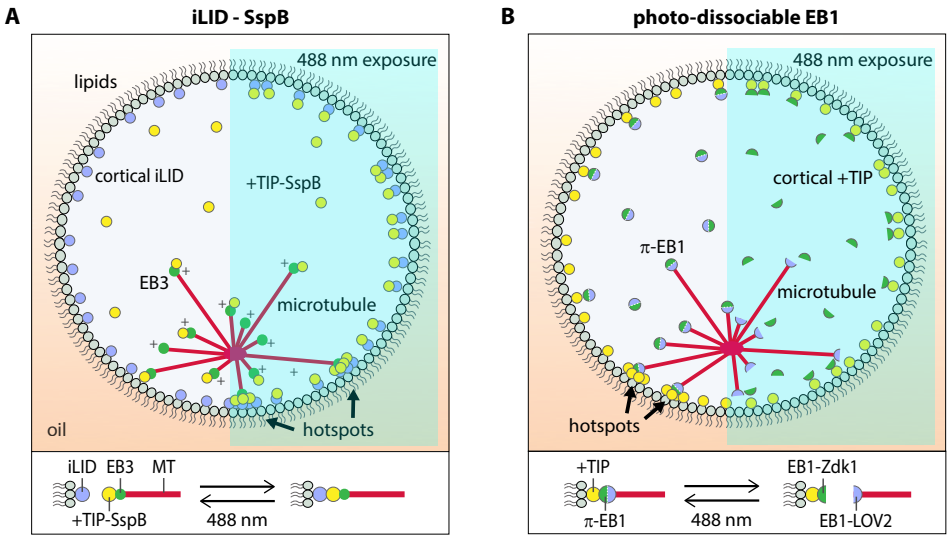

Figure 5.3: The two optogenetic systems we explored for use inside water-in-oil emulsion droplets. **(A)** iLID molecules are recruited to the droplet cortex. Activation of iLID by blue light enables binding of iLID to SspB, which is fused to a +TIP. The iLID functions as a light-sensitive on-off switch for local recruitment of +TIPs to the droplet cortex. **(B)** +TIP molecules are recruited to the droplet cortex and the photodissociable π-EB1 is in solution where it can bind the MT plus ends. Upon blue light exposure, π-EB1 falls apart into EB1-LOV2 (purple), which can still bind the MT tip, and EB1-Zdk1 (green), which can bind the +TIP. The π-EB1 functions as a light-sensitive on-off switch for interactions between MTs and the cortical +TIP.

5.3. RESULTS

5.3.1. iLID AND SspB BINDING PAIR

At first, we tested the iLID-SspB interaction in flow channels. To this end, we passivated the glass surfaces of the flow channels with consecutively PLL-PEG-biotin, neutravidin, κ-casein and biotin-iLID (Fig. 5.4A). The reaction mix contained SspB-nano fused to mCherry for visualization of the SspB recruitment to activated iLID molecules. A short, local pulse of 488 nm laser light induced exponential recruitment of SspB-mCh followed by an exponential decay when the iLID returned to its inactive state over time (Fig. 5.4). Continuous illumination with 488 nm light in the full field of view of the camera (80x80 μm^2) resulted in an exponential increase of SspB-mCh signal on the surface (Fig. 5.4C) up to a level where the on-rate and off-rate of SspB binding to iLID were in equilibrium. A maximum level of SspB recruitment existed, which depended on the on and off rates of SspB to active iLID and on the fraction of activated iLID molecules. The higher the laser power, the more photons were emitted and the more iLID molecules could be activated, up to a threshold to activate all iLID molecules. After this threshold, more photons did not lead to more activation. We see this effect in the curves from Fig. 5.4C, where the SspB recruitments of 5.0% and 6.0% were very similar to each other and to the continuous activation.

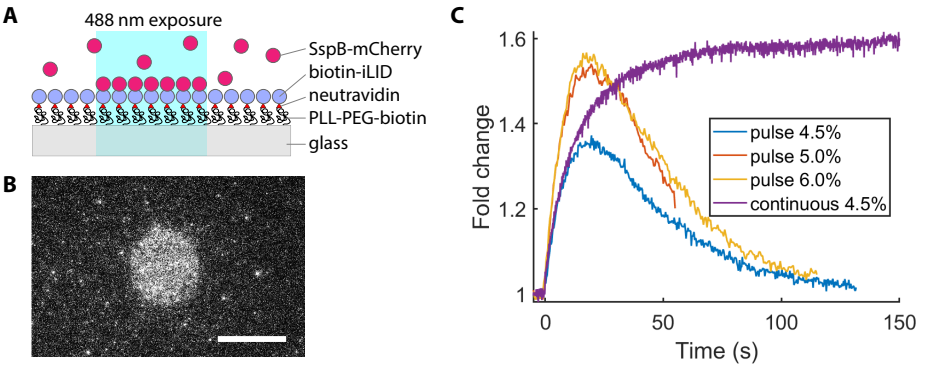

Figure 5.4: **(A)** Side view of a flow channel experiment with biotin-iLID attached through neutravidin to PLL-PEG-biotin molecules on the glass surface and SspB-mCh in solution. Upon local activation of iLID by a pulse of 488 nm light, SspB-mCh is recruited only to the activatid iLID molecules. **(B)** SspB-mCh signal upon local activation of the biotin-iLID molecules in a circular area. Scalebar is 20 µm. **(C)** Comparison of the SspB-mCh signal within the activated area for different laser powers of the pulse 488 nm light. We also compared it to continuous illumination with 4.5% laser power (purple) of the full field of view of the camera.

Extensive quantitative characterization of the binding kinetics of iLID and SspB was performed by Maurits Kok and can be found in his PhD thesis [Kok, 2019]. He determined all the involved reaction rates (e.g. the k_{on} and k_{off} for the interaction between active iLID and SspB, k_{decay} for the decay of active iLID to inactive iLID and the dissociation constant K_D) and found an *in vitro* K_D for the SspB of 139 ± 43 nM for the active state of iLID, which was in agreement with previously reported values [Guntas et al., 2015]. Furthermore, he found that with increasing laser power of the illumination, ini-

tially the recruitment of SspB increased, but for laser powers above a threshold of 100 µW the recruitment decreased. Moreover, for these higher laser powers a fraction of iLID was irreversibly activated and permanently active.

LIGHT-INDUCED RECRUITMENT OF SSPB TO ILID IN DROPLETS

Because the iLID-SspB interaction worked very well in flow channels, we shifted to experiments inside water-in-oil emulsion droplets. A lipid mix was prepared (Sec. 5.5) with biotinyl-cap-PE lipids to bind biotin-iLID to the droplet cortex through streptavidin (Fig. 5.5).

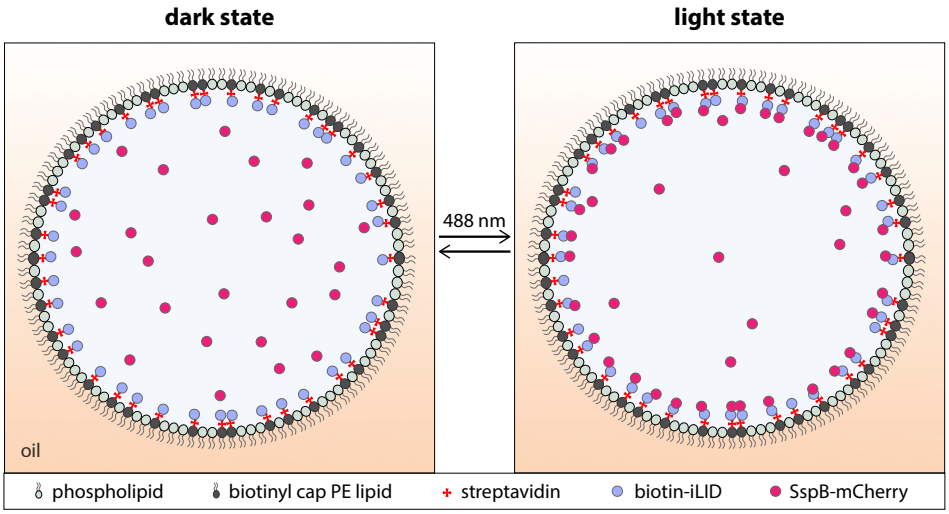

Figure 5.5: Schematic of the light-induced recruitment of SspB-mCherry to the droplet cortex. Biotin-iLID molecules are bound to biotinyl cap PE lipids in the cortex through streptavidin and become active upon illumination by 488 nm light to bind SspB.

Upon illumination of the droplets with 488 nm laser light for 30 seconds, SspB-mCh was indeed recruited to biotin-iLID on the droplet cortex (Fig. 5.6A,B). While the SspB-mCh intensity on the cortex increased, the intensity in the droplet interior decreased. After switching off the 488 nm light, the recruited SspB-mCh dissociated from the cortical iLID back to the interior of the droplets.
Local activation of cortical iLID was achieved by illuminating a certain region of activation (ROA) with a 488 nm laser pulse (Fig. 5.6C). After this pulse, the intensity of SspB-mCh on the cortex increased around 15% within the activated area and only a few percent outside of it (Fig. 5.6D).

These experiments demonstrated that it is possible to locally and reversibly recruit SspB by local activation of biotin-iLID on the cortex of emulsion droplets. However, we struggled to reproduce the results. The problem turned out to be inefficient cortex-binding of biotin-iLID. Experiments with fluorescently labeled biotin-iLID-YFP and

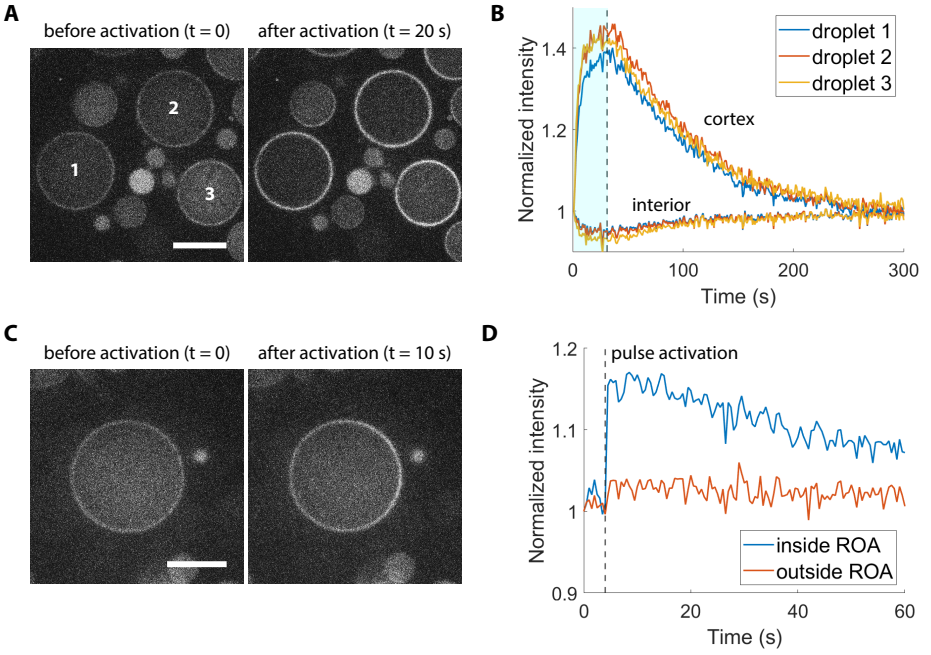

Figure 5.6: Light-induced recruitment of SspB-mCh to biotin-iLID at the cortex of water-in-oil emulsion droplets. **(A)** Continuous illumination of the full field of view with 40% 488 nm light (spinning disc laser) for 30 seconds led to an increase of the SspB-mCh signal on the droplet cortex. Scalebar is 20 µm. **(B)** SspB-mCh intensity on the cortex and in the interior of the droplet for the three droplets shown in (A). **(C,D)** When only a defined region of activation (ROA) was illuminated with a short localized 488 nm light pulse, SspB-mCh was mainly recruited to this area on the droplet cortex. Scalebar is 20 µm.

fluorescent streptavidin (Fig. 5.7) revealed that while streptavidin was efficiently recruited to the biotinyl cap PE lipids in the cortex, the majority of biotin-iLID-YFP remained in solution. The efficiency of the cortex-binding of iLID varied a lot between different biotin-iLID purifications, despite following the same protocol. One batch of biotin-iLID was recruited to the cortex very well (Fig. 5.6), while another batch was hardly recruited (Fig. 5.7).
For this reason, we decided to explore an alternative light-sensitive protein: the photo-dissociable π-EB1. Simultaneously, other strategies to recruit iLID to the droplet cortex were explored by other members of the lab, as well as possible solutions to increase the efficiency of biotin-iLID recruitment.

5.3.2. PHOTO-DISSOCIABLE π-EB1

As discussed in previous chapters, minimal systems inside water-in-oil emulsion droplets are extremely sensitive to experimental conditions such as protein concentrations, surfactants and phospholipids. Therefore we needed to understand the effect of all proteins on MTs and their interactions with each other in regular flow channel exper-

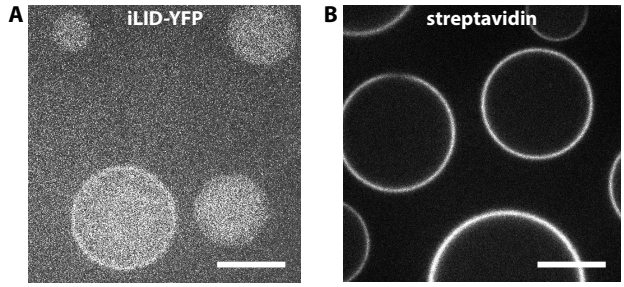

Figure 5.7: (A) Recruitment of biotin-iLID-YFP through streptavidin to biotinylated lipids in the droplet cortex. Most biotin-iLID was expected to bind to the cortex, but in reality only a minor fraction is and the majority remained in solution. **(B)** For comparison, fluorescent streptavidin is efficiently recruited to biotinylated lipids in the droplet cortex in a different yet similar experiment as in (A). Scalebars are 20 µm.

iments before we encapsulated the proteins in emulsion droplets. Since the π-EB1 protein does not possess a fluorescent label to visualize it directly, we used MACF18-mScarlet (mScl) for indirect visualization, which we will simply call MACF18 from now on in this chapter. This MACF18 protein binds EB1-Zdk1 through an SxIP motif, and thus allows us to indirectly visualize EB1-Zdk1 before, during and after exposure to blue 488 nm light which dissociates π-EB1. We could not use the GFP-tagged MACF18 from Chapter 4 because imaging GFP requires 488 nm light, which would deactivate π-EB1.

CHARACTERIZATION OF π-EB1 IN FLOW CHANNELS

First, we used flow channel experiments with dynamic MTs to study the effect of π-EB1 compared to EB3 on MT dynamics, with or without MACF18 (Fig. 5.8). All protein concentrations were 200 nM in this experiment, except for tubulin which was 15 µM. We observed no binding of MACF18 to MTs in absence of EB3 or π-EB1 (data not shown), so we concluded that the peptide can only interact with MTs through end-binding proteins. A clear difference was visible between EB3 and π-EB1 (Fig. 5.8A): the affinity of π-EB1 for the MT tip was less and its affinity for the MT lattice was more than for EB3. The intensity of MACF18 on MT tips with EB3 was 2.2 times higher than with π-EB1 (Fig. 5.8B). Small variations were measured in the growth velocities (Fig. 5.8C). The average growth velocity with π-EB1 (purple curve, $v_g = 3.7 \pm 0.5$ µm/min) was similar to that with EB3 (red curve, $v_g = 3.8 \pm 0.4$ µm/min). Addition of MACF18 increased the growth velocities to $v_g = 3.9 \pm 0.5$ µm/min (EB3, yellow curve) and $v_g = 4.2 \pm 0.5$ µm/min (π-EB1, green curve). Without end-binding proteins (blue curve, $v_g = 2.3 \pm 0.5$ µm/min) the growth velocity was much lower than with any end-binding proteins. Interestingly, the growth time distributions were similar for EB3 versus π-EB1, with or without MACF18 (Fig. 5.8D).

So the replacement of EB3 by π-EB1 did not have a major influence on MT dynamics. The main difference was the ratio of tip affinity to lattice affinity (Fig. 5.8), leading to a decreased visibility of MACF18 comets for π-EB1 compared to EB3.

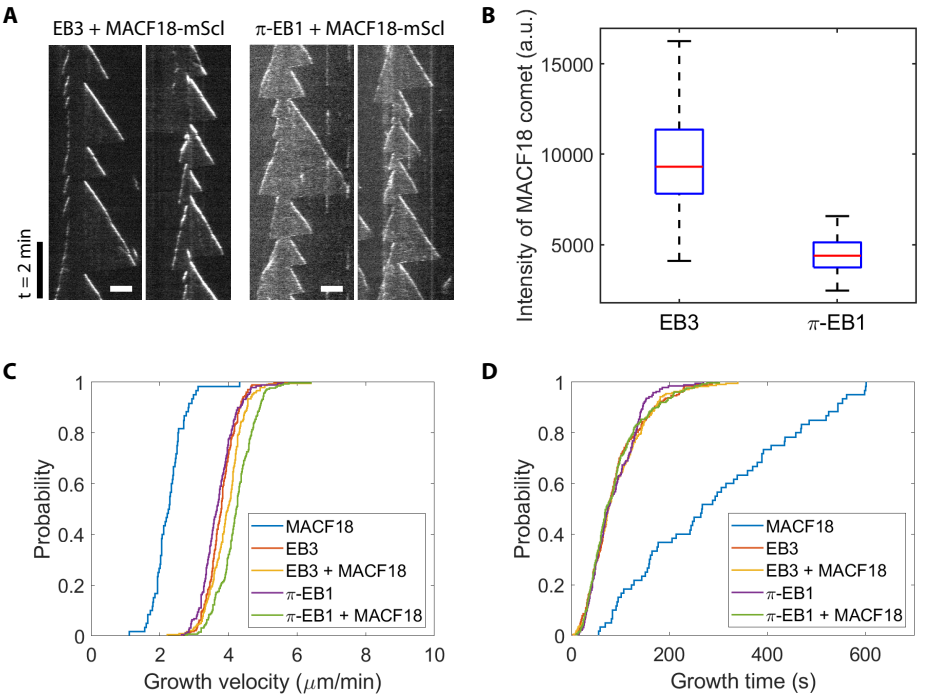

Figure 5.8: Influence of different proteins on MT dynamics. **(A)** Kymographs of dynamic MTs in the presence of EB3-GFP and MACF18 (left) or π-EB1 and MACF18 (right). The MACF18 signal is shown here and scalebars are 5 µm. **(B)** Comparison of the MACF18 protein comet intensity in the presence of either EB3 or π-EB1. The background MACF18-mScI signal was comparable (around 1500 a.u.) for both conditions after background subtraction. **(C,D)** Cumulative distribution functions of MT growth velocities (C) and growth times (D) under different conditions.

Next, we checked the functionality of the two components of π-EB1 (EB1-LOV2 and EB1-Zdk1) in a dynamic MTs assay (Fig. 5.9). We observed comets of MACF18 tip-tracking growing MTs exclusively in the presence of both EB1-LOV2 and EB1-Zdk1. Furthermore, EB1-LOV2 increased the MT growth velocity and decreased the growth time, while the addition of EB1-Zdk1 did not influence MT dynamics (Fig. 5.9A,B). So from those data we deduced that EB1-LOV2 binds to MT tips and influences MT dynamics, while EB1-Zdk1 binds to active EB1-LOV2, and enables MACF18 tiptracking (see Fig. 5.2). These conclusions from our *in vitro* work were in agreement with the *in vivo* data from van Haren et al. [van Haren et al., 2018].

LIGHT-INDUCED DISSOCIATION OF π-EB1 IN FLOW CHANNELS

Next, we characterized the light-dissociable properties of π-EB1 in flow channels. We polymerized MTs with GTPγS, a slowly hydrolyzable GTP variant. The structure of GTPγS-bound MTs resembles that of the MT tip structure (supposedly GDP-P$_i$) where end-binding proteins bind [Maurer et al., 2011] (Fig. 5.10). Indeed, we observed that MTs polymerized very slowly and did not undergo catastrophes. Moreover, the whole

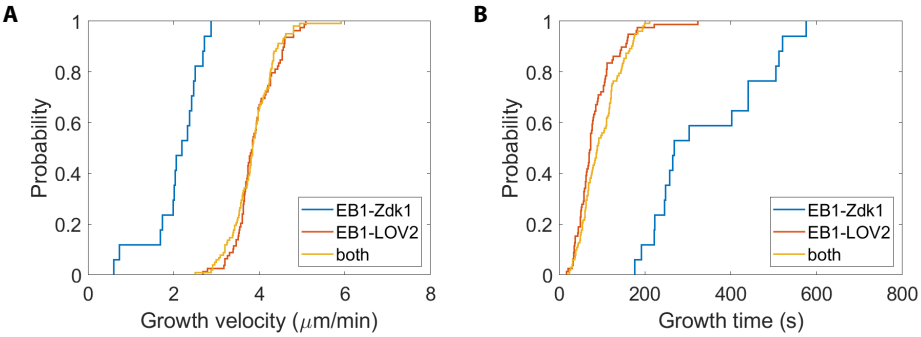

Figure 5.9: Cumulative distributions functions showing the influence of EB1-LOV2, EB1-Zdk1 or a combination of the two proteins on the MT growth velocity (**A**) and growth time (**B**).

MT lattice was covered with MACF18 and thus with π-EB1 instead of only the MT tip (Fig. 5.11A, $t = 0$).

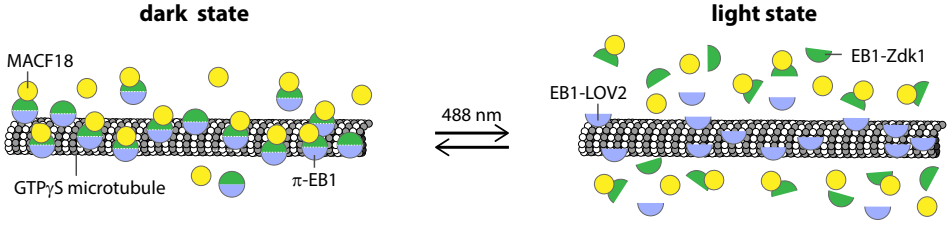

Figure 5.10: Schematic illustration of GTPγS-MTs that provide end-binding protein binding sites everywhere on the MT lattice, in contrast to only the GTP cap on dynamic MTs. The EB1-LOV2 part of the π-EB1 protein can therefore interact with the full MT. In the dark, EB1-Zdk1 can bind EB1-LOV2, leading to MACF18 signal on the MTs (left). Upon blue light exposure, the π-EB1 dissociates and EB1-Zdk1 and MACF18 detach from the MT (right).

In the experiments from Fig. 5.11 we acquired the MACF18 signal over time. Initially, no 488 nm light was present and MTs were covered with MACF18 because EB1-LOV2 was active and available for binding with EB1-Zdk1. When the 488 nm laser was switched on, we observed the dissociation of MACF18 from the MTs as a result of inactivation of EB1-LOV2 (Fig. 5.11A,B). After the 488 nm laser was switched off again, the recovery of MACF18 due to reactivation of EB1-LOV2 was measured. We repeated this experiment for different powers of the 488 nm laser. In Fig. 5.11C we show the light-induced dissociation of MACF18 from the MT lattice ($t = 0$ is defined as the moment the 488 nm laser switched on). First of all, we observed an exponential decay of MACF18 on the MT lattice for all laser powers. In addition, the higher the 488 nm laser power was, the faster the EB1-Zdk1 dissociated from EB1-LOV2 upon light exposure. Most likely this is the result of the increased photon flux for higher laser powers. A certain number of photons is required to deactivate all EB1-LOV2 molecules. A lower photon flux means that it takes longer to deactivate all molecules. In Sec. 5.6.1 we discuss how we take this delay into account and formulated Eq. 5.1 which is fitted to the

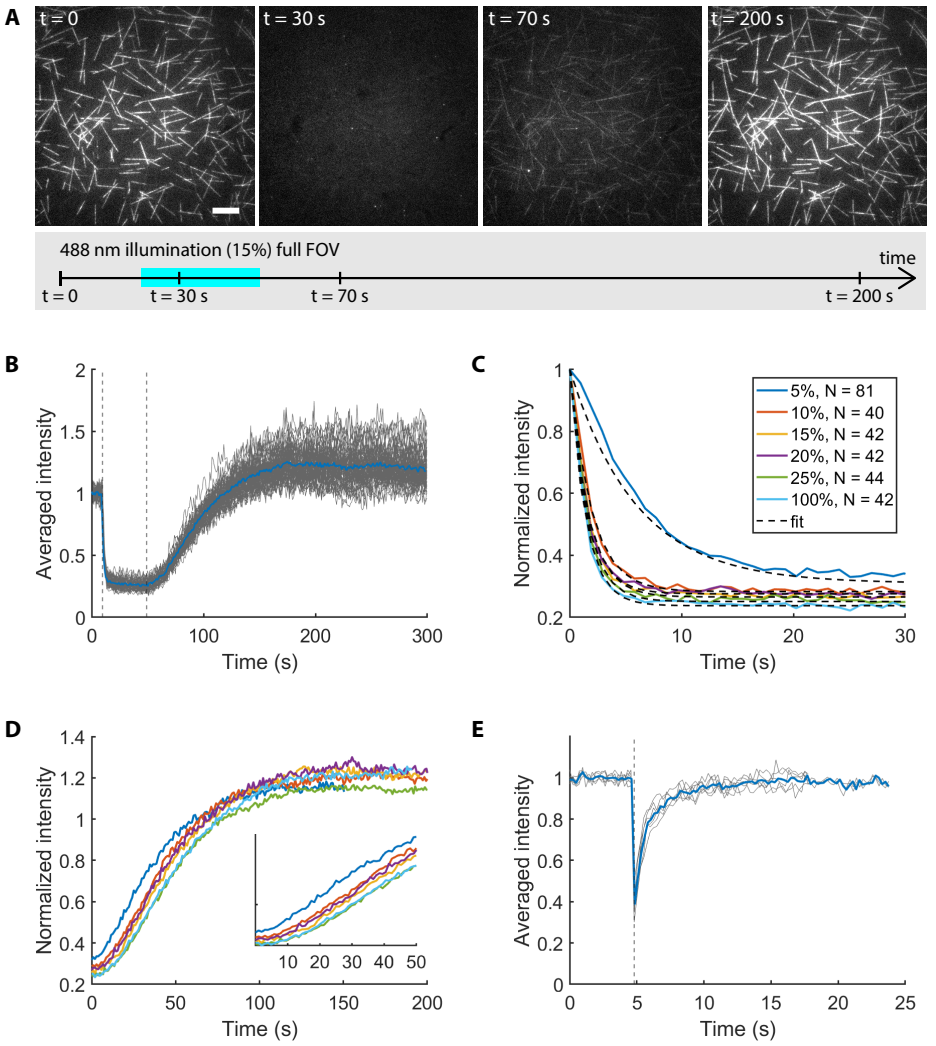

Figure 5.11: Light-induced dissociation of MACF18 from MTs. **(A)** Timeline of the experiment with snapshots of the MACF18 at different moments in time before ($t = 0$), during ($t = 30$ s) and after ($t = 70$ s and 200 s) exposure to 488 nm light in the full field of view (FOV). Upon 488 nm light exposure, the EB1-Zdk1 dissociates from EB1-LOV2 and takes MACF18 along. Scalebars are 10 µm. **(B)** Plots (grey) and average (blue) of the MACF18 intensity on MTs over time. The dotted vertical lines indicate the start and end of the 488 nm light exposure. **(C)** Light-induced dissociation of MACF18 from the MT lattice for different 488 nm laser powers ($t = 0$ in this plot is defined as the moment the 488 nm laser switched on). **(D)** Reassociation of MACF18 to the MT lattice after 488 nm light exposure for different 488 nm laser powers ($t = 0$ in this plot is defined as the moment the 488 nm laser switched off). The colors for laser powers are as in (C). The inset shows a zoom in on the the delay in the recovery curves. **(E)** Fluorescence recovery after photobleaching (FRAP) experiment: MACF18 on GTPγS-MTs was bleached and recovered with a half-time of 800 ms.

data and yields the off-rates (k) listed in table 5.1:

$$I(t) = I_1 + I_2 \cdot exp(-kt). \tag{5.1}$$

Finally, we observed that EB1-Zdk1 did not dissociate completely for the lowest laser power (5%). But even the other curves did not decrease to zero in Fig. 5.11C, which was most likely due to background signal.

Laser power	k (s^{-1})
5%	0.17 ± 0.01
10%	0.51 ± 0.02
15%	0.61 ± 0.04
20%	0.63 ± 0.03
25%	0.65 ± 0.04
100%	0.70 ± 0.03

Table 5.1: Values of the dissociation k of EB1-Zdk1 from EB1-LOV2 obtained from fitting Eq. 5.1 to the curves in Fig. 5.11. This k is a combination of the unbinding rate k_{off} of EB1-Zdk1 from EB1-LOV2 and a delay in dissociation τ_{delay} caused by a low photon flux for lower laser powers. More on the relation between k, k_{off} and τ_{delay} is discussed in Sec. 5.6.1.

After switching off the 488 nm light, the MACF18 intensity on the MT lattice recovered due to reassociation of EB1-Zdk1 to EB1-LOV2 (Fig. 5.11D). In this plot, $t = 0$ is defined by the moment that the 488 nm laser was switched off. Two interesting things became visible in this experiment.

Firstly, the intensity of MACF18 on the MTs was higher after 488 nm exposure than it was at the beginning of the measurement (Fig. 5.11B). We investigated this observation by exposing π-EB1 on MTs repeatedly to 10% 488 nm light (Fig. 5.12). Every exposure cycle, the MACF18 intensity dropped to the same level upon illumination, but recovered to a level higher than the initial intensity of that cycle. Possible explanations of this increase will be considered in the discussion section.

Secondly, a delay occurred between switching off the 488 nm light ($t = 0$ in Fig. 5.11) and the exponential recovery of MACF18 signal. This delay is caused by the time it takes the Jα-helix of the LOV2 domain to fold back such that binding of Zdk1 to LOV2 is possible again. We will discuss this matter further in the discussion.

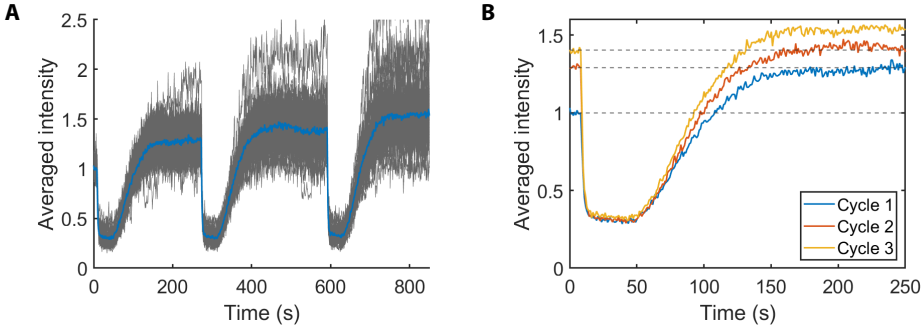

Figure 5.12: **(A)** Normalized MACF18 intensity on GTPγS-MTs (grey curves, N = 65) during repeated exposure to 488 nm light to dissociate the π-EB1. The average MACF18 intensity is plotted in blue. **(B)** Overlay of the MACF18 intensities during the three dissociation and recovery cycles from (A). The dotted lines indicate the starting level of each cycle.

Next, we prepared dynamic MTs with GTP and locally exposed the MTs within a defined region of interest (ROI) to 488 nm laser light with repeated short pulses (Fig. 5.13). We compared the binding of MACF18 to MTs before any exposure to 488 nm light (Fig. 5.13A, left) and after repeated exposure (Fig. 5.13A, right). Most of the MACF18 within the exposed ROI dissociated as a result of π-EB1 falling apart. Outside the exposed ROI, the MACF18 signal on MTs was unchanged (compare the kymographs in Fig. 5.13B). These data proved that we can locally switch the interaction between MACF18 and MTs on and off through UV light exposure of π-EB1.

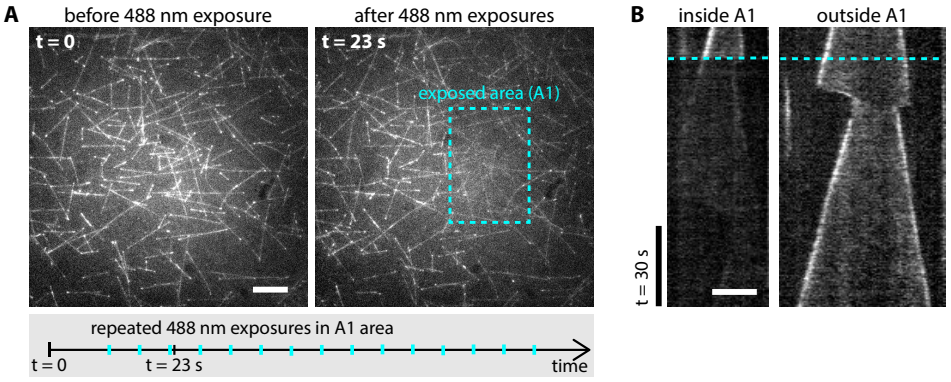

Figure 5.13: Local light-induced π-EB1 dissociation in a flow channel experiment with dynamic MTs. **(A)** Timeline of the experiment with repeated short pulse exposures of 488 nm and snapshots of the MACF18 signal before (left) and after (right) repeated exposures. The pulse exposures were 10 s apart and only in the area indicated by A1 in the right image. Scalebar is 10 µm. **(B)** Kymographs of MTs inside (left) and outside (right) the area exposed to 488 nm light. The cyan dotted line indicates the first exposure to 488 nm light. Scalebar is 5 µm.

LIGHT-INDUCED DISSOCIATION OF π-EB1 IN EMULSION DROPLETS

Our final goal was to use π-EB1 inside water-in-oil emulsion droplets as an external cue to control the interaction of MTs with the droplet cortex by light, which is a feature of cell polarity. After we had shown in channels that we could locally switch the interaction of MACF18 with dynamic MTs on and off through UV exposure of the π-EB1, the next step was to encapsulate the system inside emulsion droplets.

As a first step, we verified that EB3-mediated MACF18 protein comets on MT tips were visible inside emulsion droplets (Fig. 5.14). The MACF18 comets were less bright than the EB3-GFP comets, but bright enough to visualize. But in Fig. 5.8 we showed that the brightness of MACF18 comets was a factor 2.2 lower with π-EB1 than with EB3. If MACF18 comets are just visible inside emulsion droplets with EB3, they are most likely not visible with π-EB1. In an attempt to increase the MACF18 comet visibility, we varied the salt concentration from 50 mM KCl to 75 mM KCl and we varied the ratio of EB1-LOV2 to EB1-Zdk1 (Fig. 5.15). More KCl increased the ratio of tip binding to lattice binding of MACF18. Altering the EB1-LOV2:EB1-Zdk1 ratio did not affect the MACF18 visibility.

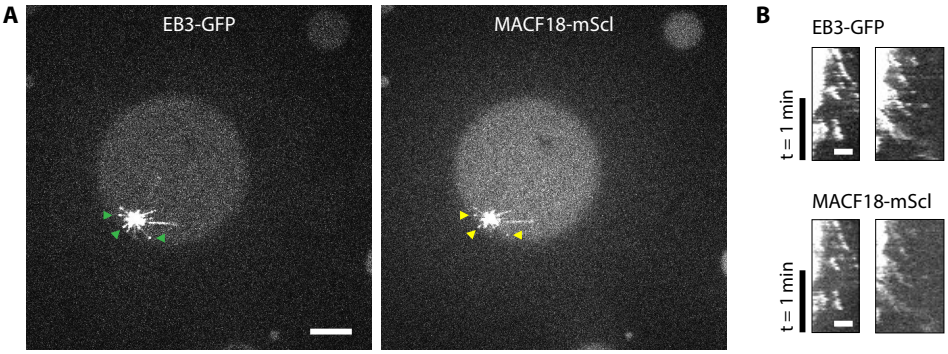

Figure 5.14: **(A)** Comparison of EB3-GFP (left, green arrows) and MACF18-mScarlet (right, yellow arrows) protein comets inside water-in-oil emulsion droplets. These images are cross-sections of the droplets, and scalebars are 10 µm. **(B)** Kymographs of EB3-GFP and MACF18 proteins comets inside emulsion droplets. Scalebars are 5 µm.

After aforementioned optimization experiments, we encapsulated MT asters, π-EB1 and MACF18 in emulsion droplets with increased KCl concentration of 75 mM (Fig. 5.16A). Unfortunably, no MACF18 comets were observed. This could either mean that the visibility was too low to distinguish the comets, or that no comets were present at all.

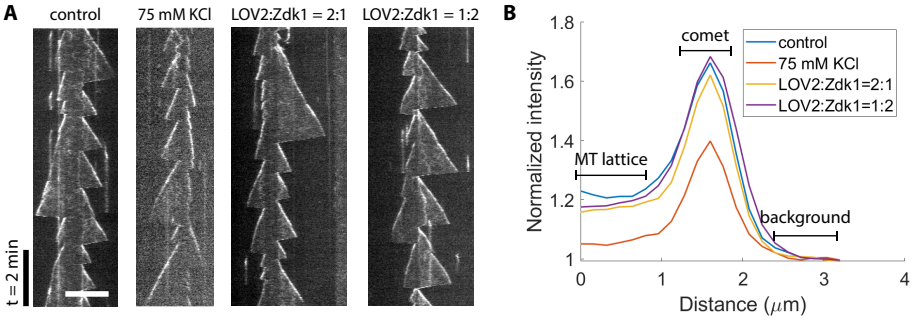

Figure 5.15: **(A)** Kymographs showing the binding of MACF18 to MTs in the presence of π-EB1 under varying conditions: 1) control with 50 mM KCl, 200 nM MACF18, 200 nM EB1-LOV2, 200 nM EB1-Zdk1, 2) with additional KCl, 3) with 100 nM EB1-Zdk1, 4) with 100 nM EB1-LOV2. The MACF18 signal is shown and the scalebar is 10 µm. **(B)** Averaged linescans ($N = 20$) in kymographs along lines like the pink dotted one to compare the MACF18 intensity on MT lattice and tip in the four different experimental conditions.

Another observation was the absence of MACF18 binding to the AurkA bead which functions as a MTOC. In the experiment with EB3 we observed a strong signal of both EB3 and MACF18 on the bead (Fig. 5.14), and also in previous experiments (for example Fig. 4.3 and Fig. 4.6) this affinity for the bead was clear. Our hypothesis was that EB3 has affinity for the centrosomal proteins at the surface of the bead (Sec. 2.2.2). The absence of MACF18 on the beads in Fig. 5.16 could mean that π-EB1 did not have affinity for the centrosomal proteins on the bead. Experiments with centrosomes, EB3

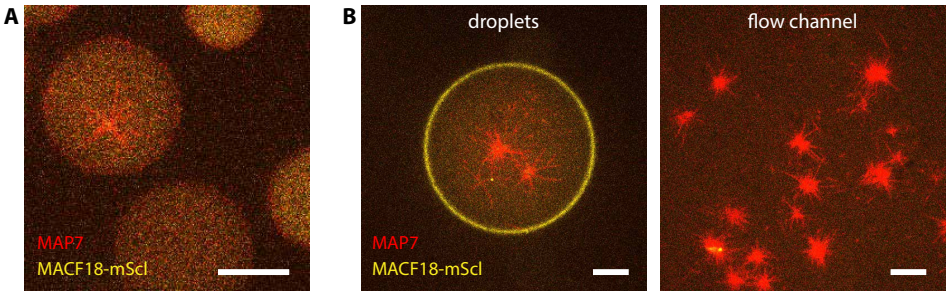

Figure 5.16: **(A)** Cross-section of water-in-oil emulsion droplets with DOPS lipids in the cortex. Droplets contained MT asters (red), π-EB1 and MACF18 (yellow) in solution. No protein comets were observed and no MACF18 was bound to the beads like in Fig. 5.14. **(B)** Comparison of the affinity of π-EB1 for AurkA beads in droplets (left, cross-section) and channels (right), visualized through MACF18 (yellow). The droplets are prepared with DGS-NTA lipids, such that most MACF18 binds to the cortex. No MACF18 affinity for the AurkA beads was observed either in channels or droplets, and also in this experiment no MACF18 comets were visible. Scalebars are 10 µm.

or π-EB1 and MACF43-mCherry also showed a higher accumulation of MACF43 on the centrosome in the presence of EB3 compared to π-EB1 (Fig. 5.17). Another possible explanation was that π-EB1 was inactive once encapsulated in emulsion droplets. We tested this explanation by comparing channels and droplets (Fig. 5.16B), where we observed no affinity for the beads both in channels and droplets. So we concluded that the fact that π-EB1 lacked affinity for the AurkA beads was not a result of encapsulation in droplets but rather a property of the protein, which has lower binding affinity to centrosomal proteins on the beads than EB3.

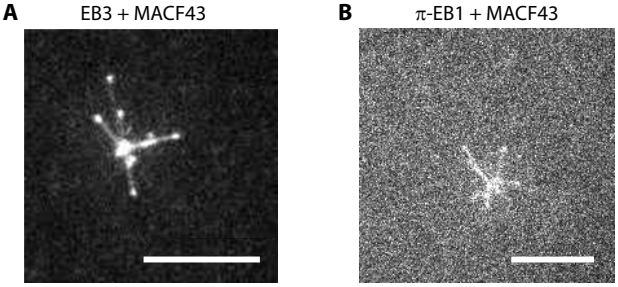

Figure 5.17: Flow channel experiments with centrosomes as MTOCs. MACF43-mCherry signal (greyscale) on MTs and centrosomes in the presence of EB3 **(A)** and π-EB1 **(B)**. The overall intensity of MACF43 was higher in (A), but nevertheless the binding of MACF43 to the centrosome seemed higher in the presence of EB3 than π-EB1. Scalebars are 10 µm.

To check the activity of the π-EB1 inside emulsion droplets, we encapsulated GTPγS-MTs together with π-EB1 and MACF18 (Fig. 5.18). MTs were nucleated from GMPCPP-stabilized seeds instead of AurkA beads for reasons explained in the discussion. Histidine-tagged MACF18 was recruited to DGS-NTA lipids in the droplet cortex, and we observed MTs being tethered to the cortex through π-EB1 and MACF18 on the MT lattice, comparable to the observations in Chapter 4 for MACF43. To follow the MT-cortex

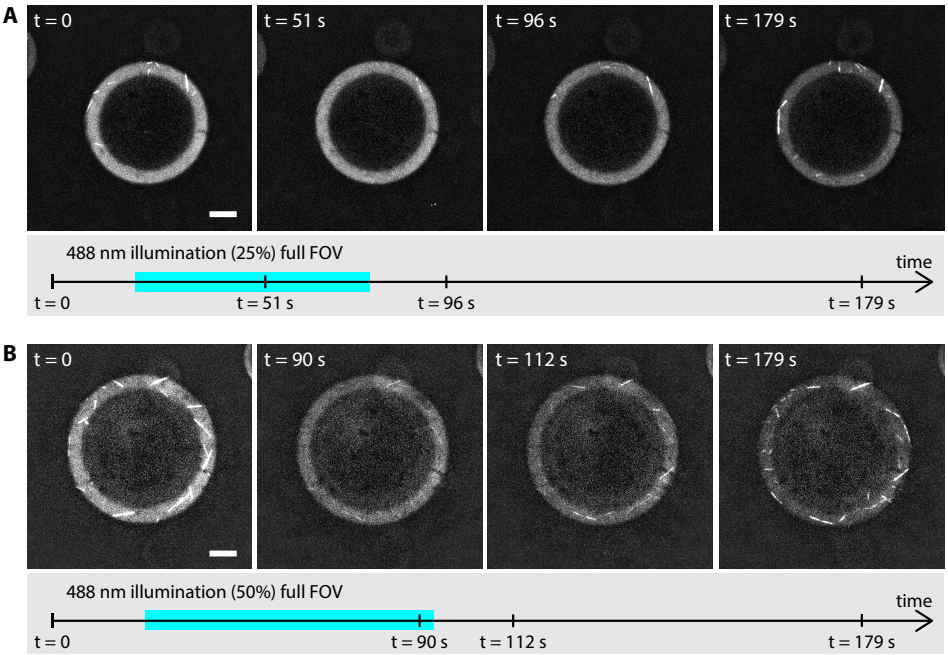

Figure 5.18: Verification of the activity of π-EB1 proteins after encapsulation inside water-in-oil emulsion droplets through MACF18 (shown in greyscale). **(A)** and **(B)** show z-projections of two different droplets at different timepoints before, during and after exposure to 488 nm light. GMPCPP-stabilized MT seeds nucleated GTPγS-MTs, which provided π-EB1 binding sites on the MT lattice. Histidine-tagged MACF18 is bound to DGS-NTA lipids in the cortex, and could bind transiently to π-EB1. When π-EB1 was active, cortical MACF18 was bound to the MTs ($t = 0$). Upon exposure to 488 nm light, π-EB1 fell apart and the connection between cortical MACF18 and MTs was mostly lost. After switching off the 488 nm light, π-EB1 returned to its active state and cortical MACF18 was decorating MTs again. Scalebars are 10 µm.

tethering through MACF18, we acquired a z-stack of part of the droplet on each timepoint of the timelapse and projected the 3D stack of each timepoint onto one 2D plane (like on p. 66). In Figure 5.18 we show those projections where bright lines of MACF18 at the droplet cortex reveal where MTs were bound to cortical MACF18. Upon illumination with 488 nm light, π-EB1 fell apart and MACF18 dissociated almost completely from the MTs (Fig. 5.18). After switching off the 488 nm light, MACF18 returned to the MTs, indicating a recovery of the π-EB1 protein. We also observed significant bleaching of the MACF18 protein over time in Fig. 5.18. Bleaching of MACF18-mScarlet was stronger than of MACF18-GFP which we used in Chapter 4.

After verifying the activity of π-EB1 inside emulsion droplets, we made first steps towards using π-EB1 to switch the interaction between MT ends and the droplet cortex on and off. To this end, AurkA beads, tubulin, GTP, π-EB1 and MACF18 were encapsulated in droplets with DGS-NTA lipids in the cortex. We were looking for hotspots of cortical MACF18 on sites where MT ends were in contact with the cortex like we observed in Chapter 4. However, only in a few cases we observed potential hotspots (Fig.

5.19). Even these potential hotspots were faint and only visible at one timepoint of the image acquisition, which is much shorter than the $T_{tip} = 65 \pm 47$ s tethering duration for EB3 and cortical MACF18-GFP measured in Chapter 4. Because they lasted such a short time, we could not be sure that they were indeed hotspots at MT tips and not random accumulations of cortical MACF18 that happened to be close to a MT tip.

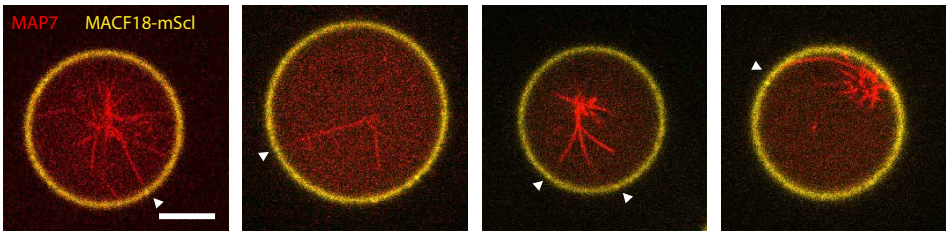

Figure 5.19: Cross sections of droplets containing MT asters (red), π-EB1 and MACF18 (yellow). The latter was bound to DGS-NTA lipids in the cortex. The white arrows indicate what might be hotspots of cortical MACF18 at the site where a MT tip touches the cortex. Scalebar is 10 µm.

Summarizing, we demonstrated that π-EB1 proteins were active inside water-in-oil emulsion droplets. Upon 488 nm light exposure of π-EB1 on GTPγS-MTs, MACF18 dissociated from the MT lattice and returned after switching off the 488 nm light. However, with dynamics GTP-MTs we observed that MACF18-mScI protein comets in droplets were only visible in combination with EB3, but too faint to observe with π-EB1. Additional fine-tuning will be needed to increase the MACF18 comet visibility. In emulsion droplets with DGS-NTA lipids in the cortex that bound MACF18, only faint hotspots were observed for very short durations that might or might not be the result of π-EB1-mediated interactions between MT tips and the droplet cortex.

5.4. DISCUSSION

IN this chapter, we explored the feasibility of optocontrol as a local, reversible on-off switch for the interactions between MTs and cortical +TIPs *in vitro* that we observed in Chapter 4. Two approaches were studied: light-induced recruitment of +TIPs to the cortex through iLID-SspB interactions and a photodissociable end-binding protein (π-EB1) in combination with cortical +TIPs. The iLID-SspB approach was promising, and we achieved local recruitment of the SspB upon local UV illumination of cortical iLID. However, reproducible recruitment of biotin-iLID to the droplet cortex remained a problem and thus we switched to the π-EB1 approach. Characterization of π-EB1 in flow channels provided information on its influence on MT dynamics, the typical timescales of light-response and the influence of UV laser power. We demonstrated local, reversible dissociation of MACF18 to MTs through the π-EB1 in flow channels, we visualized MACF18 comets inside water-in-oil emulsion droplets and we found that the interaction between MTs and cortical MACF18 through π-EB1 was not strong enough to result in clear MACF18 hotspots under the current conditions. Yet it was promising that π-EB1 was active inside emulsion droplets and could reversibly switch the interaction between cortical MACF18 and GTPγS-MTs on and off.

In the experiments with biotin-iLID at the droplet cortex and SspB-mCh in solution, we observed some SspB-mCh at the cortex even without activation of iLID. There could be a couple of reasons for this dark-state binding. First of all, many proteins bind aspecifically to the water-oil interface, despite the presence of phospholipids and surfactants. In the experiments with biotinyl cap PE lipids we left out the surfactant Tween20 to increase specific binding of streptavidin to the biotinyl cap PE lipids (as discussed in Sec. 2.3). As a consequence, aspecific binding of proteins to the water-oil interface was slightly increased. This aspecific binding was most likely the main reason for the dark-state binding of SspB-mCh to the cortex. Another small factor could be the nonzero dark-state interaction between iLID and SspB: we expect a minor fraction of iLID to be active in the dark. Thirdly, experiments in flow channels have revealed that iLID can become permanently active [Kok, 2019] as a result of high activation laser powers. A very small fraction of the cortical iLID might have been permanently active and therefore recruited SspB to the cortex even in the dark. Despite the fact that some SspB was bound before iLID activation, the increase upon activation was large enough to detect.

The recruitment of SspB to cortical iLID in droplets was 2-3 times higher for continuous activation during 30 s than for one localized pulse illumination (compare Fig. 5.6A,B with Fig. 5.6C,D). The main reason for this difference was the duration of the illumination. During 488 nm exposure, photons with 2.54 eV energy could activate iLID molecules. A short pulse only activated once and the SspB recruitment initially increased, then flattened off and later decreased when iLID molecules decayed towards the inactive state. Continuous illumination with 488 nm light reactivated the iLID molecules that decayed to the inactive state, preventing the flattening off and decrease of SspB recruitment. Another reason for the difference in SspB recruitment was diffusion of the phospholipids in the cortex to which iLID was binding. For continuous 488 nm illumination of the whole droplet, 2D diffusion of activated cortical iLID did not change local recruitment of SspB. But after local activation of cortical iLID however, those activated molecules could diffuse out of the activation region, decreasing the SspB recruitment within that region and increasing it outside of it. Indeed we observed a minor increase in cortical SspB outside the activated area (Fig. 5.6D). A final reason was that continuous illumination of the full field of view was performed with the 488 nm spinning disc laser, while local illumination was only possible with the FRAP laser. Different lasers have different powers, so separate fine-tuning of FRAP laser power and exposure times would be necessary to optimize the efficiency of local iLID activation.

The main problem with the iLID-SspB strategy for optocontrol in droplets was the limited recruitment of biotin-iLID to biotinyl cap PE lipids in the droplet cortex. We observed large differences in the recruitment of iLID from different purifications. Because all purifications followed the same protocol, it is unclear why one batch resulted in good iLID binding to the cortex and hence nice light-induced recruitment of SspB to the cortex while the next batch resulted in no recruitment at all. Different biotinylization methods were tried, without improvement of reproducibility. Also the possibility of histidine-tagged iLID binding to DGS-NTA lipids in the cortex was explored without

success. Efficient recruitment of iLID to the droplet cortex is still an ongoing project in the lab, but in the meantime we switched to the photo-dissociable EB1 protein which was published in 2018 [van Haren et al., 2018].

During characterization of MACF18 and π-EB1, we observed that MACF18 by itself did not interact with MTs, it needed an end-binding protein like EB3 or π-EB1. End-binding proteins are expected to bind only the growing MT tips, but we also observed a relatively high amount of MT lattice binding in Fig. 5.8A. The lattice binding of EB3 was an effect of the high protein concentration (200 nM), because for 50 nM the proteins only interacted with the MT tips (data not shown). For π-EB1 however, the affinity for the MT lattice is higher than for EB3 while the tip affinity was 2.2 times less (Fig. 5.8B). As a consequence, the MACF18 proteins comets at MT tips were less visible, which proved to be a problem later on in emulsion droplets where the visibility is decreased because of reduced resolution.

In Fig. 5.8 we showed that the MT growth velocity is slightly different for EB3 and π-EB1, with or without MACF18. All MT growth velocity distributions however were very similar (table 5.2). The major uncertainty in MT growth velocity determination arose in measuring the slope of growing MTs in kymographs. We estimated this uncertainty by propagation of the error in manual determination of the slopes of the growth traces in kymographs. For an error in the slope determination of 2°, the error in the growth velocity was 0.3 µm/min. Taking that error into account, the differences in growth velocities between EB3 and π-EB1 were not significant. However, the difference in growth velocity with and without MACF18 was significant. Why the MT growth velocity was slightly higher in the presence of MACF18 is unclear.

Proteins	v_{growth} **(µm/min)**
MACF18 only	2.3 ± 0.5
EB3	3.8 ± 0.4
EB3 + MACF18	3.9 ± 0.5
π-EB1	3.7 ± 0.5
π-EB1 + MACF18	4.2 ± 0.5

Table 5.2: MT growth velocities for different protein combinations.

Another interesting observation from the MT growth velocities concerned the effect of MACF18. In Fig. 5.8 the presence of MACF18 slightly increased the growth velocity. In Fig. 5.9 however, we did not measure a difference between EB1-LOV2 only (where no interaction between MTs and MACF18 was visible) and EB1-LOV2 plus EB1-Zdk1 (where clear interaction of MACF18 with MTs was observed). These results seem contradicting. The most logical explanation is that there was some interaction of MACF18 with MTs in absence of EB1-Zdk1, even though we did not observe it. Repetition of the control experiments should clarify this.

For characterization of the light-response of π-EB1, we fitted the dissociation of EB1-Zdk1 from EB1-LOV2 upon blue light exposure and obtained a measure for the dissociation rate (Fig. 5.11). The reported half-time of < 200 ms for dissociation by van Haren

et al. [van Haren et al., 2018] is 10x faster than the half-time of 2 s that we measured. The dissociation rate is determined by the unfolding time of the Jα-helix. Since van Haren et al. studied the protein *in vivo* and we *in vitro*, some differences in timescales were not surprising. We also measured a 2x longer association time ($\approx$ 150 s to full recovery) than van Haren et al. ($\approx$ 70 s). An unexpected difference was the delay we observed between switching off the 488 nm light and the start of the recovery. For van Haren et al. the recovery was exponentially increasing, with the steepest part of the recovery curve at $t = 0$. We explained the delay by the time EB1-LOV2 needs to return to its active state by refolding of the Jα-helix. The absence of a visible delay in the data from van Haren suggests that refolding of the Jα-helix is slower *in vitro* than *in vivo*.

A puzzling observation was the higher intensity of MACF18 on MTs after exposure of π-EB1 to 488 nm light than before (Fig. 5.12). Even for repeated exposure the MACF18 intensity on the MTs was higher after each cycle, although the difference per cycle was getting smaller. One hypothesis was that for part of the EB1-LOV2 molecules, the Jα-helix is improperly folded. Unfolding by UV light and refolding afterwards may lead to a higher fraction of active EB1-LOV2 and thus to a higher recruitment of EB1-Zdk1 and MACF18 to the MTs. For this hypothesis to hold, EB1-LOV2 molecules in solution should be affected by the 488 nm light as well, because of the rapid binding and unbinding of EB1-LOV2 to MTs (expected to be around 0.8 s^{-1} as for EB3, see table 4.1 on p. 64).

One of the major problems in droplets is always the visibility of our protein of interest. GFP-labeled proteins are preferred due to the brightness of GFP. However, imaging GFP with 488 nm would deactivate the π-EB1, so we needed a different fluorescent protein. We chose mScarlet because it was reported to have high brightness. Indeed, mScarlet was bright enough to visualize MACF18 protein comets inside water-in-oil emulsion droplets. But only under the condition that the comets were large.
Unfortunately, a couple of factors decreased the MACF18 comet visibility. We knew from flow channels that the MACF18 comet visibility is worse with π-EB1 than with EB3. In addition, when using MAP7 to label MTs, which is known from previous experiments (Chapter 3) to decrease comet size compared to fluorescent tubulin, we could detect vague EB3-GFP comets, but no MACF18 comets. A quick check in flow channels with GTPγS-MTs, π-EB1 and MACF18 showed that the π-EB1-mediated binding of MACF18 to the MTs is highly decreased upon addition of MAP7 (Fig. 5.20). But to observe a connection between MT tip and cortical MACF18, MAP7 is indispensible for good visibility of MTs inside emulsion droplets. Optimization of comet visibility by changing salt concentration or EB1-LOV2:EB1-Zdk1 ratio did not have enough success. Therefore further optimization will be required.

The experience from Chapter 4 was that cortical MACF18 hotspots at sites of MT-cortex contact were easier to visualize than free MACF18 comets on growing MT tips because their movements are restricted by the connection to phospholipids in the droplet cortex. We tested if perhaps we could establish and visualize the interaction between MTs and droplet cortex through π-EB1 and cortical MACF18 (Fig. 5.16B) despite the previously mentioned deterioration of the hotspot signal by π-EB1 and MAP7.

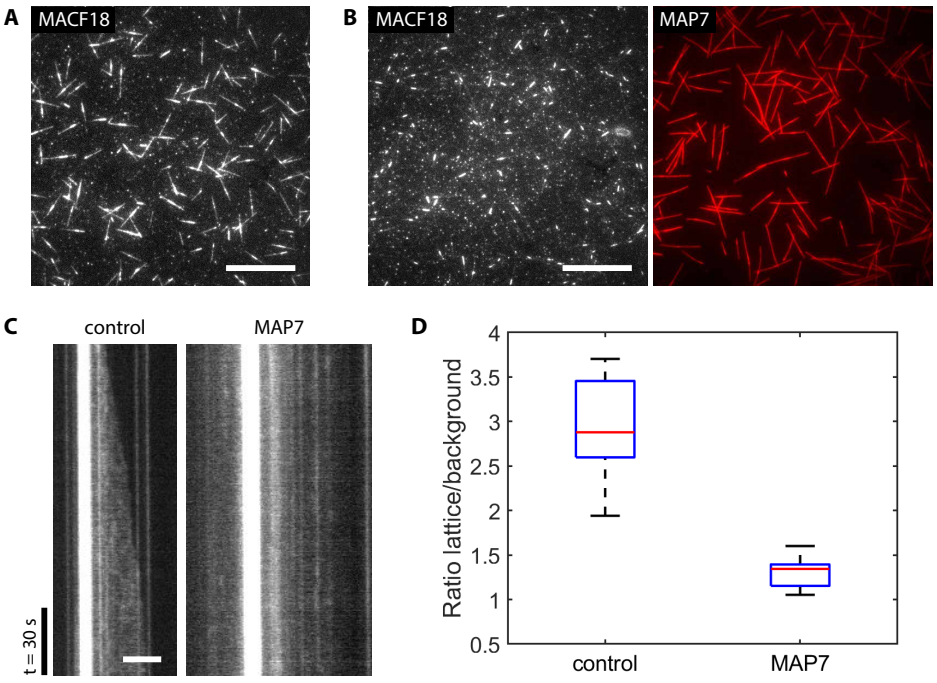

Figure 5.20: Comparison of the MACF18 visibility under two different conditions: 1. control experiment with GTPγS, π-EB1 and MACF18; 2. with additional MAP7 for MT visualization. **(A)** Control experiment: for GTPγS-MTs, MACF18 (greyscale) was well visible on both sides of the GMPCPP seeds (brighter part in center of each MT). Scalebar is 20 µm. **(B)** When using MAP7 (red) for MT visualization, the MACF18 (greyscale) visibility was highly reduced compared to (A). **(C)** Kymographs of the two conditions. Scalebar is 5 µm. **(D)** Ratio of the MACF18 signal on the MT lattice compared to the background signal for the two conditions.

The results were not conclusive, because only a few potential hotspots were observed, which were faint, lasted a very short time and for which it was not convincing that the hotspot was actually at the same site as the MT tip (Fig. 5.19).
In Chapter 4 we demonstrated that in the presence of MT-cortex tethering through cortical MACF18, MT asters were on average located closer to the droplet cortex and closer to the bottom of the droplet then without tethering. In this chapter with π-EB1 and cortical MACF18, MT asters were mostly observed around the center of the droplet, suggesting no or very weak interactions between MTs and droplet cortex.

Summarizing, it was not clear whether no hotspots were present at all or whether they were present yet not bright enough. Therefore it was not possible to test the photodissociable properties of π-EB1 inside emulsion droplets with MT asters. However, experiments with GTPγS-MTs nucleating from GMPCPP seeds inside emulsion droplets proved that π-EB1 is active inside droplets. So it could potentially function as an external cue to locally and reversibly switch the interaction between MTs and droplet cortex on and off in a minimal system. Further optimization of many components in the reaction mix (e.g. concentrations of tubulin, EB1-LOV2, EB1-Zdk1, MACF18 and

KCl) will be needed to visualize potential hotspots with π-EB1 and verify the effect of photodissociation.

5.5. METHODS

MOST of the methods are as described in Chapter 2. In this section we only list the conditions, additional methods and data analysis that are specific for the experiments in this chapter.

5.5.1. PROTEIN PURIFICATION

All proteins used for this chapter were obtained from the sources listed in Sec. 2.2.4.

PHOTO-DISSOCIABLE EB1

EB1-LOV2 and EB1-Zdk1 were designed by van Haren et al. [van Haren et al., 2018] and purified inhouse from E. coli ER2566 cells. The plasmids were a kind gift from Jeffrey van Haren. More details on the EB1-LOV2 and EB1-Zdk1 constructs can be found in their paper.

5.5.2. EMULSION DROPLETS

Two different lipid mixes were used, both prepared as explained in Sec. 2.1. One was prepared with biotinyl cap PE lipids (Sec. 2.3) for recruitment of biotin-iLID. The other one contained DGS-NTA lipids for recruitment of histidine-tagged MACF18-mScI.

5.6. DATA ANALYSIS

THE background was subtracted with ImageJ data processing tools. To make kymographs, we drew lines of 5 pixels width and used the ImageJ plugin *KymoResliceWide*. Next, analysis of the MT dynamics and intensities over time upon (de)activation were performed with ImageJ and Matlab. For fitting of of curves with a certain equation, we used the Matlab *fit* function. The 95% confidence bounds were used as the error on the fitted values.

5.6.1. REACTION SCHEME OF PD-EB1

We wrote down a reaction scheme for the interactions of EB1-LOV2, EB1-Zdk1 and MACF18 (Fig. 5.21), and made a couple of assumptions for the reactions:

1. MACF18 can bind with the same affinity to both free EB1-Zdk1 molecules and EB1-Zdk1 molecules which are bound to EB1-LOV2.

2. Light-induced inactivation of EB1-LOV2 is instantaneous, meaning that $k_{dissociate}$ is very large.

3. The on-rate for binding of EB1-Zdk1 to inactive EB1-LOV2 (k_{on}) is very low compared to the rate for active EB1-LOV2 (k^*_{on}).

4. Diffusion of molecules is very fast, so the kinetics are limited by the reaction rates and not by diffusion.

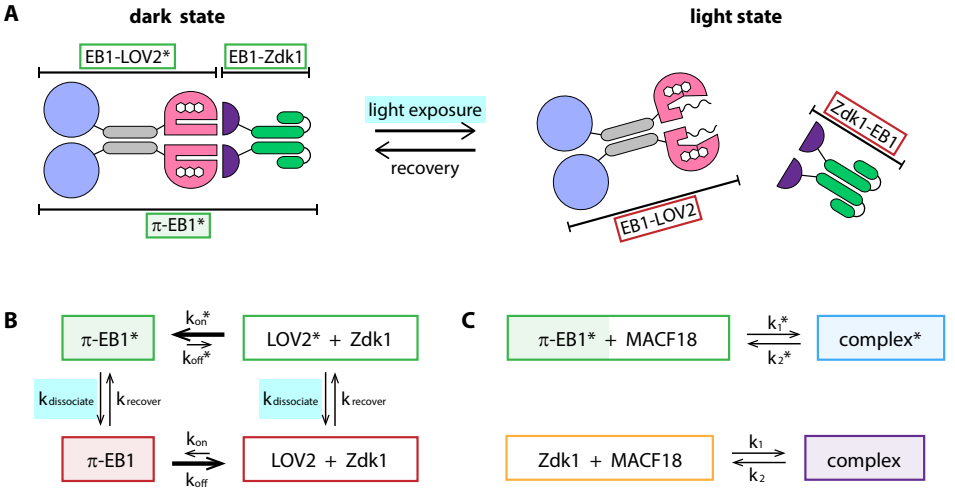

Figure 5.21: (A) Schematic illustration of the light-response of π-EB1, adapted from [van Haren et al., 2018]. Upon illumination with blue light, π-EB1 dissociates into EB1-LOV2 and EB1-Zdk1. In absence of blue light, the EB1-LOV2 recovers and can bind EB1-Zdk1 to form π-EB1. **(B)** Reaction scheme of EB1-LOV2 (called **LOV2** in this figure for simplicity), EB1-Zdk1 (**Zdk1**)and π-EB1. The active proteins are indicated with an asterisk (*). Upon exposure of EB1-LOV2 to blue light, it deactivates and as a consequence the binding affinity to EB1-Zdk1 is greatly reduced. **(C)** Reaction scheme of the interaction between π-EB1 or free EB1-Zdk1 with MACF18.

LIGHT-INDUCED INACTIVATION OF π-EB1

In absence of 488 nm light, practically all EB1-LOV2 molecules on the GTPγS-MTs were active, and the system was in equilibrium. Upon illumination with 488 nm light, we observed a rapid exponential decrease of the MACF18 signal on the MTs (Fig. 5.11). This is the result of the instantaneous inactivation of π-EB1 ($k_{dissociate}$) and subsequent unbinding of EB1-Zdk1 from EB1-LOV2 (k_{off}). In Fig. 5.11C we observed that the exponential decrease of MACF18 signal on the MTs depended on 488 nm laser power. For lower laser powers, the decrease was slower. However, we assumed both instantaneous dissociation ($k_{dissociate} >> k_{off}$) and a k_{off} that is independent of laser power, so the power dependence must come from another factor. This factor is a power-dependent delay (τ_{delay}) caused by insufficient 488 nm photons to deactivate all EB1-LOV2 molecules instantaneously. The typical timescale τ for dissociation

of EB1-Zdk1 upon blue light exposure can be described by

$$\tau = \frac{1}{k} = \tau_{off} + \tau_{delay} = \frac{1}{k_{off}} + \tau_{delay} \tag{5.2}$$

with $\tau_{off} = 1/k_{off}$. The rate k in this equation can be used to fit the exponential decay of the MACF18 signal upon deactivation of π-EB1:

$$I(t) = I_1 + I_2 \cdot exp(-kt) = I_1 + I_2 \cdot exp(-t/\tau). \tag{5.3}$$

Combining the two equations gives

$$I(t) = I_1 + I_2 \cdot exp\left(-\left(\frac{k_{off}}{1 + k_{off}\tau_{delay}}\right)t\right). \tag{5.4}$$

For low laser powers, τ_{delay} is significant, which results in slower decrease of $I(t)$. When the laser power is high and the photon flux is sufficient to deactivate all EB1-LOV2 at once, $\tau_{delay} \rightarrow 0$ and $k \rightarrow k_{off}$.

RECOVERY OF π-EB1 AFTER LIGHT EXPOSURE

After switching off the 488 nm light, the MACF18 signal on the MTs slowly recovered (Fig. 5.11). The observed delay was caused by the time EB1-LOV2 needs to become active again (see discussion) before it can bind EB1-Zdk1. After this initial delay, we observed an exponentially increasing MACF18 signal on the MTs. The increase is characterized by a combination of $k_{recover}$, $k_{on}*$ and k_{off}.

The recovery of mScarlet signal on the MTs after bleaching with a 561 nm laser pulse is the effect of several processes combined. First of all the MACF18 molecules bind only transiently to EB1-Zdk1, secondly π-EB1 binds transiently to the MTs and finally the interaction between active EB1-LOV2 and EB1-Zdk1 (with MACF18) is transient. Photobleaching the mScarlet signal on MTs results in an exponential recovery, and the recovery rate depends on the aforementioned three processes. With the current version of our proteins it is not possible to separate the processes. Addition of histidine-tags or biotin-tags to the proteins and fluorescent markers on both EB1-LOV2 and EB1-Zdk1 can solve this problem. These tags would allow non-transient binding of proteins to a functionalized glass surface and direct observation of all molecules to measure binding kinetics by FRAP experiments.

AUTHOR CONTRIBUTIONS

K.V. wrote the chapter and performed most experiments in this chapter. M.K. performed quantitative characterization of iLID-SspB interactions. N.A. was the first in our lab to test π-EB1 *in vitro*. E.B. did the characterization of π-EB1 in combination with centrosomes. A.D. and E.vd.S. purified the light-sensitive proteins. M.D. supervised the project.

6

THEORETICAL MODELS ON CELL POLARITY

Iedereen zag er anders uit, maar niet onherkenbaar.
Zelfs de olifant met stekels, kleine roze oren, een snavel
en honderd korte benen was de olifant, ook al zong hij
een weemoedig lied en dreef hij op zijn rug in het water.

Toon Tellegen

Knowledge of a cellular process generally comes from a combination of in vivo, in vitro and theoretical studies. For the reconstitution of a minimal system for microtubule-based cell polarity we need information from all three types of studies. In this chapter, we compare the predictions of a few theoretical models on the mechanisms of spontaneous cell polarity establishment by cytoskeletal filaments. We consider the differences and similarities with our reconstituted minimal system. Next, we discuss how we can use the predictions to improve our minimal system, and how we could use our minimal system to test the theoretical models.

6.1. INTRODUCTION

LIKE all cellular processes, cell polarity is the result of a complex interplay of many components and regulators. We discussed our goal to establish a minimal system for MT-based cell polarity in the general introduction of this thesis (Chapter 1). Such a minimal system was defined as a MT-based asymmetric accumulation of proteins at the periphery of a 3D confinement, reconstituted with the smallest possible number of components. A thorough understanding of the important components and interactions for cell polarity is needed to accomplish such a minimal system. This understanding comes from a combination of *in vivo*, *in vitro* and theoretical work [Vendel et al., 2019]. As discussed in Chapter 1, *in vivo* studies revealed many of the components that are involved in cell polarity, such as MTs, MT-associated proteins (MAPs), regulatory proteins and the cell membrane. In addition, *in vitro* experiments provided qualitative and quantitative information on the molecular mechanisms, for example on the effect of specific MAPs on MTs. Finally, theoretical models need to be part of the picture, as they provide predictions on the minimally needed mechanisms to achieve polarity. In this chapter, we discuss a few theoretical models for MT-based cell polarity in more detail. They provide possible answers to the question what is minimally needed to establish cell polarity. We compare the assumptions and conditions of the different models with our experiments, and discuss how we can use this to design and fine-tune future experiments.

6.2. THEORETICAL MODELS ON MICROTUBULE-BASED CELL POLARITY

IN cells, symmetry breaking or cell polarity is the result of reaction-diffusion based mechanisms, active transport-based mechanisms or a combination of both. In reaction–diffusion systems, chemical reactions and diffusion of components are responsible for pattern formation. In active transport-based systems, components are transported by cytoskeletal filaments like microtubules (MTs) or actin filaments. Already in 1952, Turing wrote about reaction-diffusion mechanisms as the chemical basis of pattern formation [Turing, 1952]. Since then, many models have been designed, varying from mechanistic to conceptual, and from focused on specific molecular interactions to very broad describing general mechanisms (for a review, see [Mogilner et al., 2012]). In this section we will discuss some theoretical models that describe a system similar to the minimal system we have in mind. A major difference is that in most of these models the so-called polarity factors (PFs) are actively transported along the MTs, while cortical polarity factors interact with MT tips through end-binding proteins in our experimental system. Models with the latter interaction are in progress. But because active transport is one of our future directions, we will discuss the models on polarity establishment based on active transport by MTs as well.

FISSION YEAST MODEL

One model exists on the effect of cortical PFs that can diffuse and bind transiently to MT tips that arrive at the cortex of a fission yeast cell [Recouvreux et al., 2016]. A discrete 1D lattice represents the cortex, on which particles can diffuse by hopping left or right (Fig. 6.1). When a MT arrives at the cortex, PFs can transiently bind to the MT before it undergoes a catastrophe and disappears. Because the model was designed for fission yeast experiments, an elongated cell shape was adopted so MTs only arrived at the cell poles. Simulations showed that the number of particles at the cell pole was on average higher than at an equal area on the cell side. In other words, membrane diffusion of PFs combined with transient interaction of PFs with MT tips suffices to accumulate proteins at the cell poles, under the condition that the MT tip density is higher at the cell poles.

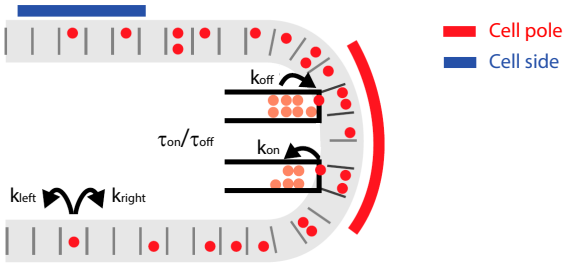

Figure 6.1: 1D model for PFs at the cortex of an elongated cell where MTs only touch the cell poles, from [Recouvreux et al., 2016]. Cortical PFs can diffuse on the cortex and interact transiently with MTs that touch the cortex. This sufficed to concentrate PFs at the cell poles compared to the cell sides.

MODELS FOR A SPHERICAL MINIMAL SYSTEM

Another type of models we want to discuss focus on cytoskeletal filaments and the implications of their geometrical organization for cell polarity [Hawkins et al., 2009, Calvez et al., 2012, Bressloff and Xu, 2015] (Fig. 6.2A). The group of Voituriez modeled a minimal system for cell polarity based on active transport of particles from cytoplasm to cell boundary by cytoskeletal filaments, followed by positive feedback between those particles and filament nucleation [Hawkins et al., 2009, Calvez et al., 2012]. Their observation was that the ability of the system to polarize spontaneously depends on the filament organization. A cortical organization with multiple nucleation points located at the membrane (like cortical actin, Fig. 6.2A bottom) can lead to spontaneous polarization. In contrast, radially organized filaments nucleating from one central point (like radial MTs nucleating from a centrosome, Fig. 6.2A top)) did not lead to spontaneous polarization, but did give an accurate response to external cues. The model from Bressloff and Xu [Bressloff and Xu, 2015] is very similar to the one from Hawkins et al. [Hawkins et al., 2009]. Only they modeled the signaling molecules as being inside vesicles and not as free particles. Those vesicles were transported along cytoskeletal filaments towards the cell membrane. Their conclusion too was that the system polarized spontaneously when filaments nucleated at the membrane, and it

polarized only upon an external cue when the filaments nucleated from one central point.

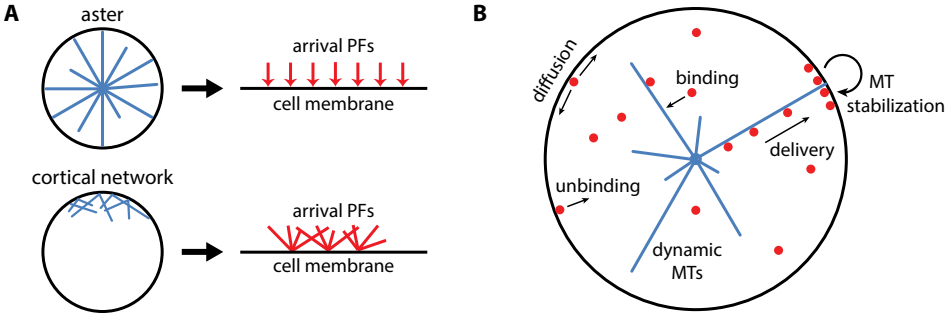

Figure 6.2: **(A)** Schematic of the two different cytoskeletal filament oranizations considered in de model from Hawkins et al. [Hawkins et al., 2009] and Bressloff and Xu [Bressloff and Xu, 2015]. One option is radial filament nucleation from one central point (top), like a MT aster. The other is a cortical filament arrangement (bottom), like an actin cortex. **(B)** Schematic representation of the minimal system modeled by Foteinopoulos and Mulder [Foteinopoulos and Mulder, 2017]: MT aster (blue) in a 3D confinement, and PFs (red) being transported with certain velocity along the MTs from the cytoplasm to the boundary. The local density of PFs at the boundary determines the local stability of MTs.

These models suggest that spontaneous polarization is impossible in a minimal system with radially organized MTs. However, the opposite conclusion was drawn by Foteinopoulos and Mulder who created an analytical model of a MT-based minimal system for spontaneous cell polarization in 3D [Foteinopoulos and Mulder, 2017]. Their minimal system is schematically shown in Fig. 6.2B and is relatively similar to the minimal system we explored in this thesis, with the difference that polarity factors (PFs) are transported along radially organized MTs from cytoplasm to cell membrane. The residence time of a MT at the membrane depends on the local concentration of PFs, leading to a positive feedback loop between MTs and PFs. The main difference between this model and the ones from Hawkins et al. and Bressloff and Xu was the non-linearity in the feedback between PFs and MTs. This non-linearity is based on Michaelis Menten reaction rates, which depend non-linearly on the substrate concentration. For this argument to hold, the principle of local activation and global inhibition is needed. Therefore the total number of PFs in the model was limited. When the number of PFs on the membrane locally increases, the total pool of PFs is depleted, which leads to global inhibition.

A related model comes from our collaborators Li and Ten Wolde (Fig. 6.3, unpublished work). The schematic picture of their model looks the same as for the Foteinopoulos model discussed before [Foteinopoulos and Mulder, 2017] (Fig. 6.2B). Radially organized MTs transport PFs towards the membrane, where the survival time of a MT at the membrane depends linearly on the PF concentration. Because they assume a linear relation, the system can not spontaneously polymerize without another source of non-linearity. One of the major differences between this model and the Foteinopoulos model is that the MT organizing center (MTOC) was fixed in the Fonteinopoulos model and it is free to move in this model. A MTOC tends to move around due to the

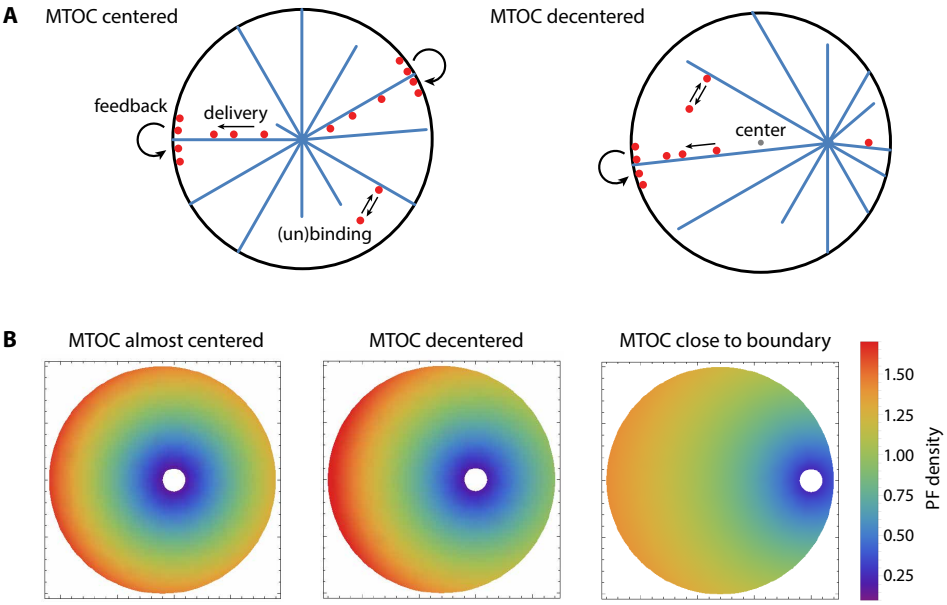

Figure 6.3: (A) Schematic representation of the model from Li and Ten Wolde: MT asters (blue) in a confinement with PFs (red) that are actively transported by MTs to the cortex. The antenna effect (longer MTs catch more PFs to transport) is illustrated for the situation that the MTOC is centered (left) or decentered (right), resulting in asymmetry of the MT lengths. **(B)** Density of polarity factors (PFs, in arbitrary units) in three different situations: (i) the MTOC is very close to the center of the spherical confinement, (ii) the MTOC is further away from the center and (iii) the MTOC is close to the boundary of the confinement.

force resulting from growing MTs that push against the boundaries of a confinement. Such pushing forces can lead to centering of the MT aster for short or intermediate MTs relative to the radius of the confinement [Holy et al., 1997, Laan et al., 2012a, Roth et al., 2019b]. But when MTs grow too long, they buckle and the MTOC steady state position is at the side of the confinement. When the MTOC is located off-center, the MTs on one side of the MTOC are longer than on the other side (Fig. 6.3A). Longer MTs collect more PFs from the cytoplasm because of the so-called antenna effect [Varga et al., 2006, 2009]. Therefore, longer MTs deliver more PFs to the membrane that stabilize the MT: a positive feedback loop. So the non-linearity in this system comes from the antenna effect combined with the possibility of off-center MTOC positioning. At the same time, the angular density of MTs is smaller for longer MTs. Smaller angular density means fewer MTs arriving at the membrane far away from the MTOC and thus fewer PFs being delivered. Fewer PFs means a shorter residence time of the MTs at the membrane: a negative feedback loop. But also, fewer MTs means lower force, so the MTOC could move more towards the center. Despite the competition between positive and negative feedback, simulations of their model showed that the non-linearity arising from the antenna effect combined with off-center MTOC positioning can be enough to result in a polarized distribution of PFs (Fig. 6.3B). However, note that these were simulations with fixed MTOC positions, not steady state solutions. Due to the

force of the MTs exerted on the MTOC, the MTOC might move away from or towards the confinement center, leading to a different PF distribution.

Summarizing, a non-linearity is required for spontaneous cytoskeleton-based symmetry breaking. A non-linearity can come from different sources, like the spatial organization of cytoskeletal filaments, non-linear feedback between PFs and MT stability (under the condition of local activation and global inhibition) or by the so-called antenna effect when the MTOC was allowed to be located off-center.

6.3. IMPLICATIONS FOR OUR *in vitro* MINIMAL SYSTEM

WHAT are the implications of the conclusions from theory for the design of our *in vitro* minimal system? Obviously there are many limitations when relating theoretical models to experimental data, because models rely on simplifying assumptions. A few examples of such assumptions are:

1. The MTOC position is fixed in the Foteinopoulos model, which is not representative for an experimental minimal system where the MTOC will move around as a result of diffusion and forces exerted by MTs pushing against the boundaries.
2. The MTs are infinitely rigid in both the model from Foteinopoulos as from Li and Ten Wolde, meaning that bending of MTs is not taken into account. Inside water-in-oil emulsion droplets, bending MTs are often observed when the MT length is long compared to the droplet radius. So only when we are in the regime of MT lengths shorter than the droplet radius, this is a realistic assumption.
3. No sliding of MTs at the point of contact with the boundary of the confinement is included. This effect was shown to play a role in MT aster positioning in confinement [Laan et al., 2012a, Pavin et al., 2012, Ma et al., 2014].

These assumptions are useful to be able to study one mechanism without interference of other processes. For example the possibility of a system with just MTs, directed transport of PFs and non-linear positive feedback to polarize. But as a consequence, the resulting model is not an accurate description of an experimentally feasible system. Some of the assumptions might enhance polarization establishment, while some others might inhibit it.

To get an idea of the applicability of a model, either the assumptions could be tested *in vitro* or *in vivo*, or the outcomes of the models could be compared with experimental data. In fact, our proposed minimal system could serve as a starting point to test the theoretical models. At the same time, we could use conclusions from the models to design future experiments.

6.3.1. FISSION YEAST MODEL

The experiment from Recouvreux et al. in fission yeast served as an inspiration for our reconstituted minimal system. The transient interaction between MT tips and dif-

fusing PFs at the cortex was shown to be sufficient to accumulate PFs at the poles of an elongated cell, both experimentally and by simulations. We employed a similar transient interaction between MT tips and cortical proteins. However, our confinement was spherical and not elongated, and the MTs were radially organized instead of linearly and predominantly along the long axis of the cell. We designed the minimal system in this way because we aim to study the general mechanisms behind MT-based cell polarity and not the specific fission yeast case. A question is whether the transient interaction between MT tips and cortical PFs is also sufficient in that situation to locally accumulate PFs.
So far, our experimental results suggested that this is not the case. A local accumulation of cortical PFs was observed when a MT touched the cortex, but only for the duration of the MT-cortex contact. This could be explained by the fact that the density of MT tips at the cortex is much higher in the elongated confinement than in the spherical one, especially because the size of our water-in-oil emulsion droplets was much larger than a fission yeast cell (Fig. 6.4). Another explanation could be that diffusion of PFs in the cortex was faster in our minimal system than in de model, so the equilibration of PFs is too fast to maintain the local accumulation when a MT detaches from the cortex.

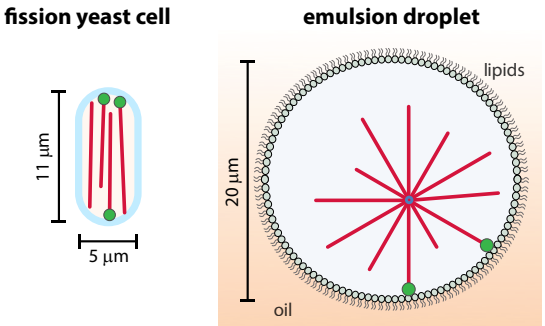

Figure 6.4: Comparison of the size and geometry of a typical fission yeast cell like those in the experiment and simulations of Recouvreux et al. [Recouvreux et al., 2016] (left) and a water-in-oil emulsion droplet like in our minimal system (right). MTs are shown in red and cortical PFs at the contact site between MTs and cortex in green.

6.3.2. MODELS FOR A SPHERICAL MINIMAL SYSTEM

Both the Foteinopoulos model [Foteinopoulos and Mulder, 2017] and the model from Li and Ten Wolde assume a spherical confinement with a MT aster as a basis, like we do *in vitro*. Also, we could consider the cortical +TIP peptides we used (like MACF18 and MACF43 in Chapter 4) as PFs. However, their findings could never be directly applicable to our current experimental system, because the PFs in the models are transported along the MTs like molecular motors and in our experiments the PFs only transiently interact with MT tips. We will discuss this and other differences between the models and our current experimental minimal system below.

THE TRANSPORTATION METHOD OF PFS BY MICROTUBULES

The major difference between the models and our current *in vitro* reconstitution is the transportation method of the PFs. In the theoretical models PFs are transported like molecular motors along the MT with a certain velocity. In contrast, cortical PFs interact with the MT tips through end-binding proteins in our water-in-oil emulsion droplets. The aforementioned antenna effect as a source of non-linearity will therefore not work. However, also in our minimal system there is a relation between the angular density of MTs at the boundary and the local density of PFs (the hotspots we found in Chapter 4). And the MTOC position was found to be influenced by MT-cortex interactions (Chapter 4): the MTOC was positioned closer to the cortex in presence of MT-cortex tethering and closer to the droplet center in absence of tethering. So in our system, tethering of a MT to the cortex by interaction with cortical PFs leads to both a local increase of the PF concentration and to repositioning of the MTOC towards the tethering location. The model from Li and Ten Wolde suggests that an off-center position of the MTOC combined with the antenna efect can lead to spontaneous cell polarity. Even though the antenna effect does not yet exist in our minimal system, off-center MTOC positioning combined with positive feedback between MT stability and cortical PFs might lead to a polarized PF distribution on the droplet cortex. Simulations of a system like this are on the list of future work to study the effect of off-center MTOC positioning combined with the interaction of MT tips and cortical PFs that increase the MT residence time.

IMPLEMENTING A POSITIVE FEEDBACK MECHANISM

An actual feedback mechanism between PFs at the cortex and the MT residence time was not yet incorporated in our system. When a MT reached the cortex, a local hotspot of cortical PF appeared at the tip, and disappeared as soon as the MT detached. The MT residence time at the droplet cortex seemed unaltered by the interaction with the cortex (Sec. 4.3.2). However, we did observe that the MT stability increased a lot (by reduction of catastrophes) when cortical PFs could interact with the whole MT lattice instead of only the tip (Sec. 4.3.2 and Sec. 4.3.3). In that case, MTs were bound to the cortex laterally and covered with the cortical PFs. One could argue that this situation with an asymmetric PF density and asymmetric MT aster positioning is similar to cell polarity. However, in cells the MTs are usually not observed to grow along the cell membrane (except for plant cells) and the PF density in polarized cells is not only increased at the MT contact sites. Therefore this is not the asymmetric PF distribution that we were aiming for in our minimal system.

LOCAL ACTIVATION, GLOBAL INHIBITION

In the Foteinopoulos model, the number of PFs was limited to ensure local activation and global inhibition [Foteinopoulos and Mulder, 2017]. Our experiments were performed with 300 nM cortical PFs. In a droplet of 10 μm radius, this means approximately 10^5 molecules. In principle, one MTOC can nucleate around 100 MTs. However, usually only a few MTs were in contact with the droplet cortex (Chapter 4). Each

MT tip can interact with several hundred PFs, but even then only a small fraction of the 10^5 cortical PFs is bound to a MT. So the protein concentration was too high and that might explain why we did not observe a global decrease of the cortical PF density when it was locally increased at the MT-cortex interaction site.

SPONTANEOUS POLARITY VERSUS EXTERNAL CUES

Finally, the models in this chapter discussed sources of non-linearity in the system to obtain spontaneous MT-based symmetry breaking. In many situations however, cells polarize in response to an external cue. Examples are chemical gradients originating from a food source or mating partner, and epithelial cells with the extra-cellular matrix on one side and an external environment on the other side. In those situations, polarization of the cell mainly means that the external asymmetry is transferred to the internal cellular level. In the example of epithelial cells, receptor proteins at the basal membrane (facing the extra-cellular matrix) will sense a different environment and hence respond differently than the receptors on the apical membrane (facing the external environment). Thus different signals will be transmitted and different regulatory mechanisms initiated, which will eventually lead to different proteins accumulating at the apical and basal membranes.
Polarization driven by an external cue was modeled to some extent by Hawkins et al. [Hawkins et al., 2009], who found that a radial MT organization could not lead to spontaneous cell polarization (assuming linear feedback between PFs and MTs) but it did lead to stable polarization in response to an external gradient. This suggests that the non-linearity is not required to polarize upon an external cue, in contrast to spontaneous cell polarity establishment. We can also compare the situation to elongated fission yeast cells, where the MTs predominantly orient along the long axis due to the geometrical asymmetry [Hagan and Hyams, 1988, Tran et al., 2001, Carazo-Salas and Nurse, 2006, Lagomarsino et al., 2007]. As a result, only active transport of proteins by MTs to the cell membrane is enough to achieve a polarized protein distribution, which is enhanced by positive feedback loops. These examples suggest that it is easier to reconstitute a system *in vitro* which polarizes in response to an external cue than spontaneously. Therefore, we worked on an artificial external cue *in vitro*. Optogenetics provides a method to locally and reversibly switch protein interactions on and off (Chapter 5).

6.4. CONCLUSION

IN summary, theoretical modeling on spontaneous cell polarity establishment by cytoskeletal filaments has shown that a non-linearity in the system is required. The origin of this non-linearity varied for the different models: cytoskeletal filament organization, feedback between PF density and MT stability or the so-called antenna effect combined with off-center positioning of MT asters. These differences mean that the mechanism of cell polarity is not yet fully understood. However, there may also be multiple non-linearities existing simultaneously, increasing the efficiency of the polarization.

Many similarities exist between our *in vitro* minimal system and the existing models, but none of the models really resembles our experimental conditions. We first discussed simulations of a fission yeast system where cortical PFs are accumulated at the cell pole by transient interaction between the PFs and MTs that touch the cortex [Recouvreux et al., 2016]. The interaction between PFs and MTs is similar to our minimal system, yet the geometry and size of elongated fission yeast cells is completely different from our emulsion droplets. The models from Foteinopoulos and Mulder and from Li and Ten Wolde did consider spherical confinements with radial MT aster, like we did in our minimal system. However, PFs in the model are transported like molecular motors along the MTs towards the cell membrane, where they influence the MT residence time and therefore the influx of PFs. In contrast, in our *in vitro* minimal system the PFs interacted transiently with MT tips through end-binding proteins. The transportation method of PFs was the main difference between our minimal system and these models, next to the presence of a positive feedback mechanism and local activation global inhibition effects.

We are planning to implement some changes in our experimental minimal system to increase the similarity with the models and hopefully be able to test some of the theoretical predictions and achieve a polarized PF distribution. In the next chapter we will elaborate on these proposed changes. In parallel, simulations that do not involve molecular motors for PF transport but transient interaction between PFs and the MT tip are on the list of future work. Such simulations would be more comparable to our current minimal system reconstitutions.

ACKNOWLEDGEMENTS

We thank Yao Li and Pieter Rein ten Wolde for their work on a model for MT-based cell polarity in a minimal system. We thank Bela Mulder for helpful discussions on the models for MT-based minimal cell polarity.

7

DISCUSSION AND OUTLOOK

'Dat wij hier zitten is een wonder,' zei de mier.
'Maar dát is op zichzelf nu juist weer heel gewoon.'

Toon Tellegen

A MYRIAD of organisms and cell types exist, all of them very different yet very similar at the same time. Despite their diverse appearances, proteins and functions, basic processes like energy consumption, synthesis of components, growth and reproduction are conserved in most cells. Also cell polarity, the subject of this thesis, is one of those conserved processes. Cell polarity refers to the spatial organization of cellular components (e.g. cytoskeleton, organelles, proteins, membrane domains) in a directional manner. It is needed to define the directionality of processes such as cell division, differentiation, motility and growth. For many decades, scientists have been looking for answers on the questions about cell polarity establishment and maintenance. How does budding yeast regulate where to form a bud? How can a nerve cell control in which direction to grow its axon? And how can an epithelial cell coordinate proper polarization in response to its extremely asymmetric external environment? The cells in these three examples employ a different set of proteins to establish cell polarity. Still, the underlying mechanisms are presumably the same. And that is what we aim to investigate: the underlying mechanisms of cell polarity establishment, with a focus on the role of microtubules (MTs). The ultimate tool for such a study is a minimal system. We defined minimal systems as "a subgroup of the *in vitro* methodology in which a particular cellular function is reconstituted with a minimal number of required components" [Vendel et al., 2019].

In this thesis, we worked on a bottom-up reconstituted minimal system for MT-based cell polarity. In Chapter 1, we reviewed how *in vivo*, *in vitro* and *in silico* studies con-

tributed to our current understanding of (MT-based) cell polarity. Using this knowledge, we formulated a simple design for our minimal system: MT asters were encapsulated inside water-in-oil emulsion droplets, and polarity factors (PFs) at the droplet cortex could interact with MT tips through end-binding proteins (EB). Once this minimal system is functional, the complexity can be increased step-by-step. Our system was not based on the specific polarity mechanism of a certain cell type, but aimed to investigate the more general mechanism behind polarity establishment by directed transport of PFs, combined with positive feedback. With this minimal system, we wanted to address questions like:

1. Can we locally accumulate cortical PFs by EB-mediated interactions between MT tips and cortical PFs?
2. Are those EB-mediated MT-cortex interactions enough for polarization or do we need molecular-motor based directed transport?
3. What is the role of positive feedback between PFs and MT dynamics?
4. Can spontaneous polarity happen or is an external cue required?

To reconstitute our proposed minimal system, we had to overcome some experimental challenges (Chapter 2). *In vitro* reconstitutions are very sensitive to experimental conditions, so we had to fine-tune protein concentrations, phospholipids in the cortex, surfactants to prevent aspecific interactions and fluorescent labels to increase the visibility inside emulsion droplets. One of the major changes compared to other *in vitro* reconstitutions with MTs was to use MAP7 as a tool for MT visualization (Chapter 3). This protein increased the signal-to-background ratio a lot, enabling us to visualize single MTs inside emulsion droplets all the way from MT organizing center to the droplet cortex. MAP7 also had a strong stabilizing effect on MTs, and we even ran into the unexpected observation that the MT depolymerization rate changed when the MT lattice was saturated with MAP7. Despite those effects of MAP7 on MT dynamics, we decided to use the protein in emulsion droplets, because the visibility of MTs was only good enough with MAP7 and not with fluorescent tubulin.

Our minimal system allowed MTs to interact with cortical MACF2-derived peptides (functioning as PFs) through EB (Chapter 4). Interestingly, captured MTs could locally accumulate cortical PFs, but only for the duration of the MT-cortex interaction. Two possible scenarios were observed: only the MT tip was captured by the +TIP, or also (part of) the MT lattice was captured. In the first scenario, capture of MT tips stabilized the MTOC position close to the droplet cortex. However, MT capture did not influence the MT residence time at the cortex, because positive feedback between local PF density and MT residence time was absent. In the second scenario, when the cortical PF had a MT lattice-affinity, we did observe a strong increase of the MT rescue rate leading to stabilized MTs. The duration of the MT residence time at the droplet cortex was independent of the local PF concentration. Theoretical models have shown that this feedback is required for polarity establishment (Chapter 6), so positive feedback will be one of the first things to add to our system.

In Chapter 6 we discussed the predictions of several models for spontaneous MT-

based cell polarity establishment, and the implications for future directions of our *in vitro* minimal system. The models suggest that a non-linearity in the system is needed to achieve spontaneous polarization, but the source of the non-linearity could be found in different aspects of the system. One of the applications of our *in vitro* minimal system will be to test assumptions and outcomes of theoretical modeling.
In parallel to spontaneous polarization, we worked on the implementation of an external cue. Cells often polarize in response to an external signal, like a chemical gradient. Optogenetics provide a local and reversible tool to switch specific interactions between proteins on and off. We tested two light-sensitive binding pairs *in vitro* and showed a local and reversible response of those proteins, even inside water-in-oil emulsion droplets (Chapter 5). However, further fine-tuning of the experimental conditions is needed before we can combine it with the EB-mediated MT-cortex interactions from Chapter 4.

Our *in vitro* reconstituded system is clearly not yet a minimal system for MT-based cell polarity. MT capture at the cortex through EB did locally accumulate PFs, but only for the duration of the contact. Different strategies are under consideration to achieve more persistent accumulation of PFs, which we will discuss hereafter.

FINE-TUNING OF THE CURRENT SYSTEM

Our reconstituted minimal system is not yet finished, the work is ongoing and more optimization is needed. First of all, we observed in Chapter 4 that MTs were quite short compared to the droplet radius, and the observed number of MTs growing from one MTOC was much lower than expected (about an order of magnitude). More and longer MTs would result in more MT tips reaching the droplet cortex to locally accumulate cortical PFs through EB. More of those local accumulations could potentially lead to a global asymmetric distribution of the PFs. XMAP215 is one of the proteins that could stimulate MT nucleation from the MTOCs and at the same time increase the growth rate, leading to longer MTs as well.
2D diffusion of PFs in the cortex also plays a role in the establishment of a polarized PF distribution. When diffusion is very fast, PFs quickly redistribute after a MT detached from the cortex. But the local accumulation of PFs will fade out slower when diffusion is slower. Potential ways to influence diffusion are to change the phospholipid composition of the cortex, or to make the diffusing particles larger. The latter could be achieved by clustering. Multiple PFs clustered together will diffuse slower, both because of the larger size of the complex and because together they are bound to more NTA-lipids.

Furthermore, the theoretical model from Foteinopoulos and Mulder has shown the importance of a limited number of PFs in the system. In that case, local activation leads to global inhibition, which helps polarity establishment. As discussed in Chapter 6, we are not in that regime at the moment. We need to lower the concentration of cortical PFs by 1-2 orders of magnitude, and then re-optimize the experimental conditions with the new concentrations.

Finally, we plan to continue the characterization and optimization of the photo-disso-

ciable EB (π-EB1) protein discussed in Chapter 5. Afterwards, we can exchange EB3 in the reconstituted system from Chapter 4 by π-EB1 to achieve light-sensitive EB-mediated MT capture by cortical PFs. Combined with the aforementioned optimization of the number of MTs, MT lengths and number of PFs, we want to study whether asymmetric effects occur when we locally inhibit the EB-mediated MT capture by light-inactivation of π-EB1.

DIFFERENT GEOMETRY

The idea to mediate MT-cortex interactions by EB came from experiments with an Mal3p-based chimera protein which could bind to MT tips and to the membrane of fission yeast cells [Recouvreux et al., 2016]. The combination of only those two functionalities sufficed to achieve a polarized distribution of the chimera protein, even though the MTs were not continuously in contact with the cell membrane (Fig. 7.1A). Positive feedback enhanced the degree of polarization, but was not strictly required. Because the experiment was performed *in vivo*, it is difficult to completely exclude the influence of other proteins or regulatory factors of the cell. Therefore we wanted to repeat it in an *in vitro* reconstitution. The main difference between the experiment and our system was the geometry of the confinement and the subsequent MT organization. Fission yeast cells are elongated, which makes the MTs predominantly grow along the long axis of the cell. As a result, the MT tips mostly reached the cell membrane at the cell poles, where they led to an accumulation of the chimera protein. In addition, fission yeast cells are much smaller than our emulsion droplets at the moment. Combined with a different MT organization (along the long axis of the cell in yeast, and radial MT asters in droplets) this leads to a higher concentration of MT tips at the cortex (illustrated in Fig. 6.4).

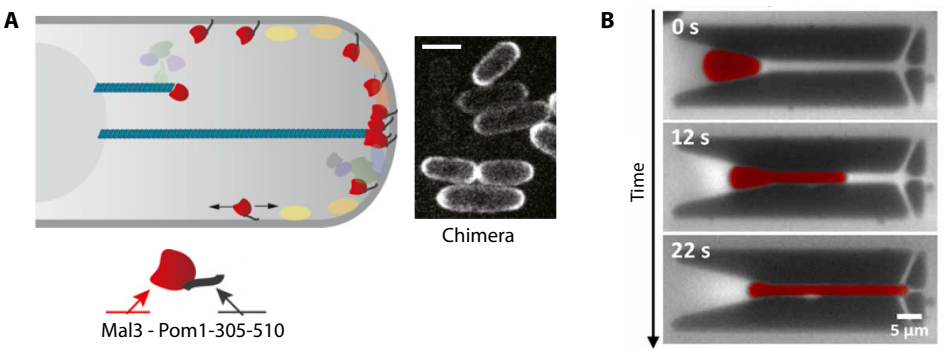

Figure 7.1: (A) The experiment from Recouvreux et al. [Recouvreux et al., 2016] with a chimera protein, combining the MT tip-binding fission yeast Mal3p protein with the membrane-binding tail of Pom1p. Merely this sufficed to accumulate the chimera protein at the cell poles. Figure from [Recouvreux et al., 2016]. **(B)** Strategy to create elongated water-in-oil emulsion droplets by Fanalista et al. [Fanalista et al., 2019]. Pre-formed spherical emulsion droplets are trapped in elongated traps of desired dimensions. Figure from [Fanalista et al., 2019].

We are planning to repeat the experiments described in Chapter 4 inside elongated water-in-oil emulsion droplets (Fig. 7.1B) with the dimensions of fission yeast cells

[Fanalista et al., 2019]. In this way, we want to verify *in vitro* whether merely the interaction between MT tips and droplet cortex is indeed enough to result in a polarized protein distribution.

Positive feedback

Both *in vivo* and theoretical studies have shown the need of positive feedback between polarity proteins at the cortex and MT stability to establish cell polarity. We propose to incorporate feedback by exchanging the current PF by a MT-stabilizing protein. The current PFs only bind to EB and Ni-NTA lipids, and one of the two types we used in Chapter 4 has an additional MT lattice affinity, but neither of them directly changes the MT dynamics. Ideal for our experiments would be a protein that can only bind MTs through EB and influences MT dynamics by reducing the catastrophe rate. CLASP is an example of such a protein, although it has some MT lattice affinity as well [Aher et al., 2018]. In case this proves problematic, a truncated version containing the SxIP motif for EB-binding and one or multiple of the TOG domains for MT stabilization might solve this problem.

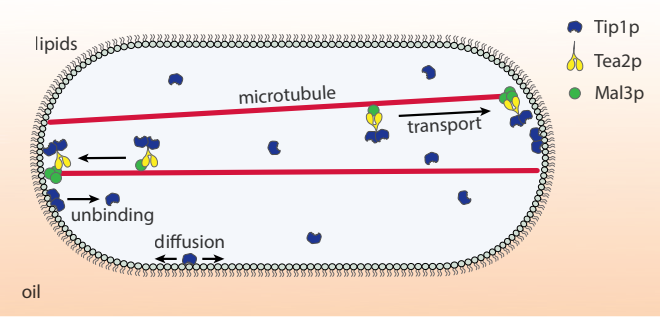

Figure 7.2: The fission yeast Mal3p-Tip1p-Tea2p system for motor based delivery of Tip1 to the cortex of elongated water-in-oil emulsion droplets.

Molecular motors for directed transport

MTs serve as roads for molecular motors to transport cargo through the cell. This directed transport plays an important role to bring PFs from cytoplasm to cell membrane. Also theoretical modeling was based on directed transport along MTs rather than EB-mediated MT-cortex interactions (Chapter 6). An ongoing project in our lab is the *in vitro* reconstitution of the fission yeast polarity mechanism with end-binding protein Mal3p, molecular motor Tea2p and cargo Tip1p [Taberner Carretero, 2016, Taberner and Dogterom, 2019] in an elongated confinement. The combination of these three proteins was chosen because Mal3p and Tip1p are necessary and sufficient to make Tea2p processive [Bieling et al., 2007]. Tip1p is fluorescently labeled and histidine-tagged, so it can bind to Ni-NTA functionalized phospholipids in the droplet cortex. The goal is to have Tip1p being delivered from cytoplasm to droplet cortex by Mal3p-Tea2p (Fig. 7.2). Imidazole can be used to reduce the binding of histidine-tags

to Ni-NTA lipids, to prevent that all Tip1p is bound to the cortex. Experiments in elongated 2D microchambers with Ni-NTA functionalized walls have shown Mal3p-Tea2p-mediated delivery of clusters of Tip1p to the walls [Taberner and Dogterom, 2019]. Transfer of those experiments into elongated emulsion droplets is work in progress. Parallel to this we propose to encapsulate the Mal3p-Tip1p-Tea2p system inside spherical emulsion droplets with Ni-NTA lipids. It will be interesting to compare the results of EB-mediated MT capture by cortical PFs and molecular motor-mediated delivery of the PFs.

FUTURE DIRECTIONS OF THE PROJECT

THE project discussed in this thesis was part of a bigger project: how does the combination of MT-based directed transport with reaction-diffusion-based signaling lead to spatio-temporal protein patterns at the membrane and how do those patterns regulate cellular morphogenesis. Those shape changes are important for cellular processes like division, migration or growth. Several research groups work together on *in vitro* reconstitutions and theoretical modeling to gain more quantitative understanding of protein patterns and morphogenesis, and the roles of both MTs as well as reaction-diffusion.

The system of EB-mediated MT capture at the cortex of water-in-oil emulsion droplets to create a local accumulation of PFs is therefore only one aspect of the bigger project. When we would accomplish a MT-induced asymmetric distribution of cortical PFs, the next step is to replace the water-in-oil emulsion droplets by vesicles. Because vesicles have a much lower surface tension, growing MTs can deform the vesicle [Fygenson et al., 1997, Cortès et al., 2006, Pinot et al., 2009, Hayashi et al., 2016]. Deformation will influence the MT organization and PF distribution on the membrane.

Furthermore, a question is how directed transport and protein signaling based on reaction-diffusion work together in cell polarity establishment. In cells, cytosolic signaling proteins often arrive in an inactive state at the membrane (either by diffusion or by directed transport), and there get activated by other proteins. But the signaling proteins also continuously dissociate from the membrane back into the cytoplasm where they deactivate again. This cycle of transport-activation-dissociation-deactivation can work in a feedback loop with MTs.
A possible reconstitution experiment to connect signaling proteins with MTs employs p21-activated kinase (PAK) signaling proteins (for a review, see [Bokoch, 2003]) and a protein called stathmin. Stathmin can bind tubulin dimers and thereby lower the local tubulin concentration, which negatively effects MT dynamics [Belmont and Mitchison, 1996, Niethammer et al., 2004]. In the reconstitution, PAKs would be transported by MTs to the cortex of the emulsion droplet or vesicle. After delivery to the cortex, the PAKs are activated. Active PAKs can phosphorylate stathmin and thereby lower the affinity of stathmin for tubulin, which increases the availability of free tubulin. A local accumulation of PAKs at the membrane would locally phosphorylate stathmin near the membrane. Because stathmin elsewhere in the confinement is dephosphorylated, we obtain a stathmin gradient. It has been suggested that a stathmin gradient plays a

role in polarized MT organizations [Niethammer et al., 2004], because MTs are more stable at the phosphorylated side of the stathmin gradient. Recently, an *in vitro* reconstitution was reported of a membrane system where the MT organization in a vesicle was influenced by a stathmin gradient [Gavriljuk et al., 2019]. In this system however, PAKs were not transported by MTs, but instead the stathmin was locally phosphorylated by light-induced recruitment of a kinase (Aurora B).

TOWARDS A SYNTHETIC CELL

IN a broader perspective, our efforts to reconstitute a minimal system for MT-based cell polarity fit in the scope of the development of a synthetic cell. The goal of this research program is to develop an "autonomous, self-reproducing synthetic cell with a bottom-up approach, that is, through integration of molecular building blocks" (BaSyC website). The aim is to gain understanding of the cellular processes by *in vitro* reconstitution. Different modules in the synthetic cell project are cell fueling, DNA transcription and translation, cell division, spatio-temporal regulation, synthesis of a genome and the ethics of creating such a synthetic cell. Research labs with their own expertise work on the separate modules. Eventually, the aim is to step-by-step combine multiple modules to learn more about the interplay of cellular processes.
The encapsulation of a MT cytoskeleton in emulsion droplets or liposomes and spatiotemporal regulation of those MTs with cortical proteins to establish pattern formation are part of the cell division module. Protein patterns are indispensable for proper spatio-temporal regulation of cell division. Well known examples are the MT-based Pom1 gradient in fission yeast and the FtsZ ring in bacteria which forms by reaction-diffusion of the Min-system.

The reconstitution of a synthetic cell is a very challenging and long-term project. But every bit of information obtained from reconstitution experiments of cellular processes bring us a step closer to understanding the complexity of cells.

BIBLIOGRAPHY

Abeysundara, N., Simmonds, A. J., and Hughes, S. C. Moesin is involved in polarity maintenance and cortical remodeling during asymmetric cell division. *Molecular biology of the cell*, 29(4):419–434, 2018.

Aher, A., Kok, M., Sharma, A., Rai, A., Olieric, N., Rodriguez-Garcia, R., Katrukha, E. A., Weinert, T., Olieric, V., Kapitein, L. C., et al. Clasp suppresses microtubule catastrophes through a single tog domain. *Developmental cell*, 46 (1):40–58, 2018. https://www.sciencedirect.com/science/article/pii/S1534580718304532.

Akhmanova, A. and Steinmetz, M. O. Control of microtubule organization and dynamics: two ends in the limelight. *Nature reviews Molecular cell biology*, 16(12):711, 2015. https://www.nature.com/articles/nrm4084.

Alfaro-Aco, R. and Petry, S. Building the microtubule cytoskeleton piece by piece. *Journal of Biological Chemistry*, 290(28):17154–17162, 2015. http://www.jbc.org/content/290/28/17154.short.

Andreu, J., Bordas, J., Diaz, J., de Ancos, J. G., Gil, R., Medrano, F. J., Nogales, E., Pantos, E., and Towns-Andrews, E. Low resolution structure of microtubules in solution: Synchrotron x-ray scattering and electron microscopy of taxol-induced microtubules assembled from purified tubulin in comparison with glycerol and map-induced microtubules. *Journal of molecular biology*, 226(1):169–184, 1992.

Barlan, K., Lu, W., and Gelfand, V. I. The microtubule-binding protein ensconsin is an essential cofactor of kinesin-1. *Current Biology*, 23(4):317–322, 2013.

Barsegov, V., Ross, J., and Dima, R. Dynamics of microtubules: highlights of recent computational and experimental investigations. *Journal of Physics: Condensed Matter*, 2017. http://iopscience.iop.org/article/10.1088/1361-648X/aa8670/meta.

Baumann, H. and Surrey, T. Motor-mediated cortical versus astral microtubule organization in lipid-monolayered droplets. *Journal of Biological Chemistry*, 289(32): 22524–22535, 2014. http://www.jbc.org/content/289/32/22524.short.

Behrens, R. and Nurse, P. Roles of fission yeast tea1p in the localization of polarity factors and in organizing the microtubular cytoskeleton. *The Journal of cell biology*, 157(5):783–793, 2002.

Belmont, L. D. and Mitchison, T. J. Identification of a protein that interacts with tubulin dimers and increases the catastrophe rate of microtubules. *Cell*, 84(4):623–631, 1996.

Bendezú, F. O., Vincenzetti, V., Vavylonis, D., Wyss, R., Vogel, H., and Martin, S. G. Spontaneous cdc42 polarization independent of gdi-mediated extraction and actin-based trafficking. *PLoS biology*, 13(4):e1002097, 2015. https://journals.plos.org/plosbiology/article?id=10.1371/journal.pbio.1002097.

Bicho, C. C., Kelly, D. A., Snaith, H. A., Goryachev, A. B., and Sawin, K. E. A catalytic role for mod5 in the formation of the tea1 cell polarity landmark. *Current Biology*, 20 (19):1752–1757, 2010. http://www.sciencedirect.com/science/article/pii/S0960982210010389.

Bieling, P., Laan, L., Schek, H., Munteanu, E. L., Sandblad, L., Dogterom, M., Brunner, D., and Surrey, T. Reconstitution of a microtubule plus-end tracking system in vitro. *Nature*, 450(7172):1100–1105, 2007. http://www.nature.com/nature/journal/v450/n7172/abs/nature06386.html.

Block, S. M. Kinesin motor mechanics: binding, stepping, tracking, gating, and limping. *Biophysical journal*, 92(9):2986–2995, 2007.

Bokoch, G. M. Biology of the p21-activated kinases. *Annual review of biochemistry*, 72(1):743–781, 2003. https://www.annualreviews.org/doi/abs/10.1146/annurev.biochem.72.121801.161742.

Bose, I., Irazoqui, J. E., Moskow, J. J., Bardes, E. S., Zyla, T. R., and Lew, D. J. Assembly of scaffold-mediated complexes containing cdc42p, the exchange factor cdc24p, and the effector cla4p required for cell cycle-regulated phosphorylation of cdc24p. *Journal of Biological Chemistry*, 276(10):7176–7186, 2001. http://www.jbc.org/content/276/10/7176.short.

Bressloff, P. C. and Xu, B. Stochastic active-transport model of cell polarization. *SIAM Journal on Applied Mathematics*, 75(2):652–678, 2015.

Brouhard, G. J., Stear, J. H., Noetzel, T. L., Al-Bassam, J., Kinoshita, K., Harrison, S. C., Howard, J., and Hyman, A. A. Xmap215 is a processive microtubule polymerase. *Cell*, 132(1):79–88, 2008. https://www.sciencedirect.com/science/article/pii/S0092867407015474.

Brunner, D. and Nurse, P. Clip170-like tip1p spatially organizes microtubular dynamics in fission yeast. *Cell*, 102(5):695–704, 2000.

Buey, R. M., Mohan, R., Leslie, K., Walzthoeni, T., Missimer, J. H., Menzel, A., Bjelić, S., Bargsten, K., Grigoriev, I., Smal, I., et al. Insights into eb1 structure and the role of its c-terminal domain for discriminating microtubule tips from the lattice. *Molecular biology of the cell*, 22(16):2912–2923, 2011.

Bulinski, J. C. and Bossler, A. Purification and characterization of ensconsin, a novel microtubule stabilizing protein. *Journal of Cell Science*, 107(10):2839–2849, 1994. https://jcs.biologists.org/content/107/10/2839.short.

Burton, P., Hinkley, R., and Pierson, G. Tannic acid-stained microtubules with 12, 13, and 15 protofilaments. *The Journal of cell biology*, 65

(1):227–233, 1975. https://rupress.org/jcb/article/65/1/227/48183/Tannic-acid-stained-microtubules-with-12-13-and-15.

Burute, M., Prioux, M., Blin, G., Truchet, S., Letort, G., Tseng, Q., Bessy, T., Lowell, S., Young, J., Filhol, O., et al. Polarity reversal by centrosome repositioning primes cell scattering during epithelial-to-mesenchymal transition. *Developmental cell*, 40(2):168–184, 2017. https://www.sciencedirect.com/science/article/pii/S1534580716308681.

Calvez, V., Hawkins, R. J., Meunier, N., and Voituriez, R. Analysis of a nonlocal model for spontaneous cell polarization. *SIAM Journal on Applied Mathematics*, 72(2): 594–622, 2012.

Caplow, M., Ruhlen, R., and Shanks, J. The free energy for hydrolysis of a microtubule-bound nucleotide triphosphate is near zero: all of the free energy for hydrolysis is stored in the microtubule lattice. *The Journal of Cell Biology*, 127 (3):779–788, 1994. https://rupress.org/jcb/article/127/3/779/59760/The-free-energy-for-hydrolysis-of-a-microtubule.

Carazo-Salas, R. E. and Nurse, P. Self-organization of interphase microtubule arrays in fission yeast. *Nature Cell Biology*, 8(10):1102–1107, 2006.

Cassimeris, L., Gard, D., Tran, P., and Erickson, H. P. Xmap215 is a long thin molecule that does not increase microtubule stiffness. *Journal of cell science*, 114(16):3025–3033, 2001.

Chang, F. and Martin, S. G. Shaping fission yeast with microtubules. *Cold Spring Harbor perspectives in biology*, 1(1):a001347, 2009. http://cshperspectives.cshlp.org/content/1/1/a001347.short.

Chaudhary, A. R., Lu, H., Krementsova, E. B., Bookwalter, C. S., Trybus, K. M., and Hendricks, A. G. Map7 regulates organelle transport by recruiting kinesin-1 to microtubules. *Journal of Biological Chemistry*, pages jbc–RA119, 2019. http://www.jbc.org/content/early/2019/05/13/jbc.RA119.008052.short.

Christie, J. M., Swartz, T. E., Bogomolni, R. A., and Briggs, W. R. Phototropin lov domains exhibit distinct roles in regulating photoreceptor function. *The Plant Journal*, 32(2):205–219, 2002.

Conduit, P. T., Wainman, A., and Raff, J. W. Centrosome function and assembly in animal cells. *Nature Reviews Molecular Cell Biology*, 16(10):611, 2015. https://www.nature.com/articles/nrm4062.

Consolati, T., Locke, J., Roostalu, J., Asthana, J., Lim, W. M., Gannon, J., Martino, F., Costa, A., and Surrey, T. Microtubule nucleation by single human γturc in a partly open asymmetric conformation. *bioRxiv*, page 853218, 2019.

Cortès, S., Glade, N., Chartier, I., and Tabony, J. Microtubule self-organisation by reaction–diffusion processes in miniature cell-sized containers and phospholipid vesicles. *Biophysical chemistry*, 120(3):168–177, 2006.

Cueva, J. G., Hsin, J., Huang, K. C., and Goodman, M. B. Posttranslational acetylation of α-tubulin constrains protofilament number in native microtubules. *Current biology*, 22(12):1066–1074, 2012.

Daga, R. R., Lee, K.-G., Bratman, S., Salas-Pino, S., and Chang, F. Self-organization of microtubule bundles in anucleate fission yeast cells. *Nature Cell Biology*, 8(10): 1108, 2006. https://www.nature.com/articles/ncb1480.

de Forges, H., Bouissou, A., and Perez, F. Interplay between microtubule dynamics and intracellular organization. *The international journal of biochemistry & cell biology*, 44(2):266–274, 2012.

Desai, A., , and Mitchison, T. J. Microtubule polymerization dynamics. *Annual Review of Cell and Developmental Biology*, 13(1):83–117, 1997. doi: 10.1146/annurev.cellbio.13.1.83. https://doi.org/10.1146/annurev.cellbio.13.1.83. PMID: 9442869.

Dogterom, M. and Yurke, B. Measurement of the force-velocity relation for growing microtubules. *Science*, 278(5339):856–860, 1997. http://science.sciencemag.org/content/278/5339/856.

Drubin, D. G. and Nelson, W. J. Origins of cell polarity. *Cell*, 84(3):335–344, 1996. http://www.sciencedirect.com/science/article/pii/S0092867400812787.

Duellberg, C., Trokter, M., Jha, R., Sen, I., Steinmetz, M. O., and Surrey, T. Reconstitution of a hierarchical+ tip interaction network controlling microtubule end tracking of dynein. *Nature cell biology*, 16(8):804, 2014. https://www.nature.com/articles/ncb2999.

Duellberg, C., Cade, N. I., Holmes, D., and Surrey, T. The size of the eb cap determines instantaneous microtubule stability. *eLife*, 5:e13470, 2016. https://elifesciences.org/content/5/e13470.

Elie, A., Prezel, E., Guérin, C., Denarier, E., Ramirez-Rios, S., Serre, L., Andrieux, A., Fourest-Lieuvin, A., Blanchoin, L., and Arnal, I. Tau co-organizes dynamic microtubule and actin networks. *Scientific reports*, 5:9964, 2015.

Faire, K., Waterman-Storer, C. M., Gruber, D., Masson, D., Salmon, E., and Bulinski, J. C. E-map-115 (ensconsin) associates dynamically with microtubules in vivo and is not a physiological modulator of microtubule dynamics. *J Cell Sci*, 112(23):4243–4255, 1999. https://jcs.biologists.org/content/112/23/4243.short.

Faivre-Moskalenko, C. and Dogterom, M. Dynamics of microtubule asters in microfabricated chambers: the role of catastrophes. *Proceedings of the National Academy of Sciences*, 99(26):16788–16793, 2002. http://www.pnas.org/content/99/26/16788.short.

Fanalista, F., Birnie, A., Maan, R., Burla, F., Charles, K., Pawlik, G., Deshpande, S., Koenderink, G. H., Dogterom, M., and Dekker, C. Shape and size control of artificial cells for bottom-up biology. *ACS nano*, 13(5):5439–5450, 2019. https://pubs.acs.org/doi/abs/10.1021/acsnano.9b00220.

Feldman, J. L. and Priess, J. R. A role for the centrosome and par-3 in the hand-off of mtoc function during epithelial polarization. *Current Biology*, 22(7): 575–582, 2012. https://www.sciencedirect.com/science/article/pii/S0960982212001959.

Felgner, H., Frank, R., and Schliwa, M. Flexural rigidity of microtubules measured with the use of optical tweezers. *Journal of cell science*, 109(2):509–516, 1996.

Felgner, H., Frank, R., Biernat, J., Mandelkow, E.-M., Mandelkow, E., Ludin, B., Matus, A., and Schliwa, M. Domains of neuronal microtubule-associated proteins and flexural rigidity of microtubules. *The Journal of cell biology*, 138(5):1067–1075, 1997.

Foteinopoulos, P. and Mulder, B. M. A microtubule-based minimal model for spontaneous and persistent spherical cell polarity. *PloS one*, 12(9): e0184706, 2017. http://journals.plos.org/plosone/article?id=10.1371/journal.pone.0184706.

Freisinger, T., Klünder, B., Johnson, J., Müller, N., Pichler, G., Beck, G., Costanzo, M., Boone, C., Cerione, R. A., Frey, E., et al. Establishment of a robust single axis of cell polarity by coupling multiple positive feedback loops. *Nature communications*, 4:1807, 2013. https://www.nature.com/articles/ncomms2795.

Fukata, M., Watanabe, T., Noritake, J., Nakagawa, M., Yamaga, M., Kuroda, S., Matsuura, Y., Iwamatsu, A., Perez, F., and Kaibuchi, K. Rac1 and cdc42 capture microtubules through iqgap1 and clip-170. *Cell*, 109(7):873–885, 2002. https://www.sciencedirect.com/science/article/pii/S0092867402008000.

Fygenson, D. K., Flyvbjerg, H., Sneppen, K., Libchaber, A., and Leibler, S. Spontaneous nucleation of microtubules. *Physical Review E*, 51(5):5058, 1995. https://journals.aps.org/pre/abstract/10.1103/PhysRevE.51.5058.

Fygenson, D. K., Elbaum, M., Shraiman, B., and Libchaber, A. Microtubules and vesicles under controlled tension. *Physical Review E*, 55(1):850, 1997.

Gallaud, E., Caous, R., Pascal, A., Bazile, F., Gagné, J.-P., Huet, S., Poirier, G. G., Chrétien, D., Richard-Parpaillon, L., and Giet, R. Ensconsin/map7 promotes microtubule growth and centrosome separation in drosophila neural stem cells. *J Cell Biol*, 204(7):1111–1121, 2014. http://jcb.rupress.org/content/204/7/1111.short.

Gavriljuk, K., Scocozza, B., Ghasemalizadeh, F., Nandan, A. P., Medina, M. C., Seidel, H., Schmick, M., Koseska, A., and Bastiaens, P. I. H. A synthetic morphogenic membrane system that responds with self-organized shape changes to local light cues. *bioRxiv*, 2019. doi: 10.1101/481887. https://www.biorxiv.org/content/early/2019/10/30/481887.

Gennerich, A. and Vale, R. D. Walking the walk: how kinesin and dynein coordinate their steps. *Current opinion in cell biology*, 21(1):59–67, 2009.

Gennerich, A., Carter, A. P., Reck-Peterson, S. L., and Vale, R. D. Force-induced bidirectional stepping of cytoplasmic dynein. *Cell*, 131(5):952–965, 2007.

Gigant, B., Curmi, P. A., Martin-Barbey, C., Charbaut, E., Lachkar, S., Lebeau, L., Siavoshian, S., Sobel, A., and Knossow, M. The 4 å x-ray structure of a tubulin: stathmin-like domain complex. *Cell*, 102(6):809–816, 2000. https://www.sciencedirect.com/science/article/pii/S0092867400000696.

Glynn, J. M., Lustig, R. J., Berlin, A., and Chang, F. Role of bud6p and tea1p in the interaction between actin and microtubules for the establishment of cell polarity in fission yeast. *Current Biology*, 11(11):836–845, 2001. http://www.sciencedirect.com/science/article/pii/S0960982201002354.

Gouveia, S. M., Leslie, K., Kapitein, L. C., Buey, R. M., Grigoriev, I., Wagenbach, M., Smal, I., Meijering, E., Hoogenraad, C. C., Wordeman, L., et al. In vitro reconstitution of the functional interplay between mcak and eb3 at microtubule plus ends. *Current Biology*, 20(19):1717–1722, 2010.

Grishchuk, E. L., Molodtsov, M. I., Ataullakhanov, F. I., and McIntosh, J. R. Force production by disassembling microtubules. *Nature*, 438(7066):384, 2005. https://www.nature.com/articles/nature04132.

Guillabert-Gourgues, A., Jaspard-Vinassa, B., Bats, M.-L., Sewduth, R. N., Franzl, N., Peghaire, C., Jeanningros, S., Moreau, C., Roux, E., Larrieu-Lahargue, F., et al. Kif26b controls endothelial cell polarity through the dishevelled/daam1-dependent planar cell polarity–signaling pathway. *Molecular biology of the cell*, 27(6):941–953, 2016. http://www.molbiolcell.org/content/27/6/941.short.

Guntas, G., Hallett, R. A., Zimmerman, S. P., Williams, T., Yumerefendi, H., Bear, J. E., and Kuhlman, B. Engineering an improved light-induced dimer (ilid) for controlling the localization and activity of signaling proteins. *Proceedings of the National Academy of Sciences*, 112(1):112–117, 2015. https://www.pnas.org/content/112/1/112.short.

Hagan, I. M. and Hyams, J. S. The use of cell division cycle mutants to investigate the control of microtubule distribution in the fission yeast schizosaccharomyces pombe. *Journal of Cell Science*, 89(3):343–357, 1988.

Hannak, E., Oegema, K., Kirkham, M., Go?nczy, P., Habermann, B., and Hyman, A. A. The kinetically dominant assembly pathway for centrosomal asters in caenorhabditis elegans is γ-tubulin dependent. *The Journal of cell biology*, 157(4):591–602, 2002.

Harper, S. M., Neil, L. C., and Gardner, K. H. Structural basis of a phototropin light switch. *Science*, 301(5639):1541–1544, 2003. https://science.sciencemag.org/content/301/5639/1541.

Hawkins, R. J., Benichou, O., Piel, M., and Voituriez, R. Rebuilding cytoskeleton roads: Active-transport-induced polarization of cells. *Physical Review E*, 80(4):040903,

2009. http://journals.aps.org/pre/abstract/10.1103/PhysRevE.80.040903.

Hawkins, T., Mirigian, M., Yasar, M. S., and Ross, J. L. Mechanics of microtubules. *Journal of biomechanics*, 43(1):23–30, 2010. https://www.sciencedirect.com/science/article/pii/S0021929009004965.

Hayashi, I. and Ikura, M. Crystal structure of the amino-terminal microtubule-binding domain of end-binding protein 1 (eb1). *Journal of Biological Chemistry*, 278(38): 36430–36434, 2003. http://www.jbc.org/content/278/38/36430.

Hayashi, M., Nishiyama, M., Kazayama, Y., Toyota, T., Harada, Y., and Takiguchi, K. Reversible morphological control of tubulin-encapsulating giant liposomes by hydrostatic pressure. *Langmuir*, 32(15):3794–3802, 2016.

Hirokawa, N. Kinesin and dynein superfamily proteins and the mechanism of organelle transport. *Science*, 279(5350):519–526, 1998.

Holy, T. E., Dogterom, M., Yurke, B., and Leibler, S. Assembly and positioning of microtubule asters in microfabricated chambers. *Proceedings of the National Academy of Sciences*, 94(12):6228–6231, 1997. http://www.pnas.org/content/94/12/6228.short.

Honnappa, S., Gouveia, S. M., Weisbrich, A., Damberger, F. F., Bhavesh, N. S., Jawhari, H., Grigoriev, I., van Rijssel, F. J., Buey, R. M., Lawera, A., et al. An eb1-binding motif acts as a microtubule tip localization signal. *Cell*, 138(2):366–376, 2009. http://www.sciencedirect.com/science/article/pii/S0092867409006382.

Hooikaas, P. J., Martin, M., Mühlethaler, T., Kuijntjes, G.-J., Peeters, C. A., Katrukha, E. A., Ferrari, L., Stucchi, R., Verhagen, D. G., van Riel, W. E., et al. Map7 family proteins regulate kinesin-1 recruitment and activation. *J Cell Biol*, pages jcb–201808065, 2019. http://jcb.rupress.org/content/218/4/1298/tab-article-info.

Howard, J. and Hyman, A. A. Growth, fluctuation and switching at microtubule plus ends. *Nature Reviews Molecular Cell Biology*, 10(8):569–574, 2009.

Howell, A. S., Jin, M., Wu, C.-F., Zyla, T. R., Elston, T. C., and Lew, D. J. Negative feedback enhances robustness in the yeast polarity establishment circuit. *Cell*, 149 (2):322–333, 2012. http://www.sciencedirect.com/science/article/pii/S009286741200342X.

Huala, E., Oeller, P. W., Liscum, E., Han, I.-S., Larsen, E., and Briggs, W. R. Arabidopsis nph1: a protein kinase with a putative redox-sensing domain. *Science*, 278 (5346):2120–2123, 1997. https://science.sciencemag.org/content/278/5346/2120.

Huisman, S. M. and Brunner, D. Cell polarity in fission yeast: a matter of confining, positioning, and switching growth zones. In *Seminars in cell & developmental biology*, volume 22, pages 799–805. Elsevier, 2011. http://www.sciencedirect.com/science/article/pii/S1084952111000991.

Inaba, M., Venkei, Z. G., and Yamashita, Y. M. The polarity protein baz forms a platform for the centrosome orientation during asymmetric stem cell division in the drosophila male germline. *Elife*, 4:e04960, 2015. https://www.ncbi.nlm.nih.gov/pmc/articles/PMC4391501/.

Ishihara, K., Nguyen, P. A., Groen, A. C., Field, C. M., and Mitchison, T. J. Microtubule nucleation remote from centrosomes may explain how asters span large cells. *Proceedings of the National Academy of Sciences*, 111(50):17715–17722, 2014. https://www.pnas.org/content/111/50/17715.

Ishihara, K., Korolev, K. S., and Mitchison, T. J. Physical basis of large microtubule aster growth. *Elife*, 5:e19145, 2016.

Janke, C. and Bulinski, J. C. Post-translational regulation of the microtubule cytoskeleton: mechanisms and functions. *Nature reviews Molecular cell biology*, 12(12): 773, 2011.

Janson, M. E. and Dogterom, M. A bending mode analysis for growing microtubules: evidence for a velocity-dependent rigidity. *Biophysical journal*, 87 (4):2723–2736, 2004a. https://www.sciencedirect.com/science/article/pii/S0006349504737431#bib3.

Janson, M. E. and Dogterom, M. Scaling of microtubule force-velocity curves obtained at different tubulin concentrations. *Physical review letters*, 92(24):248101, 2004b. http://journals.aps.org/prl/abstract/10.1103/PhysRevLett.92.248101#fulltext.

Jiang, K. and Akhmanova, A. Microtubule tip-interacting proteins: a view from both ends. *Current opinion in cell biology*, 23(1):94–101, 2011. http://www.sciencedirect.com/science/article/pii/S0955067410001316.

Jiang, T., McKinley, R. A., McGill, M. A., Angers, S., and Harris, T. J. A par-1-par-3-centrosome cell polarity pathway and its tuning for isotropic cell adhesion. *Current Biology*, 25(20):2701–2708, 2015. https://www.sciencedirect.com/science/article/pii/S0960982215010799.

Joshi, H. C., Palacios, M. J., McNamara, L., and Cleveland, D. W. γ-tubulin is a centrosomal protein required for cell cycle-dependent microtubule nucleation. *Nature*, 356(6364):80, 1992.

Juniper, M. P., Weiss, M., Platzman, I., Spatz, J. P., and Surrey, T. Spherical network contraction forms microtubule asters in confinement. *Soft matter*, 2018. http://pubs.rsc.org/en/content/articlehtml/2018/sm/c7sm01718a.

Karsenti, E. Self-organization in cell biology: a brief history. *Nat Rev Mol Cell Biol*, 9(3):255–262, 2008. doi: 10.1038/nrm2357. http://www.ncbi.nlm.nih.gov/pubmed/18292780.

Keating, T. J. and Borisy, G. G. Immunostructural evidence for the template mechanism of microtubule nucleation. *Nature cell biology*, 2(6):352, 2000. https://www.nature.com/articles/ncb0600_352.

Kinoshita, K., Arnal, I., Desai, A., Drechsel, D. N., and Hyman, A. A. Reconstitution of physiological microtubule dynamics using purified components. *Science*, 294 (5545):1340–1343, 2001.

Klünder, B., Freisinger, T., Wedlich-Söldner, R., and Frey, E. Gdi-mediated cell polarization in yeast provides precise spatial and temporal control of cdc42 signaling. *PLOS Computational Biology*, 9(12):e1003396, 2013. http://journals.plos.org/ploscompbiol/article?id=10.1371/journal.pcbi.1003396.

Knaus, M., Cameroni, E., Pedruzzi, I., Tatchell, K., De Virgilio, C., and Peter, M. The bud14p–glc7p complex functions as a cortical regulator of dynein in budding yeast. *The EMBO journal*, 24(17):3000–3011, 2005.

Kok, M. *The dynamics of microtubule stability: A reconstitution of regulated microtubule assembly under force*. PhD thesis, Delft University of Technology, 4 2019.

Kollman, J. M., Merdes, A., Mourey, L., and Agard, D. A. Microtubule nucleation by γ-tubulin complexes. *Nature reviews Molecular cell biology*, 12(11):709, 2011. https://www.nature.com/articles/nrm3209.

Komarova, Y., De Groot, C. O., Grigoriev, I., Gouveia, S. M., Munteanu, E. L., Schober, J. M., Honnappa, S., Buey, R. M., Hoogenraad, C. C., Dogterom, M., et al. Mammalian end binding proteins control persistent microtubule growth. *The Journal of cell biology*, 184(5):691–706, 2009. http://jcb.rupress.org/content/184/5/691.short.

Kumar, P. and Wittmann, T. + tips: Sxipping along microtubule ends. *Trends in cell biology*, 22(8):418–428, 2012. http://www.sciencedirect.com/science/article/pii/S096289241200092X.

Kurz, J. C. and Williams Jr, R. C. Microtubule-associated proteins and the flexibility of microtubules. *Biochemistry*, 34(41):13374–13380, 1995.

Laan, L., Pavin, N., Husson, J., Romet-Lemonne, G., Van Duijn, M., López, M. P., Vale, R. D., Jülicher, F., Reck-Peterson, S. L., and Dogterom, M. Cortical dynein controls microtubule dynamics to generate pulling forces that position microtubule asters. *Cell*, 148(3):502–514, 2012a. http://www.sciencedirect.com/science/article/pii/S009286741200013X.

Laan, L., Roth, S., and Dogterom, M. End-on microtubule-dynein interactions and pulling-based positioning of microtubule organizing centers. *Cell Cycle*, 11(20):3750–3757, 2012b. http://www.tandfonline.com/doi/abs/10.4161/cc.21753.

Lagomarsino, M. C., Tanase, C., Vos, J. W., Emons, A. M. C., Mulder, B. M., and Dogterom, M. Microtubule organization in three-dimensional confined geometries: evaluating the role of elasticity through a combined in vitro and modeling approach. *Biophysical journal*, 92(3):1046–1057, 2007. http://www.sciencedirect.com/science/article/pii/S0006349507709128.

Lansbergen, G. and Akhmanova, A. Microtubule plus end: a hub of cellular activities. *Traffic*, 7(5):499–507, 2006. https://onlinelibrary.wiley.com/doi/full/10.1111/j.1600-0854.2006.00400.x.

Levskaya, A., Weiner, O. D., Lim, W. A., and Voigt, C. A. Spatiotemporal control of cell signalling using a light-switchable protein interaction. *Nature*, 461(7266):997–1001, 2009. http://www.nature.com/nature/journal/v461/n7266/abs/nature08446.html.

Li, R. and Gundersen, G. G. Beyond polymer polarity: how the cytoskeleton builds a polarized cell. *Nature reviews. Molecular cell biology*, 9(11):860, 2008. http://www.nature.com.tudelft.idm.oclc.org/doifinder/10.1038/nrm2522.

Ligon, L. A., Shelly, S. S., Tokito, M., and Holzbaur, E. L. The microtubule plus-end proteins eb1 and dynactin have differential effects on microtubule polymerization. *Molecular biology of the cell*, 14(4):1405–1417, 2003.

Lin, T.-c., Neuner, A., and Schiebel, E. Targeting of γ-tubulin complexes to microtubule organizing centers: conservation and divergence. *Trends in cell biology*, 25(5):296–307, 2015. https://www.sciencedirect.com/science/article/pii/S0962892414002128.

Lindeboom, J. J., Nakamura, M., Hibbel, A., Shundyak, K., Gutierrez, R., Ketelaar, T., Emons, A. M. C., Mulder, B. M., Kirik, V., and Ehrhardt, D. W. A mechanism for reorientation of cortical microtubule arrays driven by microtubule severing. *Science*, 342(6163):1245533, 2013.

Loose, M., Fischer-Friedrich, E., Ries, J., Kruse, K., and Schwille, P. Spatial regulators for bacterial cell division self-organize into surface waves in vitro. *Science*, 320(5877):789–792, 2008. https://science.sciencemag.org/content/320/5877/789.

Lüders, J., Patel, U. K., and Stearns, T. Gcp-wd is a γ-tubulin targeting factor required for centrosomal and chromatin-mediated microtubule nucleation. *Nature cell biology*, 8(2):137–147, 2006.

Lukinavičius, G., Reymond, L., D'este, E., Masharina, A., Göttfert, F., Ta, H., Güther, A., Fournier, M., Rizzo, S., Waldmann, H., et al. Fluorogenic probes for live-cell imaging of the cytoskeleton. *Nature methods*, 11(7):731–733, 2014. https://www.nature.com/articles/nmeth.2972. SiR tubulin.

Ma, R., Laan, L., Dogterom, M., Pavin, N., and Jülicher, F. General theory for the mechanics of confined microtubule asters. *New Journal of Physics*, 16(1):013018, 2014. http://iopscience.iop.org/article/10.1088/1367-2630/16/1/013018/meta.

Mahmood, M. E. and Al-Koofee, D. A. Effect of temperature changes on critical micelle concentration for tween series surfactant. *Global Journal of Science Frontier Research Chemistry*, 13(4):1–7, 2013.

Manna, T., Honnappa, S., Steinmetz, M. O., and Wilson, L. Suppression of microtubule

dynamic instability by the+ tip protein eb1 and its modulation by the cap-gly domain of p150glued. *Biochemistry*, 47(2):779–786, 2008.

Martin, S. G. Spontaneous cell polarization: Feedback control of cdc42 gtpase breaks cellular symmetry. *Bioessays*, 37(11):1193–1201, 2015. https://onlinelibrary.wiley.com/doi/full/10.1002/bies.201500077.

Martin, S. G., McDonald, W. H., Yates III, J. R., and Chang, F. Tea4p links microtubule plus ends with the formin for3p in the establishment of cell polarity. *Developmental cell*, 8(4):479–491, 2005. https://www.sciencedirect.com/science/article/pii/S153458070500078X.

Masson, D. and Kreis, T. E. Identification and molecular characterization of e-map-115, a novel microtubule-associated protein predominantly expressed in epithelial cells. *The Journal of cell biology*, 123(2):357–371, 1993. http://jcb.rupress.org/content/123/2/357.abstract.

Mata, J. and Nurse, P. tea1 and the microtubular cytoskeleton are important for generating global spatial order within the fission yeast cell. *Cell*, 89(6):939–949, 1997.

Maurer, S. P., Bieling, P., Cope, J., Hoenger, A., and Surrey, T. Gtpγs microtubules mimic the growing microtubule end structure recognized by end-binding proteins (ebs). *Proceedings of the National Academy of Sciences*, 108(10):3988–3993, 2011. http://www.pnas.org/content/108/10/3988/tab-figures-data.

Maurer, S. P., Fourniol, F. J., Bohner, G., Moores, C. A., and Surrey, T. Ebs recognize a nucleotide-dependent structural cap at growing microtubule ends. *Cell*, 149(2):371–382, 2012. https://www.sciencedirect.com/science/article/pii/S0092867412003418.

Maurer, S. P., Cade, N. I., Bohner, G., Gustafsson, N., Boutant, E., and Surrey, T. Eb1 accelerates two conformational transitions important for microtubule maturation and dynamics. *Current Biology*, 24(4):372–384, 2014. https://www.sciencedirect.com/science/article/pii/S0960982213016011.

Mazel, T. Crosstalk of cell polarity signaling pathways. *Protoplasma*, pages 1–18, 2017. http://link.springer.com/article/10.1007/s00709-017-1075-2.

McIntosh, J. R. The centrosome as an organizer of the cytoskeleton. *Modern Cell Biology*, 2:115–142, 1983.

McNally, K., Audhya, A., Oegema, K., and McNally, F. J. Katanin controls mitotic and meiotic spindle length. *The Journal of cell biology*, 175(6):881–891, 2006.

Metzger, T., Gache, V., Xu, M., Cadot, B., Folker, E. S., Richardson, B. E., Gomes, E. R., and Baylies, M. K. Map and kinesin-dependent nuclear positioning is required for skeletal muscle function. *Nature*, 484(7392):120–124, 2012.

Mickey, B. and Howard, J. Rigidity of microtubules is increased by stabilizing agents. *The Journal of cell biology*, 130(4):909–917, 1995.

Minc, N., Bratman, S. V., Basu, R., and Chang, F. Establishing new sites of polarization by microtubules. *Current biology*, 19(2):83–94, 2009. http://www.sciencedirect.com/science/article/pii/S0960982208016291.

Mitchison, T. and Kirschner, M. Dynamic instability of microtubule growth. *nature*, 312(5991):237, 1984a. https://www.nature.com/articles/312237a0.

Mitchison, T. and Kirschner, M. Microtubule assembly nucleated by isolated centrosomes. *Nature*, 312(5991):232, 1984b. https://www.nature.com/articles/312232a0.

Mogilner, A., Allard, J., and Wollman, R. Cell polarity: quantitative modeling as a tool in cell biology. *Science*, 336(6078):175–179, 2012. http://science.sciencemag.org/content/336/6078/175.

Monroy, B. Y., Sawyer, D. L., Ackermann, B. E., Borden, M. M., Tan, T. C., and Ori-McKenney, K. M. Competition between microtubule-associated proteins directs motor transport. *Nature communications*, 9(1):1487, 2018. https://www.nature.com/articles/s41467-018-03909-2.

Moritz, M., Braunfeld, M. B., Sedat, J. W., Alberts, B., and Agard, D. A. Microtubule nucleation by γ-tubulin-containing rings in the centrosome. *Nature*, 378(6557):638, 1995. https://www.nature.com/articles/378638a0.

Moritz, M., Braunfeld, M. B., Guénebaut, V., Heuser, J., and Agard, D. A. Structure of the γ-tubulin ring complex: a template for microtubule nucleation. *Nature cell biology*, 2(6):365, 2000. https://www.nature.com/articles/ncb0600_365.

Moudjou, M. and Bornens, M. Method of centrosome isolation from cultured animal cells. *Cell biology: a laboratory handbook*, 2:111–119, 1998.

Müller-Reichert, T., CHREtien, D., Severin, F., and Hyman, A. A. Structural changes at microtubule ends accompanying gtp hydrolysis: information from a slowly hydrolyzable analogue of gtp, guanylyl (α, β) methylenediphosphonate. *Proceedings of the National Academy of Sciences*, 95(7):3661–3666, 1998. https://www.pnas.org/content/95/7/3661.short.

Nakamura, M., Zhou, X. Z., and Lu, K. P. Critical role for the eb1 and apc interaction in the regulation of microtubule polymerization. *Current Biology*, 11(13):1062–1067, 2001.

Nédélec, F., F., Surrey, T., Maggs, A. C., and Leibler, S. Self-organization of microtubules and motors. *Nature*, 389(6648):305, 1997. https://www.nature.com/articles/38532.

Nguyen, P. A., Groen, A. C., Loose, M., Ishihara, K., Wühr, M., Field, C. M., and Mitchison, T. J. Spatial organization of cytokinesis signaling reconstituted in a cell-free system. *Science*, 346(6206):244–247, 2014. https://science.sciencemag.org/content/346/6206/244.

Niethammer, P., Bastiaens, P., and Karsenti, E. Stathmin-tubulin interaction gradients in motile and mitotic cells. *Science*, 303(5665):1862–1866, 2004. https://science.sciencemag.org/content/303/5665/1862.

Pampaloni, F., Lattanzi, G., Jonáš, A., Surrey, T., Frey, E., and Florin, E.-L. Thermal fluctuations of grafted microtubules provide evidence of a length-dependent persistence length. *Proceedings of the National Academy of Sciences*, 103(27): 10248–10253, 2006. ISSN 0027-8424. doi: 10.1073/pnas.0603931103. https://www.pnas.org/content/103/27/10248.

Pavin, N., Laan, L., Ma, R., Dogterom, M., and Jülicher, F. Positioning of microtubule organizing centers by cortical pushing and pulling forces. *New Journal of Physics*, 14(10):105025, 2012. http://iopscience.iop.org/article/10.1088/1367-2630/14/10/105025/meta.

Pierson, G. B., Burton, P. R., and Himes, R. H. Alterations in number of protofilaments in microtubules assembled in vitro. *The Journal of cell biology*, 76 (1):223–228, 1978. https://rupress.org/jcb/article/76/1/223/18876/Alterations-in-number-of-protofilaments-in.

Pinot, M., Chesnel, F., Kubiak, J., Arnal, I., Nedelec, F., and Gueroui, Z. Effects of confinement on the self-organization of microtubules and motors. *Current Biology*, 19(11):954–960, 2009. http://www.sciencedirect.com/science/article/pii/S0960982209010252.

Portran, D., Zoccoler, M., Gaillard, J., Stoppin-Mellet, V., Neumann, E., Arnal, I., Martiel, J., and Vantard, M. Map65/ase1 promote microtubule flexibility. *Molecular biology of the cell*, 24(12):1964–1973, 2013. https://www.molbiolcell.org/doi/full/10.1091/mbc.e13-03-0141.

Preciado Lopez, M. *In vitro studies of actin-microtubule coordination*. PhD thesis, Vrije Universiteit Amsterdam, 2015. Exacte Wetenschappen Naam instelling promotie: VU University Naam instelling onderzoek: VU University.

Pudasaini, A., El-Arab, K. K., and Zoltowski, B. D. Lov-based optogenetic devices: light-driven modules to impart photoregulated control of cellular signaling. *Frontiers in molecular biosciences*, 2:18, 2015. https://www.frontiersin.org/articles/10.3389/fmolb.2015.00018/full.

Rale, M. J., Kadzik, R. S., and Petry, S. Phase transitioning the centrosome into a microtubule nucleator. *Biochemistry*, 2017. http://pubs.acs.org/doi/abs/10.1021/acs.biochem.7b01064.

Raviv, U., Nguyen, T., Ghafouri, R., Needleman, D. J., Li, Y., Miller, H. P., Wilson, L., Bruinsma, R. F., and Safinya, C. R. Microtubule protofilament number is modulated in a stepwise fashion by the charge density of an enveloping layer. *Biophysical journal*, 92(1):278–287, 2007.

Reck-Peterson, S. L., Yildiz, A., Carter, A. P., Gennerich, A., Zhang, N., and Vale, R. D.

Single-molecule analysis of dynein processivity and stepping behavior. *Cell*, 126 (2):335–348, 2006.

Recouvreux, P., Sokolowski, T. R., Grammoustianou, A., ten Wolde, P. R., and Dogterom, M. Chimera proteins with affinity for membranes and microtubule tips polarize in the membrane of fission yeast cells. *Proceedings of the National Academy of Sciences*, page 201419248, 2016. http://www.pnas.org/content/early/2016/01/27/1419248113.abstract.

Reid, T. A., Coombes, C., Mukherjee, S., Goldblum, R. R., White, K., Parmar, S., McClellan, M., Zanic, M., Courtemanche, N., and Gardner, M. K. Structural state recognition facilitates tip tracking of eb1 at growing microtubule ends. *eLife*, 8, 2019. https://www.ncbi.nlm.nih.gov/pmc/articles/PMC6742484/.

Rogers, G. C., Rusan, N. M., Peifer, M., and Rogers, S. L. A multicomponent assembly pathway contributes to the formation of acentrosomal microtubule arrays in interphase drosophila cells. *Molecular biology of the cell*, 19(7):3163–3178, 2008.

Roostalu, J. and Surrey, T. Microtubule nucleation: beyond the template. *Nature reviews. Molecular cell biology*, 2017. http://www.nature.com/nrm/journal/vaop/ncurrent/full/nrm.2017.75.html?foxtrotcallback=true.

Roth, D., Fitton, B. P., Chmel, N. P., Wasiluk, N., and Straube, A. Spatial positioning of eb family proteins at microtubule tips involves distinct nucleotide-dependent binding properties. *J Cell Sci*, 132(4):jcs219550, 2019a. http://jcs.biologists.org/content/132/4/jcs219550.abstract.

Roth, S., Laan, L., and Dogterom, M. Reconstitution of cortical dynein function. *Methods in enzymology*, 540:205–230, 2014. http://www.sciencedirect.com/science/article/pii/B9780123979247000121.

Roth, S., Gârlea, I. C., Vleugel, M., Mulder, B. M., and Dogterom, M. Reconstitution of basic mitotic spindles in cell-like confinement. *bioRxiv*, page 770602, 2019b. https://www.biorxiv.org/content/10.1101/770602v1.abstract.

Rubinstein, B., Slaughter, B. D., and Li, R. Weakly nonlinear analysis of symmetry breaking in cell polarity models. *Physical biology*, 9(4):045006, 2012. https://iopscience.iop.org/article/10.1088/1478-3975/9/4/045006.

Sakamoto, K. and Briggs, W. R. Cellular and subcellular localization of phototropin 1. *The Plant Cell*, 14(8):1723–1735, 2002.

Salomon, M., Eisenreich, W., Dürr, H., Schleicher, E., Knieb, E., Massey, V., Rüdiger, W., Müller, F., Bacher, A., and Richter, G. An optomechanical transducer in the blue light receptor phototropin from avena sativa. *Proceedings of the National Academy of Sciences*, 98(22):12357–12361, 2001. https://www.pnas.org/content/98/22/12357.short.

Sawin, K. E. and Snaith, H. A. Role of microtubules and tea1p in establishment and maintenance of fission yeast cell polarity. *Journal of cell science*, 117(5):689–700, 2004. http://jcs.biologists.org/content/117/5/689.short.

Seetapun, D., Castle, B. T., McIntyre, A. J., Tran, P. T., and Odde, D. J. Estimating the microtubule gtp cap size in vivo. *Current Biology*, 22(18):1681–1687, 2012. https://www.sciencedirect.com/science/article/pii/S0960982212007440.

Serbus, L. R., Cha, B.-J., Theurkauf, W. E., and Saxton, W. M. Dynein and the actin cytoskeleton control kinesin-driven cytoplasmic streaming in drosophila oocytes. *Development*, 132(16):3743–3752, 2005. https://dev.biologists.org/content/132/16/3743.

Shima, T., Morikawa, M., Kaneshiro, J., Kambara, T., Kamimura, S., Yagi, T., Iwamoto, H., Uemura, S., Shigematsu, H., Shirouzu, M., et al. Kinesin-binding–triggered conformation switching of microtubules contributes to polarized transport. *Journal of Cell Biology*, 217(12):4164–4183, 2018. https://rupress.org/jcb/article/217/12/4164/120306/Kinesin-binding-triggered-conformation-switching.

Siegrist, S. E. and Doe, C. Q. Microtubule-induced cortical cell polarity. *Genes & development*, 21(5):483–496, 2007. http://genesdev.cshlp.org/content/21/5/483.short.

Slaughter, B. D., Smith, S. E., and Li, R. Symmetry breaking in the life cycle of the budding yeast. *Cold Spring Harbor perspectives in biology*, 1(3):a003384, 2009. https://cshperspectives.cshlp.org/content/1/3/a003384.

Snaith, H. A. and Sawin, K. E. Fission yeast mod5p regulates polarized growth through anchoring of tea1p at cell tips. *Nature*, 423(6940):647–651, 2003. http://www.nature.com/nature/journal/v423/n6940/abs/nature01672.html.

Sprague, B. L., Pego, R. L., Stavreva, D. A., and McNally, J. G. Analysis of binding reactions by fluorescence recovery after photobleaching. *Biophysical journal*, 86(6):3473–3495, 2004. http://www.sciencedirect.com/science/article/pii/S0006349504743921.

Srayko, M., Kaya, A., Stamford, J., and Hyman, A. A. Identification and characterization of factors required for microtubule growth and nucleation in the early c. elegans embryo. *Developmental cell*, 9(2):223–236, 2005.

St Johnston, D. Establishing and transducing cell polarity: common themes and variations. *Current Opinion in Cell Biology*, 51:33–41, 2018. https://www.sciencedirect.com/science/article/pii/S0955067417301357.

Strickland, D., Lin, Y., Wagner, E., Hope, C. M., Zayner, J., Antoniou, C., Sosnick, T. R., Weiss, E. L., and Glotzer, M. Tulips: tunable, light-controlled interacting protein tags for cell biology. *Nature methods*, 9(4):379, 2012. https://www.nature.com/articles/nmeth.1904.

Strome, S., Powers, J., Dunn, M., Reese, K., Malone, C. J., White, J., Seydoux, G., and Saxton, W. Spindle dynamics and the role of γ-tubulin in early caenorhabditis elegans embryos. *Molecular biology of the cell*, 12(6):1751–1764, 2001.

Sun, X., Shi, X., Liu, M., Li, D., Zhang, L., Liu, X., and Zhou, J. Mdp3 is a novel microtubule-binding protein that regulates microtubule assembly and stability. *Cell Cycle*, 10(22):3929–3937, 2011. https://www.tandfonline.com/doi/abs/10.4161/cc.10.22.18106.

Sung, H.-H., Telley, I. A., Papadaki, P., Ephrussi, A., Surrey, T., and Rørth, P. Drosophila ensconsin promotes productive recruitment of kinesin-1 to microtubules. *Developmental cell*, 15(6):866–876, 2008.

Suzuki, K., Miyazaki, M., Takagi, J., Itabashi, T., and Ishiwata, S. Spatial confinement of active microtubule networks induces large-scale rotational cytoplasmic flow. *Proceedings of the National Academy of Sciences*, page 201616001, 2017. http://www.pnas.org/content/114/11/2922.

Svoboda, K., Schmidt, C. F., Schnapp, B. J., and Block, S. M. Direct observation of kinesin stepping by optical trapping interferometry. *Nature*, 365(6448):721, 1993.

Swartz, T. E., Corchnoy, S. B., Christie, J. M., Lewis, J. W., Szundi, I., Briggs, W. R., and Bogomolni, R. A. The photocycle of a flavin-binding domain of the blue light photoreceptor phototropin. *Journal of Biological Chemistry*, 276(39):36493–36500, 2001.

Taberner, N. and Dogterom, M. Motor-mediated clustering at microtubule plus ends facilitates protein transfer to a bio-mimetic cortex. *bioRxiv*, page 736728, 2019. https://www.biorxiv.org/content/10.1101/736728v1.

Taberner, N., Lof, A., Roth, S., Lamers, D., Zeijlemaker, H., and Dogterom, M. In vitro systems for the study of microtubule-based cell polarity in fission yeast. *Methods in cell biology*, 128:1–22, 2015. http://www.sciencedirect.com/science/article/pii/S0091679X15000710.

Taberner Carretero, N. *A minimal system to establish microtubule-based cell polarity in vitro*. PhD thesis, 2016.

Teixidó-Travesa, N., Roig, J., and Lüders, J. The where, when and how of microtubule nucleation–one ring to rule them all. *J Cell Sci*, 125(19):4445–4456, 2012. https://jcs.biologists.org/content/125/19/4445.short.

Thawani, A., Stone, H. A., Shaevitz, J. W., and Petry, S. Molecular mechanism of microtubule nucleation from gamma-tubulin ring complex. *bioRxiv*, page 853010, 2019.

Théry, M., Racine, V., Piel, M., Pépin, A., Dimitrov, A., Chen, Y., Sibarita, J.-B., and Bornens, M. Anisotropy of cell adhesive microenvironment governs cell internal organization and orientation of polarity. *Proceedings of the National Academy of Sciences*, 103(52):19771–19776, 2006. https://www.pnas.org/content/103/52/19771.short.

Theurkauf, W. E. Premature microtubule-dependent cytoplasmic streaming in cappuccino and spire mutant oocytes. *Science*, 265(5181):2093–2096, 1994. https://science.sciencemag.org/content/265/5181/2093.

Tilney, L. G., Bryan, J., Bush, D. J., Fujiwara, K., Mooseker, M. S., Murphy, D. B., and Snyder, D. H. Microtubules: evidence for 13 protofilaments. *The Journal of cell biology*, 59(2):267–275, 1973. https://rupress.org/jcb/article/59/2/267/18231/MICROTUBULES-EVIDENCE-FOR-13-PROTOFILAMENTS.

Tirnauer, J. S., Grego, S., Salmon, E., and Mitchison, T. J. Eb1–microtubule interactions in xenopus egg extracts: role of eb1 in microtubule stabilization and mechanisms of targeting to microtubules. *Molecular biology of the cell*, 13(10):3614–3626, 2002.

Toya, M., Kobayashi, S., Kawasaki, M., Shioi, G., Kaneko, M., Ishiuchi, T., Misaki, K., Meng, W., and Takeichi, M. Camsap3 orients the apical-to-basal polarity of microtubule arrays in epithelial cells. *Proceedings of the National Academy of Sciences*, 113(2):332–337, 2016. http://www.pnas.org/content/113/2/332.full.

Tran, P., Marsh, L., Doye, V., Inoue, S., and Chang, F. A mechanism for nuclear positioning in fission yeast based on microtubule pushing. *The Journal of cell biology*, 153(2):397–412, 2001.

Tsai, M.-Y. and Zheng, Y. Aurora a kinase-coated beads function as microtubule-organizing centers and enhance rangtp-induced spindle assembly. *Current biology*, 15(23):2156–2163, 2005. https://www.sciencedirect.com/science/article/pii/S0960982205013072.

Turing, A. M. The chemical basis of morphogenesis. *Philosophical Transactions of the Royal Society of London B: Biological Sciences*, 237(641):37–72, 1952. rstb.royalsocietypublishing.org/content/royptb/237/641/37.full.pdf.

Tymanskyj, S. R., Yang, B. H., Verhey, K. J., and Ma, L. Map7 regulates axon morphogenesis by recruiting kinesin-1 to microtubules and modulating organelle transport. *Elife*, 7:e36374, 2018. https://elifesciences.org/articles/36374.

Vale, R. D. and Milligan, R. A. The way things move: looking under the hood of molecular motor proteins. *Science*, 288(5463):88–95, 2000.

Vale, R. D., Reese, T. S., and Sheetz, M. P. Identification of a novel force-generating protein, kinesin, involved in microtubule-based motility. *Cell*, 42(1):39–50, 1985.

Van Den Heuvel, M., Bolhuis, S., and Dekker, C. Persistence length measurements from stochastic single-microtubule trajectories. *Nano letters*, 7(10):3138–3144, 2007.

van Haren, J., Charafeddine, R. A., Ettinger, A., Wang, H., Hahn, K. M., and Wittmann, T. Local control of intracellular microtubule dynamics by eb1 photodissociation. *Nature Cell Biology*, page 1, 2018. https://www.nature.com/articles/s41556-017-0028-5.

Varga, V., Helenius, J., Tanaka, K., Hyman, A. A., Tanaka, T. U., and Howard, J. Yeast kinesin-8 depolymerizes microtubules in a length-dependent manner. *Nature cell biology*, 8(9):957–962, 2006.

Varga, V., Leduc, C., Bormuth, V., Diez, S., and Howard, J. Kinesin-8 motors act coop-

eratively to mediate length-dependent microtubule depolymerization. *Cell*, 138 (6):1174–1183, 2009.

Vendel, K. J., Tschirpke, S., Shamsi, F., Dogterom, M., and Laan, L. Minimal in vitro systems shed light on cell polarity. *J Cell Sci*, 132(4):jcs217554, 2019. http://jcs.biologists.org/content/132/4/jcs217554.abstract.

Vendel, K. J., Alkemade, C., Andrea, N., Koenderink, G. H., and Dogterom, M. In vitro reconstitution of dynamic co-organization of microtubules and actin filaments in emulsion droplets. In *Cytoskeleton Dynamics*, pages 53–75. Springer, 2020. https://link.springer.com/protocol/10.1007/978-1-0716-0219-5_5.

Venier, P., Maggs, A. C., Carlier, M.-F., and Pantaloni, D. Analysis of microtubule rigidity using hydrodynamic flow and thermal fluctuations. *Journal of biological chemistry*, 269(18):13353–13360, 1994.

Vitre, B., Coquelle, F. M., Heichette, C., Garnier, C., Chrétien, D., and Arnal, I. Eb1 regulates microtubule dynamics and tubulin sheet closure in vitro. *Nature cell biology*, 10(4):415, 2008. https://www.nature.com/articles/ncb1703.

Vladar, E. K., Bayly, R. D., Sangoram, A. M., Scott, M. P., and Axelrod, J. D. Microtubules enable the planar cell polarity of airway cilia. *Current Biology*, 22(23): 2203–2212, 2012. http://www.sciencedirect.com/science/article/pii/S0960982212011487.

Vleugel, M., Roth, S., Groenendijk, C. F., and Dogterom, M. Reconstitution of basic mitotic spindles in spherical emulsion droplets. *J. Vis. Exp*, 2016:e54278, 2016. http://www.jove.com/video/54278/.

Voter, W. A. and Erickson, H. P. The kinetics of microtubule assembly. evidence for a two-stage nucleation mechanism. *Journal of Biological Chemistry*, 259(16): 10430–10438, 1984. http://www.jbc.org/content/259/16/10430.short.

Wade, R. H., Chrétien, D., and Job, D. Characterization of microtubule protofilament numbers: how does the surface lattice accommodate? *Journal of molecular biology*, 212(4):775–786, 1990.

Walker, R., O'brien, E., Pryer, N., Soboeiro, M., Voter, W., Erickson, H., and Salmon, E. Dynamic instability of individual microtubules analyzed by video light microscopy: rate constants and transition frequencies. *The Journal of cell biology*, 107(4):1437–1448, 1988. https://rupress.org/jcb/article/107/4/1437/58973/Dynamic-instability-of-individual-microtubules.

Wang, H., Vilela, M., Winkler, A., Tarnawski, M., Schlichting, I., Yumerefendi, H., Kuhlman, B., Liu, R., Danuser, G., and Hahn, K. M. Lovtrap: an optogenetic system for photoinduced protein dissociation. *Nature methods*, 13(9):755, 2016. https://www.nature.com/articles/nmeth.3926.

Wang, X., He, L., Wu, Y. I., Hahn, K. M., and Montell, D. J. Light-mediated activation reveals a key role for rac in collective guidance of cell movement in vivo. *Nature cell biology*, 12(6):591–597, 2010.

Watanabe, T., Wang, S., Noritake, J., Sato, K., Fukata, M., Takefuji, M., Nakagawa, M., Izumi, N., Akiyama, T., and Kaibuchi, K. Interaction with iqgap1 links apc to rac1, cdc42, and actin filaments during cell polarization and migration. *Developmental cell*, 7(6):871–883, 2004.

Wedlich-Soldner, R., Altschuler, S., Wu, L., and Li, R. Spontaneous cell polarization through actomyosin-based delivery of the cdc42 gtpase. *Science*, 299(5610):1231–1235, 2003. http://science.sciencemag.org/content/299/5610/1231.short.

Wedlich-Soldner, R., Wai, S. C., Schmidt, T., and Li, R. Robust cell polarity is a dynamic state established by coupling transport and gtpase signaling. *The Journal of cell biology*, 166(6):889–900, 2004. http://jcb.rupress.org/content/166/6/889.short.

Wen, W. and Zhang, M. Protein complex assemblies in epithelial cell polarity and asymmetric cell division. *Journal of Molecular Biology*, 2017. http://www.sciencedirect.com/science/article/pii/S0022283617304503.

Wen, Y., Eng, C. H., Schmoranzer, J., Cabrera-Poch, N., Morris, E. J., Chen, M., Wallar, B. J., Alberts, A. S., and Gundersen, G. G. Eb1 and apc bind to mdia to stabilize microtubules downstream of rho and promote cell migration. *Nature cell biology*, 6(9):820, 2004.

Westermann, S. and Weber, K. Post-translational modifications regulate microtubule function. *Nature Reviews Molecular Cell Biology*, 4(12):938, 2003.

Wieczorek, M., Bechstedt, S., Chaaban, S., and Brouhard, G. J. Microtubule-associated proteins control the kinetics of microtubule nucleation. *Nature cell biology*, 17(7):907, 2015. https://www.nature.com/articles/ncb3188.

Wieczorek, M., Urnavicius, L., Ti, S.-C., Molloy, K. R., Chait, B. T., and Kapoor, T. M. Asymmetric molecular architecture of the human γ-tubulin ring complex. *Cell*, 180(1):165–175, 2020.

Wiese, C. and Zheng, Y. Microtubule nucleation: gamma-tubulin and beyond. *Journal of Cell Science*, 119(20):4143–4153, 2006. ISSN 0021-9533. doi: 10.1242/jcs.03226. http://jcs.biologists.org/content/119/20/4143.

Witte, K., Strickland, D., and Glotzer, M. Cell cycle entry triggers a switch between two modes of cdc42 activation during yeast polarization. *Elife*, 6, 2017. https://www.ncbi.nlm.nih.gov/pmc/articles/PMC5536948/.

Woodruff, J. B., Wueseke, O., and Hyman, A. A. Pericentriolar material structure and dynamics. *Phil. Trans. R. Soc. B*, 369(1650):20130459, 2014. http://rstb.royalsocietypublishing.org/content/369/1650/20130459.short.

Woodruff, J. B., Wueseke, O., Viscardi, V., Mahamid, J., Ochoa, S. D., Bunkenborg, J., Widlund, P. O., Pozniakovsky, A., Zanin, E., Bahmanyar, S., et al. Regulated assembly of a supramolecular centrosome scaffold in vitro. *Science*, 348(6236):808–812, 2015. http://science.sciencemag.org/content/348/6236/808.

Woodruff, J. B., Gomes, B. F., Widlund, P. O., Mahamid, J., Honigmann, A., and Hyman, A. A. The centrosome is a selective condensate that nucleates microtubules by concentrating tubulin. *Cell*, 169(6):1066–1077, 2017. http://www.sciencedirect.com/science/article/pii/S0092867417305895.

Wu, C.-F. and Lew, D. J. Beyond symmetry-breaking: competition and negative feedback in gtpase regulation. *Trends in cell biology*, 23(10): 476–483, 2013. https://www.sciencedirect.com/science/article/pii/S096289241300086X?via%3Dihub.

Wu, Y. I., Frey, D., Lungu, O. I., Jaehrig, A., Schlichting, I., Kuhlman, B., and Hahn, K. M. A genetically encoded photoactivatable rac controls the motility of living cells. *Nature*, 461(7260):104–108, 2009. http://www.nature.com/nature/journal/v461/n7260/abs/nature08241.html.

Yadav, S., Verma, P. J., and Panda, D. C-terminal region of map7 domain containing protein 3 (map7d3) promotes microtubule polymerization by binding at the c-terminal tail of tubulin. *PloS one*, 9(6):e99539, 2014. https://journals.plos.org/plosone/article?id=10.1371/journal.pone.0099539.

Yao, X., Rosen, M. K., and Gardner, K. H. Estimation of the available free energy in a lov2-jα photoswitch. *Nature chemical biology*, 4(8):491, 2008. https://www.nature.com/articles/nchembio.99.

Yazawa, M., Sadaghiani, A. M., Hsueh, B., and Dolmetsch, R. E. Induction of protein-protein interactions in live cells using light. *Nature biotechnology*, 27(10):941–945, 2009. https://www.nature.com/articles/nbt.1569.

Yi, K., Rubinstein, B., and Li, R. Symmetry breaking and polarity establishment during mouse oocyte maturation. *Philosophical Transactions of the Royal Society B: Biological Sciences*, 368(1629):20130002, 2013. https://royalsocietypublishing.org/doi/10.1098/rstb.2013.0002.

Yoo, S. K., Deng, Q., Cavnar, P. J., Wu, Y. I., Hahn, K. M., and Huttenlocher, A. Differential regulation of protrusion and polarity by pi (3) k during neutrophil motility in live zebrafish. *Developmental cell*, 18(2):226–236, 2010.

Yoo, S. K., Lam, P.-y., Eichelberg, M. R., Zasadil, L., Bement, W. M., and Huttenlocher, A. The role of microtubules in neutrophil polarity and migration in live zebrafish. *J Cell Sci*, 125(23):5702–5710, 2012. http://jcs.biologists.org/content/125/23/5702.eLetters.

Zanic, M., Stear, J. H., Hyman, A. A., and Howard, J. Eb1 recognizes the nucleotide state of tubulin in the microtubule lattice. *PloS one*, 4(10): e7585, 2009. https://journals.plos.org/plosone/article?id=10.1371/journal.pone.0007585.

Zanic, M., Widlund, P. O., Hyman, A. A., and Howard, J. Synergy between xmap215 and eb1 increases microtubule growth rates to physiological levels. *Nature cell biology*, 15(6):688, 2013. https://www.nature.com/articles/ncb2744.

ACKNOWLEDGEMENTS

Due to COVID-19, the last part of my PhD looked differently than I imagined, and also the defense will not be what I pictured throughout the last four years. Even though being in lockdown turned out to be pretty beneficial for writing productivity, I realized once again what a great environment the BN department is, how important colleagues are for work pleasure and that friends, family and sports were the things that kept me sane during my PhD.

First of all, I want to thank Marileen for being my supervisor. As a PhD student in your lab, one has lots of freedom and responsibility. Nevertheless, you were always available when I really needed your help. Thanks for guiding me through the PhD while letting me take charge and find my own way, I've grown a lot.

Next, I would like to thank the FOM consortium on cell polarity for the fun yearly meetings that always resulted in new ideas. I also owe a great deal to the lab of Anna Akhmanova, as most of the proteins I used were generous gifts from them. In a similar manner, I am grateful to Tim Mitchison and James Pelletier for supplying the functionalized beads which saved my experiments when I got stuck with the centrosomes. Without those beads about half of this thesis would not exist.

Our lab has been a warm place where I could be myself and be accepted just like that. I enjoyed our barbecues, labtrips, game nights, microtubule meetings, kubb games and countless delicious homemade cakes! But most of all I loved our joined lunches, coffee breaks and random chitchat in the lab or office. Dear all, I'm sad to leave and I'm going to miss you so much!
Essie and Renu, my fellow crazy-plant-ladies. How much I liked our walks and raids for plant pots at the second hand shop. The sudden appearance of new plants on our desks that "nobody knew where they came from". I will cherish the plants and cuttings from my time at BN. Renu, I loved to have you as an office mate and to team up in the battle of the droplets. I am grateful for all the laughs and daily little big things that we shared. Esengül, thanks for your company on many walks to escape the building, for your social energy and for running the lab so organized, neat and tidy. Louis, it was great fun sharing an office with you. I admire your original way of thinking and learned a lot from your view on science and life. Roland, I hope you realize how much I liked our discussions, they often forced me to look at things from a different point of view. As soon as we have a suitable garden I come to you to discuss apple tree decisions! Vladimir, you're not blunt and direct like Sinterklaas once wrote.. You're honest, passionate about science and always in for everything social. Thanks for being you and for your feedback on my chapters. Eli, beware, slowly you are starting to like cycling as much as I do. Your calm and friendly presence always makes the lab a happy place. Maurits, when I started you were my (somewhat terrifying) example of the senior PhD

student that seemed to know everything about anything. Thanks for being such a great example. Reza, you're the senior PhD student now. Good luck with your bacterial microtubules and remember to climb a lot whenever you get stressed. Anne, thanks for the fun gamenights and all the best in Germany with your new job and house! Tomo, your presence in our lab this year is valuable. I hope it also is for you. Ilina, it's a tough time to start a new life in a new country during a lockdown. I hope you'll find your place in The Netherlands soon and come visit me in my new town. Yash, silent and independent, but determined to get those light-sensitive dyneins working, I hope you'll succeed! Celine, it was fun to work with you on centrosomes or combining actin and microtubules in droplets. Ashmiani, our lab radio, your presence always brightens up the lab. Nemo, Jard, Hester and Erik. It was fun to work with you and I learned a lot from taking on the supervisor role. You all contributed to the research in our lab and especially to the work that's written down in this thesis.

Of course many more people made my time at BN a pleasant experience: Johannes, Nuria, Mathijs, Marian Harmen, Marco, Andrea, Liedewij, Sophie, Fayezeh, Roland K., Siddharth, Anthony, Greg, Federico, Sonja, Martin, Kasper, Nicole, Pauline, Alicia, Jonás, Jeremie, Sacha, Theo, Erwin, Jeff, Ilja, Jolijn, Esther, Christophe.

Eveline, without your help I would not even have considered starting a PhD let alone been able to do it the relatively positive and relaxed way I did. I will always be grateful for everything I learned from you and the self-confidence and freedom I gained since then.

During these four years, sports has been an important way to relax, deal with stress or get satisfaction when research was hard. Thanks to my climbing buddies from the last years, Bobo, Jing, Magali, Roland, Dominik, Wim, Mike, Ellen. It's impossible to be stressed about anything else when hanging on to tiny grips on the wall trying not to fall or while puzzling on how to get through a challenging boulder. TC de Kampioen, even though the frequency of me joining dropped since I moved to Delft, I have such great memories of cycling with you guys. Especially the Ardens, Italy with the Stelvio and the Twaalf Provinviëntocht showed me that I'm much stronger than I thought.

Mariëlle, we first met at the very beginning of my PhD and now I am so lucky with you as a friend. We cycled the mountains, traveled through Thailand, shared our high and low points of the last years and now we're both starting in a new job. I am grateful to know that you are always there for me, and I can't wait until December..!! Jet, our friendship goes way back and I still see us as 16/17-year olds wearing labcoats and pipetting in the LUMC or trying to read medical papers. Our beautiful Stubaier Höhenweg hike is still one of my best holidays. Thanks for so many years of friendship. Irina, thanks for being such a funny person, good listener and sweet friend. I always enjoy talking to you over a cup of tea, it is valuable to have a friend with similar experiences as me. Qian Wei, I love how you have your own way of living life, usually totally different than I would do or feel, and I love how that doesn't matter for our friendship. Annelies, we share many good memories from studying, Rino, bestuursjaar, Hilebrandpad, etc. I'm happy to know that I can always reminisce about them with you. Steffie, I enjoyed our lunches and dinners during our time at TU Delft, it was

nice to share the PhD experience with a friend in the same situation.

Mamma, dank je dat je ook nu ik al 29 ben mijn mamma blijft die er altijd voor me is, dat ik met je kan praten en mijn zorgen of twijfels kan delen, dat je meedenkt en adviezen geeft en dat je dat allemaal zo goed kan omdat je me al 29 jaar kent. Ik ben heel blij en dankbaar dat we samen door de Himalaya zijn getrokken, letterlijk en figuurlijk een hoogtepunt.
Pappa, ik kom er steeds meer achter hoeveel ik op je lijk. We delen onze liefde voor boeken en alles wat groeit, bloeit en zoemt, we delen een behoefte aan rust en alleen zijn, maar ook delen we onze zorgen over natuur, milieu en de wereld. Ik ben dankbaar voor onze jaarlijkse culturele avondjes en de vele kleine contacten over plantjes, boeken, insecten, gedachtes, etc. Ik weet dat je de epigrafen in mijn proefschrift over onze kleine grote helden kan waarderen.
Mirte, dankjewel voor de mooie cover. Ik ben blij dat we tegelijkertijd in Delft hebben gewoond en daar zoveel zussen-avondjes hebben gehad. Soms heb ik het gevoel dat jij de oudste en meest volwassene van ons twee bent met je wijze adviezen. Ik ben trots op je!
Sjoerd, het voelt goed om een broer te hebben die zoveel op me lijkt, zowel qua hobby's als qua innerlijk en humor. Sri Lanka, Tour du Mont Blanc, multipitch rotsklimmen; ik ben blij dat we de afgelopen jaren zoveel samen hebben beleefd en hoop dat we dit blijven doen.

Carla en Adriaan, Martine en Arjan, Emma en Lex en ook Céline, Aimée en Wouter, bedankt voor het warme welkom in de familie. Ik kan me geen leukere schoonfamilie wensen.

Finally yet most importantly, lieve Karel, zelfs een corona lockdown en samen thuiswerken op onze 38 m^2 slaat ons niet uit het veld. Ik had nooit gedacht zoveel tijd met iemand door te kunnen brengen en daar nog gelukkig van te worden ook. Bedankt voor je liefde en geduld in dit stressvolle jaar, voor je positieve instelling, grenzeloze enthousiasme en alle gekke plannen die we samen hebben.

CURRICULUM VITÆ

Kim Jikke Anna VENDEL

19-03-1991 Born in Amsterdam, The Netherlands.

EDUCATION

2003–2009 Stedelijk Gymnasium Haarlem

2007–2008 Pre-University College
Leiden University

2009–2013 Bachelor in Physics & Bachelor in Astronomy
Leiden University

2013–2015 Master in Physics
Leiden University

2016–2020 PhD. Biophysics
Delft University of Technology
Thesis: On the role of microtubules in cell polarity: A reconstituted minimal system
Promotor: Prof. dr. M. Dogterom

LIST OF PUBLICATIONS

5. **K.J.A. Vendel** and M. Dogterom, *Reconstitution of microtubule capture at the cortex mediated by end-binding proteins*, in preparation.

4. **K.J.A. Vendel**[†], C. Alkemade[†], N. Andrea, G. Koenderink and M. Dogterom, *In vitro reconstitution of dynamic co-organization of microtubules and actin filaments in emulsion droplets*, Cytoskeleton Dynamics, p. 53–75 (2020).

3. **K.J.A. Vendel**[†], S. Tschirpke[†], F. Shamsi, M. Dogterom and L. Laan, *Minimal in vitro systems shed light on cell polarity*, Journal of Cell Science **4**, 132 (2019).

2. F. Mariani, F. de León-Pérez, **K.J.A. Vendel**, L. Martín-Moreno and M.P. van Exter, *Angle resolved transmission through metal hole gratings*, Optics Express **8**, 25 (2017).

1. F. Silvestri, F.B. Arango, **K.J.A. Vendel**, G. Gerini, S.M.B. Bäumer and A.F. Koenderink, *Optical antennas for far and near field metrology*, 2016 10th European Conference on Antennas and Propagation (EuCAP), IEEE, p.1–4 (2016).

[†]contributed equally to this work